Search for solar chameleons with an InGrid based X-ray detector at the CAST experiment

Dissertation
zur
Erlangung des Doktorgrades (Dr. rer. nat.)
der
Mathematisch-Naturwissenschaftlichen Fakultät
der
Rheinischen Friedrich-Wilhelms-Universität Bonn

von
Christoph Krieger
aus
Engelskirchen

Bonn, 2017

Dieser Forschungsbericht wurde als Dissertation von der Mathematisch-Naturwissenschaftlichen Fakultät der Universität Bonn angenommen und ist auf dem Hochschulschriftenserver der ULB Bonn `http://hss.ulb.uni-bonn.de/diss_online` elektronisch publiziert.

1. Gutachter:	Prof. Dr. Klaus Desch
2. Gutachter:	Prof. Dr. Jochen Dingfelder

Tag der Promotion:	28.06.2018
Erscheinungsjahr:	2018

Abstract

Chameleons are particles with a density dependent effective mass and couplings to matter as well as photons. They are introduced in modifications to General Relativity involving scalar fields and aiming at explaining Dark Energy, which is needed for the observed self-accelerated expansion of the universe. Chameleons can be produced in the tachocline region of the Sun. On Earth these solar chameleons can be detected by axion helioscopes such as the CERN Axion Solar Telescope (CAST) where they are converted into low energy X-ray photons inside a strong magnet pointed towards the Sun. Due to weak couplings corresponding to a very low number of expected signal events, X-ray detectors with low background rates and high efficiency are required.

In this thesis an X-ray detector based on the GridPix technology, a pixelized readout combined with an integrated gas amplification stage, was developed and built. This detector, which features a low energy threshold and allows for an eventshape based background suppression, was characterized at a variable X-ray generator and afterwards commissioned at CAST behind an X-ray telescope. From the data taken at CAST in 2014 and 2015 with this detector an improved upper bound on the chameleon photon coupling was derived.

Zusammenfassung

Chamäleons sind Teilchen deren effektive Masse dichteabhängig ist und die an Materie sowie Photonen koppeln. Sie sind Teil von Modifikationen der Allgemeinen Relativitätstheorie, die skalare Felder beinhalten und Dunkle Energie erklären sollen, welche für die beobachtete, sich beschleunigende Expansion des Universums benötigt wird. Chamäleons können in der Tachocline der Sonne produziert werden. Diese solaren Chamäleons können auf der Erde mit Axion Helioskopen, wie dem CERN Axion Solar Telescope (CAST), nachgewiesen werden in dem sie in einem starken, auf die Sonne gerichteten Magneten in niederenergetische Röntgenphotonen umgewandelt werden. Aufgrund der schwachen Kopplungen und entsprechend niedrigen Anzahl an erwarteten Ereignissen, benötigt man dazu hocheffiziente Röntgendetektoren mit niedrigen Untergrundraten.

Im Rahmen dieser Arbeit wurde ein Röntgendetektor entwickelt und gebaut, welcher auf der GridPix-Technologie, der Kombination einer pixelierten Auslese mit einer integrierten Gasverstärkungsstufe, basiert. Dieser Detektor besitzt eine niedrige Detektionsschwelle und erlaubt eine Untergrundunterdrückung basierend auf der Form der Ereignisse. Der Detektor wurde an einer variablen Röntgenquelle charakterisiert und anschließend bei CAST hinter einem Röntgenteleskop in Betrieb genommen. Mittels der Daten, welche mit diesem Detektor 2014 und 2015 bei CAST gesammelt wurden, konnte ein verbessertes oberes Limit für die Chamäleon-Photon-Kopplung bestimmt werden.

Contents

CHAPTER 1

Introduction

Within the last ten years two satellite missions, the Wilkinson Microwave Anisotropy Probe (WMAP) [1] and the Planck Surveyor [2], have precisely mapped the cosmic microwave background in order to look for anisotropies. The results of these indicate that the total energy density in our universe is dominated by two contributions, Dark Energy and Dark Matter. Both contributions are required to arrive at an almost flat universe, as it is observed. While Dark Matter is a new kind of matter almost exclusively interacting gravitationally, Dark Energy, as by the far the largest contribution to the total energy density, is driving the observed, self-accelerating expansion of the universe.

One of the possible ways to introduce Dark Energy is the modification of General Relativity (GR) with a scalar field coupling to matter. To avoid unnatural effects, such as a long range fifth force, the chameleon screening mechanism can be applied, which results in the scalar particle arising from the introduced field to receive a density dependent effective mass. Hence, this particle is called chameleon and features a coupling to matter as well as in some models to photons.

If chameleons exist they could be produced in the strong magnetic field of the tachocline region of the Sun in a process similar to the Primakoff effect for axions. Therefore, helioscope experiments, such as the CERN Axion Solar Telescope (CAST), looking for solar axions can also be used to search for solar chameleons. For the solar chameleon search at helioscopes, highly efficient X-ray detectors sensitive to X-ray photons below 2 keV and with low background rates are required.

In the course of this thesis an X-ray detector based on the GridPix technology, a combination of a pixelized readout with an integrated gas amplification stage, was developed, built and characterized. Through its high spatial resolution and capability to detect individual electrons, this kind of detector features a very low energy threshold and allows for an eventshape based background suppression. The detector was commissioned at CAST behind an X-ray optic, the MPE X-ray telescope (XRT). There the detector was operated successfully from late 2014 until end of 2015 continuing CAST's search for solar chameleons. In this thesis, the detector, the results from its characterization and operation as well as an improved bound on the chameleon photon coupling will be presented.

As the search for solar chameleons at CAST is based on the helioscope approach introduced for the solar axion search, in chapter 2 the axion will be briefly introduced including the principle of helioscope experiments searching for solar axions. Chapter 3 shortly covers the chameleon, its origin and possible production in the solar tachocline. CAST will be described in chapter 4 including a short summary of its previous searches for solar axions and chameleons. Chapter 5 covers the physics and basic principles of a gaseous X-ray detector before in chapter 6 the GridPix (or Integrated Grid (InGrid)) technology is introduced. The InGrid based X-ray detector developed and built in the course of this thesis is described in chapter 7 including its characterization at the variable X-ray generator in the CAST Detector Lab (CDL).

Chapter 8 covers the commissioning of the detector at CAST and behind the MPE XRT. A short summary of the data taking campaign 2014 and 2015 is given in chapter 9, before the data reconstruction and especially the background suppression method including the resulting background rates are presented in chapter 10. The derivation of an improved upper bound on the chameleon photon coupling from the data taken at CAST is explained in chapter 11. Chapter 12 gives a brief description of an upgraded version of the InGrid based X-ray detector, which was developed and installed at CAST late in 2017 and will presumably take data until March 2018 continuing the search for solar chameleons and solar axions at CAST.

CHAPTER 2

The QCD axion – A Dark Matter candidate

The strong CP problem is the non-observation of CP violation in strong interaction, which, among other observables, manifests itself in the absence of an electric dipole moment for the neutron. It can be solved in an elegant way via the Peccei-Quinn mechanism. The Peccei-Quinn mechanism involves the introduction of a new symmetry, which is spontaneously broken, giving rise to the axion, a pseudoscalar Goldstone boson, which acquires a small mass and features only weak couplings to ordinary matter. Common to all axion models is a (direct or indirect) coupling of axions to two photons allowing for conversion of photons into axions, and vice versa, in the presence of electromagnetic fields, the Primakoff effect. Through its low mass and weak couplings, resulting in a high lifetime, the axion provides a valuable candidate for Dark Matter.

In this chapter, the strong CP problem as well as the Peccei-Quinn mechanism will be briefly introduced followed by the axion interactions with ordinary matter including the Primakoff effect. The axion's ability to provide a Dark Matter candidate will be discussed as well as axion like particles (ALPs), particles with similar properties like the axion but unrelated to the strong CP problem.

Different approaches are followed to search for axions (and ALPs), which can be divided into three types of experiments: haloscope experiments, helioscope experiments and laboratory experiments. The different approaches will be briefly discussed with a focus on the helioscope approach utilizing axion to photon conversion in strong magnetic fields (inverse Primakoff effect) as applied for the CERN Axion Solar Telescope (CAST). CAST will be introduced in chapter 4.

2.1 The strong CP problem

The strong CP problem arises from the term $\mathcal{L}_\theta$, which appears as part of the Lagrangian of Quantum Chromodynamics (QCD) as a consequence of solving the $\mathrm{U_A(1)_A}$ problem [3] through an anomalous breaking of the $\mathrm{U(1)_A}$ symmetry [4, 5]. The Lagrangian of QCD can be given as

$$\mathcal{L}_{\mathrm{QCD}} = \sum_n \bar{q}_n(\gamma^\mu iD_\mu - m_n)q_n - \frac{1}{4}G^a_{\mu\nu}G^{\mu\nu}_a + \underbrace{\theta\frac{g^2}{32\pi^2}G^a_{\mu\nu}\tilde{G}^{\mu\nu}_a}_{\mathcal{L}_\theta} \tag{2.1}$$

where n are the quark flavours, q_n the quark fields and m_n the quark masses. D_μ is the covariant derivative defined as

$$D_\mu = \partial_\mu - igT^aG^a_\mu \tag{2.2}$$

with G^a the gluon field tensors with colour index $a = 1 \dots 8$, g the coupling constant of strong interaction and T^a the generators of the group SU(3). $\tilde{G}_a^{\mu\nu}$ is the dual of the gluon field tensor, defined as

$$\tilde{G}_a^{\mu\nu} = \frac{1}{2}\epsilon^{\mu\nu\rho\sigma} G_{\rho\sigma}^a, \tag{2.3}$$

and θ is an arbitrary parameter, which can be between 0 and 2π. When electroweak interactions are taken into account θ is replaced by

$$\bar{\theta} = \theta + \theta_{\text{weak}}. \tag{2.4}$$

For $\bar{\theta} \neq 0$ the Lagrangian of strong interaction $\mathcal{L}_{\text{QCD}}$ is not invariant under CP transformations, resulting in the prediction of CP violation in strong interaction, which is not observed experimentally. An example for an observable related to CP violation in the strong interaction is the electric dipole moment of the neutron d_n, the existence of the latter would directly translate into an observed violation of CP in the strong interaction. But, latest measurement give an upper limit of $|d_n| < 2.9 \times 10^{-26}\, e\,\text{cm}$ [6].

The non-observation of any CP violation in the strong interaction would require $\bar{\theta}$ to be zero or very small, e.g. the measured upper limit for the electric dipole moment of the neutron can be translated into $\bar{\theta} < 10^{-10}$. There is no ad-hoc reason for $\bar{\theta}$ to be zero or as small as required to fit the observations, also there is no reason why θ and θ_{weak} should cancel each other. The question why $\bar{\theta}$ has such s small value, is known as the strong CP problem.

Basically, there are three possible solutions for the strong CP problem. One could set one quark mass to zero, which would eliminate the parameter θ, but this would have to be justified with physics beyond the Standard Model (SM). Another approach is to set θ to zero, but this still does not cause $\bar{\theta}$ to become zero and, additionally, would generate problems regarding the CP violation in the weak interaction. A third approach is given by the Peccei-Quinn mechanism, which is an elegant way to solve the strong CP problem not requiring any fine tuning.

2.2 The Peccei-Quinn mechanism

The Peccei-Quinn mechanism was introduced by Peccei and Quinn in 1977 [7], it is one of the most favoured solutions to the strong CP problem. By introducing a new global, chiral symmetry U(1)_{PQ}, the Peccei-Quinn symmetry, which is spontaneously broken at an energy scale f_a, $\bar{\theta}$ is promoted to the role of a dynamic variable of the theory instead of a static parameter. This implies that different values of $\bar{\theta}$ correspond to different vacuum states instead of different theories. Showing that $\bar{\theta} = 0$ is the true vacuum state, the strong CP problem is solved in an elegant way.

As the Peccei-Quinn symmetry is spontaneously broken, a new Goldstone boson is introduced, the axion[1], which is a pseudoscalar particle. Through the axial anomaly and instanton interactions, the axion acquires a small mass [8, 9]. The coupling of gluons to the axion field a is described by

$$\mathcal{L}_a = \frac{a}{f_a}\xi\frac{g^2}{32\pi^2}G_{\mu\nu}^b\tilde{G}_b^{\mu\nu} \tag{2.5}$$

where ξ is a model dependent theory parameter and g the coupling constant of strong interaction. The

---

[1] The particle was named axion after an American detergent by Wilczek as it cleans up a long standing problem in theoretical physics, the strong CP problem [8].

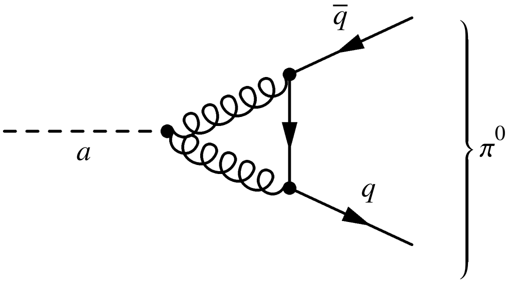

Figure 2.1: Feynman graph showing the mixing between axion and neutral pion by means of the axion gluon coupling. Figure taken from [10].

expectation value for the axion field a can be derived as

$$\langle a \rangle = -\frac{f_a}{\xi}\bar{\theta} \tag{2.6}$$

and leads to canceling of $\mathcal{L}_{\bar{\theta}}$ in the QCD Lagrangian. The mass of the axion can be calculated from the expectation value $\langle a \rangle$ by looking at the curvature of the effective potential around its minimum to be

$$m_a^2 = -\frac{\xi}{f_a}\frac{g^2}{32\pi^2}\frac{\partial}{\partial a}\left\langle G_b^{\mu\nu}\tilde{G}_{\mu\nu}^b\right\rangle\Big|_{\langle a \rangle = -\frac{f_a}{\xi}\bar{\theta}}. \tag{2.7}$$

2.3 Axion interactions with ordinary matter

The axion can be described by its mass m_a and its couplings to other particles g_{ai} (i is the other particle, e.g. γ), both are anti-proportional to the energy scale f_a at which the Peccei-Quinn symmetry is broken. The coupling to other particles, especially to which particles the axion couples, depends strongly on the axion model. Common to most axion models is the axion gluon coupling, which is described by the interaction part of the Lagrangian

$$\mathcal{L}_{aG} = -\frac{\alpha_s}{8\pi f_a} a G_b^{\mu\nu}\tilde{G}_{\mu\nu}^b \tag{2.8}$$

where α_s is the finestructure constant of the strong interaction. The coupling to gluons also implies the axion coupling to two photons due to mixing with the neutral pion, which is depicted in the Feynman graph in Fig. 2.1. This mixing is possible because axion and neutral pion share the same quantum numbers. Thus, also a coupling of axions to two photons is common to most axion models and would allow a decay channel into two photons. As one of the two photons may be virtual a photon can be converted into an axion in the presence of an electromagnetic field, this is described by the Primakoff effect.

The axion models can be divided into visible and invisible axion models of which the visible axion models already have been excluded only leaving the invisible axion with a small mass and weak couplings to ordinary matter.

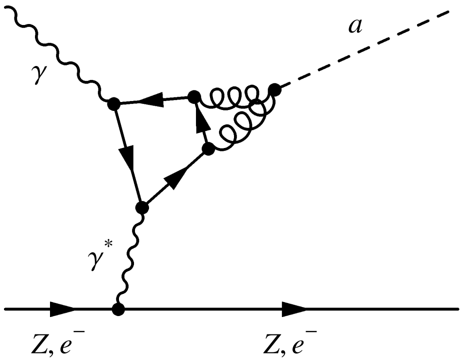

Figure 2.2: Feynman graph showing the Primakoff effect for axions implemented with the axion gluon coupling present in almost all axion models. Figure taken from [10].

2.3.1 The Primakoff effect

The Primakoff effect describes the conversion of a photon to an axion in the presence of an electromagnetic field and vice versa. This coupling can be described by

$$\mathcal{L}_{a\gamma} = -\frac{1}{4} g_{a\gamma} F_{\mu\nu} \tilde{F}^{\mu\nu} a = g_{a\gamma} \vec{E} \cdot \vec{B} \cdot a \tag{2.9}$$

where $F_{\mu\nu}$ is the electromagnetic field strength tensor, $g_{a\gamma}$ the axion photon coupling constant, a the axion field, $\vec{E}$ and $\vec{B}$ are the electric and magnetic field respectively. The axion photon coupling constant can be expressed as

$$g_{a\gamma} = \frac{\alpha}{2\pi f_a} \left| \frac{E}{N} - \frac{2(4+z+w)}{3(1+z+w)} \right| \tag{2.10}$$

with α the finestructure constant, $z = m_u/m_d$ and $w = m_u/m_s$ the quark mass ratios. E/N is a model parameter, which varies between 0 and 6. Additional couplings, e.g. an axion fermion coupling, give further contributions to $g_{a\gamma}$ and are implemented in some of the axion models.

The conversion of a photon into an axion via the Primakoff effect in an electromagnetic field is depicted in the Feynman graph shown in Fig. 2.2 using only the axion gluon coupling. The Primakoff effect and its inverse (conversion of axions into photons in electromagnetic fields) is exploited in almost all searches for axions as it is more or less independent of the axion model under test.

2.3.2 Visible axion models

The visible axion model was the first model proposed by Peccei, Quinn, Weinberg and Wilczek [8, 9, 11]. For the visible axion model the symmetry breaking is assumed to happen at an energy scale $f_a < 42\,\text{GeV}$, which would result in an axion mass of $m_a \approx 200\,\text{keV}$ and a rather large coupling constant, which should have visible effects observable in experiments, hence the name visible axion.

The visible axion has been ruled out both by experiments and astrophysical constraints, e.g. it would imply the branching ratio of the decay of a positive charged kaon into a positive charged pion and an axion to be about one order of magnitude larger than the experimentally found upper bound [12].

2.3.3 Invisible axion models

For invisible axion models f_a is assumed to be much larger than the energy scale of the symmetry breaking in the weak interaction. Thus, the mass of invisible axions is small and the couplings to ordinary matter weak, making it hard to detect. At the same time, this implies a very long life time for invisible axions making it a suitable candidate for Dark Matter. The two most prominent invisible axion models are the KSVZ model, introduced by Kim, Shifman, Vainshtein and Zakharov [13, 14], and the DFSZ model, introduced by Dine, Fischler and Srednicki [15]. While in the KSVZ model axions only couple to gluons (and indirectly to photons), they couple to charged leptons, nucleons, and directly to photons in the DFSZ model.

2.4 The axion as a dark matter candidate

Its weak couplings and low mass make the axion a suitable candidate for Dark Matter. Taking into account the decay channel of axions decaying into two photons one can approximate the lifetime of an axion as [16]

$$\tau_a \approx 4.6 \times 10^{40}\,\mathrm{s} \cdot \left(\frac{E}{N} - 1.92\right)^{-2} \left(\frac{f_a/N}{10^{10}\,\mathrm{GeV}}\right)^{5}. \tag{2.11}$$

Assuming $E/N = 0$ and $f_a/N \geq 3 \times 10^5$ GeV, this gives an axion life time longer than the age of the universe ($\sim 10^{17}$ s). A light, neutral particle with only weak couplings and a long life time, indeed is a good candidate for Dark Matter. With the aforementioned assumptions the axion mass would be lower than 20 eV, which is also favoured considering astrophysical and cosmological constraints. The latter can also be used to derive upper bounds on the axion mass as well as on its coupling strength.

2.5 Axion like particles

For the axion related to the solution of the strong CP problem through the Peccei-Quinn mechanism, a dependence of the axion mass m_a on its coupling strength, e.g. to photons (see equation 2.10), is given through the model. For particles with similar properties as the axion, so called axion like particles (ALPs), mass and coupling strength can be decoupled. Often, the axion is called QCD axion to underline the difference to ALPs.

2.6 Detection of axions

To detect axions (or ALPs) the (inverse) Primakoff effect can be exploited as it allows to convert photons into axions or vice versa in strong electromagnetic fields. The experimental approaches for the detection of axions, especially invisible axions, can be divided into three branches [17, 18]. Those experiments looking for axions of galactic origin are called haloscope experiments while those looking for axions produced in the Sun are called helioscope experiments. In addition there are laboratory experiments, which try to produce and detect axions (or their implications on other observables) directly.

2.6.1 Haloscope experiments

Haloscope experiments rely on the assumption that axions indeed are (part of) Dark Matter and therefore are present everywhere. To convert those axions into detectable photons exploiting the inverse Primakoff effect, typically, a microwave cavity is exposed to a strong magnetic field. Usually, the cavity and connected microwave detectors are operated at cryogenic temperatures to reduce noise and increase the sensitivity. When axions, with a mass matching the resonance frequency of the cavity, are converted into photons, this results in an increase of the power inside the cavity, which can be measured by very sensitive

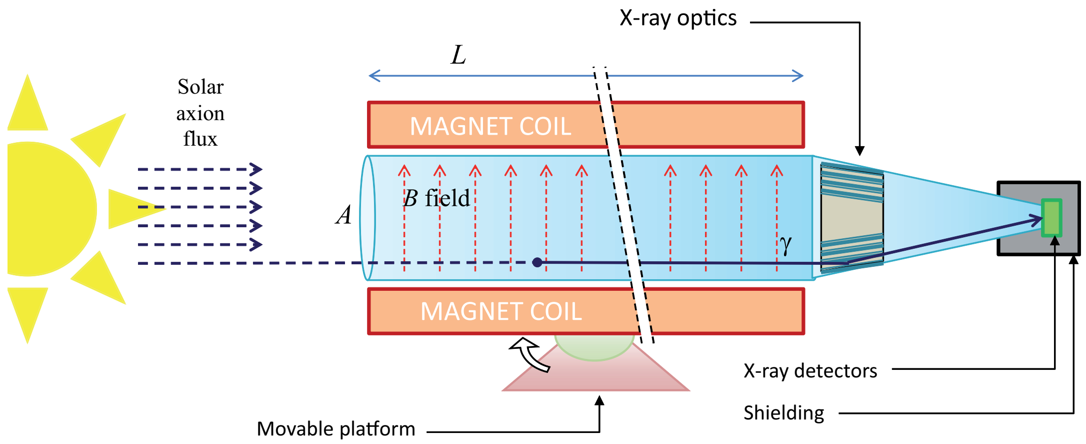

Figure 2.3: Sketch of an axion helioscope. Axions produced in the solar core through the Primakoff effect reach the Earth where they can be reconverted into X-ray photons inside a strong magnetic field. X-ray optics may be used to focus these onto low background X-ray detectors inside a shielding. Figure taken from [24].

microwave receivers. By tuning the resonance frequency of the cavity different axion mass ranges in the µeV regime can be covered. One of the first axion haloscope experiments was the Axion Dark Matter eXperiment (ADMX) operated at Lawrence Livermore National Laboratory (LLNL), which could exclude KSVZ axions in the mass range of $2.9\,\mu\text{eV} < m_a < 3.53\,\mu\text{eV}$ [19, 20] and the KSVZ as well as the DFSZ model in the case of cold Dark Matter in the mass range of $3.3\,\mu\text{eV} < m_a < 3.69\,\mu\text{eV}$ [21]. Another haloscope experiment aimed at axion masses around 20 µeV [22] but could not exclude any model, thus restraining $g_{a\gamma} \lesssim 2 \times 10^{-14}\,\text{GeV}^{-1}$ for $23.55\,\mu\text{eV} < m_a < 24\,\mu\text{eV}$.

The sensitivity of classic haloscope experiments is proportional to the volume of the cavities and thus decreases for higher axion masses as with rising resonance frequency the cavities become smaller. A new haloscope approach aiming for sensitivity in the mass region of $40\,\mu\text{eV} < m_a < 400\,\mu\text{eV}$ is the dielectric haloscope [23]. Axions can convert to photons at a dielectric surface inside a strong magnetic field. By placing several of these surface in the right distances lead to a boost of the axion to photon conversion. The Magnetized Disc and Mirror Axion Experiment (MADMAX) is the first experiment to be built following the dielectric haloscope approach. MADMAX is supposed to be hosted by DESY in Hamburg.

2.6.2 Helioscope experiments

The helioscope approach makes use of the fact that axions, if they exist, are produced in the solar core through conversion of photons in the electric field of nuclei in the Sun's core by the Primakoff effect. These axions emitted by the Sun can easily reach Earth almost unhindered due to their weak couplings to ordinary matter. There they can be reconverted back to photons in a strong magnetic field exploiting the inverse Primakoff effect and be detected. Due to the axion production in the solar core, the resulting photons are in the X-ray regime. The general helioscope principal is depicted in Fig. 2.3. The magnet providing the magnetic field is usually mounted on a movable structure to allow for tracking of the Sun. X-ray optics can be used, but are not mandatory in the helioscope concept, to focus the reconverted X-ray photons onto X-ray detectors. Due to the low expected rate of X-ray photons originating from converted axions, X-ray detectors with very low background rates and high efficiency are required. Therefore, these are usually shielded, e.g. with lead bricks.

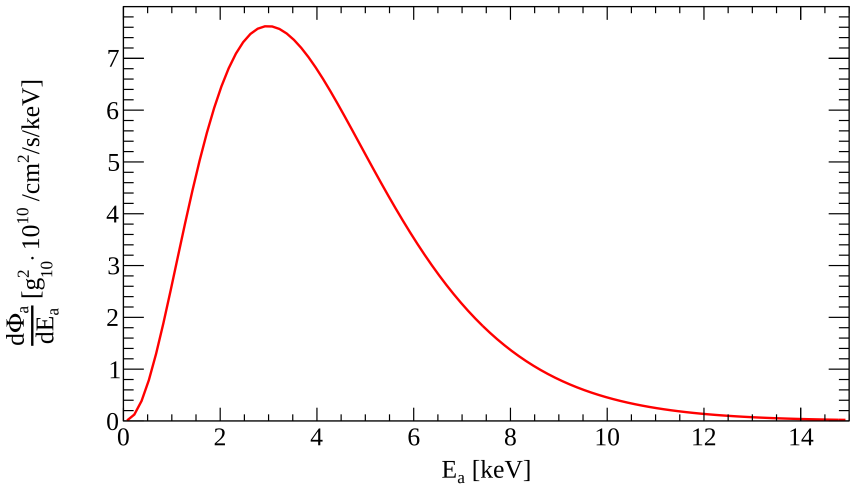

Figure 2.4: Differential solar axion flux as function of axion energy E_a and given in units of the coupling constant $g_{10} \equiv g_{a\gamma} \cdot 10^{10}\,\text{GeV}$.

Relying on the standard solar model and taking into account the axion photon coupling it is possible to compute the solar axion luminosity as well as the differential solar axion flux reaching Earth as [25]

$$L_a = g_{10}^2 \cdot 1.85 \times 10^{-3} \cdot L_{\text{sun}} \tag{2.12}$$

$$\frac{d\Phi_a}{dE_a} = g_{10}^2 \cdot 6.02 \times 10^{10} \cdot E^{2.481} e^{-E_a/1.205} /\text{cm}^2/\text{s}/\text{keV} \tag{2.13}$$

where $g_{10} \equiv g_{a\gamma} \cdot 10^{10}$ GeV, E_a the axion energy and L_{sun} the solar luminosity from [26]. The differential axion flux from the Sun is shown in Fig. 2.4 as a function of axion energy E_a and g_{10}^2. The maximum intensity is reached at about 3 keV with an average axion energy of $\langle E_a \rangle$ of 4.2 keV. Thus, for the detection of reconverted axions in the helioscope, X-ray detectors are required.

The probability for an axion to convert into a photon inside a magnetic field of strength B and a length L is given by [17]

$$P_{a\rightarrow\gamma} = \left(\frac{Bg_{a\gamma}}{2}\right)^2 \frac{1}{q^2 + \Gamma^2/4} \left(1 + e^{-\Gamma L} - 2 \cdot e^{-\Gamma L/2} \cos(qL)\right) \tag{2.14}$$

where Γ is the inverse absorption length for photons in the medium inside the magnetic field and

$$q = \frac{|m_a^2 - m_\gamma^2|}{2E_a} \tag{2.15}$$

the momentum difference between axion and photon with m_a the axion mass and m_γ the photon mass in the medium, which can be related to the plasma frequency via

$$m_\gamma^2 = \omega_{\text{pl}}^2 = \frac{4\pi\alpha n_e}{m_e} \tag{2.16}$$

where n_e is the medium's electron density and m_e the electron mass. For the conversion of axions into photons to happen the coherence condition $qL < \pi$ must be fulfilled, which translates to axions and photons being in phase over the distance L. The coherence condition defines the axion mass range for which a helioscope is sensitive.

For vacuum inside the magnetic field, thus $\Gamma = 0$ and $q = m_a^2/(2E_a)$, equation 2.14 can be simplified to

$$P_{a\to\gamma} = \left(\frac{Bg_{a\gamma}}{q}\right)^2 \sin^2\left(\frac{qL}{2}\right). \tag{2.17}$$

Thus, the conversion probability, and so the sensitivity, is approximately proportional to B^2L. To restore sensitivity outside the mass range given by the coherence condition, a buffer gas can be introduced in the magnetic field, which results in a virtual mass m_γ leading to sensitivity being significantly increased in a narrow axion mass range around the given m_γ.

Axion helioscopes set the most stringent limits on the axion photon coupling $g_{a\gamma}$ over a large axion mass range. Starting with the work of Lazarus et al. [27] followed by the SUMICO helioscope in Japan [28, 29] and the CERN Axion Solar Telescope (CAST) [25, 30–35] in total an upper bound of $g_{a\gamma} < 6.6 \times 10^{-11}\,\mathrm{GeV}^{-1}$ for $m_a \lesssim 0.02\,\mathrm{eV}$ could be set until 2017. A next generation helioscope currently in the planing phase and supposed to surpass the results achieved by CAST is the International Axion Observatory (IAXO) [24].

A different kind of axion helioscopes uses crystals for the axion conversion and detection. The energies of solar axions correspond to wavelengths in the order of typical lattice spacings in crystals. In case the condition for Bragg reflection is fulfilled this leads to coherent conversion of axions to X-ray photons, which can be detected in the crystal when instrumenting it as a calorimeter. An advantage of this method is that is almost independent of the axion mass. The DAMA experiment used NaI crystals and could set an upper bound of $g_{a\gamma} < 1.7 \times 10^{-9}\,\mathrm{GeV}^{-1}$ [36].

2.6.3 Laboratory experiments

Laboratory experiments search for axions by examining the propagation of an intense laser beam inside a strong magnetic field. They do not rely on assumptions about Dark Matter or processes in the Sun like haloscope and helioscope experiments respectively. As they only exploit the Primakoff effect laboratory experiments are almost independent of the axion model under test. The axion mass range of these experiments is limited by the wavelength of the laser beam. There are two kinds of laboratory experiments for axions.

In the first type, a circular polarized laser beam is shone through an intense magnetic field, which causes the polarization to rotate. If a small fraction of the photons in the laser beam is converted into photons and back to axions after they have travelled, this changes the polarization of the laser beam as the polarization is not affected by the magnetic field while the photon propagates as axion. An experiment following this approach is Polarizzazione del Vuoto con LASer (PVLAS) [37].

The second type of axion laboratory experiments uses the light-shining-through-wall (LSW) approach. The optical path between the laser and a highly sensitive photon detector is blocked by an opaque wall inside the magnetic field. Photons converting into axions can surpass the opaque wall due the weak couplings of axions (or ALPs) to ordinary matter. Axions traversing the wall may convert back into a photon in the magnetic field behind the wall and can, thus, be detected by the photon detector. To increase sensitivity optical cavities may be used to increase both the total laser power circulating in front of the wall and the back conversion probability on the other side of the opaque wall. Experiments using the LSW approach were the Any Light Particle Search (ALPS) [38] and the Optical Search for QED Vacuum Bifringence, Axions and Photon Regeneration (OSQAR) [39]. Currently a next generation LSW experiment, ALPS II [40], is under construction at DESY in Hamburg.

CHAPTER 3

The chameleon – A Dark Energy model

One way to explain the effects observed as Dark Energy is to extend General Relativity (GR) with a scalar field providing the potential required to model Dark Energy. To avoid unnatural effects and a fifth force with long range a screening mechanism has to be utilized. In case of the chameleon screening a density dependent effective mass for the chameleon is introduced, hence the name. The chameleon screening avoids the presence of a fifth force on large scales but may result in a fifth force on small scales.

A coupling between chameleons and photons can be easily introduced in a fashion similar to the Primakoff effect for axions and axion like particles (ALPs). The latter would result in chameleons being produced in the solar tachocline, a transition region inside the Sun where strong magnetic fields arise from differential rotation. Solar chameleons could be detected with axion helioscope experiments such as the CERN Axion Solar Telescope (CAST).

In this chapter a brief summary of the modifications to GR using chameleon screening will be given, followed by the implementation of a chameleon photon coupling. An insight on the prediction of a solar chameleon flux from the solar tachocline will be given. At the end different methods will be summarized, which provide sensitivity to chameleon models, including searches for effects of a fifth force, atom and neutron interferometry as well as searches using a potential coupling of chameleons to photons. Due to the similarity of the chameleon photon coupling to the Primakoff effect for axions and ALP, many axion experiments can be used to search for chameleons. This approach was followed at CAST, see chapter 4, with its first chameleon search in 2013, which was continued with the InGrid based X-ray detector, see chapter 7, in the course of this thesis.

3.1 Modified General Relativity and chameleon screening

By introducing a scalar tensor field in General Relativity, which is conformally coupled to matter, it is possible to create a potential modelling of what is observed as Dark Energy. But, usually this would create significant deviations from observations on astrophysical as well as on terrestrial scales by introducing a fifth force. The trivial options to avoid this by either making the effective mass of the scalar so large or its coupling to matter so small that the contributions of the fifth force virtually vanish, would cause the effects of this modified theory of gravity to be negligible on all scales and additionally would require fine-tuning of parameters [41]. A different, and more interesting approach, are screening mechanisms as they allow to fulfil astrophysical constraints and tests while at the same time predicting observable effects on terrestrial and especially small scales, which could be observed in experiments.

One of these screening mechanisms is the chameleon screening, which works with an effective mass for the corresponding scalar, which depends on the local density and thus, gives interesting effects. In the following the basics of modifying GR by adding a scalar field using chameleon screening will be briefly explained including its (observable) consequences. For this, the summary in [41] is followed.

By adding the scalar field ϕ with the corresponding potential $V(\phi)$ to GR one gets the total action as

$$S = \int \mathrm{d}^4x \sqrt{-g}\left[\frac{R}{16\pi G} - \frac{1}{2}\nabla_\mu\phi\nabla^\mu\phi - V(\phi)\right] + S_m[\tilde{g}_{\mu\nu}, \phi] \tag{3.1}$$

where the matter coupling of the scalar field ϕ is described with the Jordan frame metric

$$\tilde{g}_{\mu\nu} = A^2(\phi)g_{\mu\nu} \tag{3.2}$$

with the coupling function $A(\phi)$ which leads to the non-trivial deviations from GR.

For models using chameleon screening the potential $V(\phi)$ is given by

$$V(\phi) = \Lambda^4 + \frac{\Lambda^{n+4}}{\phi^n} \tag{3.3}$$

where the index n describes the model used and Dark Energy is modelled for $\Lambda = \Lambda_{\mathrm{DE}} = 2.4\,\mathrm{meV}$. From this potential it is already obvious that, for most values of n, the chameleon model includes non-trivial self-interactions, which may lead to interesting, observable phenomena. The coupling function $A(\phi)$ is usually given as

$$A(\phi) = \exp\left(\frac{\beta_m\phi}{M_{\mathrm{Pl}}}\right) \tag{3.4}$$

where β_m is the matter coupling of the chameleon scalar and M_{Pl} the reduced Planck mass. Following [41] this gives an effective potential

$$V_{\mathrm{eff}}(\phi) = \Lambda^4 + \frac{\Lambda^{n+4}}{\phi^n} + \rho\frac{\beta_m\phi}{M_{\mathrm{Pl}}} \tag{3.5}$$

where ρ is the local density. The minimum of the effective potential is reached at

$$\phi_{\mathrm{min}}(\rho) = \left(\frac{nM_{\mathrm{Pl}}\Lambda^{n+4}}{\rho\beta_m}\right)^{\frac{1}{n+1}} \tag{3.6}$$

and depends on the energy. Therefore the effective mass of the chameleon scalar is given by the curvature of the effective potential at $\phi = \phi_{\mathrm{min}}$ as

$$m_{\mathrm{eff}}^2 = V''_{\mathrm{eff}}(\phi_{\mathrm{min}}) = n(n+1)\Lambda^{n+4}\left(\frac{\rho\beta_m}{nM_{\mathrm{Pl}}\Lambda^{n+4}}\right)^{\frac{n+2}{n+1}} \tag{3.7}$$

which depends on the local density, as intended. This also gives the chameleon screening its name, as the chameleon blends in with its environment. The geodesic equation in the Newtonian limit allows for giving an expression for the fifth force generated by the chameleon field:

$$\vec{F}_5 = -\frac{\beta_m}{M_{\mathrm{Pl}}}\vec{\nabla}\phi. \tag{3.8}$$

The chameleon screening features some interesting effects. One of them is the thin shell effect [41] which is common to most of the screening mechanisms. For large objects, e.g. astrophysical objects,

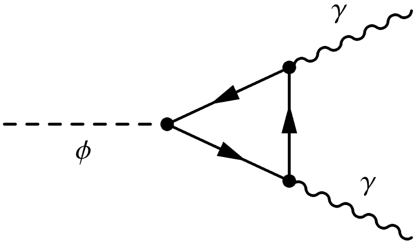

Figure 3.1: Feynman graph for the chameleon coupling to two photons via a triangle-loop involving a heavy, charged fermion. If the fermion is sufficiently heavy, the chameleon photon interaction can be described by an effective theory at low energies.

only a thin outer shell contributes to the fifth force sourced by the chameleon field, which allows for not violating astrophysical constraints and bounds. Another effect is connected to the density dependent effective mass, a chameleon can only enter a medium if its effective mass in the medium does not exceed its energy, else energy conservation would be violated. Thus, chameleons of a certain energy can bounce off a dense surface on impact as they cannot enter or traverse the medium. Due to the non-trivial self-interactions, the initial chameleon may not only be reflected, but even may fragment into several chameleons with the energy of the initial chameleon being split.

3.2 Introducing a chameleon photon coupling

The chameleon theory does not contain a coupling to photons from start, but it can be easily introduced in the form of quantum effects [41]. By assuming the existence of a heavy, charged fermion (which couples to photons) one can construct a coupling of chameleons to photons. The chameleon couples to the heavy fermion through its coupling to matter β_m. A triangle-loop of the heavy fermion allows to introduce a coupling between a chameleon and two photons, as depicted in the Feynman graph shown in Fig. 3.1. If the heavy fermion is heavy enough, it can be integrated out, leaving an effective coupling of the chameleon to two photons, which is added to the Standard Model (SM) at low energies. This chameleon photon interaction is very similar to the interaction of axions (or ALPs) with photons and can be also described by the Primakoff effect where one of the photons is virtual, allowing for the conversion of a chameleon into a photon and vice versa in the presence of electromagnetic fields. The corresponding Lagrangian contributing to the SM Lagrangian is given by

$$\mathcal{L}_{\phi\gamma} = \frac{\beta_\gamma \phi}{M_{\mathrm{Pl}}} \cdot F_{\mu\nu} F^{\mu\nu} \tag{3.9}$$

where β_γ is the chameleon photon coupling and $F_{\mu\nu}$ the electromagnetic field strength tensor. Indeed, this equation resembles the axion photon coupling described in equation 2.9 in chapter 2. The main difference, except for the different coupling constants, arises from the chameleon being a scalar particle in contrast to the axion as pseudoscalar particle.

The chameleon photon coupling and its similarity to the axion photon coupling imply that the principles used for searching axions and ALPs can be utilized to search for chameleons as well. In some cases the specific differences, like the density dependent effective mass, of course have to be taken into account. Also, it should allow for production of chameleons in the Sun, making the Sun an axion as well as a chameleon source. Thus, also axion helioscopes, like CAST, may be used in chameleon searches.

3.3 Chameleon production in the solar tachocline

Chameleons can be produced in the Sun by conversion of photons emitted by the solar core, similar to axions. Although, theoretically the conversion could take place in the high electric fields of nuclei in the solar core's plasma, the calculation of the chameleon flux emitted by the solar core does not exist yet [42]. But, the conversion can also be realized in strong magnetic fields, which are believed to exist in the solar tachocline, a region located at $0.7\,R_\odot$ where strong magnetic fields, of the order of 10 T, are formed through differential rotation [43–45]. Solar chameleons can be reconverted on Earth in strong magnetic fields into photons which then can be detected. Thus, very similar as for solar axions, solar chameleons can be searched for using the helioscope technique. Due to the different production region (tachocline instead of solar core) and the resulting lower temperature in this region of the Sun, the energy of solar chameleons is lower than for axions, typically the maximum of the solar chameleon flux is reached at about 1 keV [42, 43]. Thus, with detectors sufficiently sensitive to very low energy X-ray photons, an axion helioscope like CAST can be turned into a chameleon helioscope.

Of course, for a solar chameleon search, a prediction of the solar chameleon flux is required. The latter can be computed numerically by making assumptions on the tachocline and the magnetic fields in this solar region. Here, the approach described in [42, 43] is followed and briefly summarized. Starting with the conversion probability of a photon into a chameleon inside a region of length l and with a magnetic field B can be given as [43]

$$p_{\gamma\to\phi}(l) = \frac{\beta_\gamma^2 B^2 l_\omega^2}{4M_{\rm Pl}^2} \cdot \sin^2 \frac{l}{l_\omega} \tag{3.10}$$

where $l_\omega = 4\omega/m_{\rm eff}^2$ is the coherence length and ω the photon energy. The effective chameleon mass $m_{\rm eff}$ can be written as

$$m_{\rm eff}^2 = \beta_m^{(n=2)/(n+1)} \omega_\rho^2 - \omega_{\rm pl}^2 \tag{3.11}$$

where $\omega_{\rm pl}^2 = 4\pi\alpha\rho/(m_e m_p)$ is the plasma frequency and ω_ρ^2 defined as [42]

$$\omega_\rho^2 = \frac{(n+1)\rho}{M_{\rm Pl}} \left(\frac{\rho}{nM_{\rm Pl}\Lambda^{n+4}} \right)^{\frac{1}{n+1}} \tag{3.12}$$

and $\Lambda = \Lambda_{\rm DE}$ is used. For the calculation it is assumed that photons perform a random walk in the solar plasma. This means that photons which have traversed a radial distance $d(l)$ in one second will have undergone $N(l)$ collisions, here l is the distance between two collisions, which is distributed according to a Poisson distribution with mean λ given by the mean free path length in the solar plasma. Thus, $N(l)$ and $d(l)$ can be given as [42, 43]

$$N(l) \;=\; \frac{c}{l} \tag{3.13}$$

$$d(l) \;=\; l\sqrt{N(l)}. \tag{3.14}$$

For a solar region of width ΔR in which λ and B can be treated as constant, the conversion probability for photons into chameleons is then given by [42]

$$\mathrm{d}\mathcal{P}(l) = \frac{\Delta R}{d(l)} N(l) p_{\gamma\to\phi}(l) e^{-l/\lambda} \cdot \frac{\mathrm{d}l}{\lambda} \tag{3.15}$$

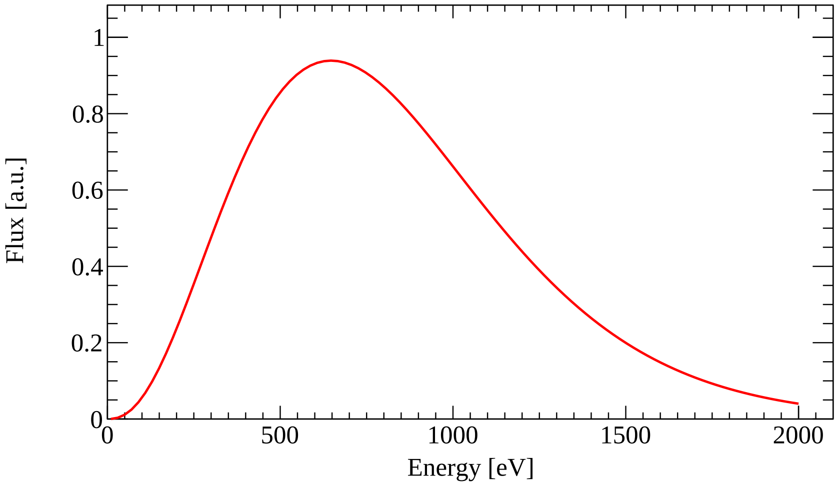

Figure 3.2: Solar chameleon flux originating from the tachocline. The tachocline is assumed to start at 0.7 $R_\odot$ and provide a magnetic field of 10 T over a width of 0.01 $R_\odot$. The spectrum depends on β_γ^2 and is given here in arbitrary units. Derived from the spectrum given in [42].

from which the conversion rate per length can be derived by summing up all shells:

$$\frac{\mathrm{d}\mathcal{P}}{\mathrm{d}x} = \sqrt{\frac{c}{l_\omega(r)}} \cdot \frac{\beta_\gamma^2 B^2(r) l_\omega^2(r) R_\odot}{4 M_{\mathrm{Pl}}^2 \lambda(r)} \int_0^\infty \frac{\sin^2 y}{y^{3/2}} e^{-l_\omega(r) y/\lambda(r)} \mathrm{d}y. \tag{3.16}$$

Of course, the conversion rate per length depends on the radial position r in the Sun. The total conversion rate is obtained by integrating over $x = r/R_\odot$. The magnetic field $B(r)$ vanishes outside the tachocline, in the tachocline and for the energy relevant here, one can assume $l_\omega(r) \ll \lambda(r)$ which allows for simplifying equation 3.16 to

$$\frac{\mathrm{d}\mathcal{P}}{\mathrm{d}x} = C \cdot \sqrt{\frac{c}{l_\omega(r)}} \cdot \frac{\beta_\gamma^2 B^2(r) l_\omega^2(r) R_\odot}{4 M_{\mathrm{Pl}}^2 \lambda(r)} \tag{3.17}$$

with $C = \int_0^\infty \frac{\sin^2 y}{y^{3/2}} \mathrm{d}y$. Assuming non-resonant chameleon production, m_{eff}^2 is almost independent of β_m. Therefore the conversion rate and the resulting solar chameleon spectrum only depends on β_γ [42]. But, this restricts β_m to $1 < \beta_m < 10^6$. Resonant production would imply that m_{eff}^2 vanishes somewhere in the tachocline, this case is not considered here, but information on it can be found in [43].

To get the flux of solar chameleons leaving the Sun, one has to integrate equation 3.17:

$$\Phi_{\mathrm{cham}}(\omega) = \int_0^1 n_\gamma(\omega) p_\gamma(\omega) \frac{\mathrm{d}\mathcal{P}}{\mathrm{d}x} \mathrm{d}x \tag{3.18}$$

where n_γ is the photon flux and p_γ the photon spectrum. The energy dependence of the resulting solar chameleon flux is $\omega^{3/2} p_\gamma(\omega)$, which is proportional to $\omega^{7/2}/(e^{\omega T} - 1)$ with $T \approx 600\,\mathrm{eV}$ the photon temperature in the tachocline [42]. The dependence on $\omega^{3/2}$ is caused by the random walk in the solar plasma. $\Phi_{\mathrm{cham}}(\omega)$ can be computed numerically which gives a spectrum as shown in Fig. 3.2.

By integrating equation 3.18 it is possible to compute the total luminosity radiated by the Sun in form of chameleons:

$$L_{\mathrm{cham}} = \int_0^\infty \omega \Phi_{\mathrm{cham}}(\omega) \mathrm{d}\omega \tag{3.19}$$

which of course depends on β_γ^2. With the condition that L_{cham} should not exceed 10 % of the total luminosity one can set an upper bound $\beta_\gamma^{\mathrm{sun}}$. For the tachocline starting at $0.7\,R_\odot$, a width of $0.01\,R_\odot$ and assuming a tachocline magnetic field of 10 T, the upper bound can be calculated to be $\beta_\gamma^{\mathrm{sun}} = 10^{10.81} \approx 6.46 \times 10^{10}$ [42].

To determine the flux of X-ray photons originating from solar chameleons being reconverted inside the magnetic field of an helioscope experiment, the solar chameleon flux $\Phi_{\mathrm{cham}}(\omega)$ given in equation 3.18 has to be multiplied with the conversion probability taking into account the magnetic field B and length L of the helioscope. The probability for a chameleon into a photon can be written as [43]

$$p_{\phi \to \gamma} = \frac{B^2 L^2 \beta_\gamma^2}{4 M_{\mathrm{Pl}}^2} \tag{3.20}$$

given that L is smaller than the coherence length. The resulting X-ray spectrum then depends on β_γ^4.

3.4 Detection of chameleons

There exist several approaches to detect chameleons or the effects of the fifth force introduced by the scalar chameleon field. In general the experiments sensitive to chameleons can be divided into two groups, those sensitive to the chameleon matter coupling β_m and those sensitive to the chameleon photon coupling β_γ. Here, a few selected experiments will be briefly introduced and their recent results presented. From the experiments sensitive to β_m, the torsion pendulum as well as atom and neutron interferometers will be discussed. CAST as a chameleon helioscope and in addition the afterglow experiments will be introduced as examples for experiments sensitive to β_γ. The different experimental constraints on β_m and β_γ are depicted in Fig. 4.4 in chapter 4.

3.4.1 Torsion pendulum experiments

Torsion pendulum experiments like Eöt-Wash [46] use two test masses, usually made from materials with high density, to probe deviations in gravity from the inverse square law. For Eöt-Wash one of the masses is suspended on a torsion wire while the other one is rotating in a defined distance below the first mass. The whole set-up is electrically shielded and suspended in vacuum to avoid external effects. Both masses feature precisely machined holes in them. The gravitational field sourced by the masses and the resulting force acting on the suspended mass therefore depend on the orientation of the rotating mass, the force becomes minimal when the holes overlap and maximal when the solid regions overlap. As one mass is rotating the resulting force on the suspended mass becomes periodic and causes it to oscillate around the axis given by the torsion wire. This allows to probe the inverse square law of gravity at different distances.

By simulating the chameleon field sourced by these masses one can interpret and evaluate the upper bounds on deviations from the inverse square law of gravity in terms of a lower bound on the chameleon matter coupling as done in [47]. There chameleons with a matter coupling

$$0.01 \lesssim \beta_m \lesssim 15 \tag{3.21}$$

could be excluded for specific models and with the approximation for the chameleon field sourced by the test masses. Next generation torsion pendulum experiments are expected to allow for exclusion of a chameleon models up to $\beta_m \lesssim 1\,000$ [47].

3.4.2 Atom and neutron interferometry

The usual challenge for achieving sensitivity to modified gravity models with a screening mechanism, is that extended masses are screened due to the thin shell effect. In atom and neutron interferometry experiments this is solved by one of the test masses being neutrons or single atoms, microscopic objects where the screening can be neglected. In these interferometry experiments the chameleon field sourced by test masses (e.g. the vacuum chamber in which the experimental set-up is housed or explicit spheres) influence the propagating particles and therefore should show an effect on the observed interference pattern.

For the neutron interferometry experiment conducted in [48], the vacuum chamber (and bars therein) served as source for the chameleon field. From the observed interference patterns and phase shifts an upper bound of

$$\beta_m < 1.9 \times 10^7 \tag{3.22}$$

for chameleon models with $n = 1$ could be derived.

In the atom interferometry experiments cold caesium atoms were used first with an aluminium sphere [49] and later with a tungsten cylinder [50] leading to an upper bound

$$\beta_m \lesssim 3.57 \times 10^2 \tag{3.23}$$

for chameleon models with $n = 1$. Together with the results of the torsion pendulum experiments [47] this only leaves a small range in β_m, which is yet not excluded but could be completely closed with the expected sensitivity of next generation torsion pendulum experiments.

3.4.3 Experiments sensitive to the chameleon photon coupling

Due to the possible production of chameleons in the solar tachocline, an axion helioscope like CAST (see chapter 2 for details) is sensitive to the chameleon photon coupling β_γ in a limited β_m range. From CAST's first chameleon search an upper bound [42]

$$\beta_\gamma \lesssim 10^{11} \tag{3.24}$$

could be derived for $1 < \beta_m < 10^6$. This results will improve with the results obtained in the course of the work conducted in this thesis, see chapter 11.

A different kind of experiments sensitive to β_γ are the afterglow experiments which are in a way similar to the laboratory experiments for axions and ALPs. A powerful laser beam is shone into a closed vessel inside a strong magnetic field. Photons may convert into chameleons inside the vessel. Due to their energy being lower than their effective mass corresponding to the density of the vessel's walls they cannot leave. So, when the laser is shut off, chameleons may circulate inside the vessel. Here, possible chameleon fragmentation due to the non-trivial chameleon self-interactions has to be taken into account.

While the laser is off, the magnetic field is kept on, which allows for chameleons converting back to photons resulting in an afterglow, which could be detected with highly sensitive photon detectors. An experiment using this approach was the Chameleon Afterglow Search (CHASE), which could provide an upper bound on the chameleon photon coupling [51]

$$\beta_\gamma < 7.6 \times 10^{10} \tag{3.25}$$

but was only sensitive up to $\beta_\gamma \lesssim 3.3 \times 10^{15}$ due to an additional orange afterglow appearing in a short period after switching off the laser which cannot be attributed to chameleons. The bounds on β_γ achieved by CHASE however only are valid for a certain range of effective chameleon masses and thus chameleon matter couplings β_m [51].

CHAPTER 4

The CERN Axion Solar Telescope

The CERN Axion Solar Telescope (CAST) is a surface experiment at CERN looking for solar axions using the helioscope principle introduced in chapter 2: Axions produced in the solar core through the Primakoff effect and reaching the Earth are reconverted inside a strong magnetic field into X-ray photons, which then can be detected with X-ray detectors. CAST has first been proposed in 1999 and started data taking in 2003. Due to the small couplings of axions to ordinary matter the expected count rates are very low, making CAST a low rate experiment. Thus, requiring highly efficient X-ray detectors with very low background rates to achieve sensitivity. Since its start in 2003 the X-ray detectors of CAST have been continuously advanced to increase CAST's sensitivity, allowing the experiment for setting the most stringent limits for solar axions so far [35]. In 2013 CAST started its first search for solar chameleons with a commercially available silicon drift detector (SDD) [42]. The search for solar chameleons was continued in the course of this thesis with the development, commissioning and operation of an InGrid based X-ray detector at CAST in 2014 and 2015.

Here, the experimental set-up used for the CERN Axion Solar Telescope, will be described. The X-ray detectors used at CAST at present and in the past will be briefly introduced. The physics program of CAST and the results achieved so far in the search for solar axions and chameleons are presented. At the end, the International Axion Observatory (IAXO), a possible CAST successor, will be mentioned.

4.1 The CAST experimental set-up

The CERN Axion Solar Telescope was first proposed as a new experiment in 1999 [52, 53] following previous helioscope experiments operated in Japan [28, 29] and the USA [27]. CAST uses a decommissioned prototype dipole magnet build for the Large Hadron Collider (LHC). The superconducting magnet provides a magnetic field of 9 T over a length of 9.26 m and is operated at a cryogenic temperature of $\sim$1.8 K using superfluid helium for cooling. The magnet features two vacuum pipes, called coldbores, inside the magnetic field with a diameter of 43 mm each.

To track the Sun, the magnet was mounted on a large, movable structure. A picture of the whole experiment is shown in Fig. 4.1. Guided on rails, the magnet can be moved horizontally over a range of 80°. Vertically the magnet can be tilted by ±8° with respect to the horizontal plane. Together with the horizontal movement this allows for tracking of the Sun for most times of the year for about 1.5 h during sunrise and sunset respectively. The restrictions of movement, and therefore the maximum tracking times, are caused on the one hand by the available space in the experimental hall (horizontal movement) and on the other hand by the mechanical rigidity and strength of the magnet, which was not designed to be tilted at large angles (vertical movement). The cold mass of the magnet is suspended in a cryostat, surrounded

Figure 4.1: Picture of the CERN Axion Solar Telescope (CAST). The dipole magnet (blue) is mounted on a movable structure (green and yellow structures) allowing for tracking of the Sun during sunrise and sunset. The sunrise side with the MPE XRT is visible in the lower right while the sunset side (left) is pointing towards the Sun. Twice a year the alignment with the Sun can be visually checked when the Sun passes the window of the experimental hall (upper left) during sunrise. Power and cryogenics for the magnet are supplied via the tower like structure connected to the magnet (right).

by an isolation vacuum. For large vertical angles, the mechanical forces acting on some of the supports may cause these to break.

During sunrise the X-ray detectors mounted to one end of the magnet are pointed towards the Sun while the detectors mounted to the other end track the Sun during sunset. Hence, the two sides are called sunrise and sunset side respectively. In Fig. 4.1 the sunrise side of the magnet (and the X-ray detectors mounted on this side) can be seen in the lower right while the sunset side of the magnet is pointing towards the Sun, visible in the window in the upper left. On each side two detector stations, corresponding to the two coldbores, are available for X-ray detectors to be mounted. On the sunset side, or the sunset platform, the detector stations are called VT1 and VT2 while on the sunrise platform VT3 and VT4 are available for X-ray detectors. The sunrise platform, and especially detector station VT4, will be described in more detail in chapter 8. While detector station VT4 was equipped with an X-ray optic, called the MPE XRT [54][1], right from the very beginning of CAST, detector station VT3 was first equipped with an X-ray optic in 2014, an XRT developed at Lawrence Livermore National Laboratory (LLNL) [59] as part of a pathfinder project for IAXO [24].

When the coldbores are evacuated, CAST is sensitive to axion masses up to $\sim 0.02\,\mathrm{eV}$ [25, 30, 35] as for higher masses the coherence condition is not fulfilled any more. To restore sensitivity for axion masses above $0.02\,\mathrm{eV}$ CAST has been equipped with a system, which allows for filling the coldbores with defined and precise quantities of a buffer gas (^{4}He or ^{3}He). The system used to fill the coldbores with the buffer gas not only had to allow for a precise metering but also a safe operation and recovery of the gas, especially in the case of a quench of the superconducting magnet. Also, ultrathin windows to be put inside the coldbores had to be developed and introduced to confine the buffer gas inside the

---

[1] A spare XRT from the A Broadband Imaging X-ray All-Sky Survey (ABRIXAS) space mission [55–58]. It was contributed by the Max-Planck-Institut für extraterrestrische Physik (MPE), hence the name MPE XRT.

coldbores in the region of the magnetic field. By introducing a virtual photon mass, related to the plasma frequency, this allows for restoring the sensitivity to solar axions in a narrow range around the virtual photon mass, see also chapter 2.6.2. The virtual photon mass depends on the buffer gas' density, therefore on the gas used and its pressure. By increasing the pressure stepwise it is possible to scan higher axion mass ranges [31–34]. To reach axion masses above $\sim 0.4\,\mathrm{eV}$ instead of ^{4}He, ^{3}He has to be used because at pressures above $\sim 16\,\mathrm{mbar}$, corresponding to axion masses above 0.4 eV, ^{4}He would condensate in the coldbores, which are at a temperature of $\sim 1.8\,\mathrm{K}$.

To verify CAST's pointing accuracy a small window has been made at one of the experimental hall's walls (see upper left in Fig. 4.1). Twice a year, for a couple of days, the rising Sun can be seen through this window during parts of sunrise tracking of the Sun. This allows for comparing the pointing direction of CAST with the position of the Sun in the sky. A camera mounted to an optical telescope is fixed on the magnet and its optical axis aligned to the axis of one of the coldbores. Of course, the refraction of the atmosphere has to be taken into account as it affects the position of the visible Sun in the images taken with the optical telescope and camera.

4.2 CAST's X-ray detectors

Axions or chameleons reconverting into X-ray photons in the magnetic field of CAST's coldbores can be detected at the corresponding side, sunrise or sunset, of the magnet. The expected count rates are very low, thus requiring highly efficient X-ray detectors with very low background rates, which can be measured in situ whenever CAST is not tracking the Sun. While for solar axion searches the detectors have to be sensitive in the range of 2 to 7 keV [17] for solar chameleon searches sensitivity is needed below 2 keV [43]. For sensitivity to the axion photon coupling constant $g_{a\gamma}$ an approximate relation can be given as

$$g_{a\gamma} \propto \frac{b^{1/8}}{\epsilon^{1/4} t^{1/8}}. \tag{4.1}$$

This gives a rough estimate of the lowest value of $g_{a\gamma}$ the experiment is sensitive to detectorwise with b the background rate, ϵ the efficiency and t the total measurement time (solar tracking). The same relation holds for the chameleon photon coupling β_γ.

The X-ray detectors used at CAST for the solar axion searches, and later also for the solar chameleon searches, have been continuously developed and improved throughout CAST's lifetime. Some detectors were upgraded others replaced by ones reaching better performance. Especially since 2016, new kinds of detectors, also non-X-ray detectors, have been implemented in the experiment to use different measurement concepts or to extend CAST's scientific agenda.

In the following the X-ray detectors operated during 2014 and 2015, in parallel with the InGrid based X-ray detector, will be introduced briefly. Also, previous X-ray detectors of CAST will be mentioned as well as detectors currently taking data at CAST.

4.2.1 CAST detectors operated in 2014 and 2015

Along with the InGrid based X-ray detector, which will be described in chapter 7, three detectors using the Micro-Mesh Gaseous Structure (MicroMegas) technology were operated at CAST in 2014 and 2015. The MicroMegas detectors are gaseous X-ray detectors as the InGrid based X-ray detector, they use Microbulk MicroMegas stages for the gas amplification. The MicroMegas technology, Microbulk MicroMegas and the Integrated Grid (InGrid) technology will be introduced in chapter 6.

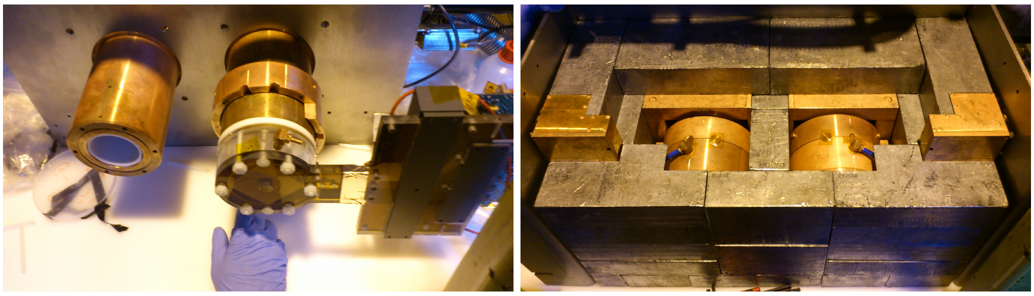

(a) (b)

Figure 4.2: Pictures of the sunset MicroMegas detectors used at CAST in 2014 and 2015. In (a) one of the two sunset MicroMegas detectors is mounted to its detector station, the readout electronics are visible on the right. In (b) both detectors have been mounted and enclosed with their inner copper shielding. The detectors are enclosed by a lead shielding which is here still partially open to allow view to the detectors. Both pictures taken from [60].

Two of the MicroMegas detectors, the sunset MicroMegas detectors [60], are mounted on CAST's sunset side covering detector stations VT1 and VT2. The third MicroMegas detector is mounted to detector station VT3, next to the InGrid based X-ray detector at detector station VT4, on the sunrise platform of CAST, hence it is referred to as sunrise MicroMegas detector [59]. Each of the three detectors instruments an area of $60 \times 60\,\mathrm{mm}^2$ and is filled with an argon based gas mixture containing small amounts of isobutane as quencher at a pressure of $\sim 1.4\,\mathrm{bar(a)}$. This allows to achieve a reasonable absorption efficiency for X-ray photons up to 10 keV. The detectors are shielded with about 10 cm of lead bricks plus copper Faraday cages. An off-line background suppression allows to reach very low background rates in the energy range of 2 to 7 keV. Large veto scintillators are used for off-line discrimination of X-ray fluorescence photons created through cosmic rays activating the material of the detector itself or its surrounding.

The sunset MicroMegas detectors feature a 5 µm thick aluminized Mylar® film on a copper support structure as X-ray entrance window. They reach an energy threshold of about 1.5 keV [35]. Their gas mixture contains 2 % isobutane. An energy resolution of about 20 % full width half maximum (FWHM) at 5.9 keV [60] could be achieved with the sunset MicroMegas detectors. They are built from materials known to be radiopure: acrylic glass and copper. The Microbulk MicroMegas stages are intrinsically radiopure as they only consist of Kapton® and copper. In Fig. 4.2 pictures of the sunset MicroMegas detectors inside their lead shielding are shown. They were able to reach background rates down to roughly $1 \times 10^{-6}\,/\mathrm{keV/cm^2/s}$ in the range of 2 to 7 keV [35].

The sunrise MicroMegas detector installed in 2014 and the LLNL XRT it was mounted at, were part of a IAXO pathfinder project [59]. The detector was a consequent advancement of the sunset and other previous CAST MicroMegas detectors in terms of background rate and efficiency. The sunrise MicroMegas detector uses a 4 µm thick aluminized polypropylene (PP) film with a copper support structure as X-ray entrance window and is operated with 2.3 % isobutane. It could reach an energy resolution of 13 % FWHM at 5.9 keV [35, 59]. The detector consisted only of copper, Kapton and polytetrafluorethylene (PTFE), all materials known to be very radiopure. During operation at CAST background rates of about $1 \times 10^{-6}\,/\mathrm{keV/cm^2/s}$ in the range of 2 to 7 keV [35] were reported. In an underground laboratory and with an increased amount of lead shielding background rates down to $1 \times 10^{-7}\,/\mathrm{keV/cm^2/s}$ could be achieved [24, 60], giving the intrinsic background rate of the detector, and demonstrating what is possible given adequate shielding and screening of detector materials. The sunrise MicroMegas detector and the LLNL XRT were the major contribution to CAST's latest results [35].

4.2.2 Previous CAST detectors

Prior to the InGrid based X-ray detector a pnCCD detector [54] was mounted behind the MPE XRT. Despite its background rate being larger compared to the sunset and sunrise MicroMegas detectors it achieved a high sensitivity as it could be operated directly in vacuum and therefore with high quantum efficiency. Its contribution was especially valuable for CAST's constraints on the axion electron coupling g_{ae} [61]. The pnCCD detector was decommissioned begin of 2013.

While the MPE XRT was removed from the sunrise platform for a recalibration at the X-ray test facility PANTER [62] from mid 2013 until begin of 2014, a detector built on basis of a commercially available SDD was installed at detector station VT4 to carry out CAST's first search for solar chameleons [42]. When the MPE XRT returned to CAST at begin of 2014 the SDD was replaced by the InGrid based X-ray detector to continue the search for solar chameleons with increased sensitivity.

Before the sunset MicroMegas detectors were installed on the sunset side of CAST in 2007 and 2008, a single Time Projection Chamber (TPC) was mounted on the sunset side covering both detector stations [63]. It was able to reach background rates of 4.1×10^{-5} /keV/cm^2/s in the range of 1 to 10 keV [63] using a specialized shielding consisting of several layers of different materials including copper, lead, polyethylene (PE) and cadmium [64].

4.2.3 Present CAST detectors

Since 2017 an upgraded version of the InGrid based X-ray detector, see chapter 12 for a brief description, has been installed at CAST behind the LLNL XRT at detector station VT3 to continue the hunt for solar chameleons with increased sensitivity. The sunrise MicroMegas detector was dismounted at the end of 2015.

The sunset MicroMegas detectors were also dismantled at the end of 2015, since then the sunset end of CAST is not equipped anymore with X-ray detectors. But, in 2016 and 2017 respectively, parts of the coldbores were filled with cavities from the sunset side, the CAST-CAPP and RADES cavities [35] which are used for relic axion search using the haloscope approach and utilizing the magnetic field provided by the CAST magnet but not its capability to track the sun.

Also, the Kinetic WISP detection (KWISP) detector, a highly sensitive force sensor is tested at CAST in different development stages since 2016, partially behind the MPE XRT to search for solar chameleons with a different approach, detecting solar chameleons by their radiation pressure on a tiny membrane inside an optical cavity [65]. This kind of detector is sensitive to the chameleon matter coupling β_m as well as to the chameleon photon coupling β_γ.

4.3 Physics program and results

Since CAST started data taking in 2003 it has continuously improved its sensitivity for solar axions and also extended its physics program by a search for solar chameleons in 2013. In the following the a brief timeline of the search for solar axions as well as solar chameleons will be given along with the latest results concerning the upper bound on the axion photon and chameleon photon couplings $g_{a\gamma}$ and β_γ respectively.

4.3.1 Search for solar axions

The search for solar axions at CAST started in 2003 with CAST's phase I where axion masses up to ~ 0.02 eV were explored until 2004 [25, 30]. After upgrading the experiment to allow for filling of the coldbores with ^{4}He as a buffer gas sensitivity was restored for higher axion masses ranging from 0.02 to 0.39 eV starting CAST's phase II in 2005 [31]. In 2007 CAST's systems were upgraded to allow for using ^{3}He as buffer gas but also detectorwise and CAST's phase II continued after the restart of data taking in 2008 until 2011 with a sensitivity to axion masses ranging from 0.39 to 1.15 eV [32, 33]. The latter search allowed for excluding QCD axions for the KSVZ model in a mass range around 1 eV. In 2012 again ^{4}He was used as buffer gas in CAST's ^{4}He Run intended to rescan the transition region between the mass range accessible with ^{4}He and ^{3}He as buffer gases respectively [34], with increased sensitivity due to upgraded X-ray detectors achieving lower background rates. From 2013 to 2015 CAST was operated with the coldbores under vacuum and improved sensitivity for the axion mass range below ~ 0.02 eV reached through consequent development of the X-ray detectors and also the equipping of the sunrise MicroMegas line with an XRT [59], leading to CAST's latest results concerning the search for solar axions which excludes axion photon couplings above $6.6 \times 10^{-11}\,\mathrm{GeV}^{-1}$ for $m_a \lesssim 0.02$ eV at 95 % confidence level [35]. The latest results are visualized and compared to constraints from other experiments as well as astrophysical bounds in the exclusion plot shown in Fig. 4.3 using the axion parameter space m_a-$g_{a\gamma}$. In addition to the upper bounds on the axion photon coupling $g_{a\gamma}$ CAST was also able to set constraints on the axion electron coupling g_{ae} [61].

4.3.2 Search for solar chameleons

In 2013 CAST conducted its first search for solar chameleons using an X-ray detector built on basis of a commercially available SDD. With this first shot at the chameleon photon coupling β_γ CAST was able to set an upper bound of $\beta_\gamma \lesssim 10^{11}$ for a range of the chameleon matter coupling β_m from 1 to 10^6, excluding a part of the chameleon parameter space β_γ-β_m, which had not been constraint before completely. The region excluded by CAST in its first solar chameleon search is illustrated in the exclusion plot shown in Fig. 4.4. It is shown along with constraints derived from other experiments using different methods and approaches. The solar chameleon search at CAST was continued in 2014 and 2015 with the InGrid based X-ray detector increasing the sensitivity. The upper bound on β_γ derived from the search with the InGrid based X-ray detector will be presented and discussed in chapter 11.

The solar chameleon search is continued at CAST with an upgraded version of the InGrid based X-ray detector (see chapter 12) installed in 2017 and the KWISP detector [65].

4.4 The International Axion Observatory

The International Axion Observatory (IAXO) is envisioned as a possible follow-up experiment to continue the search for solar axions on a large scale. For IAXO a dedicated magnet of 20 m length and eight bores with 60 cm diameter and an average magnetic field of 2.5 T is foreseen [24]. The magnet is to be suspended in a way allowing for tracking of the Sun 12 h per day. For each of the large bores a full scale XRT with large focal length is planned focusing X-ray photons onto highly efficient low background detectors, each equipped with an individual lead shielding with maximized coverage. With IAXO it would be possible to exclude axions in a wide mass range down to axion photon couplings of a few $10^{-12}\,\mathrm{GeV}^{-1}$ and also achieve sensitivity to the axion electron coupling beyond astrophysical exclusions [24]. Most likely, prior to building the full scale IAXO, a small prototype, babyIAXO will be constructed which could be hosted by DESY in Hamburg.

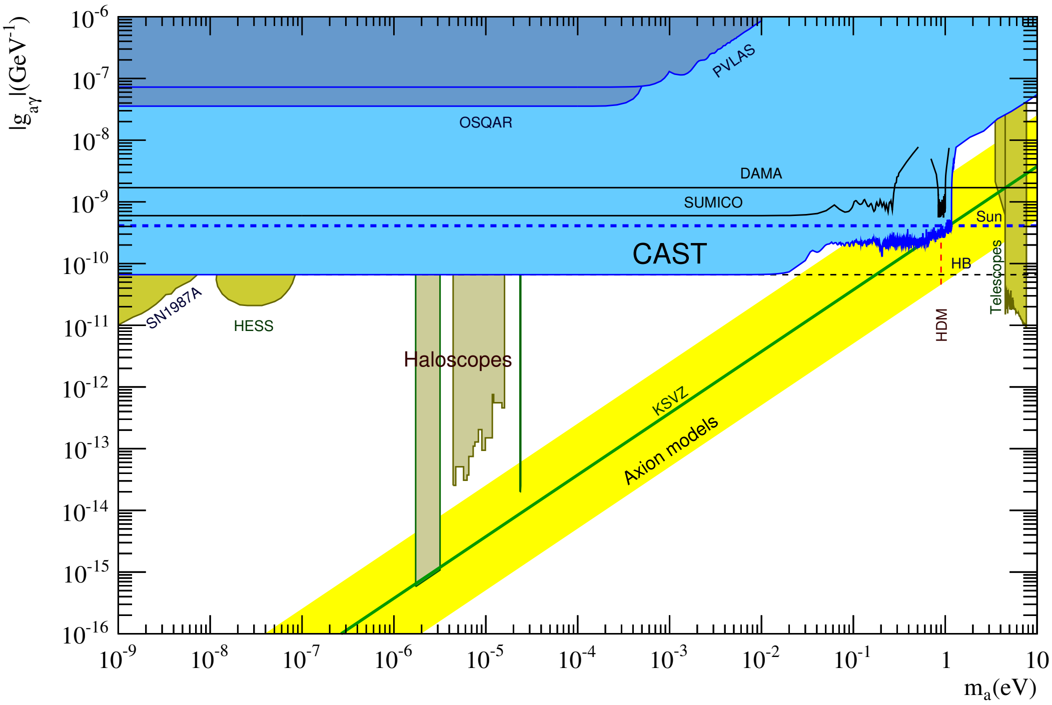

Figure 4.3: Constraints on the axion photon coupling $g_{a\gamma}$ in dependence of the axion mass m_a. The upper bound achieved by CAST [35] is shown in light blue. Results from a previous helioscope experiment [28, 29], SUMICO, are represented as black line while the upper bound from laser propagation experiments, OSQAR [39] and PVLAS [37], are indicated in dark blue. The excluded regions obtained from high-energy photon propagation in astrophysical magnetic fields (H.E.S.S.), the SN1987A observation [66] and telescopes searching for cosmic axion decay lines are shown as well as the best limit obtained with Bragg technique by DAMA [36]. Horizontal dashed lines indicate limits obtained from solar properties [67] and the energy loss of horizontal branch (HB) stars [68]. The vertical dashed line denotes the cosmic hot dark matter (HDM) limit [69], which only applies to QCD axions. For the haloscope limits it is assumed that axions are the galactic dark matter. The yellow band shows the region predicted for QCD axion models with the KSVZ model indicated as green line. Figure taken from [35].

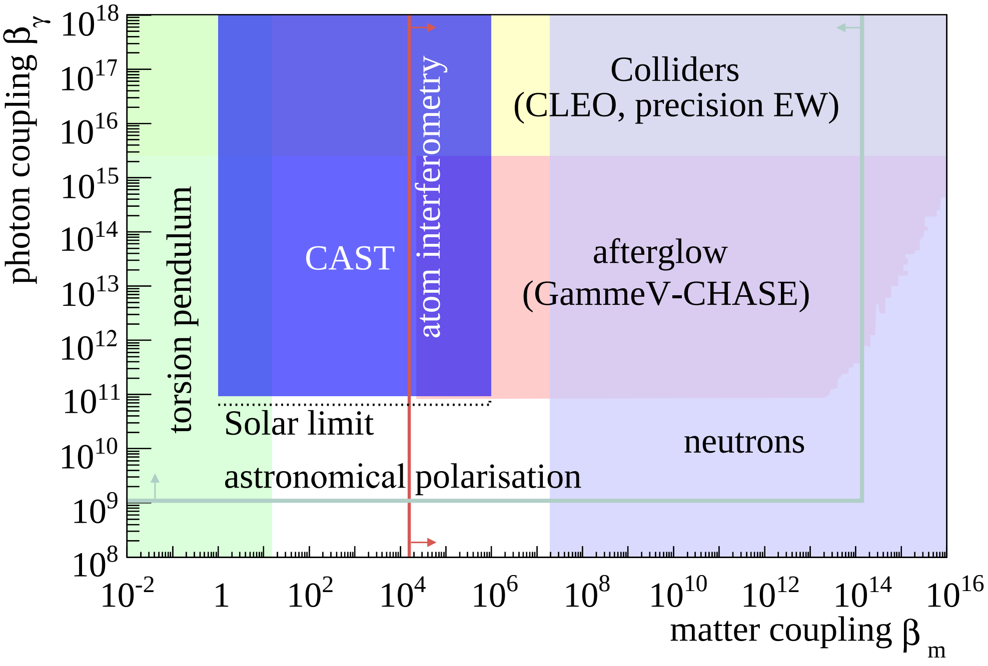

Figure 4.4: Exclusion plot for chameleons in the β_γ-β_m plane. The region excluded by CAST in 2013 with an SDD [42] is presented in purple along with the limit derived from a solar luminosity bound (dashed line). Also shown are the bounds set by torsion pendulum tests (green) [47], neutron interferometry measurements (lilac) [48], CHASE (pale orange) [51] and collider experiments (yellow) [70]. The forecasts of the atom-interferometry technique [49] (this bound has been improved towards lower values of β_m since then [50]) and the astronomical polarization [71] are represented with lines. Figure taken from [42].

CHAPTER 5

The physics of gaseous detectors

The InGrid based X-ray detector developed, build and deployed at the CERN Axion Solar Telescope (CAST) for the solar chameleon search is a Micropattern Gaseous Detector (MPGD). Therefore, the basic physics processes happening inside gaseous detectors will be described in this chapter. Starting with ionization processes leading to primary electrons being freed which then are transported in an electric drift field towards the readout plane. There the arriving primary electrons are multiplied in a gas amplification process so they can be detected.

5.1 Ionization processes and energy loss

In case of an MPGD, charged particles as well as (X-ray) photons, are not detected directly but by the ionization trace they leave when traversing or being stopped/absorbed in the detector's gas volume. Charged particles traversing the gas volume will loose energy when they encounter gas atoms or molecules. The energy transferred to the gas atoms or molecules causes ionization or excitation. (X-ray) photons, however, loose energy in a medium through different processes, absorption or scattering which results in energy being transferred to electrons of the gas atoms or molecules which then themselves may loose these energy through ionization resulting in an ionization trace.

As the processes involved in the absorption or energy loss of photons are quite different to those involved for charged particles, loosing energy through ionization, they will be discussed separately. Starting with the photon interactions with matter as these result in charged particles (electrons) being released and causing ionization. The latter processes will be described in terms of charged particles' interactions with matter where a focus will be put on the energy loss for electrons. At the end, the resulting number of ionizations and its spread for a given absorbed energy or energy loss will be discussed.

5.1.1 Interactions of photons with matter

When photons interact with matter, they are either absorbed or scattered. These interactions happen randomly. Therefore, no range in a medium can be given for a photon, but as the interactions are statistical processes an attenuation for a photon beam of initial intensity I_0 can be stated after traversing a distance x in a medium:

$$I(x) = I_0 e^{-\mu x} \tag{5.1}$$

where μ is the attenuation coefficient. It can be calculated from the cross sections σ_i for the different interactions of photons with matter as

$$\mu = \rho \frac{N_A}{A} \sum_i \sigma_i \tag{5.2}$$

with ρ the density of the medium, A the atomic weight of the medium's atoms or molecules and N_A Avogadro's number. Of course, as the σ_i are energy dependent also μ depends on the photon's energy.

For detection purposes only three of the photon interactions with matter are of relevance: the photoelectric effect, Compton scattering and pair production. Other processes like interactions of photons with nuclei or Rayleigh scattering are not important. The cross sections of the different processes depend differently on the photon's energy and/or the properties of the medium. The energy dependent contribution of the different processes to the total cross section of photons interacting with matter is shown in Fig. 5.1 for two different materials, carbon and lead, with very low and high atomic number respectively. It is obvious that for the purpose of X-ray detection photon nucleon interactions can be neglected. Rayleigh scattering is the elastic scattering of a photon off an atom, in this process no energy is transferred. Thus, Rayleigh scattering does not contribute to ionization. Independent of the medium it is visible from Fig. 5.1 that the photoelectric effect is dominant for photon energies up to few tens of keV, in this energy range the other processes contribute less than one percent to the total cross section and, thus, may be neglected for application of the InGrid based X-ray detector. In the energy dependence of the photoelectric effect's cross section, local increases are visible which stem from the medium's absorption lines depending on the medium's electron configuration and binding energies.

Photoelectric effect

The full energy of a photon can be transferred to an electron in the photoelectric effect. To satisfy energy and momentum conservation for this process a recoil partner is necessary. Therefore, the photoelectric effect is only possible for electrons bound in the electric field of a nucleus and only if the photon energy exceeds the binding energy of the electron. Then, the electron is freed in the interaction of the photon with an atom A and carries the energy difference between photon energy and its own binding energy:

$$\gamma A \to A^+ e^- . \tag{5.3}$$

The energy transfer is mediated through the electromagnetic force. The photoelectric cross section is highest for electrons from the deepest shells of an atom (K- shell), because there the distance to the recoil partner is minimal allowing for transferring the maximum recoil momentum. Also on the deepest shell the screening of the nucleus by the electron shells is low. For electrons of the K-shell the cross section for the photoelectric effect is given by [73]

$$\sigma^{\mathrm{K}}_{\mathrm{p.e.}} = \sqrt{32} \left(\frac{m_e c^2}{E_\gamma} \right)^{3.5} \alpha^4 Z^5 \sigma_{\mathrm{Th}} \tag{5.4}$$

using the non-relativistic Born approximation with the fine structure constant $\alpha \sim 1/137$, the photon energy E_γ, the atomic number of the medium Z, the electron mass m_e and the Thomson cross section for elastic photon electron scattering $\sigma_{\mathrm{Th}} = 8/3 \cdot \pi r_e^2$ where r_e is the classical electron radius. It is obvious that the photoelectric effect contributes most for low photon energies ($E_\gamma \lesssim 5\,\mathrm{MeV}$) as can be seen in Fig. 5.1. The highest cross section is reached for materials with high atomic number. Close to absorption lines, defined by the electron binding energies in the material, the photoelectric cross section is enhanced.

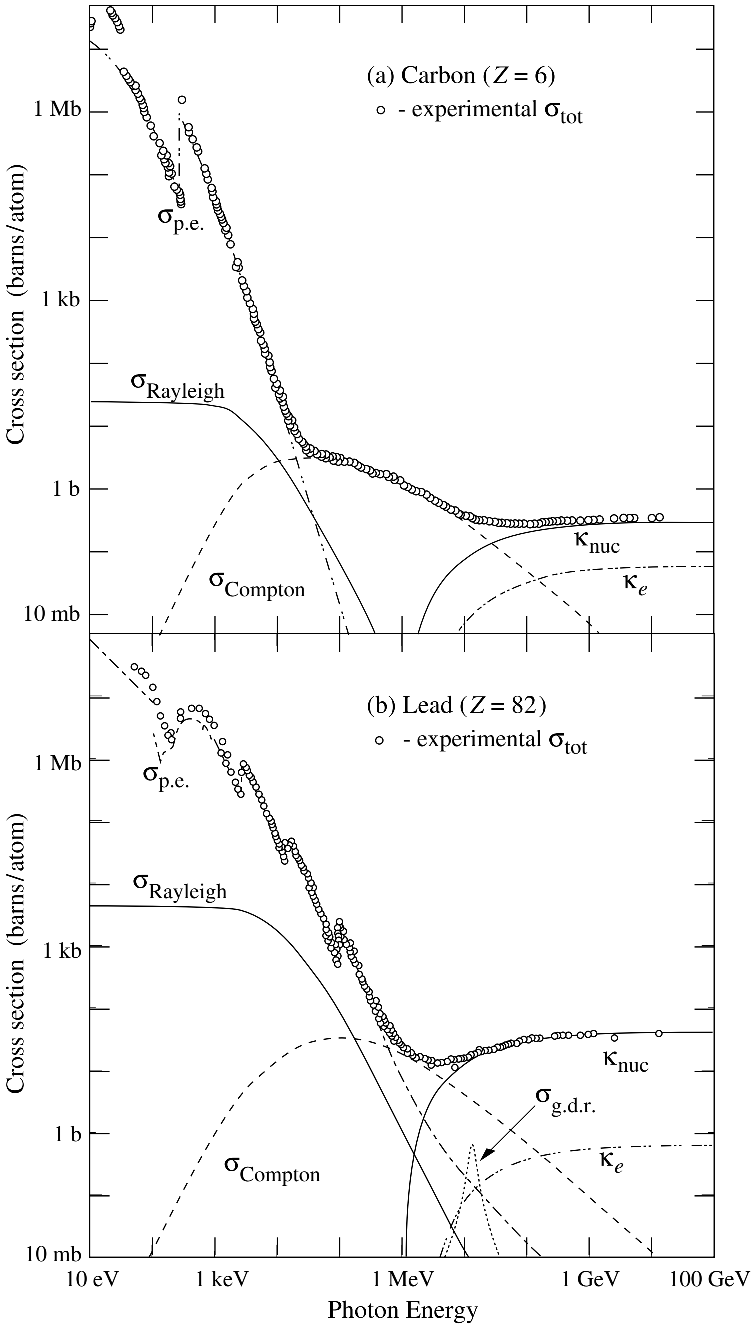

Figure 5.1: Cross sections for photon interactions with matter in carbon (top) and lead (bottom) as function of the photon energy. Different contributions to the total cross section σ_{tot} are shown: the photoelectric cross section $\sigma_{\text{p.e.}}$, the Compton scattering cross section σ_{Compton}, the Rayleigh scattering cross section σ_{Rayleigh} (elastic scattering), the cross section for pair production in nuclear κ_{nuc} and electron electric fields κ_e as well as the cross section of photonuclear interactions $\sigma_{\text{g.d.r}}$. Figure taken from [72].

When an electron from an inner atomic shell (e.g. the K-shell) is released through the photoelectric effect (or any other process), an electron from a higher shell will fill the resulting gap. The difference of binding energy freed in this can either be emitted in form of a photon (characteristic fluorescence lines of an element) or it can be transferred onto another electron bound in the atom, which then will be released. The latter process is called Auger effect and the electron emitted by it is called an Auger electron. The Auger effect may happen several times after absorption of a single photon through the photoelectric effect, resulting in a cascade of Auger electrons until the remaining holes can no longer be filled from higher shells.

Compton scattering

A photon can scatter off a free electron resulting in part of its energy being transferred to the electron and the photon being deflected. When neglecting the binding energy an electron from a high shell of an atom can be treated as quasi free. Therefore the cross section for the Compton scattering on a single electron is independent of the material properties, such as its atomic number. But, the cross section for Compton scattering on the electrons of an atom depends on the atomic number of the atom as it relates to the number of electrons a photon can scatter off per atom. According to [73] the energy dependence of the Compton scattering cross section for high energies can be approximated as

$$\sigma_{\text{Compton}} \propto \frac{\ln E_\gamma}{E_\gamma}. \tag{5.5}$$

From this dependence it is obvious that the contribution of Compton scattering to the total cross section decreases for very high photon energies.

The photon energy E'_γ after scattering off the electron can be derived from energy and momentum conservation and depends on its initial energy E_γ and the scattering angle θ

$$E'_\gamma = \frac{E_\gamma}{1 + \frac{E_\gamma}{m_e c^2}(1 - \cos\theta)}. \tag{5.6}$$

The energy difference $E_\gamma - E'_\gamma$ is transferred onto the electron, it becomes maximum for backscattering ($\theta = 180°$). Assuming that the electron is at rest prior to the scattering process, its direction with respect to the initial direction of the photon can be written as

$$\cot\varphi = \left(1 + \frac{E_\gamma}{m_e c^2}\right)\tan\frac{\theta}{2} \tag{5.7}$$

where φ is the angle between the initial photon direction and the scattered electron.

Pair production

In the presence of a charged particle P a photon can convert into an electron positron pair

$$\gamma P \rightarrow P e^+ e^- \tag{5.8}$$

given its energy E_γ exceeds a certain threshold. The charged particle P is required to take on the recoil to satisfy energy and momentum conservation. The pair production can happen in the electric field of a nucleus but also in the electric field of an electron, although the latter is rather unlikely. Assuming energy and momentum conservation the threshold for pair production can be calculated as

$$E_\gamma \geq 2m_e c^2 + 2\frac{m_e^2 c^2}{m_P} \tag{5.9}$$

where m_P is the mass of the charged particle P absorbing the recoil. If P is a nucleus ($m_P = m_{\text{nucleus}} \gg m_e$) the threshold energy can be approximated to

$$E_\gamma \gtrsim 2m_e c^2 \approx 1\,\text{MeV}. \tag{5.10}$$

The cross section for pair production in the electric field of the nucleus can be given for low photon energies as [73]

$$\kappa_{\text{nuc}} = 4\alpha r_e^2 Z^2 \left(\frac{7}{9}\ln 2\frac{E_\gamma}{m_e c^2} - \frac{109}{54}\right), \tag{5.11}$$

if the photon gets close enough to the nucleus to avoid screening of the nucleus' electric field by the electron shells. For complete screening of the nucleus pair production can only happen for high photon energies. In this case, κ_{nuc} becomes energy independent and can be given as

$$\kappa_{\text{nuc}} = 4\alpha r_e^2 Z^2 \left(\frac{7}{9}\ln 2\frac{183}{Z^{1/3}} - \frac{1}{54}\right). \tag{5.12}$$

From the energy threshold and the Z^2 dependence of the cross section one can see that pair production is only dominant for high photon energies and materials with high atomic number Z.

5.1.2 Interactions of charged particles with matter

Charged particles traversing a medium will transfer energy to the medium's electrons mainly through electromagnetic interactions resulting in excitation or ionization of the medium. The encounters of a charged particle and the atoms of the medium occur randomly. The mean free path λ between two encounters can be calculated as

$$\lambda = \frac{1}{\sigma_I n_e} \tag{5.13}$$

where n_e is the electron density in the medium and σ_I the ionization cross section. For a thin medium, such as a gas, the number of encounters on a path of length L is given by a Poisson distribution with mean L/λ. As σ_I depends on the charged particle's mass, energy and charge, also λ depends on these.

In an encounter of the charged particle (here a muon $\mu^\pm$) with a gas atom A different mechanisms and processes result in an ionization. The gas atom A may become directly ionized resulting in one or more electrons being released:

$$\mu^\pm A \to \mu^\pm A^+ e^-, \mu^\pm A^{2+} e^- e^-, \dots \tag{5.14}$$

which is called primary ionization. It is also possible that the gas atom does not become ionized but excited:

$$\mu^\pm A \to \mu^\pm A^*. \tag{5.15}$$

If the gas is a mixture and in addition contains gas atoms (or molecules) of type B with an ionization energy lower than the excitation energy of A, B can become ionized through a collision with A^*:

$$A^*B \rightarrow AB^+e^-. \tag{5.16}$$

This process is called Penning effect and effectively lowers the mean ionization energy of a gas mixture compared to the mean ionization energies of its compounds.

Electrons freed through primary ionization which received enough energy to ionize the gas themselves can cause secondary ionization:

$$e^-A \rightarrow e^-A^+e^-, e^-A^{2+}e^-e^-, \ldots \tag{5.17}$$

which is the main contribution to the total ionization. Some electrons may even receive enough energy to leave a visible ionization trace in a detector, those electrons are called δ-electrons and are emitted preferentially perpendicular to the incoming charged particle's trajectory.

The maximum energy which can be transferred onto an electron of a gas atom in a single encounter with the incoming charged particle is given by [73]

$$T_{\max} = \frac{2m_ec^2\beta^2\gamma^2}{1 + 2\gamma m_e/m + (m_e/m)^2} \tag{5.18}$$

where m_e is the electron mass, m the mass of the incoming charged particle, $\beta = v/c$ its velocity in units of the speed of light c and $\gamma = (1-\beta^2)^{-1/2}$ its Lorentz factor. For charged particles heavier than electrons ($m > m_e$) this can be simplified to

$$T_{\max} = \frac{m^2\beta^2\gamma^2}{\gamma m + m^2/2m_e} = \frac{p^2}{E + m^2c^2/2m_e} \tag{5.19}$$

with $E = \gamma mc^2$ the charged particles energy and $p = \beta\gamma mc$ its momentum. For heavy charged particles the mean energy loss per path length can be given through the formula of Bethe and Bloch [72]

$$-\left\langle \frac{\mathrm{d}E}{\mathrm{d}x} \right\rangle = 4\pi N_A r_e^2 m_e c^2 \frac{Z}{A} \rho \frac{1}{\beta^2} z^2 \left(\frac{1}{2} \ln \frac{2m_ec^2\beta^2\gamma^2 T_{\max}}{I^2} - \beta^2 - \frac{\delta(\beta)}{2} \right) \tag{5.20}$$

where N_A is Avogadro's number, r_e the classical electron radius, m_e the electron mass, c the speed of light, Z and A the atomic number and mass of the absorber material, ρ its density, z the charge of the incoming charged particle in units of the elementary charge, I the mean excitation energy, which can be approximated by $I = 16 \cdot Z^{0.9}\mathrm{eV}$ for $Z > 1$ [73] and $\delta(\beta)$ a density correction term. Equation 5.20 is valid in the range $0.1 \lesssim \beta\gamma \lesssim 1\,000$. Often, instead of the energy loss per length dx, the energy loss per surface mass density $\mathrm{d}X = \rho \mathrm{d}x$ is used

$$-\left\langle \frac{\mathrm{d}E}{\mathrm{d}X} \right\rangle = -\frac{1}{\rho} \left\langle \frac{\mathrm{d}E}{\mathrm{d}x} \right\rangle \tag{5.21}$$

which is almost independent of the material or medium. The energy loss per surface mass density is also referred to as stopping power. The stopping power for muons in copper is shown in Fig. 5.2 as function of $\beta\gamma$. Slow charged particles ($\beta\gamma < 0.1$) are deflected in the electric field of the nuclei, thereby loosing energy, or may even directly interact with the nuclei. For $\beta\gamma \gtrsim 0.1$ the stopping power decreases with

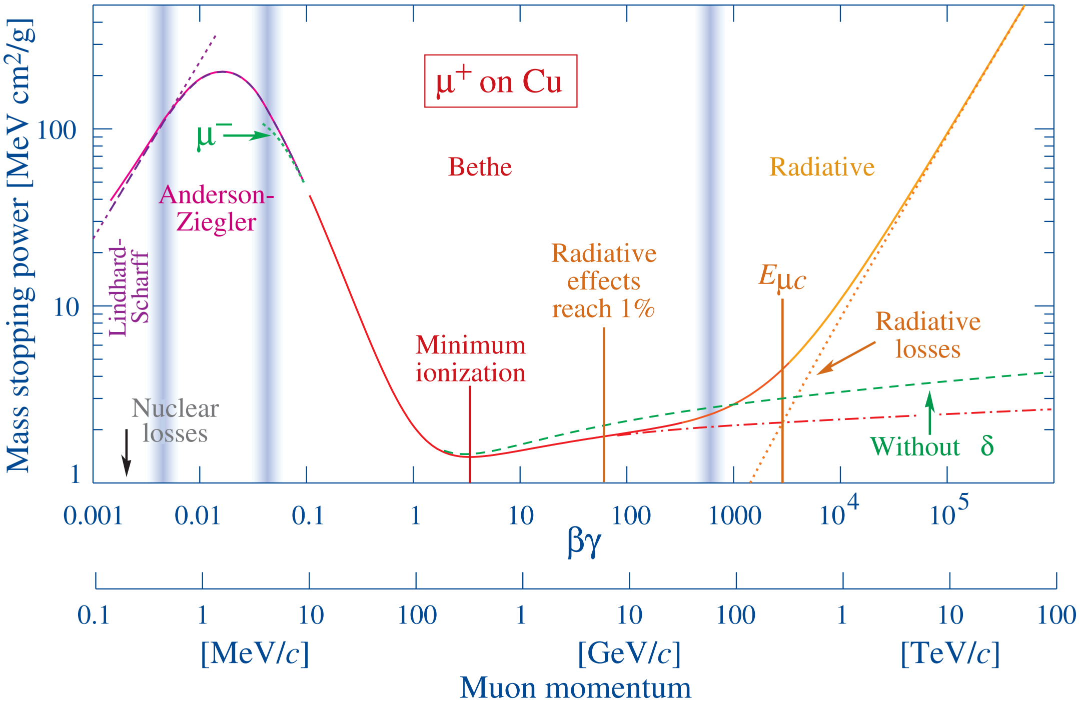

Figure 5.2: Stopping power of muons in copper as function of $\beta\gamma$. The different processes dominant in the energy loss for different ranges of $\beta\gamma$ are marked. The region in which the stopping power is well described by the formula of Bethe and Bloch is $0.1 \lesssim \beta\gamma \lesssim 1\,000$. Figure taken from [72].

$1/\beta^2$ until at $\beta\gamma \approx 4$ a minimum is reached with

$$-\left\langle\frac{\mathrm{d}E}{\mathrm{d}X}\right\rangle\bigg|_{\beta\gamma\approx 4} \approx 1.5\,\mathrm{MeV\,cm^2/g} \tag{5.22}$$

which is approximately independent of the absorber material or medium. For $\beta\gamma \gtrsim 4$ the stopping power rises logarithmically with $\beta\gamma$. As the logarithmic rise only leads to an increase of about 10 to 20 % charged particles with $\beta\gamma \gtrsim 4$ are called minimum ionizing particles (MIPs). The density correction $\delta(\beta)$ in equation 5.20 reduces the stopping power for highly relativistic particles due to screening effects. For thin media, such as gases, the density correction can be neglected. For very fast charged particles ($\beta\gamma \gtrsim 1\,000$) radiative losses (e.g. Bremsstrahlung) dominates the stopping power and energy loss. As radiative losses are not included in equation 5.20 it is only valid up to $\beta\gamma \lesssim 1\,000$. For a fixed momentum the energy loss per length becomes a function of the charged particle's mass and can therefore be used for particle identification in certain energy or momentum ranges.

The energy loss in a thin absorber is dominated by single interactions of the charged particle with an atom of the absorber, resulting in a wide spread of the observed energy loss as it can be as large as T_{max} in a single encounter. This results in the energy loss being distributed approximately according to a Landau distribution, as illustrated in Fig. 5.3 where the energy loss for 10 GeV muons in 1.7 mm silicon is shown. The mean energy loss does not coincide with the most probable value (MPV) due to the asymmetry of the distribution and its long tail towards high energy losses. For thick absorbers the distribution of the energy loss approaches a Gaussian distribution as the individual high energy losses forming the tail in the distribution for thin absorbers are averaged out.

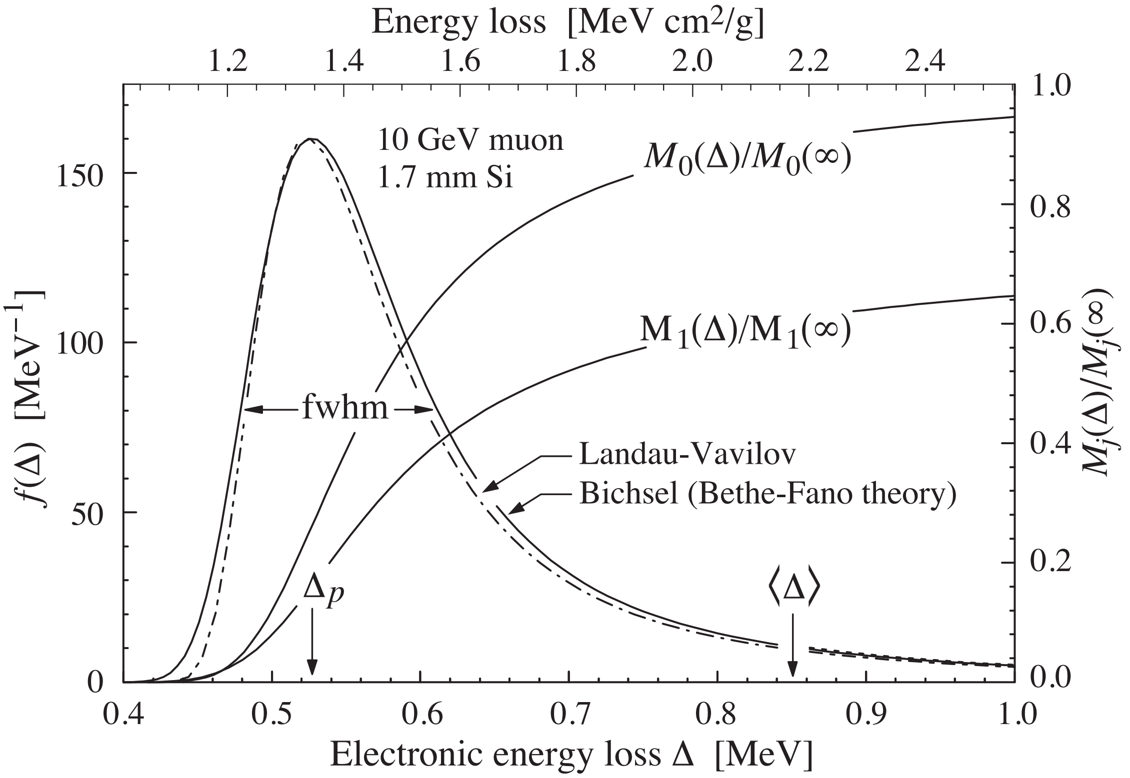

Figure 5.3: Energy loss for 10 GeV muons in 1.7 mm silicon. In this case of a thin absorber, the energy loss distribution undergoes large fluctuations and features a long tail towards high energy loss caused by the possibility to loose up to T_{max} in a single collision. The distribution follows approximately a Landau distribution with the MPV deviating from the mean value. Figure taken from [72].

Equation 5.20 is only valid for charged particles heavier than electrons which have to be treated differently as an incoming electron cannot be distinguished from the electrons part of its energy is transferred to. Also, due to their low mass, for electrons the emission of Bremsstrahlung starts at much lower energies and plays a more dominant role in the energy loss of electrons. For an electron with energy E_e in one encounter with a gas atom the maximum energy which can be transferred is given by

$$T_{\text{max}} = E_e - m_e c^2 \tag{5.23}$$

as all kinetic energy can be transferred at once. The mean energy loss per path length through ionization and energy can be expresses as [73]

$$-\left\langle \frac{\mathrm{d}E}{\mathrm{d}x} \right\rangle = 4\pi N_A r_e^2 m_e c^2 \frac{Z}{A} \rho \frac{1}{\beta^2} \left(\ln \frac{m_e c^2 \beta^2 \gamma^2 \sqrt{\gamma - 1}}{\sqrt{2} I} + \frac{1 - \beta^2}{2} - \frac{2\gamma - 1}{2\gamma^2} \ln 2 + \frac{1}{16} \left(\frac{\gamma - 1}{\gamma} \right)^2 \right) \tag{5.24}$$

including kinematics of electron electron collisions and screening effects.

The effective range R for electrons in a medium, defined as the distance between entrance and stopping point, can be given as function of the electron energy E_e with an empirically found relation given in [74] as

$$R(E_e) = \frac{A E_e}{\rho} \left(1 - \frac{B}{1 + C E_e} \right) \tag{5.25}$$

with ρ the density of the absorber material and the empirical parameters

$$\begin{aligned} A &= 5.37 \times 10^{-4}\,\mathrm{g/cm^2/keV} & (5.26)\\ B &= 0.9815 & (5.27)\\ C &= 3.123 \times 10^{-3}/\mathrm{keV}. & (5.28)\end{aligned}$$

5.1.3 Number of ionizations

The net effect of a particle (either a charged particle or a photon) loosing energy in a medium like a gas, is the creation of a number of freed electrons through primary and secondary ionization. The number n_I of ionizations caused by an energy loss of ΔE can be calculated using the mean ionization energy W_I for the medium by

$$n_I = \frac{\Delta E}{W_I}. \tag{5.29}$$

As electrons are not only freed through ionization from the outermost shells and as some energy transferred does not lead to ionization but excitation W_I is larger than the ionization energy I in a medium.

When a particle looses all its energy, the number of ionizations is expected to fluctuate according to a Poisson distribution with mean n_I. Thus, the width of the resulting distribution should be given by

$$\sigma_I^2 = n_I \tag{5.30}$$

assuming the individual ionization processes are independent of each other. But, since the individual ionization processes are correlated, the width of the resulting distribution for the number of ionization is reduced by the Fano factor F and becomes

$$\sigma_I^2 = F \cdot n_I. \tag{5.31}$$

The values for F vary for different media and also with the deposited energy ΔE, for noble gases typical values for F are in the order of 0.25 while for certain gas mixtures F can be much smaller, about 0.05 resulting e.g. in an improved energy resolution for gaseous X-ray detectors.

5.2 Charge transport – Drift & diffusion

The ionization trace left by a photon or a charged particle in a gas consists of ions and electrons with opposite charges. To avoid recombination they have to be separated by an electric field which causes the electrons to move towards the readout plane, this electric field is called drift field. The gas ions move in the opposite direction as the electrons and are usually neutralized when they reach the corresponding electrode. The movement of charged particles in an electric field is called drift. For a particle with mass m and charge e in an electric drift field $\vec{E}$ and a magnetic field $\vec{B}$ one can set up an equation of motion

$$m\frac{\mathrm{d}\vec{v}(t)}{\mathrm{d}t} = e\vec{E} + e\left[\vec{v}(t) \times \vec{B}\right] - K\vec{v}(t) \tag{5.32}$$

where $\vec{v}(t)$ is the particle's velocity and $K\vec{v}(t)$ acts as a frictional force caused by collisions of the drifting particle with the gas atoms. Although, this is only a macroscopic approximation it has been found to describe drift processes on large time scales to high extent [74]. A characteristic time scale

$$\tau = \frac{m}{K} \tag{5.33}$$

can be defined for the drift process, where for times $t \gg \tau$ a steady state can be assumed. In the steady state the time dependence of $\vec{v}(t)$ vanishes and equation 5.32 is simplified from an inhomogeneous linear differential equation to a linear equation

$$\frac{1}{\tau}\vec{v} - \frac{e}{m}\left[\vec{v} \times \vec{B}\right] = \frac{e}{m}\vec{E}. \tag{5.34}$$

It is solved by the Langevin formula

$$\vec{v} = \frac{e}{m}\tau|\vec{E}|\frac{1}{1+\omega^2\tau^2}\left(\frac{\vec{E}}{|\vec{E}|} + \omega\tau\left[\frac{\vec{E}}{|\vec{E}|} \times \frac{\vec{B}}{|\vec{B}|}\right] + \omega^2\tau^2\left(\frac{\vec{E}}{|\vec{E}|} \cdot \frac{\vec{B}}{|\vec{B}|}\right)\frac{\vec{B}}{|\vec{B}|}\right) \tag{5.35}$$

with $\omega = e/m \cdot |\vec{B}|$ the cyclotron frequency and assuming τ to be independent of the particle's energy.

In case of a vanishing magnetic field ($\omega\tau = 0$) the particles drift in the direction of the drift field and their velocity is given by

$$\vec{v} = \vec{v}(\vec{B} = \vec{0}) = \frac{e}{m}\tau\vec{E} = \mu\vec{E} \tag{5.36}$$

where μ is the mobility of the particle. Ion mobilities are much smaller compared to those for electrons as ions are much heavier than electrons.

The drift velocity with a magnetic field being present can be expressed as

$$|\vec{v}(\vec{B})|^2 = |\vec{v}(\vec{B} = \vec{0})|^2 \cdot \frac{1 + \omega^2\tau^2\cos^2\phi}{1 + \omega^2\tau^2} \tag{5.37}$$

where ϕ is the angle between $\vec{E}$ and $\vec{B}$. For $\vec{E} \parallel \vec{B}$ the drift velocity as well as drift direction remain unchanged. In case of $\vec{E} \perp \vec{B}$ the drift direction is not parallel to the electric drift field but forms an angle

$$\theta = \arctan\left(-\omega\tau\right) \tag{5.38}$$

with the electric drift field which is called the Lorentz angle.

If the results of this macroscopic approach are compared to a microscopic model taking into account the random collisions between the drifting particles and gas atoms, for $\vec{B} = \vec{0}$ the timescale τ can be identified with the mean time between two collisions [74]. Of course, τ is related to the number density of the gas and the cross section for elastic collisions which is energy dependent. The energy gained between two collisions depends on the electric drift field, thus, also τ and μ depend on the electric drift field. Still, equation 5.35 can be used as a valuable approximation, especially concerning the direction of drift and the influence of a magnetic field. To get the ion and electron mobility for a certain gas (mixture) and drift field, simulations have to be carried out, e.g. with `magboltz` [75].

Through the frequent collisions with the gas atoms, the drifting particles are scattered randomly. A particle cloud starting point-like will therefore become distributed in all directions according to Gaussian distributions. Thus, the density distribution after a time t can be expressed as

$$n(\vec{x}) = \left(\frac{1}{\sqrt{4\pi Dt}}\right)^3 \exp\left(\frac{-|\vec{x} - \vec{v}t|^2}{4Dt}\right) \tag{5.39}$$

with D as the diffusion constant and assuming the particle cloud starting at $\vec{x} = \vec{0}$. The variance for this Gaussian distribution is given by $\sigma^2 = 2Dt$ and is valid for all directions. The particle cloud widens with the drift time t. Using the microscopic model mentioned before one can express the diffusion constant D with the mean particle energy ϵ and its mobility μ

$$D = \frac{2}{3}\frac{\epsilon\mu}{e}. \tag{5.40}$$

Assuming the particles' energy is given only by their thermal energy $\epsilon = 3/2 \cdot kT$ one gets the Nernst-Townsend or Einstein formula

$$\frac{D}{\mu} = \frac{kT}{e} \tag{5.41}$$

which gives a lower limit for the diffusion constant. To calculate the width of the density distribution, also called diffusion, for a given scenario it is more practical to express it as function of the drift distance L than the drift time t. Using

$$t = \frac{L}{\mu|\vec{E}|} \tag{5.42}$$

one gets

$$\sigma^2 = 2Dt = \frac{2DL}{\mu|\vec{E}|} = \frac{4\epsilon L}{3e|\vec{E}|}. \tag{5.43}$$

Distinguishing between diffusion in drift direction (longitudinal) and transverse to it, one can define the transverse and longitudinal diffusion coefficients D_t and D_l as

$$D_{\mathrm{t/l}} = \sqrt{\frac{2D_{\mathrm{T/L}}}{\mu|\vec{E}|}} \tag{5.44}$$

where D_T and D_L are the transverse and longitudinal diffusion constants. With this the diffusion can be be expressed simply as function of the drift distance L as

$$\sigma_{\mathrm{t/l}} = D_{\mathrm{t/l}} \cdot \sqrt{L}. \tag{5.45}$$

Transverse and longitudinal diffusion differ, this was first observed in experiments in 1967 [76]. This anisotropy is caused by the energy dependence of the cross section for elastic collisions between the drifting particle and the gas atoms [74]. This results in the mobility depending on the particle's energy and therefore on the position within the particle cloud. The diffusion coefficients D_t and D_l are different but usually of same order of magnitude. With the transverse and longitudinal diffusion coefficients equation 5.39 can be rewritten as

$$n(\vec{x}) = \left(\frac{1}{\sqrt{2\pi D_\mathrm{t}^2 L}}\right)^2 \left(\frac{1}{\sqrt{2\pi D_\mathrm{l}^2 L}}\right) \exp\left(\frac{-(x^2+y^2)}{2D_\mathrm{t}^2 L}\right) \exp\left(\frac{-(z-L)^2}{2D_\mathrm{l}^2 L}\right) \tag{5.46}$$

with L the drift distance and assuming drift in z-direction. If a magnetic field is present, diffusion transverse to the direction of the magnetic field is reduced as the Lorentz force acts as a retracting force for particles with velocity components perpendicular to the magnetic field.

5.3 Gas amplification

The single or few electrons created through ionization (primary electrons) cannot be detected directly on the readout plane but first have to be multiplied in order to generate charges or signals high enough to be measured. For sufficient multiplication the detection of single primary electrons can become possible.

Electrons can be multiplied in very high electric fields. When the energy an electron gains between two collisions with gas atoms becomes large enough so the electron will ionize the gas atom. If the electric field is high enough, each inelastic collision will create an additional gas ion electron pair. The newly freed electron will then gain again enough energy to ionize further gas atoms itself in every collision, thus, forming an avalanche. Due to their high mass, multiplication does not happen for gas ions as they do not gather enough energy to ionize gas atoms in a collision. The avalanche process resulting in a multiplication of the initial electron(s) is called gas amplification and happens inside the amplification region where the high electric field is often created by a high voltage difference applied over a small distance often defined by fine structures (see also chapter 6).

Typically gas amplifications in the range of 10^3 to 10^5 can be reached. For very high electric fields, resulting in very high gas amplifications, discharges become more likely to happen preventing a stable operation. Therefore, only a certain gas amplification or gas gain can be reached with a certain type of gas amplification stage. The likeliness for a discharge, and so, the maximum gas gain at which a detector can be operated stably, depends also on the rate and type of charged particles ionizing the detector's gas.

The gas amplification process can be described using the Townsend coefficient $\alpha(\epsilon)$ which depends on the electron energy ϵ and can be derived from the number density of gas atoms n and the ionization cross section $\sigma_I(\epsilon)$ also depending on the electron energy. With

$$\alpha(\epsilon) = n \cdot \sigma_I(\epsilon) \tag{5.47}$$

one gets the mean number of ionizations per length. Many factors, e.g. gas pressure, temperature, recombination probability and the presence of the Penning effect, contribute to the Townsend coefficient [74, 77]. As the Penning effect lowers the mean energy required for an ionization, it increases the gas gain. Therefore the use of Penning gas mixtures results in a more stable operation of a detector, as the same gas gain is reached at lower electric field in the gas amplification region. To compute the gas gain from the Townsend coefficient it is more suitable to express it as a function of the electric field in the gas amplification region instead of the electron energy. Unfortunately, $\alpha(|\vec{E}|)$ cannot be calculate analytically for the high electric fields in the gas amplification region. Thus, one has to rely on simulations and measurements.

The increase $\mathrm{d}N$ in the number of electrons in the avalanche after a distance $\mathrm{d}x$ can be derived from the Townsend coefficient by

$$\mathrm{d}N = N(x)\alpha(|\vec{E}(x)|)\mathrm{d}x \tag{5.48}$$

where $N(x)$ is the number of electrons in the avalanche at the position x, $N(x = 0)$ is therefore the number of electrons entering the gas amplification region. Thus, the number of electrons at the end of the gas amplification is given by integrating $\mathrm{d}N$ from $x = 0$ where the avalanche starts to its endpoint at $x = \Delta x$. One gets

$$N(\Delta x) = \int \mathrm{d}N = N(x = 0) \exp\left(\int_0^{\Delta x} \alpha(|\vec{E}(x)|)\mathrm{d}x\right) \tag{5.49}$$

which for a constant electric field becomes

$$N(\Delta x) = N(x = 0) \exp(\alpha(|\vec{E}|)\Delta x). \tag{5.50}$$

The gas gain G gives the multiplication factor and is defined as

$$G(\Delta x) = \frac{N(\Delta x)}{N(x=0)} = \exp\left(\alpha(|\vec{E}|)\Delta x\right) \tag{5.51}$$

and can be written as

$$G(\Delta U) = \exp\left(\alpha\left(\frac{\Delta U}{\Delta x}\right)\frac{\Delta U}{|\vec{E}|}\right) \tag{5.52}$$

for the constant electric field in the amplification region formed by applying a voltage difference of ΔU between start and end point of the amplification region. Assuming that gas amplification will only happen if a certain threshold voltage difference is exceeded one can parametrize the gas gain as [77]

$$G(\Delta U) = Ae^{B\Delta U} \tag{5.53}$$

with A and B as parameters to be obtained from measurements for a certain gas amplification structure or stage for different voltages.

Of course the development of the avalanche in a gas amplification process is a statistical process underlying large fluctuations. The stated gas gain therefore only gives a mean value for the obtained multiplication in the gas amplification process. In case of a constant electric field in the amplification region the distribution of the gas amplification can be described by a Pólya distribution [74] which can be parametrized as

$$P_{\text{Pólya}}(x) = \frac{K}{G_{\text{Pólya}}}\frac{(\Theta+1)^{\Theta+1}}{\Gamma(\Theta+1)}\left(\frac{x}{G_{\text{Pólya}}}\right)^{\Theta}\exp\left(-(\Theta+1)\frac{x}{G_{\text{Pólya}}}\right) \tag{5.54}$$

with $G_{\text{Pólya}}$ as the mean of the distribution, K a scaling factor and Θ related to the width of the distribution via

$$\sigma^2 = \frac{G_{\text{Pólya}}^2}{\Theta+1}. \tag{5.55}$$

Within an avalanche ultraviolet (UV) photons are created due to excitation of gas atoms which is either caused by collisions not leading to ionization or recombination of electrons and gas ions. The UV photons can be absorbed in the gas resulting in ionization of a gas atom. If this happens inside the amplification region additional avalanches are started at different places than the original one, the range of UV photons inside the gas can range up to several millimetres. If a UV photon ionizes a gas atom outside the amplification region, either in the gas volume or by freeing an electron from a metal surface (like an electrode) through the photoelectric effect, this leads to the creation of fake signals observed in the detector. To avoid the avalanches spreading in the amplification region and the creation of fake signals, quencher gases are added to the gas (mixture) which can absorb UV photons without being ionized. Quencher gases are typically molecular gases (e.g. CO_2 or iC_4H_{10}) which feature absorption lines in the UV regime resulting in high cross sections for the absorption of UV photons. These quencher gases keep the UV photons from reaching regions outside the original gas amplification avalanche and can deexcite through emitting photons in the infrared regime through their vibrational states or in collisions with other gas atoms. Some quencher gases (e.g. iC_4H_{10}) also act as Penning gases and/or allow to achieve a small Fano factor if added in small quantities.

CHAPTER 6

InGrid – An integrated MicroMegas stage

The InGrid based X-ray detector used for the search presented in this work is based on the Integrated Grid (InGrid) technology, also called GridPix technology, and will be described in detail in chapter 7. The InGrid technology combines a Micro-Mesh Gaseous Structure (MicroMegas) gas amplification stage with a fully pixelized and integrated readout by using photolithographic post-processing techniques. Thus, overcoming the main limitations of conventional pad or strip based readout schemes usually used with MicroMegas detectors. In the following section the working principle of the MicroMegas technology will be explained. In the second section the InGrid technology will be discussed including the motivation for the development and an insight in their production process and its improvement towards a mature detector technology over time.

6.1 The Micro-Mesh Gaseous Structure technology

The MicroMegas technology was invented by G. Charpak and Y. Giomataris and first reported on in 1996 [78]. This kind of Micropattern Gaseous Detectors (MPGDs) shows a good energy and position resolution paired with high-rate capability [79, 80] and robustness. They are nowadays widely used in particle physics, especially the later developed bulk production method [81] allows for instrumenting large areas with MicroMegas in a simple and reliable process. In the following subsections the working principle of MicroMegas will be explained including a brief introduction of the development history and the bulk production method. The Microbulk MicroMegas will be introduced in more detail which are manufactured in a single process including the formation of the readout plane resulting in a radiopure detector suitable for low rate experiments as the CERN Axion Solar Telescope (CAST).

6.1.1 Development and working principle

Starting in the late 1980s the first MPGDs were developed as successor of Multiwire Proportional Chambers (MWPCs) [82] which were at that time widely used in particle physics experiments. MWPCs are limited in their position resolution by the wire spacing, which is in the order of 1 mm, and in their rate capability due to the space charge formed by the ions created in the gas amplification process slowly drifting through the active volume. One of the main drivers for developing new types of gaseous detectors at this time was the planning of the Large Hadron Collider (LHC) at CERN, requiring reliable detectors for ionizing particles with high spatial resolution which can be operated at very high rates.

The main idea behind MPGDs is to create the high electrical fields necessary for gas amplification processes by fine structured electrodes instead of wires. Of the many concepts pioneered and tested

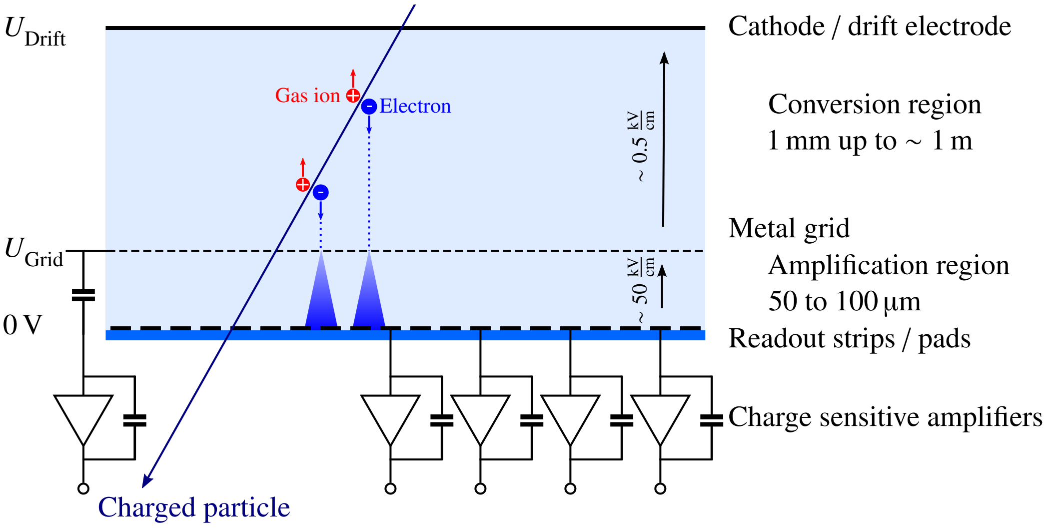

Figure 6.1: Working principle of a MicroMegas detector. The gas volume enclosed between drift electrode and readout plane is divided into a conversion region and a thin amplification region by a metal grid. The readout strips/pads of the readout plane are connected to the inputs of charge sensitive amplifiers which are read out by dedicated readout electronics. The analogue signal induced on the metal grid can be obtained by decoupling it from the grid's high voltage line. The asymmetric electric field configuration causes primary electrons created in the conversion region to drift towards the metal grid, when entering a grid hole an avalanche is created resulting in a multiplication of the electrons which are then collected on the readout strips/pads.

basically two types of MPGDs survived and are today widely used in many particle physics experiments and applications. One of these are Gas Electron Multiplier (GEM) foils [83, 84], copper-clad Kapton® foils (typical thickness 50 µm) with fine holes created through wet etching techniques. The high electrical field for the gas amplification process is here created inside the holes by applying a high voltage between the top and bottom copper electrode of the GEM.

The second type of MPGDs today widely used is the MicroMegas. Here the electrical field for the gas amplification is formed in a tiny gap between the readout plane (pads or strips connected to charge sensitive amplifiers and readout electronics) and a thin metal grid or mesh. A sketch depicting the layout and working principle of a MicroMegas detector is shown in Fig. 6.1. The thin metal grid, a few micrometers thick, rests on tiny insulating spacers or pillars above the readout plane. Typically the gap between grid and readout plane is in the order of 50 µm or 100 µm and defined by spacers which have to be very precise in height and position to achieve a good uniformity. The metal grid features holes in a regular pattern with holes sizes and pitches in the order of 10 to 50 µm and can for example be created by electroforming techniques.

The metal grid divides the detector's gas volume in two separate regions: The small amplification region between grid and readout plane and the drift and conversion region between grid and cathode. The latter can extend from a few millimetres up to several tens of centimetres depending on the application. Charged particles traversing the drift and conversion region will leave a trace of electrons and ions created through ionization while X-ray or other high energetic photons can be absorbed by gas atoms resulting in a photo-electron and, depending on the gas, several Auger electrons which carry off the initial energy of the photon except for a small amount which cannot be transferred. These electrons are usually stopped in the gas within short range and create thereby a number of electron ion pairs related to the photon's energy. In both cases the electron ion pairs are then separated by the electric drift field between cathode and grid which is typically in the order of several hundred volts per centimetre.

While the ions drift to the cathode and are neutralized there, the electrons (also called primary electrons) drift towards the metal grid undergoing diffusion resulting in a spread in all directions. When entering the amplification region through the grid holes the primary electrons start avalanches inside the strong electric field, typically several tens of kilovolts per centimetre, of the amplification region resulting in a multiplication of the incident primary electron. Amplification factors can range from a few thousand up to 10^6 depending on the application. The fraction of primary electrons entering the grid holes is determined by the collection efficiency for electrons and is usually close to 100 % [78], making the grid quasi-transparent for the primary electrons, due to the asymmetric field configuration and the grid geometry. In the gas amplification process of course, also ions are produced in the same number as electrons but the number of ions entering the drift and conversion region is strongly suppressed by the ratio of drift and amplification field so most ions are being caught at the grid resulting in an intrinsic low ion back-flow for MicroMegas detectors [78]. The ion back-flow as well as the electron collection efficiency can be tuned and optimized by varying the field configuration and the grid geometry (hole size and pitch).

After being multiplied the electrons, created in the avalanches, reach the readout plane which is typically patterned with metal strips or pads. While strips can have a pitch down to about 100 µm, pad sizes typically are several square millimetre. Each strip or pad is connected to the input of a charge sensitive amplifier and its readout electronics, measuring the charge induced on the pad or strip. The need to connect each pad or strip to an individual amplifier and readout channel limits the number and size of the pads or strips. On the one hand for each pad or strip an individual channel has to be available in the used readout electronics, thus limiting the number of pad or strips by the readout channel density. On the other hand each pad or strip has to be connected to its readout channel through a circuit path. Therefore, the minimal pitch, the number of layers in the printed circuit board (PCB), the pin density and size of connectors and as well the routing of circuit paths set a limit on the number of readout pads or strips.

There also exist conventional readout planes featuring pads with pitches in the order of a few hundred micrometer. But, while the routing and manufacturing of the required PCBs with a high circuit path density is feasible, although very expensive, still an individual readout channel is required for every pad requiring a very high number and density of channels in the used electronics, which is hard to achieve with today's (available and affordable) technologies. Therefore, the pads are interconnected along strips as illustrated in Fig. 6.2(a). By connecting for example half of the pads to strips in the x-direction and the other half to strips in the y-direction this still allows for a 2D position sensitive detector. Of course this simple high granularity is bought by the price of possible ghost hits and possible ambiguity especially when used for high rate applications due to the high occupancy of the detector.

A special type of MicroMegas especially suitable for large area detectors is called MicroMegas in a bulk [81]. Here, the metal grid is replaced by a fine, woven mesh sandwiched by layers of a photoresist[1] and laminated onto the readout plane. The photosensitive material is later exposed and developed to form the pillars on which the mesh rests. This more or less simple production process uses off the shelf machines and materials from the PCB industry and allows for rather large readout planes in the order of square meters to be equipped with MicroMegas stages in a reliable and cheap process with only small losses and differences in performance compared to the original MicroMegas. By coating the readout plane with a resistive material before adding the MicroMegas stage the detector can be made spark proof as the resistive material acts as a kind of quench resistor and actively protects the MicroMegas against sparks which is especially important for applications involving high rates of highly ionizing particles. Of

---

[1] Photoresists are materials sensitive to light which can be used to create structures on surfaces by exposing the photoresist to light through a mask defining the pattern and applying developers afterwards to remove either the exposed or unexposed parts of the material.

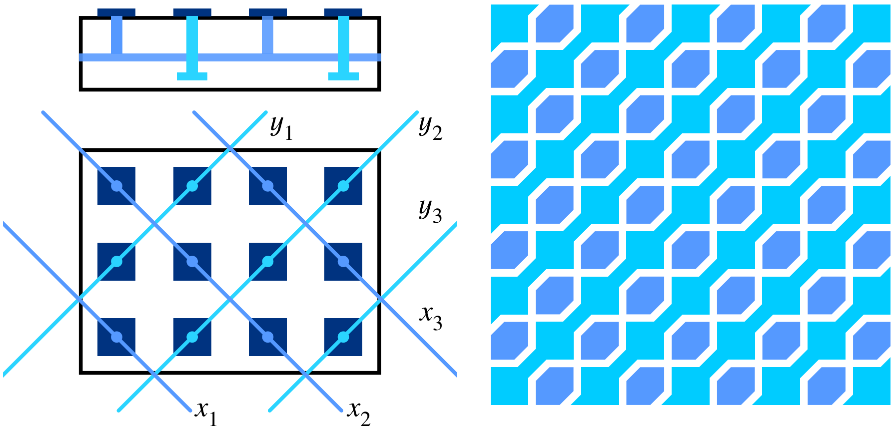

(a)

(b)

Figure 6.2: Sketch of pixel like readout planes using interconnecting strips. Small pixel like pads with pitches in the order of 500 µm can be read out conventionally by interconnecting half of the pads along strips in the x-direction and the other half in the y-direction resulting in a 2D strip readout. (a) shows the interconnecting scheme of the pixel like pads along strips. (b) shows a variant where the interconnection along one direction is implemented in the pad layer of the readout plane thus saving one interconnection layer as it is done the CAST MicroMegas detectors using the Microbulk MicroMegas technology [59, 60].

course, the resistive layer has a small impact on the detector's performance in terms of spatial and time resolution but also its rate capability due to the changed characteristics of the pads or strips.

6.1.2 Microbulk MicroMegas

The Microbulk MicroMegas [85, 86] are a newer type of MicroMegas, introduced in 2007. Here the whole MicroMegas stage including the high granular readout plane is produced in a single process based on Kapton etching and photolithography technologies. Copper clad Kapton is used as raw material and structured in photolithographic processes, by joining several copper clad Kapton films one after the other. It's possible to create fine patterned readout planes including the circuit paths connecting each pad or strip to the amplifier and readout electronics via a high density connector. The production steps are depicted in Fig. 6.3 and are described in the following paragraph using the example of a MicroMegas detector with pixel like small pitched pads interconnected along strips in x- and y-direction as it is used at CAST.

Starting with a 50 µm Kapton film coated with 5 µm of copper on both sides, at first the readout pads are created by structuring the copper on the backside using photolithography techniques. Then a 25 µm Kapton film coated with 5 µm of copper only on a single side is attached to the patterned backside. On the new copper surface the readout lines for the interconnection strips along the x-direction and the readout strips themselves are created. To connect the corresponding pads to the readout strips in x-direction vertical interconnect accesses (vias) have to be created by first etching holes in the backside Kapton layer followed by deposition of copper for the electrical connection. The readout lines and strips for the y-direction pads and the corresponding vias are created by adding another layer of 25 µm Kapton coated with 5 µm copper on one side and repeating the steps as for the strips along the x-direction. In the last steps the mesh (or grid) holes are created by patterning the front side copper layer again using photolithography techniques. To open up the holes in the top Kapton layer and finally form the actual

1. 50 μm Kapton® film sandwiched by 5 μm copper layers

2. Creation of readout pads by photolithography

3. Bonding 25 μm Kapton® film with single 5 μm copper layer to the backside

4. Forming of readout lines by photolithography

5. Kapton® etching

6. Creation of vias

7. Bonding 25 μm Kapton® film with single 5 μm copper layer to the backside

8. Forming of readout lines by photolithography

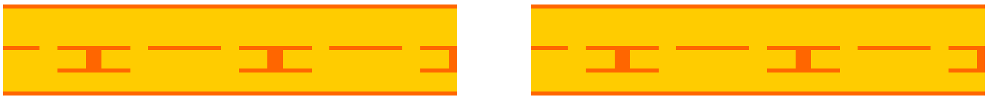

9. Kapton® etching

10. Creation of vias

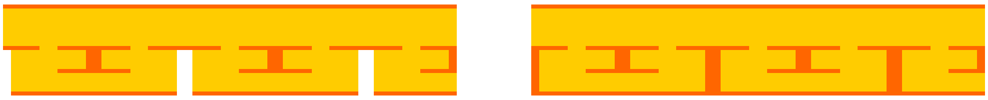

11. Opening mesh/grid holes by photolithography

12. Kapton® etching / cleaning

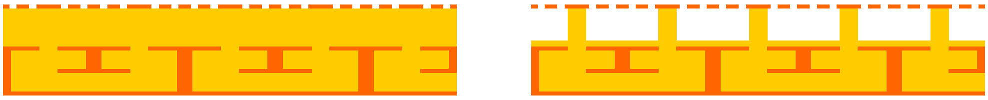

Figure 6.3: Steps of the Microbulk MicroMegas production. By using only Kapton® and copper as raw materials it is possible to create a radiopure MicroMegas stage including its patterned readout plane in a single photolithographic process. By integrating the electric lines for one readout strip direction already in the readout plane itself, steps 7 to 10 can be saved.

MicroMegas structure wet etching is used followed by dedicated cleaning procedures. To ensure the correct formation of the pillar like structures in the Kapton layer copper structures (e.g. spots) are formed during creation of the mesh structure to protect (shadow) the Kapton below these structures during the etching process. By integrating the strips and readout lines for one direction already in the pad copper layer (see Fig. 6.2(b)) one Kapton layer can be saved resulting in a reduction of detector material [85].

The well understood and controllable photolithography technologies used in the creation of this kind of MicroMegas detector results in a very good uniformity and excellent performance. Additionally, as the whole gas amplification and readout structure is composed only of Kapton and copper, both materials are very clean in terms of radiopurity [87], resulting in an overall very radiopure detector (of course assuming the remaining detector components also made from radiopure materials and undergoing proper screening and cleaning procedures) well suited for low rate experiments requiring low background detectors.

6.2 MicroMegas with pixelized readout

While MicroMegas detectors show excellent performance and are nowadays widely used in particle physics experiments, it was expected that they could be improved by combining the high granular gas amplification stage with a readout plane of matching granularity. Usually there is a mismatch between the fine mesh or grid (pitches in the order of 50 µm) and the readout plane, e.g. pads of several square millimetre. A readout plane of matched granularity should be beneficial in several points, among others it should improve the spatial resolution of a detector and it should allow for detecting single, individual primary electrons. Especially the latter could be an important improvement for low background X-ray detectors as needed for experiments like CAST. The capability to detect individual primary electrons should lower the energy threshold and allow for a (better) background suppression by using topological information from the detected events making use of the high granularity.

The main reason the granularity of a pad based readout plane cannot be easily improved is, that for each pad a circuit line is needed connecting it to the outside readout electronics. For very small pads and fine pitches the routing and reliable production of these lines gets very demanding and expensive with today's PCB technology. Also, the number of required amplifier and readout channels rises requiring very densely packed electronics and high density connectors which do not exist today or are at the edge of technology available.

A solution to overcome and bypass these hindrances is to directly integrate all necessary amplifiers and readout electronics into the readout plane which is, in fact, already available in the form of pixelized readout application specific integrated circuits (ASICs). By omitting the silicon sensor usually bump bonded to such a pixel chip and using the bump bond pads of a pixelized readout ASIC as charge collecting anodes in an MPGD one gets a fully integrated readout plane with high granularity. A pixel chip commonly used for MPGD applications is the Timepix ASIC [88], a pixelized readout ASIC featuring 256 × 256 pixels with a pitch of 55 µm. It is based on the Medipix2 ASIC [89] with features added which are desirable for the application in MPGDs such as the possibility to measure the collected charge or time of arrival in the pixels. In chapter 7 the Timepix ASIC will be described in more detail.

In a first attempt to build a MicroMegas detector with pixelized readout a conventional MicroMegas stage was attached onto a Medipix2 ASIC in 2004 [90]. Despite the first promising results of operating such a hybrid device it was obvious that a more precise matching and alignment of the pixels and MicroMegas grid are necessary to avoid Moiré patterns[2] and to reveal the full potential of a MicroMegas with a pixelized readout of matched granularity.

---

[2] Moiré patterns appear when two regular patterns with fine pitch are overlaid resulting in a coarse pattern similar to an interference pattern. The Moiré effect is also visible if two patterns of same granularity are slightly rotated against each other.

To achieve a close to perfect alignment and matching of MicroMegas grid holes to the ASIC's pixels a process based on photolithographic post-processing technology has been developed, to directly produce or integrate the MicroMegas stage on top of the pixel chip, giving rise to the name Integrated Grid [91, 92]. The development of these structures and the process will be described in the following subsection followed by a description of the process itself. A focus will be set on the transition from small scale production to a wafer based production process [93] which allows for creation of integrated MicroMegas with pixelized readouts in a reasonable number at a time.

While GridPix (or InGrid) based detectors are foreseen or considered for several applications the GridPix based X-ray detector build and operated in the course of this thesis was the first GridPix (or InGrid) based detector to be operated at a running physics experiment except for test campaigns or prototype detectors. Among the future applications of GridPix based detectors are the readout planes of the main tracking device, a large Time Projection Chamber (TPC), of the International Large Detector (ILD) [94] planned as one of two general purpose detectors of the International Linear Collider (ILC) or the neutron detector Boron Detector With Light and Ionization Reconstruction (BODELAIRE) currently developed at Bonn.

6.2.1 Development

As a first step towards the MicroMegas with pixelized readout the creation of the MicroMegas stage, the metallic grid and insulating pillars, with photolithographic post-processing techniques was demonstrated on simple readout structures, a single metallic pad per device which could be read out with the conventional amplifiers and analogue-to-digital converters (ADCs) [77, 91]. With these rather simple devices also the optimization of the process and geometry, grid hole size and pillar height, could be done. A hole size of about 30 µm and a pillar height of 50 µm on the 55 µm grid hole pitch adopted to the pixel matrix of the Medipix2 or Timepix ASIC have meanwhile been established as typical geometry parameters. In 2007 the first InGrid structures were produced on top of Medipix2 ASICs in a single chip process, to avoid obstruction, the 30 µm diameter pillars are placed between pixels with a 110 µm pitch. Later, when the Timepix ASIC became available, InGrids were produced on Timepix ASICs, due to the same pixel pitch and peripheral connections this did not require modification of the used masks or processes. A scanning electron microscope (SEM) image of an InGrid structure on top of a Timepix ASIC is shown in Fig. 6.4(a). Parts of the metallic grid have been removed to reveal the underlying bump bond pads of the pixels as well as the insulating pillars. To ensure mechanical robustness of the whole InGrid structure and flatness of the metallic grid as well dike like structures made from the same material as the insulating pillars are located at the sides of the chip, as visible in Fig. 6.4(b). To avoid thermal stress caused by different expansion coefficients of the insulating material, the metallic grid and the chip itself, small expansion gaps are created in the dike structures. Of course, the dike structures block some parts of the chip's pixel matrix reducing the active area of the GridPix device consisting of a Timepix ASIC and the InGrid stage. The inactive area (pixels blocked by dikes) could be reduced in the later iterations of the production process.

While amplifiers and readout electronics specifically designed for application in MPGDs can cope with the high amount of charges created in discharges, e.g. by the means of protection mechanisms, pixel chips like the Timepix or Medipix2 ASIC cannot. Without any additional means a single discharge may permanently damage a chip which can render it unusable. The damage inflicted by a discharge can range from individual pixels up to whole columns being electrically damaged permanently resulting in (partially) dead or noisy pixels/columns. Also damages to the chips peripheral structures like matrix and column logic as well as digital-to-analogue converters (DACs) may happen. The discharges themselves can in principal not be avoided, they can be caused e.g. by highly ionizing particles like α-particles from

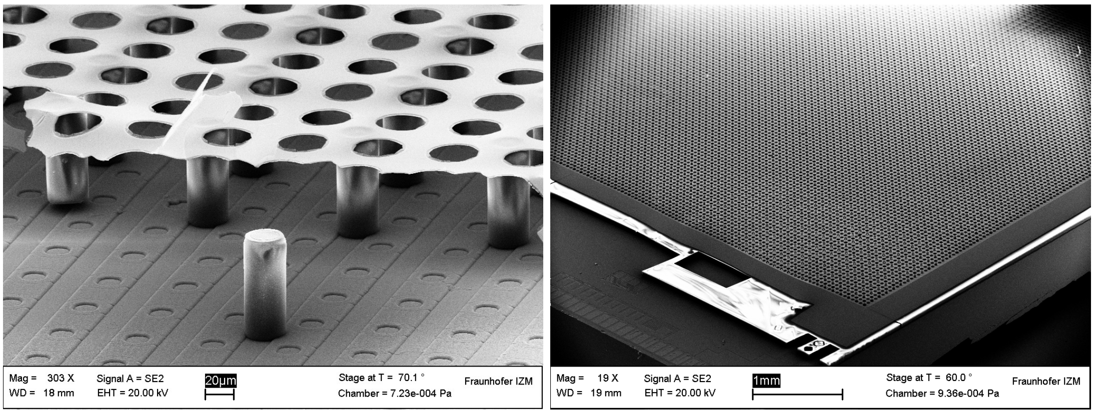

(a) (b)

Figure 6.4: SEM images of InGrid structures on top of Timepix ASICs produced in the wafer scale production process at the Fraunhofer-IZM at Berlin: (a) close-up view of a region where part of the Aluminum grid has been peeled off, revealing the underlying pixels (bump bond pads) and a single pillar; (b) image showing a larger part of an InGrid, the grid structure and the supporting dikes are visible as well as the bond pads on the periphery part of the Timepix ASIC (bottom left). Both images courtesy of IZM Berlin.

decays of environmental radon causing an avalanche in the InGrid structure to develop into a discharge through the high amount of primary electrons localized in a small area. Of course the risk of discharges and their severity increases with the applied grid voltage. As the discharges cannot be avoided their impact on the pixel chip needs to be reduced. The main cause for the damages inflicted by discharges is not entirely understood. Most likely either the high current rushing into the chip or the contact to the high voltage of the grid through the plasma like channel formed in a discharge are causing the observed damages. Therefore, a highly resistive layer was introduced [95], covering the active area of the chip and reducing the current during a discharge (and as well the voltage reaching the chip surface). Through the high resistivity also the grid voltage will drop earlier during a discharge causing it to stop earlier and thus avoiding damage to the chip. Different recipes have been tested, but a layer of 4 to 8 μm of silicon rich silicon nitride (SRSN) has shown a reliable performance without too big effects on the electrical characteristics of the chip and the overall performance of the InGrid or GridPix. Permanent or frequent discharges at the same spot can damage the structure itself by e.g. evaporating parts of the grid or burning of pillars. Another, avoidable, cause for discharges can be dust particles on or in the InGrid structure, therefore requiring proper cleaning procedures and careful handling in clean environments of the GridPix devices and of course the whole detector, especially during assembly.

More complicated, stacked InGrid structures have been build and tested in the beginning of the InGrid technology by forming another (or even two additional) InGrid structure(s) on top of the first one [96]. Similar to GEM stacks [84], this stacked structures need lower grid voltages on the individual grids to achieve the same overall amplification and can therefore reduce the risk of discharges but the alignment between the different stages becomes challenging. Also, these twin or triple structures are even more fragile and difficult to handle compared to the single InGrid stages.

6.2.2 Production process

The basic steps of creating an InGrid structure on top of Timepix ASICs have not been altered from the initial single or small scale production performed at Nikhef and the Mesa+ institute at the University of Twente. The wafer scale production at the Fraunhofer-IZM located in Berlin, has only applied small changes ensuring a good work flow and high yield in the large scale process. The procedure is depicted in Fig. 6.5 and the steps are described in the following paragraph [77, 93, 97].

Starting with a Timepix ASIC or wafer, after cleaning and inspecting the surface the resistive, protection layer formed from SRSN is created in a chemical vapour deposition (CVD) process. To keep the heat load on the chips low the protection layer is deposited in several thin layers with cooling breaks in between. A too high heat load during the post-processing can damage the chips. Next a 50 µm layer of the negative photoresist[3] SU-8[4] is deposited using a spin coating technique. A very thin layer of a positive photoresist is added on top of the SU-8 to form a sacrificial layer. Afterwards the pillars and dike structures are formed by exposure with UV light through a photolithographic mask. Where the negative photoresist is exposed to UV light, the material cross-links, the unexposed photoresist can later be removed with special chemical solvents and baths. By developing the positive photoresist right after the exposure it is only left in place above the not cross-linked parts of the SU-8 protecting these regions from heat and UV light during sputtering of the aluminium layer. The aluminium layer is sputtered on the top surface in several steps until a thickness of about 1 µm is reached. The layer cannot be sputtered in a single step again due to restraints concerning the heat load, also special care has to be taken to avoid UV light from the sputtering process causing the unexposed SU-8 to cross-link (partially), this is done here with the sacrificial positive photoresist layer which is later completely removed. On top of the aluminium layer a thin layer of photoresist is deposited. By exposure with UV light through a photolithographic mask and removal of the exposed or unexposed material a positive mask for the grid holes is created. In a wet etching process the grid holes in the aluminium layer are opened, the acid only removes the aluminium where it is not covered by the mask, the unexposed SU-8 avoids an etching from below. In a last step the unexposed SU-8 is removed from the interstitial by rinsing the whole GridPix device(s) in a chemical bath, this also removes completely the sacrificial positive photoresist layer as it is good soluble even when cross-linked. After careful drying the InGrid structure on top of a Timepix ASIC is complete resulting in a GridPix device ready to be mounted on a PCB.

Initial small scale production

The initial production of GridPix devices was done at Nikhef and the Mesa+ institute at the University of Twente, at first on a single chip basis, later with up to nine chips in one production run. To process multiple chips at once these were glued together and in between cut wafer parts to form a complete and flat silicon wafer to be processed in the machines used for the post-processing. During the deposition of the SRSN protection layer special care has to be taken to avoid the bond pads of the chips being covered. The bond pads are used to electrically connect the chip to the readout electronics via wire bonds onto a PCB. If these (or some of them) are covered with the ceramic like SRSN it may be impossible to get wire bonds to stick on the affected bond pads which can render the chip unusable depending on the purpose of the bond pad. It is very difficult to remove SRSN from bond pads (or other chip surfaces in general) as it can basically only be removed mechanically.

The small scale production was sufficient for the very first research and development applications and was especially adopted for pioneering this new kind of MPGD technology. It allowed to optimize the process steps, the parameters of the InGrid structures and also the recipe and thickness of the protection layer. But, with more parties getting interested in the InGrid and GridPix technology and the upcoming

---

[3] In case of a negative photoresist the unexposed parts of the material remain soluble in the developer and can thereby be removed. For a positive photoresist it is vice versa. Use of a negative photoresist results (after development) in a negative image of mask used for the exposure while a positive photoresist results in a positive image.

[4] SU-8 is an epoxy-based negative photoresist produced by the company Microchem Corp. and is often used in photolithography applications.

1. Start with bare Timepix wafer

2. Deposit protection layer (4 to 8 µm SRSN)

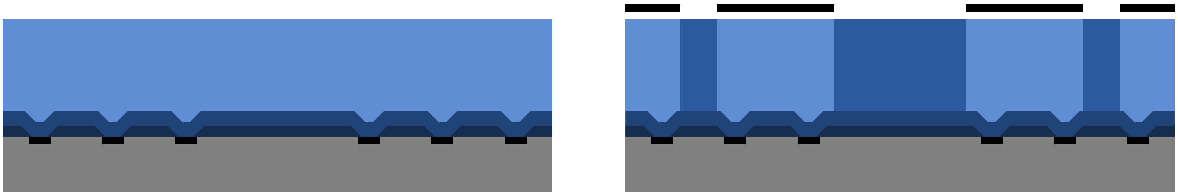

3. Spin coat 50 µm SU-8

4. Create pillars & dikes (Expose SU-8)

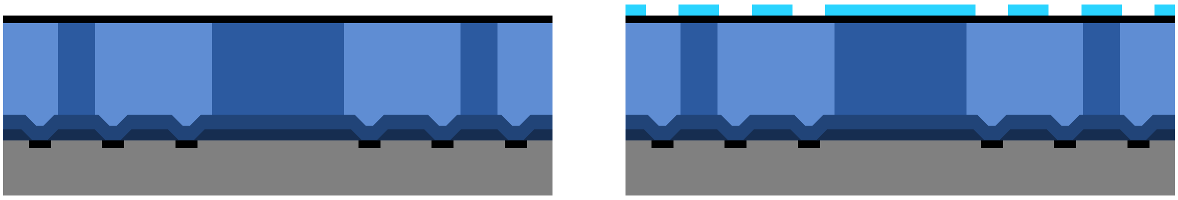

5. Sputter aluminium layer (1 µm)

6. Create mask on top of aluminium layer

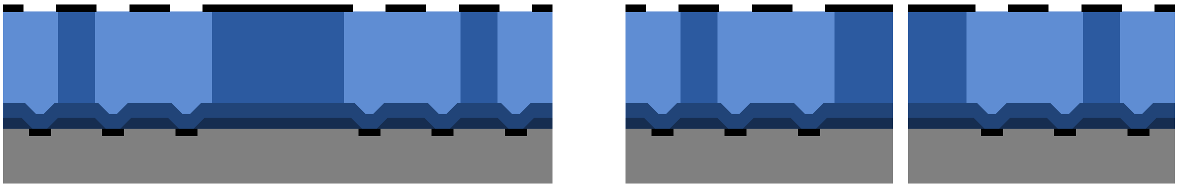

7. Open grid holes by wet etching

8. Dice wafer

9. Remove unexposed SU-8

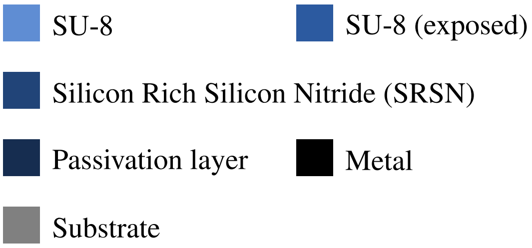

Figure 6.5: Main steps of the wafer scale InGrid production process. Some steps have been omitted in the illustration for the sake of simplicity: Between steps 1 and 2 a surface inspection and cleaning of the wafer are performed; between steps 3 and 4 an additional thin layer of a positive photoresist is put on top of the negative photoresist SU-8 to create a sacrificial layer protecting the unexposed parts of the SU-8 from heat and UV light during sputtering of the Aluminium layer in step 5. The mask in step 6 is created by photolithographic means by adding and structuring another photoresist layer on the top surface. The dicing of the wafer is done prior to developing the SU-8 (removing the unexposed parts) to ensure mechanical stability during the dicing.

applications and large scale prototypes like a 96-GridPix-module [94] a large scale process on wafer basis was needed to serve the rising need of GridPixes.

Development of a wafer scale production process

To set up a wafer scale production process in 2011 a cooperation with the Fraunhofer-IZM in Berlin was initialized. With the machinery available there full 8" Timepix wafers can be processed allowing to produce 107 GridPixes in one production cycle (per wafer). Up to three wafers can be processed at once. Of course the process had to be slightly altered with respect to the small scale production, especially a good method had to implemented to prevent the covering of bond pads with SRSN. In the first batch of GridPixes produced at IZM a shadow mask made of stainless steel was used to protect the bond pads, but this failed as the mask deformed due to the heat load in the CVD process so that many bond pads were covered. To avoid this a different method was successfully implemented, prior to the deposition of SRSN a polyimide mask is created covering the bond pads, which is removed in a chemical lift-off process after the SRSN deposition, resulting in clean bond pads [93]. This method was first used for the second batch produced at IZM. Until mid of 2017 seven batches of GridPix devices have been produced at IZM denoted as IZM-1 to IZM-7, where in the latest batches three wafers were processed at once resulting in more than 300 GridPix devices per batch.

For IZM-1 to IZM-6 the protection layer was created at the Mesa+ institute as no machine for CVD of SRSN was available at IZM. Especially in IZM-6, but also before in IZM-2, the protection layer had shown a very bad performance observed as many chips suddenly dying during operation under high voltage [93, 94]. The cause for this was found to be small cracks and defects within the protection layer. While in IZM-2 these seemed to be caused by a bad recipe or operator error, in IZM-6 the cracks and defects were caused probably by two causes: On the one hand the wafers were not properly cleaned prior to the SRSN deposition, therefore having many surface defects in form of tiny dust particles acting as seeds for the defects and cracks in the SRSN layers. On the other hand the machine used for the SRSN deposition at Nikhef seemed to cause small SRSN particles to form on the deposited surfaces acting again as seeds for cracks and defects, maybe due to a contamination (e.g. dust particles) or rising age of the machine used. The latter cause was removed by switching to a new CVD machine meanwhile available at IZM which was first used for the production of IZM-7. Also, an intense surface inspection and cleaning procedures including a high pressure water jet treatment were implemented to avoid surface defects on the wafers which could grow into cracks of the protection layer. As hoped, the change to the CVD machine at IZM and the additional cleaning resulted in an almost perfect protection layer for the IZM-7 GridPix devices which show a tremendous resistance against discharges [98]. A comparison between the SRSN protection layers of IZM-6 and IZM-7 is shown in Fig. 6.6 where a GridPix has been stripped from the InGrid structure and cut with a focussed ion beam (FIB) allowing to image the layer's cross section with a SEM.

When a Timepix wafer has been post-processed into a GridPix wafer it is diced into the individual GridPix devices. This is done prior to the last processing step, the removal of the unexposed SU-8 from under the aluminium grid as else the structures would be too fragile to be diced [93]. With currently the batch number eight (IZM-8) being in preparation a wafer scale production process has been successfully established allowing to produce larger numbers of GridPix devices with a reasonable yield and sufficient for first medium scale applications and prototypes. Over the years and through the batches IZM-1 to IZM-7 the GridPix technology and especially its wafer scale production process has been developed into a mature detector technology.

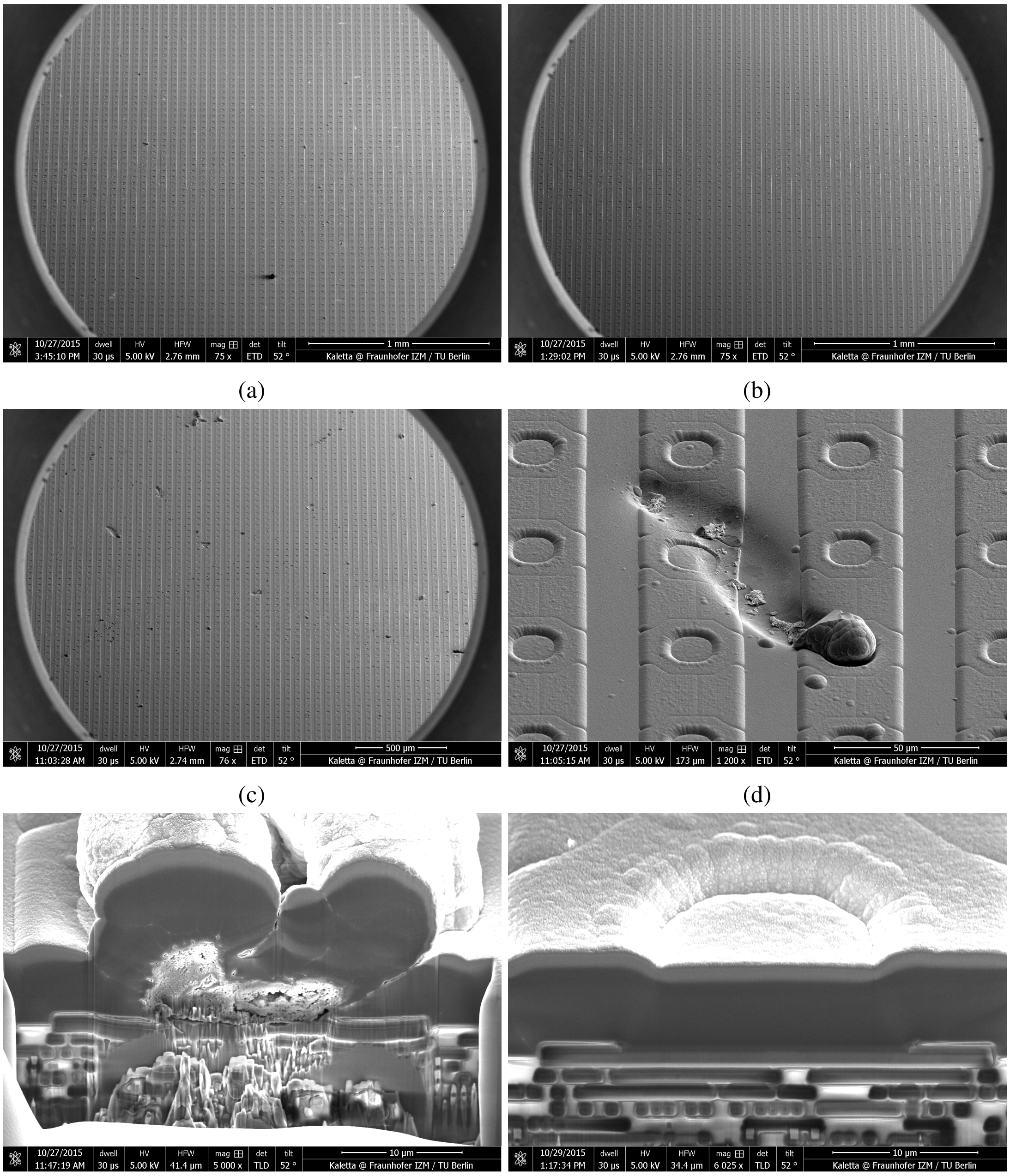

(a) (b)

(c) (d)

(e) (f)

Figure 6.6: Comparison of SRSN protection layers of batches IZM-5, IZM-6 and IZM-7. The InGrid structure has been stripped and the chip surface been imaged with a SEM. Parts of the surface of chips from batches IZM-5 (a), IZM-7 (b) and IZM-6 (c) are shown, illustrating the bad quality of the protection layer of IZM-6 (many surface defects), especially in contrast to IZM-7 where a new machine and improved wafer cleaning procedures had been introduced. Although the IZM-5 protection layer is not of perfect quality it is much better than the IZM-6 protection layer. (d) shows a zoom on one of the surface defects visible in (c). By cutting the chip with a FIB and imaging the cross section with a SEM the protection layer can be checked for internal cracks and defects. (e) shows the cut into a region where a surface defect could be identified on a chip from IZM-6, clearly cracks and inner defects are visible. (f) shows a cut into the protection layer of an IZM-5 chip, here a clean protection layer was achieved free from defects and cracks. The regular light structures in the cross section views are the metal layers of the chip's electronic circuits. All images courtesy of IZM Berlin.

CHAPTER 7

An InGrid based X-ray detector for CAST

In this chapter the InGrid based X-ray detector will be described, starting with the key components of the detector assembly: The readout module housing the central, active device, the Timepix application specific integrated circuit (ASIC) with the integrated Micro-Mesh Gaseous Structure (MicroMegas) stage on top, the detector body defining the drift volume and the cathode plate closing the detector's gas volume and featuring the thin X-ray window made from a 2 µm aluminized Mylar$^{®}$ film. Hereby, the Timepix ASIC will be introduced, as the Integrated Grid (InGrid) technology has been already described in detail in chapter 6, here only some information on the specific batch used will be added. Following the description of the detector itself, and its components the readout system used will be introduced and described along with the infrastructure necessary to operate the detector. Additionally, the working principle of the detector will be explained also giving insight into its main strengths and advantages.

During commissioning and assembling of the detector several steps are necessary to ensure a proper functioning and behaviour of the whole detector and its key components. This is especially important for a long-term operation as was aimed for at the CERN Axion Solar Telescope (CAST). The most important steps will be described here and their results stated: The electronic testing, equalization and characterization of the Timepix ASIC, the high voltage tests of the InGrid structure on top of the Timepix ASIC and the pressure and leakage test of the thin X-ray window.

Before the detector could be installed at the CAST it was necessary to characterize its behaviour and especially to confirm the detector's capability to detect X-ray photons with very low energy (below 1 keV). For this the infrastructure, in particular the variable X-ray generator, of the CAST Detector Lab (CDL) was used. Datasets with X-ray energies ranging from a few hundred eV up to 8 keV were recorded during this campaign confirming the anticipated behaviour and key features of the detector. The results of these measurements will be illustrated with a focus on the role of the recorded datasets as reference datasets for the analysis and background suppression (see chapter 10). The installation of the detector behind the MPE X-ray telescope (XRT) of CAST will be described in chapter 8.

7.1 Detector components and assembly

The InGrid based X-ray detector is made of three major components: the readout module, the detector body and the cathode plate featuring the X-ray entrance window. The main building blocks are shown in an exploded drawing of the detector in Fig. 7.1. Also, the way the detector is assembled from the three key components is illustrated. O-ring gaskets made from Viton$^{®}$ and a sufficient number of threaded bolts ensure gas tightness of the assembled detector, especially its inner gas volume. A 3D computer-aided design (CAD) model of the assembled detector is shown in Fig. 7.2.

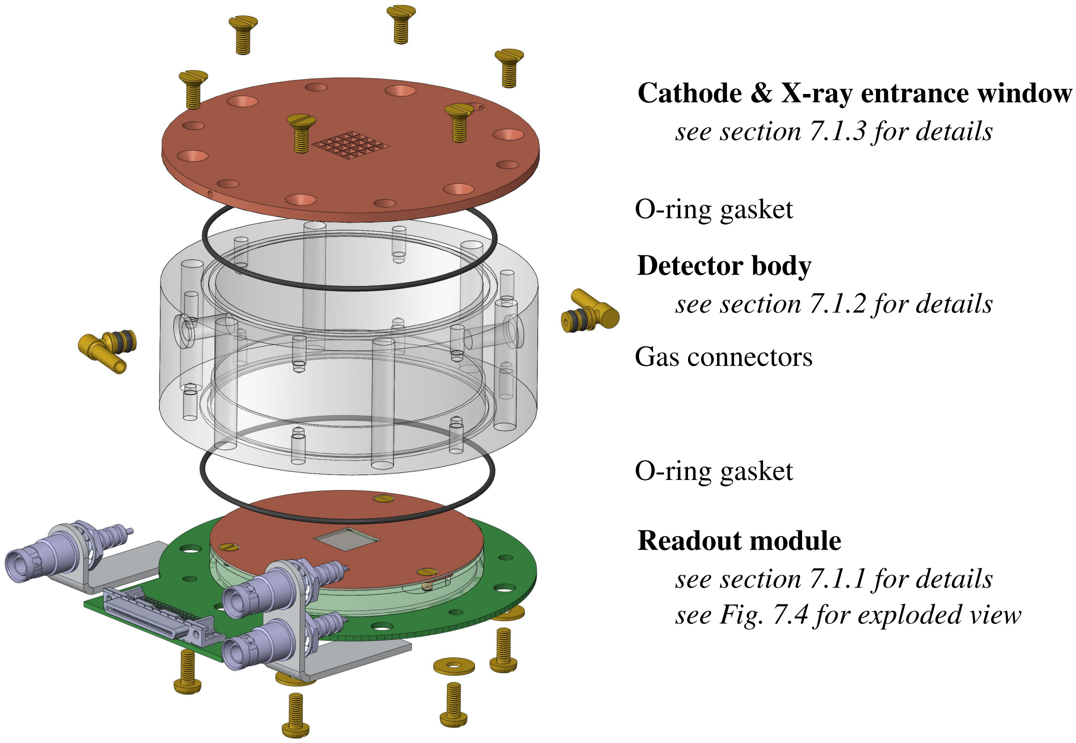

Figure 7.1: Exploded drawing of the InGrid based X-ray detector. The detector is assembled from three main building blocks: the readout module, the detector body and the cathode, where the latter also houses the X-ray entrance window. The three blocks are assembled using brass screws and O-ring gaskets. The readout module holding the detector's key element, the GridPix, is itself assembled from different components, as can be seen from an exploded view of the readout module's CAD model shown in Fig. 7.4. Cables and wires are not shown.

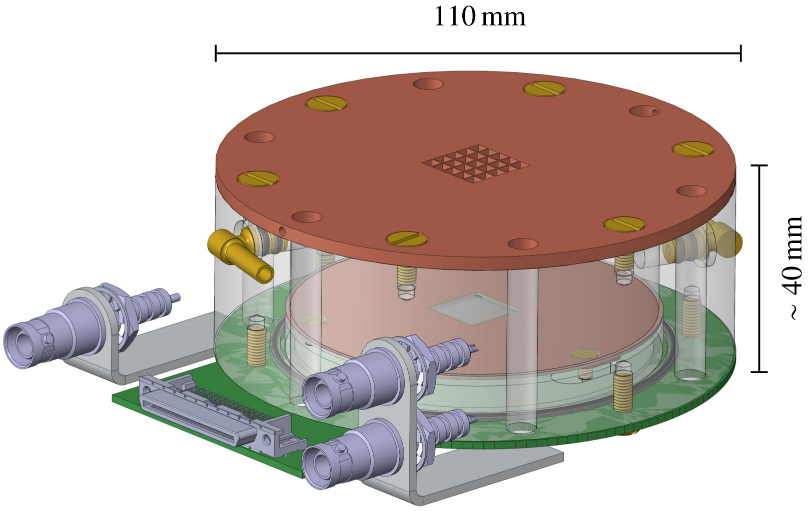

Figure 7.2: 3D CAD model of the assembled InGrid based X-ray detector. An exploded view illustrating the assembly of the detector from its main building blocks can be found in Fig. 7.1. Cables and wires are not shown.

The overall design of the InGrid based X-ray detector is based on the MicroMegas detectors already used at CAST on the sunset detector stations [60] and incorporates the experience gathered from a first prototype build in the course of a master thesis [10, 99]. This decision was based on the convenience to use existing infrastructure (especially the CDL) without manufacturing new (adapting) parts. The detector can be mounted to a detector station, beamline or any other fixture (e.g. for tests in a laboratory) using six threaded bolts made from an insulating material.

To be operated the InGrid based X-ray detector has to be flushed with a gas (mixture), for the operation at CAST an argon based gas mixture was chosen which contains 2.3 %[1] of isobutane ($i\mathrm{C}_4\mathrm{H}_{10}$) as quencher. Argon with isobutane as quencher is a Penning mixture which allows to reach reasonable gas gains already at low grid voltages ensuring a safe and stable operation. The gas mixture also defines the detector's absorption efficiency for X-ray photons and therefore together with the transmission of the X-ray window its detection efficiency, as shown in Fig. 7.3(a). The InGrid based X-ray detector is operated at a gas pressure of 1 050 mbar(a)[2], which is a compromise between high absorption efficiency (e.g. the MicroMegas detectors at CAST are operated with similar gas mixtures, but at pressures of about 1 400 mbar(a)) and a safe usage of the thin X-ray window, which has to withstand the pressure difference between the detector's gas volume and vacuum. The X-ray absorption versus energy is plotted in Fig. 7.3(b) for an $\mathrm{Ar}/i\mathrm{C}_4\mathrm{H}_{10}$ 97.7/2.3 mixture at a pressure 1 050 mbar(a) and for an absorption length of 30 mm. The absorption for X-ray energies below 2 keV, the region relevant for Solar chameleon searches, is close to 100 %. The pressure of 1 050 mbar(a) guarantees to (virtually) always have an overpressure with respect to the ambient pressure, thus keeping out oxygen and water from the ambient air. To ensure the constant overpressure inside the detector, it is flushed permanently at a flow rate of about 2 l/h during operation. On initial set-up of the detector the steady gas flow is also used to remove air (especially oxygen) and water vapour adsorbed by hygroscopic materials from the detector's inner gas volume prior to starting up the detector.

7.1.1 Readout module

The readout module houses the key element of the InGrid based X-ray detector: The Timepix ASIC with the InGrid stage on top (in combination called GridPix). It also provides the interface to connect the detector to its readout system and high voltage power supply. The composition of the readout module is illustrated in an exploded view of the CAD model in Fig. 7.4.

The GridPix is mounted on a small carrier printed circuit board (PCB), to allow for easy handling and exchange in case of a malfunction. The chip is glued onto a small PCB, the carrier board, and electrically connected via wire bonding. To connect the grid of the integrated MicroMegas stage to the corresponding high voltage pad on the carrier board a bond wire is attached to the pad and the other end fixed to the grid with a tiny drop of conductive glue. To protect (especially mechanically) the signal and supply wire bonds as well as the high voltage wire bond of the grid, they are carefully covered with a protective, insulating glue. A picture of a GridPix on a carrier board can be found in Fig. 7.5.

The carrier board is then plugged via a 32-pin connector onto a larger PCB, the intermediate board, which routes the chip's electrical lines to a Very High Density Cable Interconnect (VHDCI) connector and also a small circuitry to create test pulses by switching between two voltage levels provided by the readout system. These test pulses are transmitted to the Timepix ASIC and can be injected into selected pixels via a capacitor to create defined charge pulses for calibration and testing purposes. The

---

[1] In principle a higher isobutane concentration would be beneficial for the detector's energy resolution and general operation [100], but argon based mixtures with isobutane fractions larger than 2.3 % are considered as flammable and therefore require more safety measures due to safety regulations at CERN.

[2] The unit mbar(a) denotes an absolute pressure given in mbar.

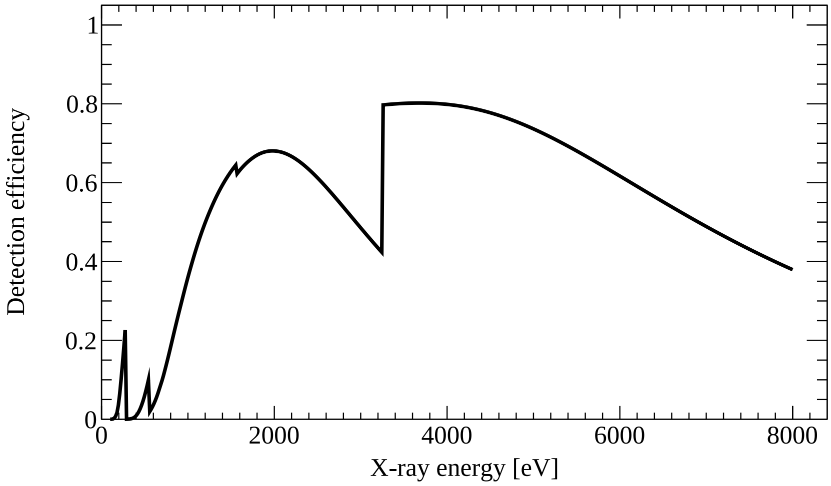

(a)

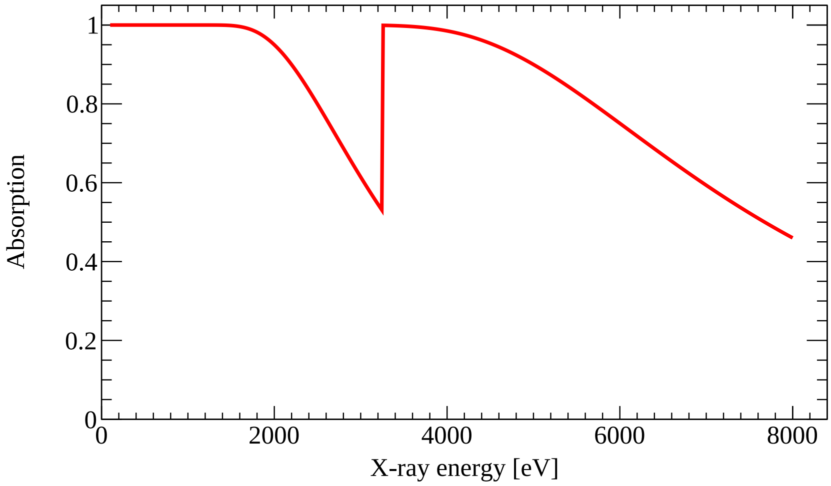

(b)

Figure 7.3: Detection efficiency of the InGrid based X-ray detector as function of X-ray energy: (a) shows the overall detection efficiency taking into account the transmission curve of the X-ray entrance window while (b) only shows the X-ray absorption of 30 mm of argon at a pressure of 1 050 mbar(a), the small isobutane fraction can be neglected. It is clearly visible that in the regime below 2 keV the limiting factor is the X-ray entrance window. Assuming an X-ray entrance window with perfect transmission the X-ray absorption in (b) would present the upper limit of the InGrid based X-ray detector's detection efficiency. Transmission and absorption data have been obtained using a web based generator [101] utilizing the semi-empirical approach described in [102].

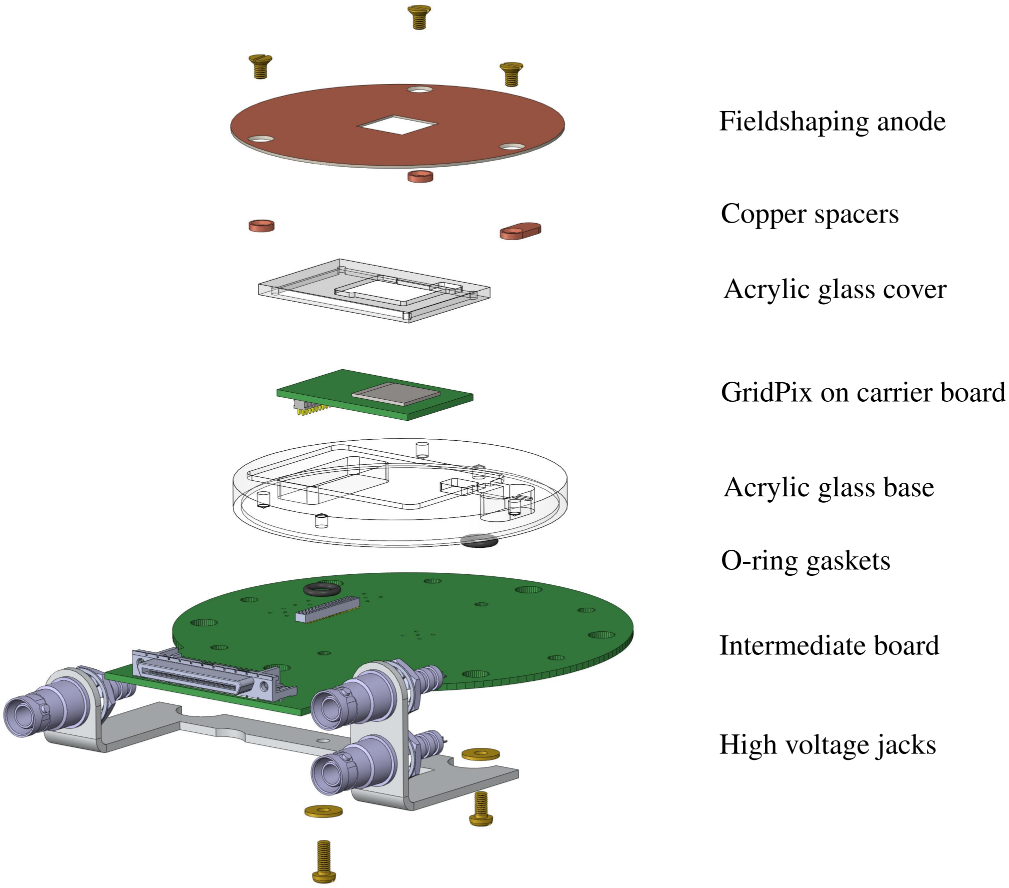

Figure 7.4: Exploded view of the readout module's CAD model with main parts labelled. Right in the centre the key element of the InGrid based X-ray detector is shown, the GridPix on its carrier board which is plugged onto the intermediate board connecting it to the readout system and power supply. Parts made from acrylic glass hold the field-shaping anode in the right position and isolate it against the rest of the readout module. Cables and wires are not shown.

intermediate board also contains a few LEMO® 00 connectors for diagnostics and feedthroughs in form of vertical interconnect accesses (vias) for two high voltage lines, one for the grid and one for the field-shaping anode. As the intermediate board represents the detector's back and closes the inner gas volume, all vias on the PCB have been closed with solder to guarantee gas tightness. The high voltage connections between intermediate board and carrier board, respectively the field-shaping anode, are done via soldering small cables in between.

To define the distance between intermediate and carrier board an insulating spacer made from acrylic glass is used, which is screwed on the intermediate board using again Viton O-ring gaskets to ensure gas tightness at the intersection. This acrylic glass piece also holds the field-shaping anode in the correct position above the GridPix. A bracket holding the high voltage jacks to connect the InGrid based X-ray detector to a high voltage power supply is fixed to the readout module.

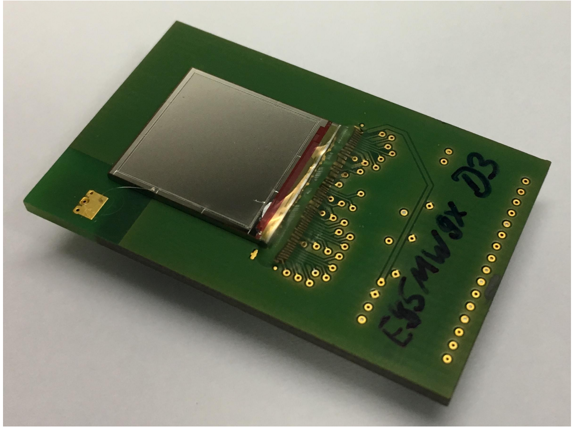

Figure 7.5: Picture of a GridPix on a carrier board, the bond wires connecting the chip's periphery to the pads on the carrier board (middle) are mechanically protected with a glue. A single wire bond connects the high voltage pad (middle left) to the grid of the GridPix where the bond wire is fixed with a tiny drop of conductive glue. Chip number and wafer name are written onto the carrier board to allow easy identification.

Timepix ASIC

The Timepix ASIC [88] is a pixelized readout chip and a successor to the Medipix2 ASIC [89], which was developed for medical imaging. Both, the Timepix as well as the Medipix2 ASIC are produced in a 250 nm complementary metal-oxide-semiconductor (CMOS) technology and feature 256×256 pixels with a 55 µm pitch in both directions. The total chip area is about $14 \times 16\,\mathrm{mm}^2$ with the active area being roughly $14 \times 14\,\mathrm{mm}^2 \approx 2\,\mathrm{cm}^2$. On one side a 2 mm stripe contains the chip's periphery and holds the bond pads used to electrically connect the chip to its readout via wire bonds and pads on a carrier PCB.

The input pads of the Timepix and Medipix2 ASIC's pixels are in fact bump bond pads meant for connecting the readout chips to pixelized silicon sensors. The bump bond pads are small openings (regular octagons with 10 µm side length) in the top passivation layer ,revealing the underlying metal layer and providing contacts to the pixels' amplifier inputs. By omitting the silicon sensor and using the bump bond pads as charge collecting anodes, one can utilize the Timepix (or Medipix2) ASIC as fully integrated and highly granular readout plane for a Micropattern Gaseous Detector (MPGD) [90, 94, 103, 104]. After first experience with the Medipix2 ASIC as an MPGD's readout plane the Timepix ASIC was developed as successor to include some specific changes to optimize it for this use. New measurement modes to allow for charge and time measurement were added.

Each of the Timepix ASIC's pixels contains a charge sensitive amplifier (CSA) using the bump bond pad as input and having a discriminator connected to its output, forming the analogue part of the pixel's electronics. The discriminator is controlled by a global polarity switch and threshold which can be adjusted pixelwise via four adjustment bits. The analogue part of a pixel is always active when the chip is powered. The equivalent noise charge (ENC) of a pixel's CSA is approximately 90 e, thus for operating quasi noise free at frame lengths in the order of a second, an effective threshold of 700 to 800 e has to be applied. The discriminator output is connected via a synchronization logic to a 14-bit shift register configured as a pseudorandom[3] counter, which together form the digital part of the pixel. A schematic of a Timepix ASIC's pixel can be found in Fig. 7.6. The synchronization logic allows each individual

---

[3] A pseudorandom counter is used here, as it is relatively easy to implement on chip level and requires moderate resources in terms of space and power consumption. The pseudorandom counter values can be decoded using a look-up table to get the real counts.

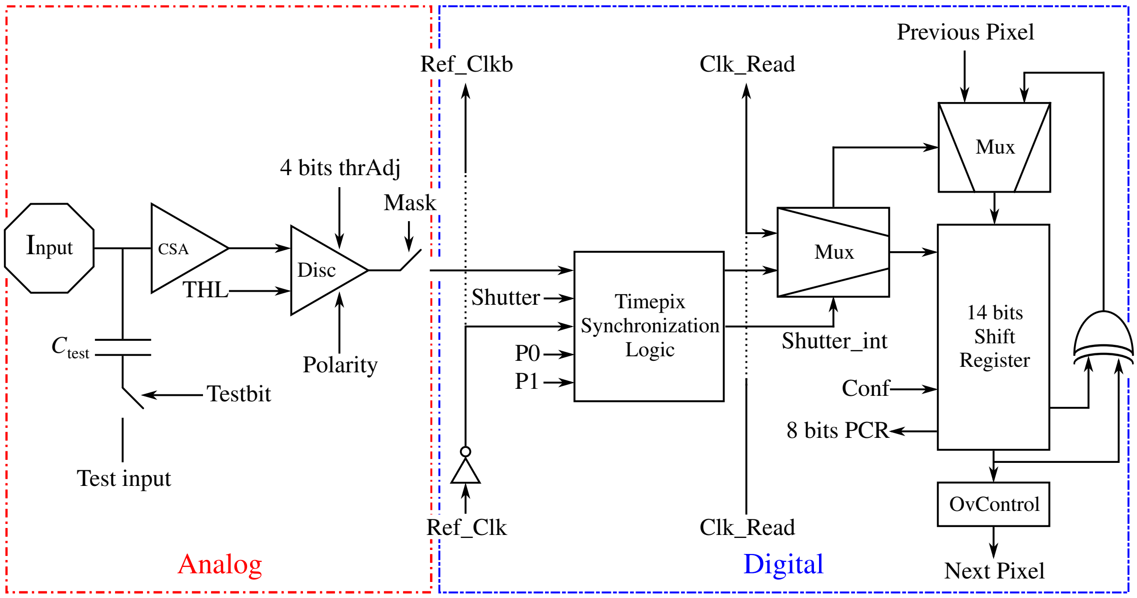

Figure 7.6: Schematic of a Timepix pixel cell showing the analogue and digital domain of a single pixel. The analogue part contains the input pad of the pixel (bump bond pad) connected to a CSA. The CSA output is fed into a discriminator of adjustable threshold and polarity. In the digital part the discriminator output is fed into the Timepix synchronization logic along with the *shutter* signal and an external clock. Each pixel is configured by 8 bits used for selection of the counting mode, masking a pixel, activating the test input and to fine adjust the threshold of each individual pixel. A 14-bit register is connected to the Timepix synchronization logic and used for counting in the different modes. Based on the schematic in [88].

pixel to be operated in one of four measurement modes. Also, it incorporates the electronic *shutter* signal and synchronizes it with the externally provided clock. Only while the *shutter* signal is low the digital part of a pixel is active and discriminator signals are processed in the logic. The *shutter* signal is part of the frame-based readout of the Timepix ASIC as a heritage of the Medipix2 ASIC being designed as an imaging chip.

Thirteen global digital-to-analogue converters (DACs) are used to configure the Timepix ASIC by setting and defining required reference voltages. While most of them are kept on default values usually three are important for the operation of the chip in the context of the InGrid based X-ray detector. The global threshold voltage is set using the two DACs *thl* and *thl_coarse*. While *thl* is used to vary the threshold voltage in fine steps (typically 40 e per *thl* step), *thl_coarse* is used only for a coarse adjustment and is typically left on an intermediate default value and only changed if necessary. The third important DAC is *ths* which defines the range accessible by the four adjustment bits in each pixel.

Additionally, each pixel is configured through an 8-bit configuration register. Two of the eight bits are used to select one out of four measurement modes. One bit can be used to mask a pixel by disabling the connection between analogue and digital part. Another bit is used to activate the charge injection by test pulses for a pixel, this is done by connecting an injection capacity of 8 fF to the input of the CSA. By switching the voltage applied to one side of this capacitor between two defined levels charge pulses are created. The polarity of the charge pulse depends on whether the voltage at the capacitor switches from a higher to a lower level or vice versa. The voltage pulses are created externally and distributed on the chip internally by a dedicated test pulse distribution network. The remaining four bits are used for the so-called threshold equalization: The effective threshold for each pixel is slightly different due to small

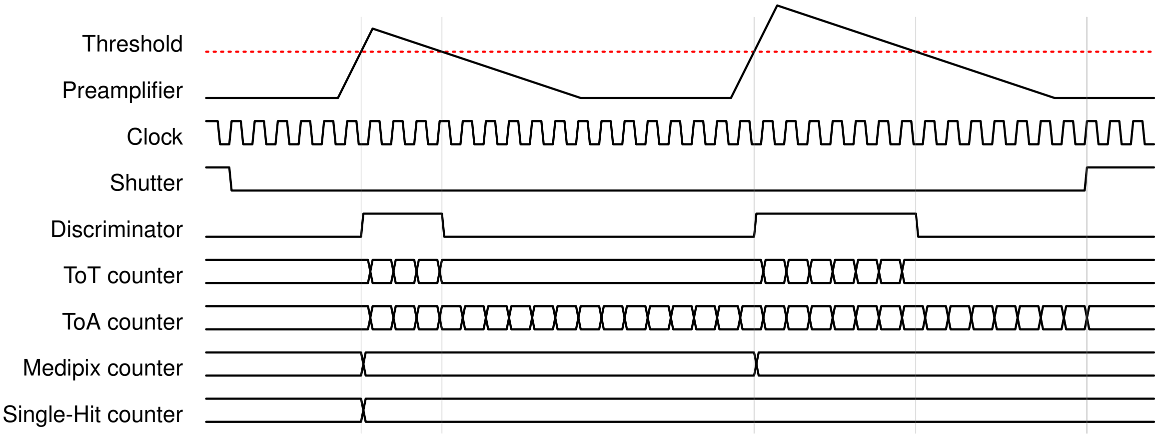

Figure 7.7: Timing scheme of the Timepix ASIC illustrating the different counting modes. During a frame (*shutter* signal low) in ToT mode the counter integrates the time over *threshold* for all charges arriving on the pixel while in ToA mode the counter starts counting with the first charge passing the *threshold* and continuous counting until the *shutter* signal rises indicating the end of the frame. The counter (as well as the *shutter* signal) are synchronized with the global clock in these modes. In Medipix mode the counter runs asynchronous to the clock, incrementing when the discriminator triggers, same in the Single-Hit mode but here only the first trigger during a frame increments the counter. Scheme based on [10, 89].

variations caused in the production process resulting in a so-called threshold dispersion or threshold spread. To reduce this spread and get closer to the optimum of all pixels triggering at the same threshold value, the individual thresholds can be tuned by switching on or off small current sources connected to the discriminator logic via the four adjustment bits. When the threshold equalization succeeds this results in a significant reduction of the threshold spread and a more uniform response of the chip. An optimal result is achieved when the *ths* DAC value has been optimized before. To allow for the detection of negative as well as positive charges the discriminators in all pixels can be configured to either trigger on a rising or falling edge by a global polarity switch.

The four measurement modes a pixel can be configured in are Single-Hit, Medipix, ToT and ToA. In the Single-Hit mode a pixel only registers if the CSA output exceeded (at least once) the discriminator threshold while the *shutter* was low and in the Medipix mode the pixel counts how often the discriminator threshold is passed while the digital part is active (*shutter* signal low). In ToT and ToA mode the external clock is used to measure times in multiples of the clock cycles. Time-over-Threshold (ToT) as a measure for the charge collected on a pixel counts the clock cycles during which the CSA output exceeds the discriminator threshold. Time-of-Arrival (ToA) measures the time at which a pixel's threshold was passed first during a frame, the counter is started by the discriminator and keeps counting as long as the *shutter* signal is low. The different modes are illustrated in a timing diagram in Fig. 7.7. The maximum value a pixel can count is 11 810.

On readout the content of all 14-bit registers is serialized and piped outwards to the readout system driven by an external clock signal. With 65 536 pixels and 264 additional bits used for synchronization, this results in a stream of 917 770 Bit $\approx$ 1 MBit. With for example a 40 MHz readout clock this results in a readout time of about 25 ms limiting the maximum readout frequency of a detector using a single Timepix ASIC to about 40 Hz[4].

---

[4] In principle a faster readout of the Timepix ASIC would be possible using its 8-bit parallel bus instead of the serial data bus but this has two main disadvantages: On the one hand using the parallel bus spoils the possibility to daisy-chain up to eight chips which allows to read them out using a single readout connection and system. On the other hand the parallel bus uses CMOS lines instead of LVDS lines as the serial interface which would require additional care and electronics close to the chip to ensure signal integrity when using similar clock frequencies.

The Timepix ASIC has a few shortcomings despite its successful application in many fields including the use as high granular and fully integrated readout plane in MPGDs. The most prominent are the slow, frame based readout, the lack of an on-chip zero suppression, the inability to measure ToA and ToT simultaneously in one pixel and the inability to detect multi-hits on a pixel during a single frame, as illustrated in Fig. 7.7 in case of ToA the time is only measured for the first charge to trigger the pixel's discriminator while for ToT the charges of multi-hits within a single frame are integrated. Many of these shortcomings are resolved in its successor, the Timepix3 ASIC [105], which allows for simultaneous ToA and ToT measurement in all pixels and features a data driven readout with up to 5.12 Gbps via eight lanes. The first Timepix3 ASICs became available in 2013 and in 2016 the first Timepix3 wafer was equipped with InGrids at IZM Berlin.

Integrated MicroMegas stage

The integrated MicroMegas stage used for the InGrid based X-ray detector operated at CAST in 2014 and 2015 is an InGrid produced at the Fraunhofer Institut für Zuverlässigkeit und Mikrointegration (IZM) at Berlin. It is from the fifth batch produced at IZM Berlin (IZM-5) and features the typical pillar height of 50 µm and a 4 µm[5] thick protection layer made from SRSN. A 4 µm thick protection layer is more than sufficient regarding the moderate grid voltages used in argon based gas mixtures with low quencher fractions. The protection layer of GridPixes from the IZM-5 batch are of rather good quality and ensure an adequate protection against occurring discharges resulting in a long life time under normal operating conditions. The production method and general properties of these devices have been presented in chapter 6.

Field-shaping anode

Inside the detector the metallic grid is put to high voltage potential of typically −300 V with respect to the common ground potential of the detector. The grid rests 50 µm above the Timepix ASIC which itself is 700 to 800 µm high. The carrier board can be considered to be on ground potential as the signal and supply voltages of the chip are small compared to the grid voltage. This results in strong distortions of the electric drift field above the GridPix especially at its edges.

A good approach to reduce the distortions of the electric field is to put the anode plane (or field-shaping anode) slightly above the grid (e.g. 1 mm) with a cut-out just the size of the GridPix' active (or instrumented) area and precisely positioned above this area. By setting the field-shaping anode to a voltage according to its position inside the electric drift field this results in a further reduction of electric field distortions although they are still slightly present at the edges of the cut-out [100]. The impact of the field distortions can still be reduced by using a higher electric drift field, as then the transverse electric field components introduced by the field distortions are smaller compared to the main longitudinal component in drift direction and thus their influence on electrons' drift trajectories is reduced [10].

The field-shaping anode used for the InGrid based X-ray detector described in this thesis is of the type resting slightly above the grid as can be seen from Fig. 7.1, detailed drawings of the field-shaping anode itself can be found in Fig. 7.8. It is made from 0.8 mm thick PCB material double-sided clad with copper. By connecting both copper sides through vias the high voltage used to set the anode's potential can be simply passed from below by a surface contact in the readout module resulting in a flat anode surface towards the detector's inner volume. Small copper spacers are used to put the field shaping anode to its correct position above the spacer made from acrylic glass on which the GridPix on its carrier board

---

[5] In the processing of IZM-5 wafers with 4 µm as well as 8 µm thick silicon rich silicon nitride (SRSN) protection layers have been produced.

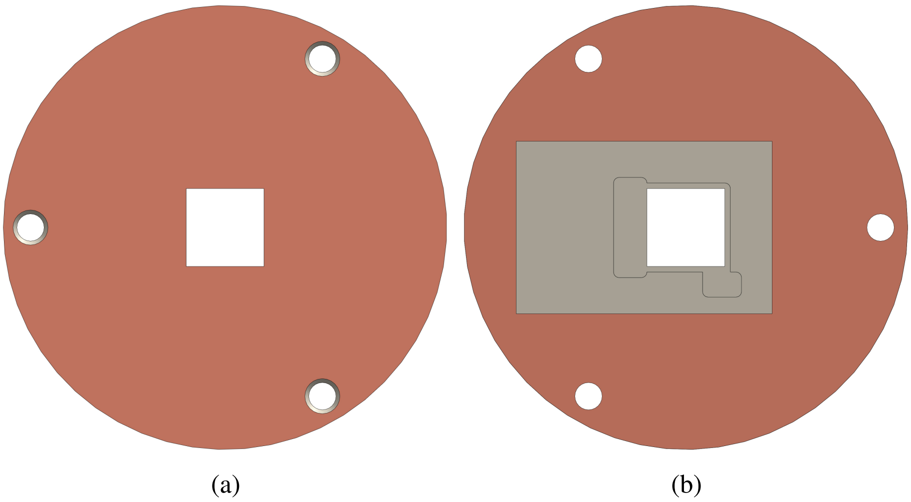

Figure 7.8: Front (a) and backside (b) of the field-shaping anode's 3D CAD model. The field-shaping anode is made from 0.8 mm thick PCB material clad with copper on both sides. The central cut-out is $14 \times 14\,\mathrm{mm}^2$, just the size of the GridPix' active area, from the backside in a small region the anode has been thinned to about 0.4 mm to avoid damaging or touching the bond wires, especially the high voltage bond wire connecting the grid. In a larger region the copper has been removed to prevent discharges between the copper surface set to high voltage and the carrier board or the GridPix itself.

rests. One of the copper spacers also provides the high voltage contact and is connected via a wire to the corresponding high voltage pad/feedthrough on the intermediate board[6]. The distance between the anode's top copper surface and the GridPix' grid is 1 mm, assuming an electric drift field of 500 V/cm the anode is therefore set to a high voltage potential 50 V above the grid high voltage.

The cut-out of the field-shaping anode is $14 \times 14\,\mathrm{mm}^2$ to match the GridPix' instrumented area, from the backside the anode material is thinned down to 0.4 mm thickness to avoid the anode touching any of the chip's wire bonds. Additionally, the copper is removed on the backside of the anode in the region above the carrier board to avoid discharges from the anode's high voltage into the chip or any of its data and supply lines on the carrier board as this could possibly damage or even destroy the Timepix ASIC.

7.1.2 Detector body

The detector body is made from acrylic glass and defines the detector's inner volume and the maximum drift distance. Acrylic glass was chosen as it is known to be a quite radiopure material and can be sufficiently machined. For the InGrid based X-ray detector described here a detector body (also called drift ring) is used with an inner diameter of 78 mm and an outer diameter of 110 mm thus ensuring a sufficient wall thickness to implement gas connections and (threaded) holes for assembling the detector. The maximum drift distance defined by the detector body used for the InGrid based X-ray detector used at CAST in 2014 and 2015 is 29.8 mm[7]. The top and bottom surface feature O-ring grooves and threaded holes to mount both readout module and cathode in a way so that the connection is sufficiently gas tight.

---

[6] Originally, the InGrid based X-ray detector described here had been designed and build using a simpler version of the field-shaping anode coinciding with the GridPix's grid plane but was later converted to the more sophisticated anode version with a kind of conversion kid not requiring changes to the other parts of the readout module.

[7] Originally the InGrid based X-ray detector was designed with a maximum drift distance of 30 mm but when changing to an improved design of the field-shaping anode, 0.2 mm were sacrificed for the comfort to not having to make a new detector body.

The inner diameter of 78 mm ensures a sufficient distance between the central GridPix and the walls so the region above instrumented area is not affected by electric field distortions arising at the edges and sides of the volume. Thus, a field forming device like a field cage is not required and eases the design, manufacturing and assembly. The gas connectors are plugged in holes located at the detector body's shell and sealed via O-ring gaskets. 6 mm diameter plastic tubes can be connected to the gas connectors. Often the detector body is covered with black tape during operation of the detector to avoid light entering the detector.

7.1.3 Cathode & X-ray entrance window

The cathode closes the detector's gas volume and has to be transparent for X-ray photons at least in the region of the detector's instrumented area. As for the operation at CAST the InGrid based X-ray detector is connected to a vacuum the cathode has to be vacuum tight as well as mechanically rigid to assuredly withstand a pressure difference of 1 050 mbar. At the same time the cathode has to be as transparent for X-ray photons as possible to serve as an X-ray entrance window. For the solar chameleon search performed at CAST high X-ray transmission is required below 1 keV. Therefore, a thin material (e.g. a thin polymer film) has to be used contradicting the rigidity and gas tightness requirements. Also, the cathode has to at least provide a conductive surface towards the detector volume to allow setting the cathode to a high voltage potential for defining/creating the electric drift field.

As a compromise between tightness, rigidity and high X-ray transmission the cathode is made from a solid 3 mm thick copper plate where in the central region (above the instrumented area) 5×5 square cut-outs of $3 \times 3\,\mathrm{mm}^2$ have been made using the technique of water jet cutting and leaving only 0.3 mm thick ribs in between the cut-outs, thus achieving an optical transparency of 82.6 % in this region. To achieve gas and vacuum tightness a thin 2 µm thick aluminized Mylar film is glued onto the copper structure. The ribs of the copper structure act as a strongback for the thin film and reinforce the window so it can withstand a pressure difference of 1 050 mbar by reducing the size of an individual cell of the window to a size were the force acting on it by the applied pressure difference is far below its limits. The 40 nm aluminium layer points towards the inner detector volume and is set to high voltage by connecting it at the very side to the copper structure by a small piece of aluminium foil. The copper structure is connected with a small screw to a high voltage cable leading to a high voltage jack on the readout module. To avoid a reduction of the overall transparency by glue being squeezed between the copper ribs and the Mylar film special care has to be taken to only use a very thin layer of glue. Pictures of cathode and X-ray entrance window are shown in Fig. 7.9. Fig. 7.10 shows the X-ray transmission of the resulting X-ray entrance window taking into account the optical transparency of the copper structure. While above 2 keV the transmission is only limited by the optical transparency of the copper structure below 2 keV it drops significantly and below 1 keV only the small transmission peaks caused by carbon and oxygen as compounds of Mylar are left. A comparison of different (possible) window materials with respect to their X-ray transmission can be found in Fig. A.1 in appendix A.

In general significant X-ray transmission below 1 keV is hard to reach, especially with windows which are required to be moderately vacuum tight and to withstand a pressure difference of 1 000 mbar or more plus the mandatory safety margins. Even beryllium windows which are commonly used in vacuum technology do not reach better transmission especially below 1 keV when used in a thickness appropriate for vacuum tightness and rigidity required here but are much harder to handle due to the high toxicity of oxidized beryllium which would cause additional trouble in case of a window burst. In principle it would be possible to use thinner Mylar films but first of all these are not commercially available in aluminized versions and second the number of pin holes rises with decreasing thickness which would spoil the required gas and vacuum tightness. A viable option to increase the transmission of the X-ray

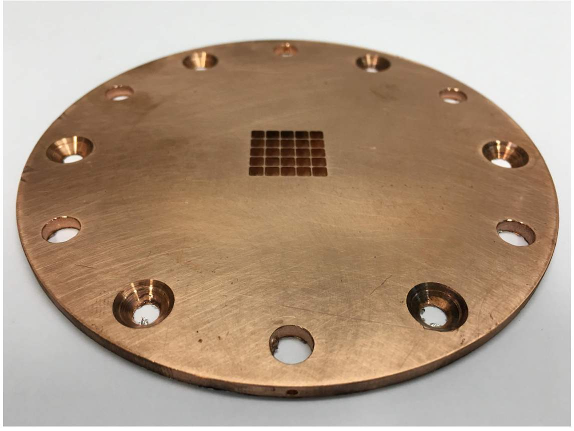

Figure 7.9: Picture of a cathode and X-ray entrance window for the InGrid based X-ray detector. The cathode is made from solid 3 mm copper and in the central region a 5×5 array of $3 \times 3\,\text{mm}^2$ cut-outs has been made using water jet cutting. A 2 µm aluminized Mylar® film is glued on from the backside to create the X-ray entrance window. The 0.3 mm thick ribs of the array of cut-outs act as strongback structure for the thin film when pressurized. Via a small threaded hole (bottom middle) the cathode can be connected to its high voltage line.

entrance window is the use of ultrathin silicon nitride windows (e.g. with 300 nm thickness) and an integrated strongback structure, but those first had to be developed and where not available before end of 2016, more information on the use of this kind of X-ray windows can be found in chapter 12.

7.2 Readout system & infrastructure

While for the prototype detector described in [10] a proprietary readout system and software were used: The Medipix Universal Read-Out System (MUROS) [106], an field programmable gate array (FPGA) based readout board using a closed source firmware, and the `Pixelman` (later the Java based `JPixelman`) software [107, 108]. These provided all necessary functions and routines to operate a Timepix or GridPix based detector but did not allow to implement custom functionalities, especially hardwarewise, and were generally inflexible due to their proprietary nature.

A new readout system and software for the Timepix ASIC [109] were being developed at Bonn the time the work on this thesis started. The new system is based on the Scalable Readout System (SRS) [110] developed by CERN: A common FPGA board which can be used as core of a readout system by adding a custom adapter board providing the connection to the front end or detector, and a custom firmware for the FPGA. One of the key features of SRS based systems is the scalability meant to allow for easy upscaling from a small set-up (e.g. a prototype detector) to a large set-up like a large-scale detector of a big particle physics experiment without having to change the type of system used. The readout system developed at Bonn for the Timepix ASIC was meant and used to demonstrate the feasibility of a fully pixelized Time Projection Chamber (TPC) [94], hence the choice of the SRS base. While waiting for SRS boards featuring a Xilinx® Virtex®-6 FPGA to become available, prototyping and development were done on a commercially available Xilinx Virtex-6 evaluation board. Over time this set-up became a fully functional readout system on its own for the Timepix ASIC and can be seen as a branch of the SRS based system, especially suitable for small-scale applications like the InGrid based X-ray detector [111].

The readout system based on the Xilinx Virtex-6 evaluation board is shown in Fig. 7.11, a small adapter board is plugged onto the evaluation board and provides the connection to the intermediate board of the InGrid based X-ray detector via a VHDCI cable of up to 1.8 m length. The supply voltages

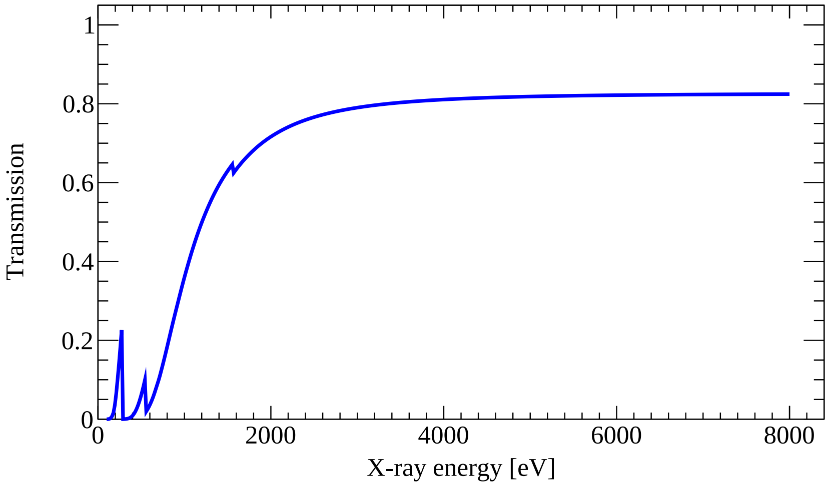

(a)

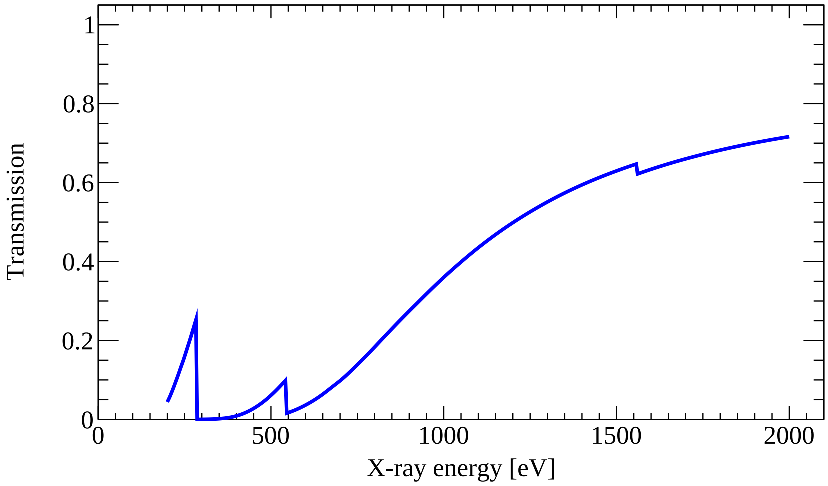

(b)

Figure 7.10: X-ray transmission of the InGrid based X-ray detector's X-ray entrance window consisting of a 2 µm thick Mylar® film metallized with 40 nm of aluminium and glued on a copper strongback with 82.6 % optical transparency. (a) shows the transmission for X-ray energies of up to 8 keV while (b) is a zoom into the region below 2 keV critical for the chameleon search as described in this thesis. For energies above 2 keV the transmission is limited only by the optical transparency of the strongback and not the window material. Transmission data was produced with a web based generator [101] using the semi-empirical approach described in [102].

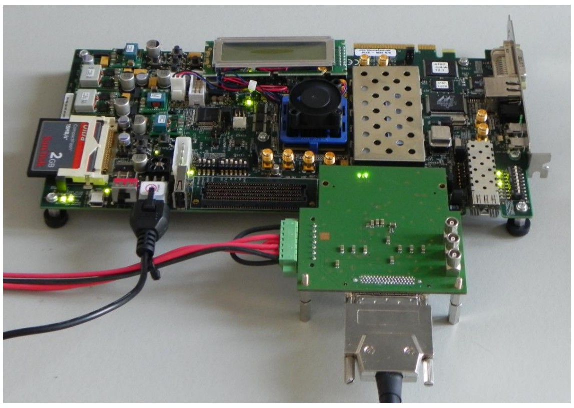

Figure 7.11: Picture of the readout system based on a Xilinx® Virtex®-6 evaluation board. An adapter board is plugged onto the Xilinx Virtex-6 evaluation board providing the VHDCI connection to the intermediate board hosting the Timepix ASIC, power for the chip is also provided through the VHDCI cable by connecting an external power supply to the adapter board. The readout system is connected to a computer via a Gigabit ethernet connection.

for the Timepix ASIC are provided by a stabilized power supply and fed into the adapter board and supplied through the VHDCI cable. Following supply voltages are needed: 2.2 V at approximately 180 to 200 mA for the analogue parts of the ASIC and another 2.2 V for the digital parts with power consumption ranging from less than 20 mA when idle up to typically 200 mA during a frame (up to 400 mA in case of high occupancy). Additionally, 3.3 V are needed for the integrated circuits (ICs) on the adapter board. These are low voltage differential signaling (LVDS) drivers, a CMOS level shifter, analogue-to-digital converters (ADCs) to measure/check the functionality of the DACs in the Timepix ASIC, as well as the DACs required to generate the voltage levels for injecting test pulses for calibration of the Timepix ASIC, the actual generation of the test pulses by switching between these two voltage levels is done on the intermediate board. The connection of the readout board to a computer is done via a single Gigabit ethernet connection. On this computer the Timepix Operation Software (TOS) is taking care of controlling/configuring the Timepix ASIC as well as the actual data acquisition. This software provides all functionalities needed, e.g. optimization of the *ths* DAC, threshold equalization, setting of the pixel configuration and running a data acquisition by recording one frame after another. The length of a recorded frame can be set by the software ranging from 1.15 µs up to 19.2 s. The system features two readout modes: full matrix and zero suppressed; in full matrix readout mode the full data stream read from the chip is sent to the computer as it is and the pseudorandom counter values are decoded softwarewise, in zero suppressed readout mode the decoding is done on the FPGA and only non-zero values are transmitted in a x-y-value format but only the last 4 096 pixels read are transmitted due to storage limitations of the used FPGA. While the full matrix readout takes a rather long time for transmitting data to the computer, the zero suppressed readout is much faster but may result in truncated frames if more than 4 096 pixels were activated on the chip.

In addition to the readout system and the supply voltages for the Timepix ASIC a gas supply and high voltages are needed for operation of the InGrid based X-ray detector. Typically the detector is continuously flushed with a mixture of argon and isobutane (Ar/iC$_4$H$_{10}$ 97.7/2.3), a flow of about 2 l/h is sufficient to keep a constant pressure of 1 050 mbar(a) in the detector. To maintain the pressure constant an inlet pressure controller on the exhaust line can be used. To control the gas flow a needle valve and a variable area flow meter on the detector's gas inlet line are the most simple way. A schematic of this gas line set-up is shown in Fig. 7.12, often a buffer volume is added in the inlet gas line right before the detector to dampen the pressure rise/fall in case of a sudden change of gas flow giving the pressure

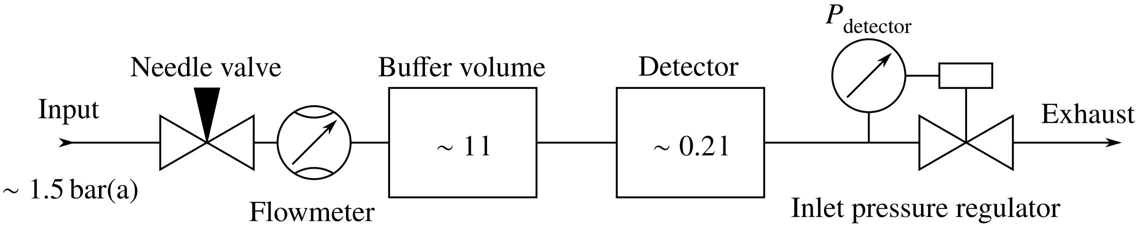

Figure 7.12: Schematic of gas supply line for the InGrid based X-ray detector. Gas supplied trough a bottle (with a pressure reducer) at about 1.5 bar(a) is connected to the input of the illustrated set-up. A needle valve in combination with a (variable area) flow meter allows to adjust and monitor the gas flow. An inlet pressure regulator on the detector's exhaust keeps the pressure P_{detector} inside the detector constant at 1 050 mbar. A buffer volume of about 1 l can be used to increase the total volume on the pressure regulator's input in order to dampen pressure changes caused by a rapid change of the gas flow.

regulator more time to compensate. Prior to start-up the InGrid based X-ray detector should be flushed with the gas mixture for at least one hour (better several hours) to remove air and especially water vapour from the detector's inner volume.

Three high voltage channels are necessary for operation of the InGrid based X-ray detector: grid voltage, anode and cathode voltage. They are needed to set the GridPix' grid, the field-shaping anode and the cathode to the required electrical potential, all three are of negative polarity. Assuming a grid voltage of −295 V, the anode voltage is set to −345 V and the cathode voltage to −1 845 V. To protect the detector in case of an internal short (e.g. caused by a discharge on the GridPix) grid and anode voltage are supplied through 10 MΩ resistors on the intermediate board to drop the voltage. Additionally, the high voltage power supply is required to allow shutting down of the channels in case the current exceeds a defined threshold of typically a few µA. To avoid a high voltage difference between grid and field-shaping anode the high voltage power supply should allow for simultaneous ramp up of these two channels. It should also be configurable in a way that both channels are shut down in case one of them exceeds its current threshold. Throughout this thesis an Iseg VHS C040n high voltage module is used if not stated otherwise. This module features twelve high voltage channels, it is powered and controlled via a Versa Module Eurocard (VME) crate, which is connected to a computer via Universal Serial Bus (USB) running the software `isegControl`.

7.3 Working principle

The working principle of the InGrid based X-ray detector relies on X-ray photons entering the detector and producing a number of primary electrons through ionization which then can be detected with the GridPix. An X-ray photon enters the gas volume if it is not absorbed by the window material or the window strongback. The probability for the X-ray photon actually entering the detector is given by the window transmission (see Fig. 7.10) and depends on the X-ray photon's energy, especially for energies below 2 keV. Inside the detector's gas filled volume the X-ray photon can interact with a gas atom or molecule, the probability for this strongly depends on the X-ray photon's energy, the type of gas, its density and of course the length of the gas volume. In the following an argon based gas mixture is assumed, the absorption probability for X-ray photons in 29.8 mm of argon as function of energy is shown in Fig. 7.3(b).

The energy of the initial X-ray photon is transferred to a photoelectron and, depending on the X-ray photon energy and binding energies of the electrons, several Auger electrons. Assuming X-ray photons with energies up to a few tens of keV, the released electrons will loose energy through ionization and will be stopped within the gas after short range[8], typically in the order of 100 μm [10] for electrons with a few keV energy, and assuming an argon based gas mixture at atmospheric pressure and room temperature. The average ionization energy W_I of argon (and also of isobutane) is 26 eV [72]. So on average per 26 eV X-ray photon energy, one electron is released by ionizing an argon atom. Due to the short range of the photoelectron and Auger electrons this results in a number of electrons, also called primary electrons, close to the initial interaction point of the X-ray photon with the gas atom or molecule.

Due to the electric drift field applied, the primary electrons will drift towards the readout plane, where the electrons can be detected. Diffusion during the drift phase causes the initially small bunch to widen transversally (perpendicular to the drift direction) as well as longitudinally (in drift direction), so that the primary electrons reach the readout plane spread over an area of approximately circular shape (for higher energies the shape becomes more elliptical due to the length of the photoelectron track).

Each of the primary electrons will then enter one of the grid holes of the GridPix in the readout plane. Optimally they have been spread by diffusion over an area large enough so that most likely each electron will enter a different hole, hence for the InGrid based X-ray detector a gas mixture with a rather large diffusion coefficient is used. When a primary electron enters a grid hole, the strong electric field between grid and underlying pixels will cause a gas amplification avalanche resulting in a multiplication of the incident electron. The multiplication factor or gas gain of course depends on the voltage applied to the grid, but typically the InGrid based X-ray detector is operated with a gas gain of 2 000 to 3 000. Through this multiplication, the charge arriving on the pixel underneath the grid hole is large enough to pass the pixel's threshold and to be registered. The charge measured on each pixel (when using ToT mode) of course fluctuates according to the distribution describing the gas gain as a statistical process. By this each X-ray photon entering the detector and interacting within the detector's gas volume is recorded as an accumulation of pixels with circular (or elliptical) shape. Typical X-ray events as recorded with the InGrid based X-ray detector are shown in Fig. 7.13. The round (or elliptical) shape allows to discriminate other type of events (e.g. tracks of charged particles) easily by applying a selection utilizing the event's shape. Typical events showing tracks of charged particles are shown in Fig. 7.14. Assuming that each primary electron entered a different grid hole one can reconstruct the X-ray photon's energy in principal by simple pixel (or primary electron) counting, otherwise the total charge of all pixels linked to one X-ray photon can be used as a measure for the X-ray photon's energy by applying a calibration.

For X-ray photons with an energy larger than 3.2059 keV, the binding energy of electrons in argon's K-shell [113], it may also happen that part of the initial energy is not visible in the detector. When a photoelectron is released from argon's K-shell the hole created is filled with an electron from a higher shell and the difference in binding energy is either transferred to a cascade of Auger electrons (86.5 % probability [100]) or emitted as an X-ray photon of 2.9575 keV energy (13.5 % probability). In the latter case, the X-ray photon may escape the region of the original interaction or, as in case of the InGrid based X-ray detector, even the instrumented area and therefore detection at all as a 2.9575 keV X-ray photon has a range of a few centimetres in argon (at normal conditions). These photons are called escape photons, resulting in the detectable energy being reduced to $E_\mathrm{det} = E_\text{X-ray} - 2.9575\,\mathrm{keV}$.

---

[8] For thin/light gases like helium this is different, in a helium based mixture the photoelectron track can be of a few millimetre length even for X-ray photons of only a few keV energy. As the direction in which the photoelectron is emitted is linked to the X-ray photon's polarization, this can be used to measure the polarization of X-ray photons [112].

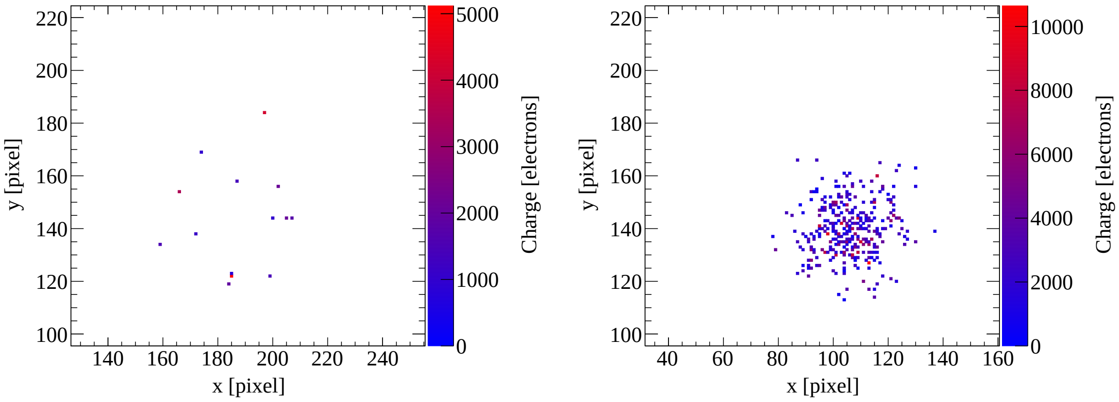

(a)

(b)

Figure 7.13: Typical X-ray events as recorded with the InGrid based X-ray detector stemming from X-ray photons with 277 eV (a) and 8 keV (b) respectively. In both cases not the full active area is shown but only a quarter of it, zoomed in on the cluster position for better visualization. Charge measured with each pixel is colour coded on the z-axis.

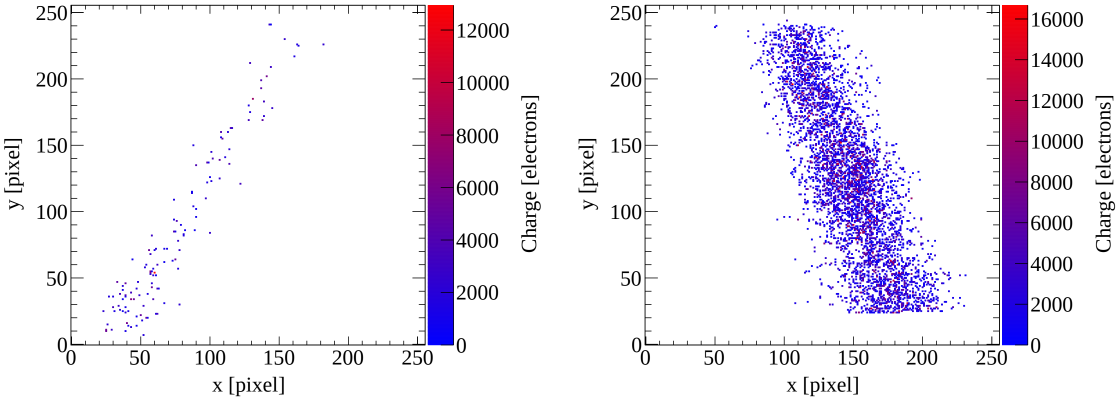

(a)

(b)

Figure 7.14: Typical charged particle tracks as recorded with the InGrid based X-ray detector stemming most likely from a cosmic muon (a) and a highly ionizing particle (e.g. an alpha particle from a radioactive decay) traversing the detector (b) respectively. In both cases the full active are of the detector is depicted and the charge measured by each pixel is colour coded on the z-axis. For (b) more than 4 096 pixels were activated resulting the read out frame to be slightly truncated in the lower part.

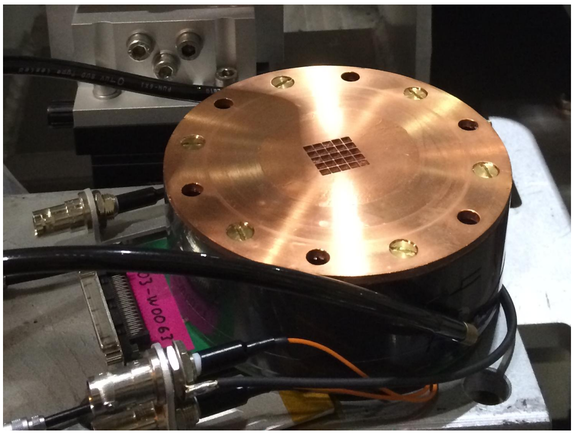

Figure 7.15: Picture of the assembled InGrid based X-ray detector, to shield the detector volume from external light the detector body has been wrapped with black tape. The black tubes (left) connect the detector to its gas supply.

7.4 Detector commissioning at Bonn

Prior to the characterization in the CDL and finally the installation at CAST, the InGrid based X-ray detector was commissioned and assembled at Bonn in the laboratory. This is done stepwise including several tests for functionality in between to guarantee a proper operation of the detector. The very first step in commissioning the InGrid based X-ray detector is the selection and testing of a GridPix, or more precisely the electronic testing of its underlying Timepix ASIC. Afterwards the readout module is assembled and the detector is completed by mounting its body and a cathode, Fig. 7.15 shows a picture of the assembled detector. Then the detector is flushed for the first time with the argon isobutane mixture. After sufficient flushing (e.g. 1 to 2 h at a flow rate of 2 l/h) to remove air and adsorbed water vapour from the detector's inner volume, the high voltages are ramped up. This is done carefully and with additional monitoring measures in place. The initial high voltage tests are followed by further tests including the use of radioactive sources (e.g. ^{55}Fe) to check and adjust the detector's working point, e.g. by tuning the applied high voltages.

For the InGrid based X-ray detector used throughout this thesis a GridPix from the IZM-5 batch with a 4 µm SRSN layer was selected: `D03-W0063`[9]. This chip was of quality level A (meaning fully functional logics and electronics; no dead columns) prior to the processing at IZM Berlin. It was glued and bonded onto a carrier board and then, before installation in the detector, electronically tested and calibrated, showing excellent performance. Additional to `D03-W0063` four more GridPixes, also from the IZM-5 batch, were mounted on carrier boards and passed through the same testing procedure. Two of these proofed to be of equal quality and were kept to provide spares in case of a failure or damage.

7.4.1 Electronic tests and characterization of the used Timepix ASIC

After the GridPix `D03-W0063` had been glued onto its carrier board and electronically been connected via wire bonding (including the high voltage bond wire connecting the grid to the high voltage pad on the carrier board) it was tested electronically. The first tests were done with the old readout system, the MUROS, using the `Pixelman` software: a digital test, a DAC scan and the recording of noise frames. The digital test checks for defect pixels in the analogue as well as in the digital domain, in case of `D03-W0063`

---

[9] A typical chip number is of form `XYY-WZZZZ` where `X` and `YY` decode the chip's position on the wafer it is cut from and `ZZZZ` is the number of the wafer.

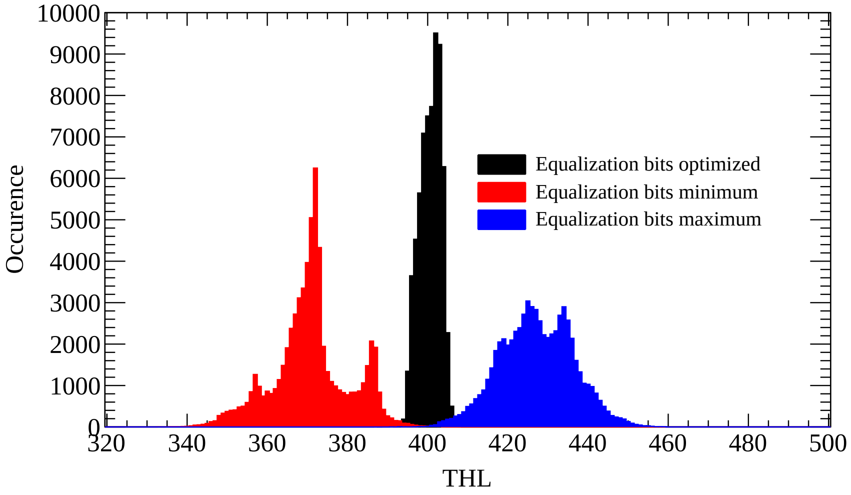

Figure 7.16: Threshold distributions of GridPix `D03-W0063` before and after threshold equalization. Threshold distributions before equalization are shown for all equalization bits set to zero (red) and one (blue) respectively. The threshold distribution after the threshold equalization, using the equalization bits optimized for each pixel, is shown in black. The reduction of the threshold spread (or dispersion) through the equalization can be clearly observed. Especially the distributions before equalization are of rather strange shape, for a perfect chip they are expected to be of Gaussian form, but still a standard deviation of less than three *threshold* steps is reached through equalization which is fine for operating the chip.

revealing no defect pixels at all and confirming that the chip was still of quality level A after the post processing. In the DAC scan the different DACs are scanned while sampling their analogue output. This allows to check that all (necessary) DACs function correctly, e.g. a flat curve for the *thl* DAC would indicate that this DAC is not responding which renders a chip unusable. In case of `D03-W0063` all DACs showed the anticipated behaviour. The recording of noise frames is used to check two things: On the hand it is used to double check the proper functioning of the *thl* DAC by testing its influence on the noise level in the recorded frames and one the other hand to verify that the *shutter* signal is reaching the pixels. If the *shutter* signal would not reach the pixels they would not record anything and all frames would be empty (assuming no noisy pixels). The double check of the *thl* DAC works by tuning it and verifying that the noise level in the frames changes accordingly (more activated pixels per frame for lower *thl* values and less for higher values). These tests as well were fully successful for `D03-W0063`.

At this point the readout system was switched to the one based on the Xilinx Virtex-6 evaluation board which would later also be used in the CDL and at CAST. Now, the power consumption of the chip was checked to be in the typical range, too high currents could indicate shorts or defects of the chip's electronics (which not necessarily render it unusable). In case of `D03-W0063`, the power consumption was as usual with 14 mA in the digital and 179 mA in the analogue domain, both at 2.2 V, while the chip is idle. To prepare `D03-W0063` an optimization of the *ths* DAC value was performed with TOS followed by a threshold equalization which both were successful, Fig. 7.16 shows the result of the threshold equalization.

Next the *threshold* (or the *thl* DAC value) with which the InGrid based X-ray detector is to be operated has to be chosen. As the detector is later operated at CAST with frames of 1 s length, the *thl* DAC value is adjusted to a point where in a 1 s long frame no pixel is activated by noise. In case of `D03-W0063` with this method the *thl* DAC value was fixed to 433 which is within the range of typical *threshold* values for these devices. Additionally, one noisy pixel was identified which is triggered, almost independent of the *threshold*, on average in one of two frames, as this pixel is not in the very central region of the chip and its position is known this does not affect the operation of the InGrid based X-ray detector.

To later allow the conversion of counted clock cycles in ToT mode into charge in electrons, a ToT calibration of the chip is performed using test pulses. Test pulses of defined voltage are sent to the pixels (all configured in ToT mode) and the mean number of counted clock cycles is recorded. With the known capacitance of each pixel's test pulse circuitry, the voltage step can be converted into an injected charge and by fitting a function of form

$$\mathrm{ToT}[\mathrm{clockcycles}] = a \cdot U_{\mathrm{inj}}[\mathrm{mV}] + b - \frac{c}{U_{\mathrm{inj}}[\mathrm{mV}] - t} \tag{7.1}$$

to the acquired data with U_{inj} being the height of the injected test pulses in mV and a, b, c and t the free parameters of the fit function, the parameters for the conversion of number of clock cycles into charge can be determined. Knowing the test pulse injection capacity C to be 8 fF and the relationship

$$Q_{\mathrm{inj}}[e] = \frac{C \cdot U_{\mathrm{inj}}}{e} \approx 50 \cdot U_{\mathrm{inj}}[\mathrm{mV}] \tag{7.2}$$

between the injected charge Q_{inj} and the test pulse voltage U_{inj} one can retype Equation 7.1 to allow for direct conversion between number of clock cycles counted in ToT mode and charge in electrons:

$$\mathrm{ToT}[\mathrm{clockcycles}] = \frac{a}{50} \cdot Q_{\mathrm{inj}}[e] + b - \frac{c}{Q_{\mathrm{inj}}[e]/50 - t}. \tag{7.3}$$

Applying this method to the calibration data from `D03-W0063` one gets the calibration curve shown in Fig. 7.17 and from a fit using `ROOT` the calibration parameters:

$$\begin{aligned} a &= 0.3484 \\ b &= 58.56 \\ c &= 1\,294 \\ t &= -12.81. \end{aligned}$$

In addition to the ToT (or charge) calibration another calibration is performed to get a relation between the *thl* DAC value and the actual *threshold* in electrons in order to confirm the detector's working point. This calibration can be done using so called S-curve scans: For a fixed test pulse height a defined number of test pulses is sent per recorded frame and a scan of the *thl* DAC values is performed with the chip configured in Medipix mode and recording the mean number of pulses the pixels have counted during a frame. Due to threshold dispersion and noise this scan does not resemble a step function at the point where the *threshold* corresponds to the charge injected by the test pulses but resembles an error function:

$$\mathrm{erf}(x) = \frac{1}{\pi} \int_{-x}^{+x} e^{-\tau^2} \mathrm{d}\tau \tag{7.4}$$

which can be fitted to the S-curve data as

$$N(x) = N_0 \cdot \frac{1}{2} \left[1 + \mathrm{erf}\left(\frac{x - \mu}{\sigma \sqrt{2}} \right) \right] \tag{7.5}$$

with x being the *thl* DAC value, N the mean number of pulses recorded, N_0 the number of pulses send, μ

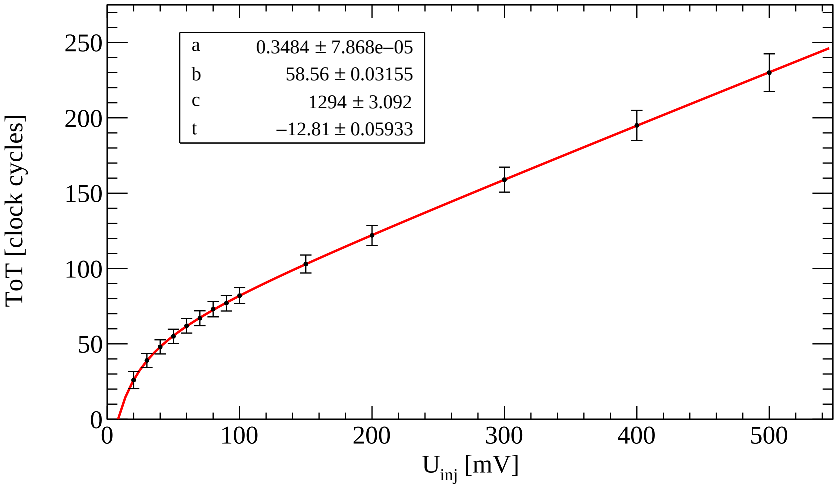

Figure 7.17: ToT calibration curve for GridPix `D03-W0063` at a *threshold* value of 433. Test pulses with heights ranging from 20 to 500 mV have been injected, the injected charge is given by equation 7.2. A function as described in equation 7.1 has been fitted to the data points using `ROOT` to obtain the calibration parameters. Due to the lack of data points close the chip's threshold, the intersect of the fitted function with the x-axis should not be interpreted as the threshold value but may give the order of magnitude. The error bars shown have been enlarged by a factor of 500 to make them visible in the plot.

the central position of the smeared step and σ the width of the step. While μ gives the *thl* DAC value corresponding to the injected charges, σ is a measure for the threshold dispersion and noise. When sending no test pulses (which can be treated as test pulses with a height of 0 mV) it is possible to sample only noise and to find the *thl* DAC value corresponding to the baseline, that means 0 e. For the latter case a Gaussian is fitted to the data. The S-curves recorded for `D03-W0063` including the fitted functions are shown in Fig. 7.18(a). Using Equation 7.2 and the results of the S-curve fits one can find the linear relationship between *threshold* and *thl* DAC value, see Fig. 7.18(b). From this it is possible to calculate the actual *threshold* of `D03-W0063` to be approximately 1 100 e and the ENC to be 140 e which is relatively large compared to the nominal ENC of the Timepix ASIC which is stated as 90 e. It is known that for an unknown reason the noise and therefore thresholds of GridPixes from the IZM-5 batch are rather large, especially when compared to e.g. the GridPix used for a first prototype with a threshold of (730 ± 65) e [99]. But this does not pose a problem, by slightly increasing the gas gain (the grid voltage) it can be easily compensated for the increased threshold, it is of much more importance to operate the GridPix quasi noise free in the InGrid based X-ray detector.

After passing all the electronic tests successfully and having all necessary calibrations performed the GridPix `D03-W0063` on its carrier board was mounted in the readout module and the InGrid based X-ray detector could be completely assembled.

7.4.2 High voltage tests and conditioning

The detector is flushed with the argon isobutane mixture (Ar/iC$_4$H$_{10}$ 97.7/2.3) for at least one hour prior to ramping up the high voltages for the first time. During the ramp up the GridPix is read out continuously with 1 s frames which are shown on a live event display to notice any effect of the high voltage, as well the desired as the undesired effects like sparks. The high voltage line supplying the grid voltage

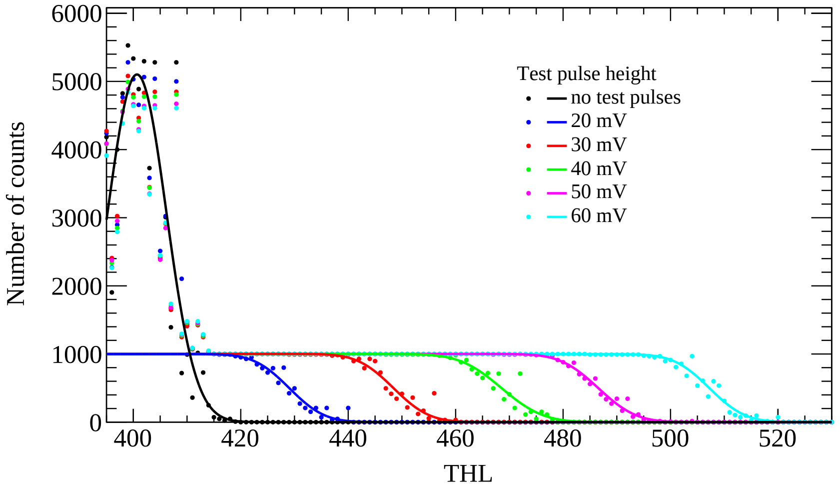

(a)

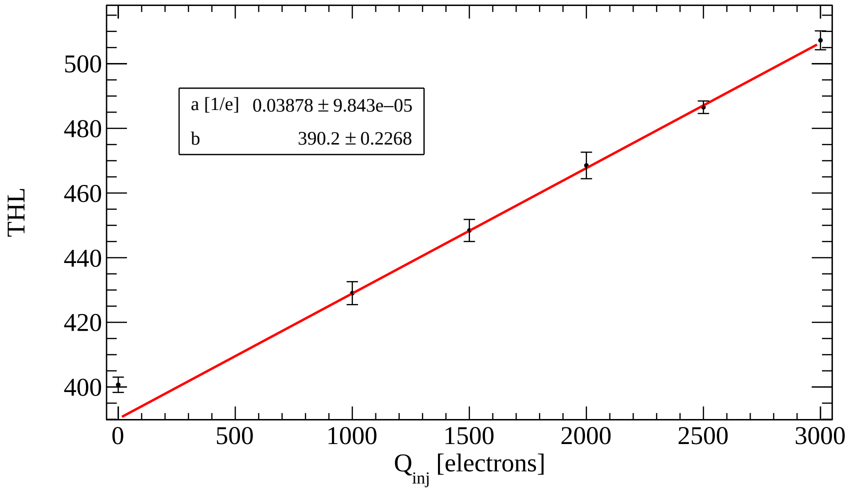

(b)

Figure 7.18: S-curves (a) and *thl* calibration (b) of GridPix `D03-W0063`. S-curves have been recorded for five different test pulse heights: 20 mV, 30 mV, 40 mV, 50 mV and 60 mV, an additional curve has been recorded without test pulses. To the S-curve data a function as described in equation 7.5 has been fitted using `ROOT` for each test pulse height, for the data without test pulses a Gaussian has been fitted. With the data extracted from the fits the *thl* calibration can be done, see (b) by fitting a straight line to the data points which allows to convert a *threshold* value into a corresponding charge in electrons. The data point from the measurement without test pulses deviates from the fit and has therefore been excluded, the error bars have been enlarged by a factor of 20.

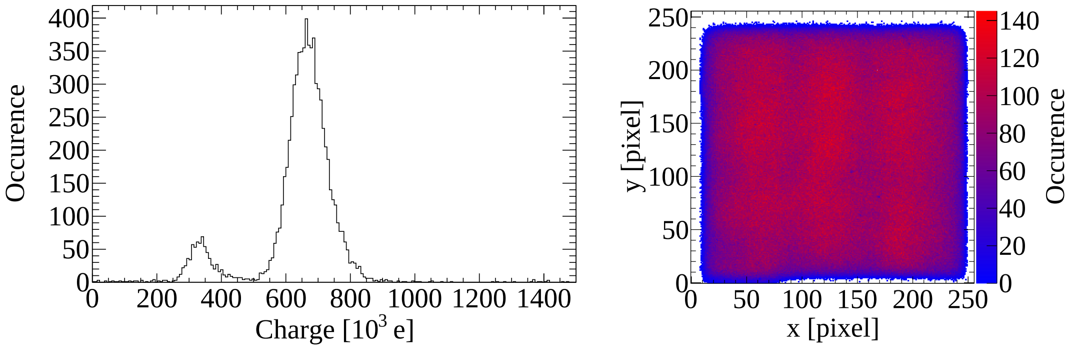

(a) (b)

Figure 7.19: Charge spectrum (a) and occupancy map (b) from measurement with an ^{55}Fe source. In the spectrum, the total charge of identified clusters is used as a measure for the X-ray photon energy, the two peaks from the manganese K_α line (merged with the K_β line) and the corresponding escape line are clearly visible. The occupancy map shows that the GridPix used, has no ineffective areas (except for few single grid holes) and that the whole surface is well illuminated by the source. The slight pattern visible is imprinted by the strongback structure of the X-ray entrance window. The non-illuminated area at the top, left and right edges stem from pixels in theses regions being covered with dike structures necessary for the GridPix mechanical stability plus minor distortions of the electric field close to the chip edges, without the field-shaping anode of the InGrid based X-ray detector the non-illuminated areas at the edges would be significantly larger.

is additionally monitored by a precise current monitor allowing measurement of currents with 10 pA resolution. The first ramp up is done manually in 25 to 50 V steps while closely monitoring the current on the grid voltage line, to avoid any accidental voltage difference between anode and grid the high voltage channels supplying these are linked softwarewise to automatically be set to the same voltage, the cathode voltage is left off for the first ramp up. Starting at roughly −250 V first events appear on the live event display, these are either caused by charged particles traversing the detector's volume close or perpendicular to the grid or by small sparks. Small sparks may be caused by dust particles or sharp edges (e.g. from dicing or at the grid holes), and usually disappear after a short time, when these are burned away, hence the settling time after each voltage step and the close monitoring of the current on the grid voltage line. When the working point of −300 V [100] grid voltage is reached, the linking of anode and grid high voltage channel is removed and the anode is put to its correct voltage of −350 V. At this point the cathode high voltage is switched on and set to −1 850 V, now the first cosmic tracks become visible on the live event display and additional tests using a radioactive source (e.g. ^{55}Fe) can be performed. For these the frame length is adjusted to the rate of the radioactive source in order to record frames with single photons.

When starting up the InGrid based X-ray detector with the GridPix `D03-W0063`, the first ramp up went smoothly, the current on the grid voltage line stabilized at about 1 nA at the working pint of −300 V which is a typical and normal value for these devices. At first `D03-W0063` showed some sparks happening at the top edge of the chip with a rate of approximately one spark per minute. Due to this low rate the sparks did not pose a major problem even for the later operation at CAST. Anyhow, the sparks disappeared completely after the first few operating hours with a radioactive source, most likely they were caused by a sharp edge or spike which was burnt away with time. Fig. 7.19 shows an occupancy plot obtained using an ^{55}Fe source as well as the recorded spectrum.

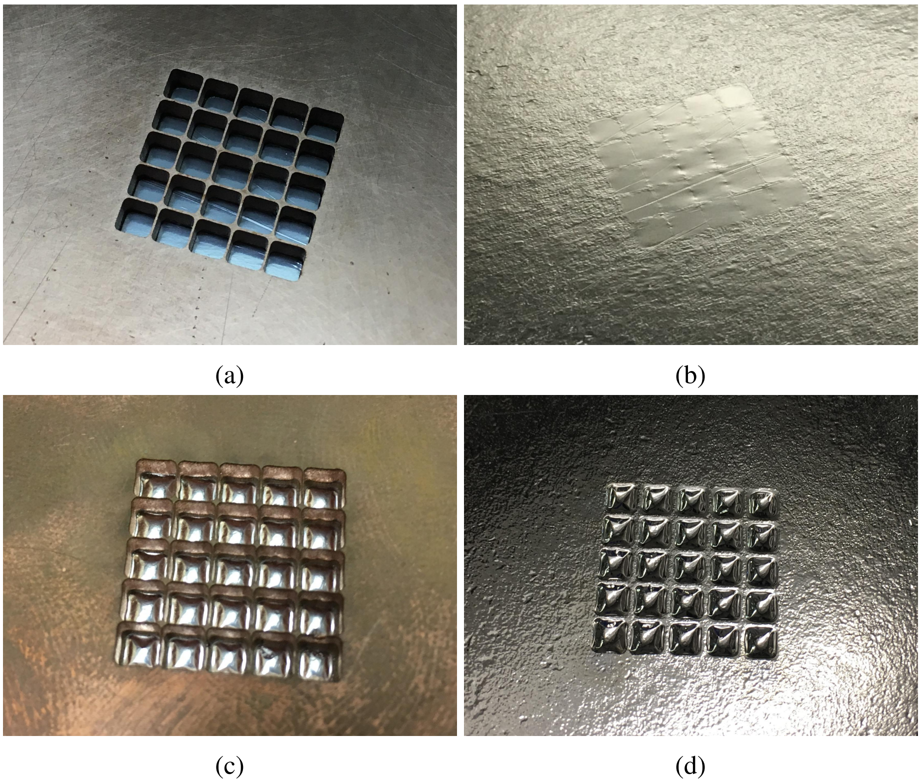
(a) (b)

(c) (d)

Figure 7.20: Pictures of X-ray windows made from 2 µm Mylar® before and after applying a pressure difference of 1 050 mbar. (a) and (b) show front and backside of a window prior to applying a pressure difference, in (b) it is slightly visible that indeed, as intended, the Mylar film also adheres to strongback ribs. (c) and (d) show front and backside of a window after applying a pressure difference, the inelastic deformation of the Mylar film is visible, for a pressure difference of 1 050 mbar the height of the deformations is approximately 0.5 mm. The window shown in (c) was unfortunately at some point handled with bare hands resulting in the visible finger prints and discoloring of the copper surface.

7.4.3 Pressure and leakage tests of the X-ray window

Before one of the cathodes with its X-ray window can be mounted on the detector it has to be tested for gas tightness as well as for robustness as it will have to withstand a pressure difference of 1 050 mbar when mounted to the beamline in the CDL or when operated at CAST. Already before glueing it onto the copper cathode the 2 µm aluminized Mylar film is visually checked for pin holes. This is repeated after the film has been glued onto the copper cathode, prior to gluing care has to be taken to proper chamfer the thin ribs of the strongback structure as those may easily puncture the Mylar film. To reduce this risk, during the gluing procedure it has to be verified that a thin layer of glue is also covering the strongback ribs. Pictures of successfully glued windows can be found in Fig. 7.20.

As a first step to check the window's gas tightness and pressure resistance the cathode is mounted on a detector body closed with a blind on the other hand, then the pressure inside is raised up to 2.5 bar(a) resulting in a pressure difference of approximately 1.5 bar, giving a safety factor of roughly 150 %, a few cycles are done to make sure the window doesn't burst. The Mylar film is deformed inelastically when a pressure difference is applied as can be seen from the pictures in Figs. 7.20(c) and 7.20(d). A few windows not intended to be used at CAST where also successfully tested at a pressure difference of up to 2.5 bar demonstrating the robustness of this rather simple design.

In a second step the windows are tested on a small vacuum test-bench using a turbomolecular pump. After fairly slow pumping with a membrane pump down to a few mbar pressure the turbomolecular pump is switched on to verify that a vacuum pressure in the order of 10^{-4} mbar can be reached within reasonable time showing that the window is at least fairly gas tight. A standard leak test, as common in vacuum applications, was not performed as with these the helium leak rate is determined which is not of relevance for the InGrid based X-ray detector as it is operated with an argon gas mixture. It is known that the thin Mylar film is rather permeable for helium. To estimate the argon leak rate of the window used in the CDL and at CAST a different approach was used: When the InGrid based X-ray detector was connected to a vacuum in the CDL (see next section for details), the gas supply lines were shut off (inlet and exhaust line) and the drop of pressure inside the detector over time measured. Within 70 s the pressure dropped by 0.1 mbar, assuming a total volume (detector, buffer volume, tubes) of about 2 l this gives an estimate for the leak rate of approximately 3×10^{-3} mbar l/s which is acceptable.

7.5 Characterization of the detector in the CAST Detector Lab

In order to characterize the InGrid based X-ray detector prior to the installation at CAST it had to be tested with X-ray photons of various energies ranging from a few keV down to a few hundred eV. This characterization was necessary mainly for two reasons: Final proof had to be provided of the detector's capability to detect low energy X-ray photons (below 1 keV) and to understand its behaviour for different X-ray energies including energy resolution, linearity of the detector response and the event shapes which are important to suppress non-X-ray background events (see. Chapter. 10).

The measurements for this characterization were carried out in April 2014 in the CAST Detector Lab (CDL) at CERN. This facility of CAST provides a variable X-ray generator connected to a beamline suitable for detector tests as well as most infrastructure needed. At the X-ray generator of the CDL datasets were successfully recorded at eight different energies ranging from 8 keV down to 277 eV thus proving that the InGrid based X-ray detector is able to detect low energy X-ray photons. The data was analysed and the detector characteristics examined. The results of this characterization campaign including a detailed look into the behaviour of event shape variables suitable for a background suppression method with energy have been published in [114] and will also be discussed here.

7.5.1 The CAST Detector Lab

The CAST Detector Lab is a dedicated facility at CERN for test, characterization and study of X-ray detectors (especially for the low energy X-ray regime) and has been set up by CAST. It features a variable X-ray generator, a vacuum beamline and most of the infrastructure required to operate a detector like the InGrid based X-ray detector. The X-ray generator and the vacuum beamline are shown in Fig 7.21.

Variable X-ray generator

The variable X-ray generator provided by the CDL uses exchangeable targets in combination with a filter wheel to create an X-ray beam of selected energy, it is described in detail in [115]. The variable X-ray generator follows the principle of an X-ray tube, an electron beam is created by applying a high voltage between a heated filament and a target anode. Its energy can be tuned with the high voltage and its intensity through the voltage/current heating the filament. The X-ray spectrum emitted is a broad Bremsstrahlungs spectrum with the maximum energy corresponding to the energy of the electron beam, plus the characteristic X-ray lines of the target material. Of course this set-up has to be operated

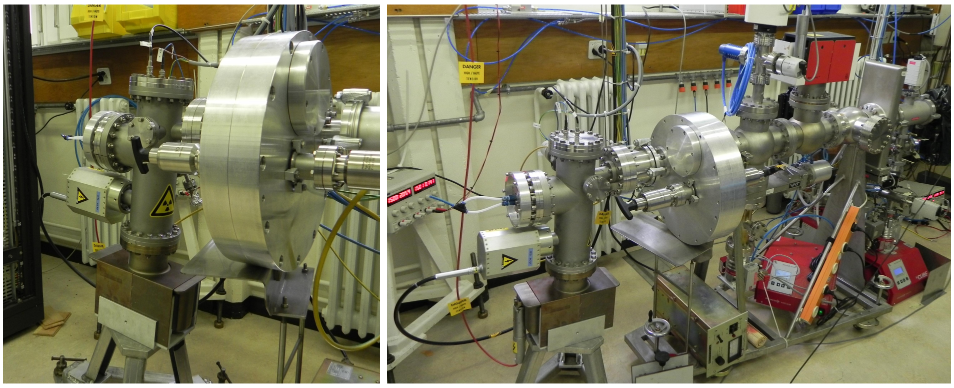

(a) (b)

Figure 7.21: Pictures of the variable X-ray generator and beamline of the CDL. A close up of the variable X-ray generator and filter wheel are shown in (a), the complete beamline can be seen in (b) including the large gate valve on the very right which separates the generator and detector vacuum regions. The filament voltage is supplied via the top and the target wheel's high voltage is supplied from the side. Turbomolecular pumps as well as SIPs used to pump the different regions of the system and to maintain a vacuum pressure suitable for operation of the X-ray generator can be seen in the two pictures.

under a high vacuum (better than 10^{-5} mbar) to work. To allow for easy exchange of the target without breaking the vacuum, several targets are mounted on a turnable target wheel. To suppress the broad Bremsstrahlungs part of the spectrum and select a specific line of the target dedicated filters are used. These are also mounted on a wheel to allow for easy selection and change without breaking the vacuum.

For example, one can use an aluminium target with an electron beam of 4 keV energy to get the characteristic aluminium K_α line at 1.486 keV [113]. The electron beam should have at least twice the energy of the line of interest for maximizing the emission rate for this line. To get rid of the Bremsstrahlungs background one can use an aluminium filter which features a transmission peak exactly at the energy of its characteristic K_α line and suppresses the other parts of the spectrum. The electron beam dumped into the target creates a heat load depending on the beam current. In principle the set-up used at the X-ray generator of the CDL would allow to actively cool the target wheel with a water cooling system but this has not been implemented, thus limiting the rates of X-ray photons at which it can be operated reasonably without exceeding the maximum heat load tolerable.

Beamline and infrastructure

Connected to the variable X-ray generator of the CDL is a vacuum beamline allowing to connect almost any kind of detector given an adequate adapter from detector to standard vacuum couplings. As the InGrid based X-ray detector's design is based on the CAST MicroMegas detectors which had already been tested and characterized before in the CDL, it could be connected to the beamline using the existing adapter piece simplifying the set-up and operation. The vacuum of the beamline is divided by a large gate valve into the detector vacuum and X-ray generator vacuum regions both pumped by turbomolecular pumps, the latter additionally by a SIP to guarantee the vacuum level required for operation of the X-ray generator. The detector vacuum region can be pumped very gently through a needle valve to allow for the use of very thin X-ray windows (like the 2 µm Mylar window of the InGrid based X-ray detector). The needle valve is adjusted to limit the pressure gradient during pumping (or venting) to about 1 mbar/s and can be bypassed for efficient pumping with the turbomolecular pump when a pressure in the millibar region has been reached.

If the pressure in the detector vacuum region is too high (above a few 10^{-3} mbar) the gate valve separating the X-ray generator cannot be opened as it would cause the pressure in the generator vacuum region to rise above levels suitable for its operation. This might happen when very thin X-ray windows are used by the detector gas leaking into the detector vacuum region. For this case the beamline allows for implementing a differential pumping scheme: An additional very thin window without strongback (e.g. 0.9 µm Mylar) further divides the detector vacuum region into a good and a bad vacuum region. Both regions are connected via a normally open bypass valve. When a vacuum pressure of at least 10^{-2} to 10^{-3} mbar has been reached in the two linked regions, the bypass valve is closed separating the good and the bad vacuum region which are now pumped by individual turbomolecular pumps. As the differential window acts as a kind of barrier for the gas permeating through the X-ray window into the bad vacuum region, typically a vacuum pressure one to two orders of magnitude better is reached in the good vacuum region compared to the bad vacuum region, thus allowing to open the gate valve to the X-ray generator. The bypass valve is usually interlocked with the vacuum pressures in the good and bad vacuum region to avoid a pressure difference larger than 1 mbar which could burst the very thin differential window.

In addition to the X-ray generator and its beamline the CDL also provides the gas supply for gaseous X-ray detectors like the CAST MicroMegas detectors or the InGrid based X-ray detector. Premixed gas bottles can be connected outside the lab to lines leading towards the detector station and incorporating needle valves, flow meters and a pressure regulator to maintain the required gas pressure inside the detector at a selected gas flow rate. Here an outlet pressure regulator is used, providing a regulated pressure at the detector's gas inlet, in combination with a needle valve and flow meter at the detector's exhaust line.

7.5.2 Measurement campaign & data analysis

For characterizing the InGrid based X-ray detector and obtaining reference datasets for the later background suppression, the detector was mounted on the beamline of the CDL connecting it to the variable X-ray generator, a picture of the mounted InGrid based X-ray detector can be found in Fig. 7.22. This was done prior to the installation at CAST in April 2014. Due to previous experience with 2 µm Mylar windows a differential window made from 0.9 µm Mylar was installed on the detector side of the vacuum system to guarantee a smooth operation and data taking. Fig. 7.23 shows the detector's efficiency/sensitivity as a function of the X-ray energy taking into account the differential as well as detector window and folding it with the absorption in 29.8 mm of argon at 1 050 mbar: A decent sensitivity is reached down to 1 keV where it drops below 25 % but at the carbon and oxygen K_α lines (~ 300 eV and ~ 500 eV respectively) sensitivity is restored due to transmission peaks of the window material.

During operation a vacuum pressure of less than 5×10^{-4} mbar[10] was maintained in the bad vacuum region of the detector side, in combination with the differential window allowing to reach about 2×10^{-6} mbar in the good vacuum region as well as in the generator region throughout the whole measurement campaign.

Data with eight different X-ray lines has been recorded in the CDL ranging from 8 keV (copper K_α line) down to 277 eV (carbon K_α line), all eight set-ups and the respective X-ray lines of interest are listed in Table 7.1. The InGrid based X-ray detector was operated with the usual argon isobutane mixture (Ar/iC$_4$H$_{10}$ 97.7/2.3) at a pressure of 1 050 mbar(a). The grid voltage was first set to −300 V following the working point of the gas mixture [100] and later slightly adjusted to achieve a gas gain of roughly

---

[10] For the bad vacuum region a Pirani pressure gauge was used which allows to measure pressures ranging from a few hundred millibar down to about 5×10^{-4} mbar, to measure pressures below 5×10^{-4} mbar different pressure gauge types like hot or cold cathode gauges have to be used [116].

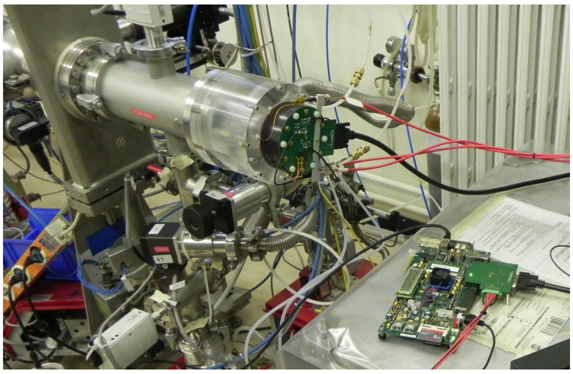

Figure 7.22: Picture of the InGrid based X-ray detector mounted to the variable X-ray generator of the CDL. The detector is mounted to the beamline via an adapter piece made from acrylic glass guaranteeing proper electrical isolation between the stainless steel pipes and the copper cathode set to a high voltage potential. The readout board based on a Xilinx® Virtex®-6 evaluation board can be seen on the lower right, connected to the detector via a VHDCI cable.

2 500, thus grid, anode and cathode voltage were set to −305 V, −355 V and −1 855 V respectively. The detector was continuously read out using frames of 600 µs length, resulting in the frame rate only being limited to about 40 Hz by the readout time of 25 ms. For each set-up of of the X-ray generator its intensity was tuned to achieve one X-ray photon in every tenth frame recorded to avoid a frame containing more than one X-ray photon at an still acceptable fraction of empty frames. Only for the lowest energies (set-ups G and H, see Table 7.1) this required the X-ray generator being operated close to its rate limits due to the low transmission of the windows used at these energies. To gather about 10 000 frames with a single X-ray photon took about 1 to 2 h per set-up plus the time required for changing the set-up and adjusting the rate. All data was taken with the GridPix of the InGrid based X-ray detector completely configured in ToT mode to register the charge arriving on all pixels.

To start with the analysis of the recorded datasets, at first all empty frames are discarded before applying the charge calibration for the GridPix used to convert the ToT value of each pixel, measured in number of clock cycles, into charge in electrons. Next a loose cut requiring at least three active pixels per frame is used to reject frames not containing any X-ray photon, of course the one pixel known to be noisy is masked softwarewise. To reconstruct the X-ray photons in the frames the `MarlinTPC` [119] software framework is used. To identify clusters originating from an X-ray photon a modified cluster finding algorithm allowing for a distance of maximum 50 pixels[11] between neighbouring pixels. Starting from the lower left corner of the chip a seed pixel is searched for a cluster and any activated pixel within a square array of 101 × 101 pixels centred around the seed pixel is assigned to the cluster. For every pixel added to the cluster the search for neighbours is repeated. More details on the data reconstruction will be given in chapter 10. Examples for the clusters originating from X-ray photons of different energies can be found in Fig. 7.13.

The overall shape of the reconstructed clusters is usually slightly asymmetric and resembles an elliptical shape due to statistical fluctuations in the diffusion process, for high X-ray photon energies also the length of the photoelectron track contributes to this asymmetry. To compensate for the not perfectly round shape of the clusters the longest and, perpendicular to it, the shortest axis of the cluster are identified by rotating the coordinate system. This rotated coordinate system is used to calculate several event shape

---

[11] This rather large distance is necessary to also correctly reconstruct X-ray photons which were absorbed close to the cathode resulting in a large spread of the primary electrons due to diffusion.

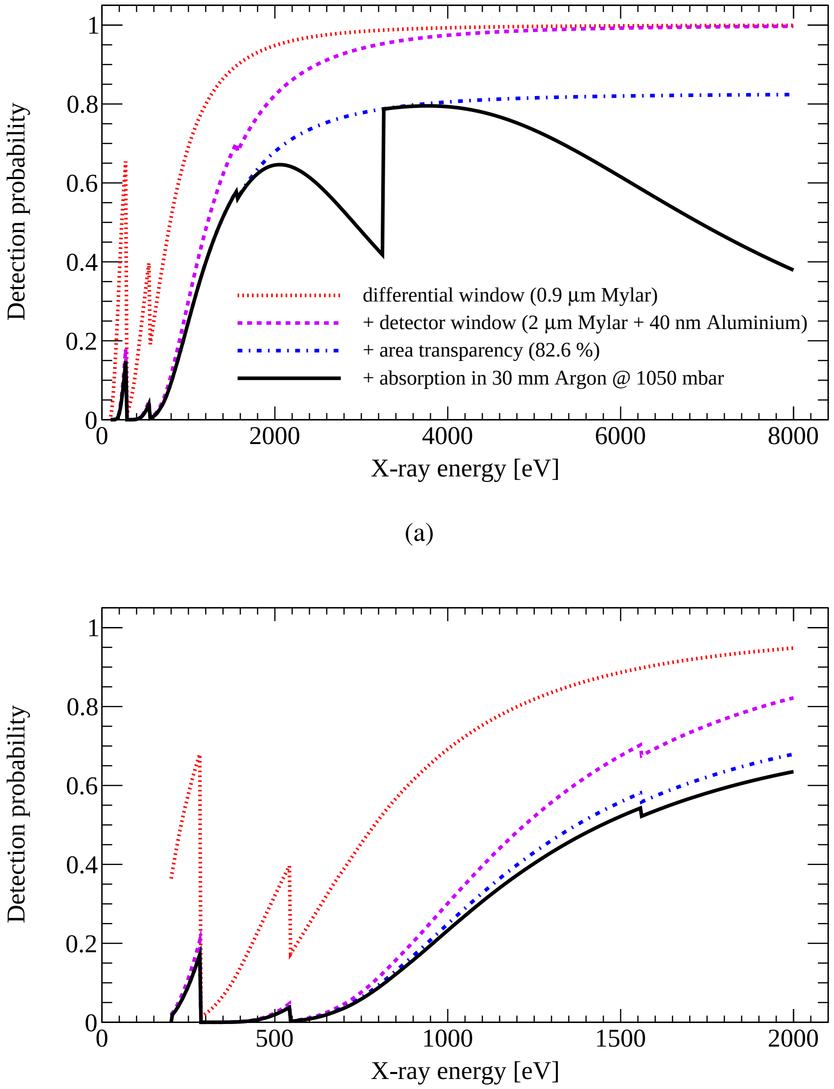

(a)

(b)

Figure 7.23: Transmission probability and absorption efficiency of the InGrid based X-ray detector in the CDL are shown as function of X-ray photon energy in a cumulative approach: First the transmission probability of the differential window is taken into account, then the detector window material is added and then its area transparency incorporated. At last the absorption probability in 30 mm of argon at 1 050 mbar(a) together with the transmission probabilities of differential and detector window, including its area transparency, give the detection probability as function of the X-ray photon energy. While (a) shows the whole range from 0.2 to 8 keV, (b) shows a zoom in on the range from 0.2 to 2 keV. The transmission and absorption data have been produced using a web-based generator [101] utilizing the semi-empirical approach described in [102]. Published in [111].

set-up	beam energy	target material	filter	fluorescence line(s)
A	15 keV	copper	nickel	Cu K_α (8.048 keV)
B	12 keV	manganese	chromium	Mn K_α (5.899 keV)
C	9 keV	titanium	titanium	Ti K_α (4.511 keV) Ti K_β (4.932 keV)
D	6 keV	silver	silver	Ag L_α (2.984 keV) Ag L_β (3.151 keV)
E	4 keV	aluminium	aluminium	Al K_α (1.487 keV)
F	2 keV	copper	EPIC	Cu L_α (0.930 keV) Cu L_β (0.950 keV)
G	0.9 keV	copper	EPIC	O K_α (0.525 keV)
H	0.6 keV	carbon	EPIC	C K_α (0.277 keV)

Table 7.1: Beam energies, target and filter materials chosen to produce photons of the listed fluorescence lines with the X-ray generator of the CDL. A letter is assigned to each set-up for reference throughout this chapter. For some settings more than one fluorescence line is listed, in these cases there was no adequate filter material available to suppress the unwanted line, e.g. the K_β lines of several target elements. The filter material EPIC is a composite filter composed of a 330 nm thick polypropylene carrier sandwiched by two 90 nm aluminium layers with a 35 nm tin layer on top of one side, also known as *Thick filter* and developed as UV filter for the European Photon Imaging Cameras utilized in the XMM-Newton satellite [117, 118]. The energies of the lines were taken from the X-ray data booklet [113].

properties for each cluster by projecting it either on the longest or shortest axis. Typical event shape variables are the standard deviation of the cluster, referred to as σ_{long} and σ_{trans} for projection on the longest (longitudinal) and shortest (transverse) axis respectively, the eccentricity $\epsilon = \sigma_{\mathrm{long}}/\sigma_{\mathrm{trans}}$, length l (distance between outermost pixels in projection on longest axis) and higher statistical momenta such as skewness or kurtosis. In addition for each reconstructed cluster the centre position (mean of x and y positions of all pixels in the cluster) in the GridPix' coordinate system is stored as well as the number of pixels and total charge of each cluster which both can be used as a measure for the X-ray photon's energy. The total charge is calculated as sum of all pixel's charges in the cluster.

To obtain clean spectra from the datasets for each X-ray generator set-up they have to be cleaned from those frames where the X-ray photon is not completely contained on the GridPix and from those where more than one X-ray photon was within the frame but could not be separated in the reconstruction of the clusters as they were too close to each other. By requiring the cluster centre to be in a distance of at maximum 4.5 mm from the GridPix' centre incomplete X-ray photons are easily removed while fully contained X-ray photons are kept as a minimum distance of 2.5 mm to the chip's edges is ensured. The expected radius $r \approx 3 \cdot \sigma_{\mathrm{t}}(3\,\mathrm{cm})$ of a cluster at full drift distance can be calculated taking the transverse diffusion constant D_{t} as simulated with `Magboltz` [75] for the gas mixture used at the given conditions:

$$\sigma_{\mathrm{t}}(z) = D_{\mathrm{t}} \cdot \sqrt{z} \tag{7.6}$$

$$\sigma_{\mathrm{t}}(3\,\mathrm{cm}) = 470\,\mu\mathrm{m}/\sqrt{cm} \cdot \sqrt{3\,\mathrm{cm}} \approx 815\,\mu\mathrm{m} \tag{7.7}$$

$$r \approx 2.45\,\mathrm{mm}. \tag{7.8}$$

The fraction of frames containing more than one X-ray photon proved to be larger than expected, possibly due to non-optimal adjustment of the X-ray generator's rate, and therefore required cleaning of the datasets. To get rid of those frames a set of loose cuts on l, ϵ and σ_{trans} have been applied to only exclude those frames which are not compatible with the single X-ray photon hypothesis. The list containing the cuts applied to the dataset of each X-ray generator set-up can be found in Table B.1 in appendix B.

The resulting X-ray spectra can be produced in the pixel or the charge representation using either the number of activated pixels or the total charge as measure for the X-ray photon's energy. The spectra for set-ups E (aluminium K_α line at 1.487 keV) and H (carbon K_α line at 277 eV) are shown in Fig. 7.24, the complete set of spectra for all eight set-ups can be found in appendix B. Some of the spectra do not contain only the X-ray line of interest but also additional lines, those can either be the corresponding escape lines (only for X-ray energies above 3.2059 keV) or for example K_β lines close to the line of interest if no filter material was available to suppress the additional line. But also, especially for the low energy X-ray lines, additional lines can stem from contaminations on the target material (e.g. in Fig. 7.24(c) a small, additional peak close to the main carbon K_α line is visible which can be linked to an oxygen contamination) or stainless steel screws used to fix the target on its wheel. In the spectra using the charge representation all visible peaks can be described by Gaussian distributions of form

$$f(x) = N \cdot \exp - \left(\frac{(x-\mu)^2}{2\sigma^2} \right) \tag{7.9}$$

with N the height, μ the centre and σ the width of the distribution. Some of the peaks in the spectra using the pixel representation show a tail to the left of the peak like for example the aluminium K_α peak in Fig. 7.24(a). This tail is caused by X-ray photons which were absorbed further inside the detector resulting in a shorter drift distance for the primary electrons. As diffusion is reduced with shorter drift distance the probability of more than one primary electron entering the same grid hole increases. If for example two primary electrons enter the same grid hole they are only registered as one activated pixel instead of two if the diffusion was sufficient to separate them far enough to enter individual grid holes. As the pixels measure the total charge arriving on them the charge representation of the spectra is not affected. The resulting peak can however be described by joining an exponential function to the left side of a Gaussian distribution [99]:

$$f(x) = \begin{cases} N \cdot \exp\left(-\frac{(x-\mu)^2}{2\sigma^2}\right) & \text{for} : x > c \\ \exp\left(ax+b\right) & \text{for} : x < c \end{cases} \tag{7.10}$$

with a and b the parameters describing the exponential part of the function, the joining point c is determined by the other parameters to get a continuous function. For peaks of low energy (e.g. escape lines) the effect can be neglected.

To each spectra a dedicated function has been fitted taking into account all known or identifiable peaks. The parameters of additional peaks (K_β lines and contaminations) have been restrained when possible to reduce the number of free fit parameters to reasonable amount: The mean positions (μ) of those peaks has been linked to the main peak using the information from [113] and the width (σ) of close-by peaks has been assumed to be identical. A list of all lines visible in the spectra of the different set-ups can be found in Table B.4 in appendix B together with a list of the complete fit function used for each spectra in Tables B.2 (pixel spectra) and B.3 (charge spectra). From the fitted functions it was possible to extract the positions of the different X-ray lines and their energy resolution in the pixel as well as in the charge representation.

7.5.3 Characterization results and reference datasets

Taking the mean charge or number of electrons μ of the main peaks and plotting them versus the known energy of the lines, one can characterize the InGrid based X-ray detector's response to photons of various energies. The resulting calibration curves are shown in Fig. 7.25 using both the pixel as well as the charge

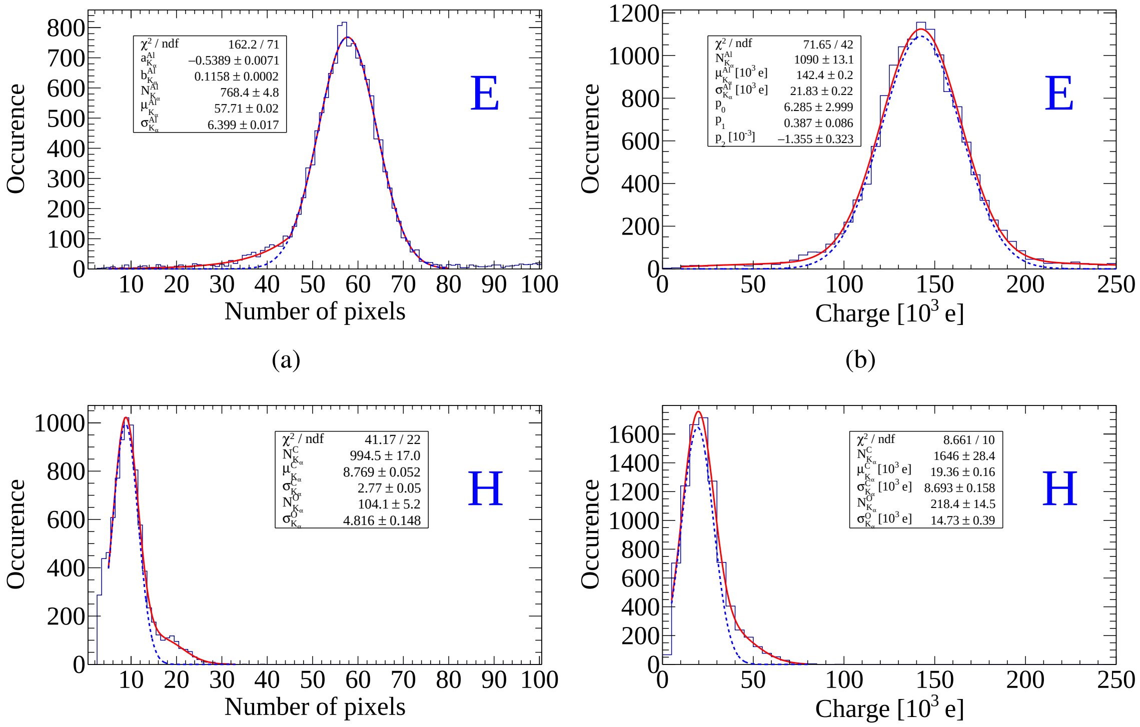

(a) (b)

(c) (d)

Figure 7.24: X-ray spectra of settings E and H (see Table 7.1) using both the pixel representation (left) and the charge representation (right). Main peaks shown are the aluminium K_α line at 1.5 keV: (a) and (b); and the carbon K_α line at 277 eV: (c) and (d). The functions fitted to the spectra are shown in solid red while the Gaussian distributions describing the main peaks are plotted in addition as blue dashed line. Published in [114].

information. By fitting straight lines of form

$$N(E) = a_N \cdot E \tag{7.11}$$

$$Q(E) = a_Q \cdot E \tag{7.12}$$

with N the number of activated pixels, Q the total charge, E the X-ray photon energy, and a_N and a_Q calibration factors, one can show the good linearity of the detector's response to various X-ray photon energies, see Fig. 7.25. Only, the data points recorded with set-up B, the manganese K_α line and the corresponding escape line, do not fit the linear behaviour. This is caused by the lab temperature being lower by approximately 5 to 10 °C[12] during this measurement compared to all other set-ups resulting in a different gas gain. Anyhow, both points can be brought to agreement with the straight line fit by using the same correction factor. In the calibration curve using the pixel information (Fig. 7.25(a)) also the data point for 8 keV deviates slightly from the straight line fit, this is caused by the chance for multiple primary electrons entering the same grid hole and being registered only as one active pixel rises with higher X-ray photon energy. In both fits the data points from set-up B have been excluded from the fit as well as the 8 keV data point in the calibration curve using the pixel information.

The good linearity demonstrated for the detector's response is important as later the energy calibration can be checked in situ with requiring only one data point. Taking a closer look at the energy calibration

---

[12] The CDL's temperature monitoring and logging system was not available at the time of this campaign.

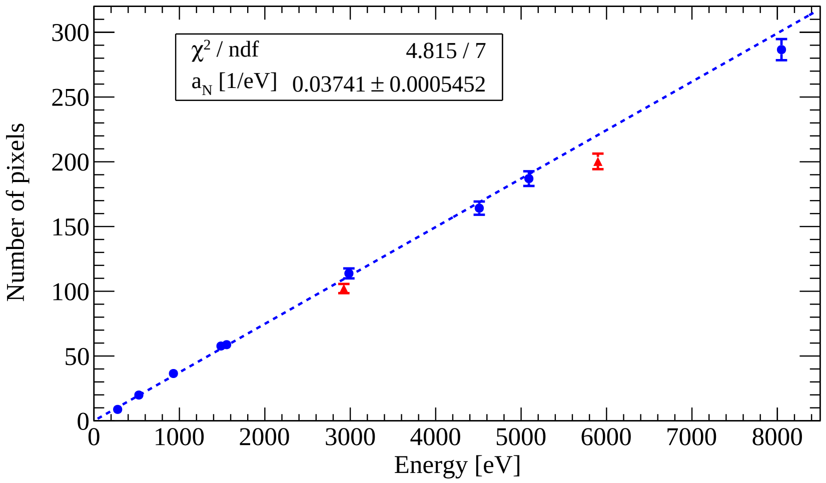

(a)

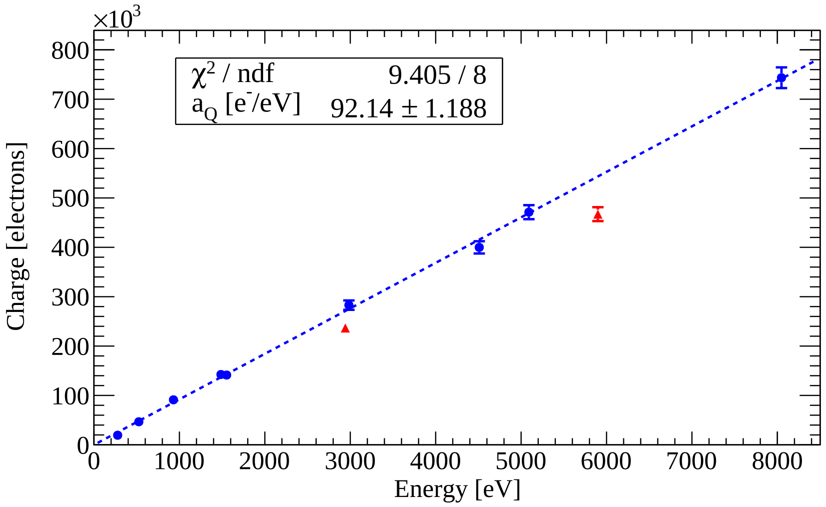

(b)

Figure 7.25: Energy calibration of the InGrid based X-ray detector using the pixel information (a) or the charge information (b). To both calibration curves a straight line of form $y = a \cdot x$ has been fitted to obtain the calibration factors a_N and a_Q (see equations 7.11 and 7.12). In both calibration curves the data points from set-up B (manganese K_α line and corresponding escape line, shown as red triangles) deviate from the rest, this is explained by a different room temperature in the CDL at the time of these measurements, altering the gas gain. These points have therefore been excluded from the fit. For higher X-ray energies the probability of more than one primary electron entering the same grid hole increases, resulting in decrease of the observed number of activated pixels, in (a) this can be observed with the 8 keV point being lower than expected from the straight line fit. This point has therefore also been excluded from the fit in (a). Published in [114].

factors a_N and a_Q: a_N gives the number of activated pixels per energy which should be the number of primary electrons created per energy through ionization or the inverse of the mean ionization energy W_I, of course assuming the gas gain of the GridPix to be high enough to result in a high single electron efficiency. For an argon isobutane mixture W_I is 26 eV [72]. Taking a_N from the fit, one gets

$$a_N^{-1} = (26.7 \pm 0.4)\,\mathrm{eV} \approx W_\mathrm{I} \tag{7.13}$$

confirming the assumed high single electron efficiency of the GridPix at the applied grid voltage. As a_Q gives the amount of charge detected per energy, together with a_N one can estimate the gas gain

$$G_a = \frac{a_Q}{a_N} = 2\,460 \pm 50 \tag{7.14}$$

confirming the working point. The gas gain can be also measured by looking at the charge collected per pixel, assuming one primary electron per grid hole and pixel a histogram of the charge per pixel should roughly follow a Pólya distribution. In Fig. 7.26 the charge per pixel is shown for two different X-ray photon energies, 1.5 keV and 8 keV where the latter is split in two histograms: one for all pixels within a radius of 1 mm around the reconstructed cluster centre and one with all pixels at least 1.75 mm away from the reconstructed centre. While the curve for 1.5 keV photons and the pixels from the rim of 8 keV clusters agree well, the pixels from the core of the 8 keV clusters result in a broader distribution with higher mean and most probable value (MPV). This is caused by the afore mentioned effect also leading to a deviation of the 8 keV data point in the calibration curve using the pixel information: For higher energy clusters it is more likely for multiple electrons to enter the same grid hole, especially in the cluster's core due to the Gaussian distribution of primary electrons inflicted by diffusion. In general three different measures for the gas gain can be obtained from the distributions in Fig. 7.26: The mean gas gain G_mean, the most probable gas gain G_MPV and, from fitting a Pólya distribution as described in equation 5.54 to the data and obtaining $G_\mathrm{Pólya}$. Only G_mean can be directly compared to the estimated gas gain G_a and taking the numbers shown in Fig. 7.26 also confirms the gas gain to be roughly 2 500.

In addition to the energy calibration curves also the energy resolution σ_E/E as function of energy can be obtained from the fits to the spectra. For both, the pixel as well as the charge representation the measured energy resolution are plotted in Fig. 7.27 as function of energy. As expected both datasets can be described by functions of form

$$\frac{\sigma_E}{E} = \sqrt{\frac{a^2}{E} + b^2} \tag{7.15}$$

where $a/\sqrt{E}$ describes the statistical contribution to the energy resolution and b a systematical contribution. A few deviations can be observed in the plot, especially at low energies, which stem from the fact, that e.g. for set-ups F and G it was not possible to accurately fit a function to the main peak as it was either fused with the Bremsstrahlungs background or with other lines from target contaminations which could not be clearly identified or fitted. Also, the Fano factor enters in the energy resolution and is known to be energy dependent. Thus, the energy resolution follows roughly the expected behaviour and is better than 10 % for energies above 2 keV and still better than 15 % for energies above 1 keV using the pixel information. When using the charge instead of the pixel information the numbers change to 15 % and 20 % respectively. Taking a look at the values obtained from the carbon K_α peak where an energy resolution of about 33 % using the pixel information is achieved (respectively about 43 % using the charge representation) it is clear that, especially for low X-ray energies, this relative quantity has to be regarded with suspicion as it is lightly misleading indicating rather bad energy resolutions in this range

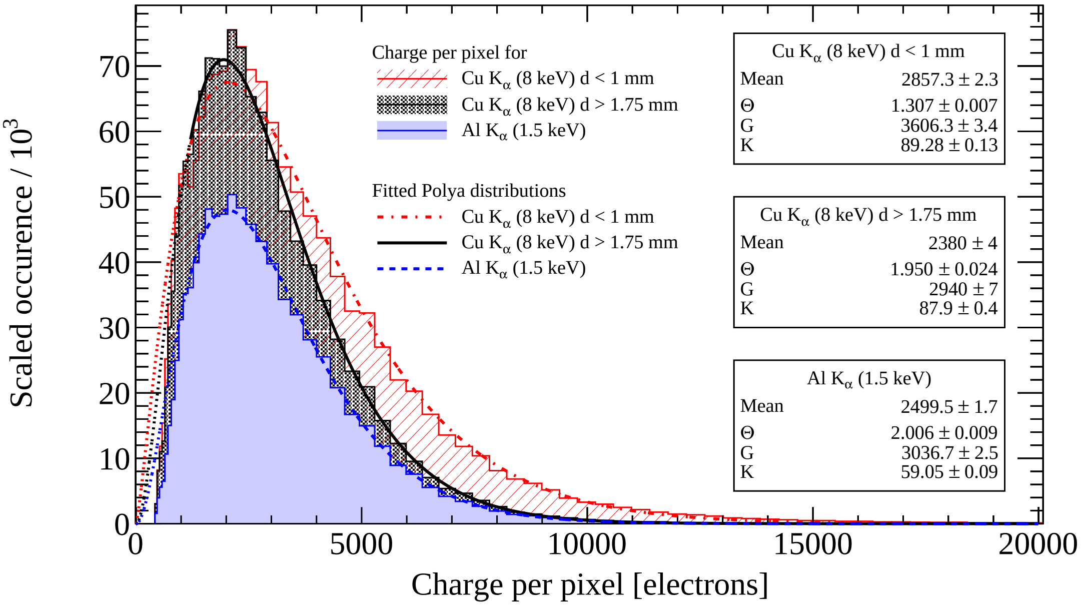

Figure 7.26: Charge per pixel distributions for three different data selections: all pixels from clusters of the 1.5 keV dataset (aluminium K_α line), pixels from clusters of the 8 keV dataset (copper K_α line), the latter split into those pixels with at least 1.75 mm distance to the cluster's centre and those with less than 1 mm distance. To each distribution a parametrization of the Pólya distribution (see equation 5.54) has been fitted, the resulting fit parameters and the mean of the distributions are shown in the boxes on the right. It is clearly visible that for high X-ray energies the charge per pixel distribution is broadened for pixels close to the cluster's centre, most likely caused by some primary electrons entering the same grid hole. Published in [114].

but taking the absolute numbers for σ_E of roughly 90 eV and 120 eV respectively the energy resolution shows to be indeed quite good for a gaseous detector.

In addition to the characterization of the InGrid based X-ray detector the datasets recorded in CDL can be used as reference datasets for a background suppression method. The background suppression method described later in chapter 10 uses a likelihood method based on the distributions of a few selected eventshape variables extracted from these reference datasets. The eventshape variables should be especially sensitive to the typical shape of clusters originating from X-ray photons and also be independent of drift properties affected by external factors to allow easy use of the CDL datasets without the necessity to apply a correction. The three variables found to satisfy these requirements are:

- Eccentricity $\epsilon = \frac{\sigma_{\text{long}}}{\sigma_{\text{trans}}}$: A measure for the circularity of the cluster, by definition $\epsilon \geq 1$
- Length l divided by σ_{trans}
- Fraction $F_{1\sigma_{\text{trans}}}$ of pixels contained within a radius of σ_{trans} around the cluster's centre

where the two latter variables give a handle on how good the distribution of pixels within the cluster fits to a Gaussian distribution along long and short axis as expected for diffusion, l/σ_{trans} thereby focuses on the distribution along the long axis.

When taking a look at the distributions of the three event shape variables and their behaviour with energy one notices that the mean as well as the width of the distributions change. The dependence of the

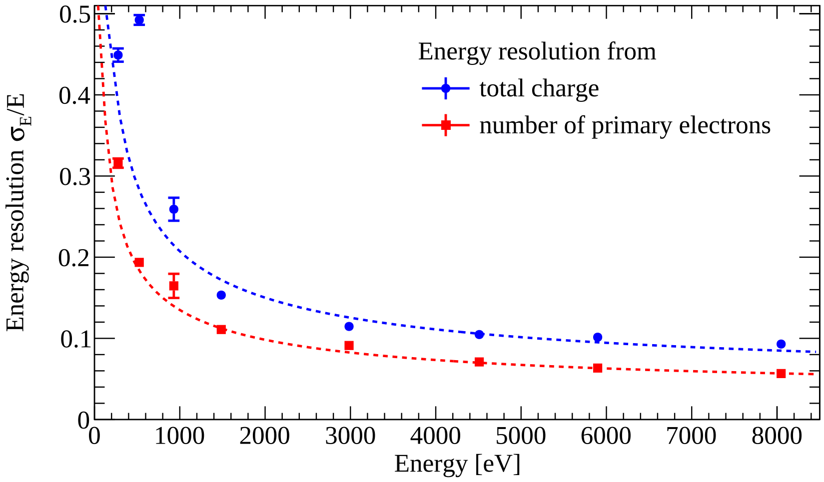

Figure 7.27: Energy resolution of the InGrid based X-ray detector, red squares show the energy resolution obtained using the pixel information while for the data shown as blue dots the charge information was used. The pixel information gives an estimate of the number of primary electrons created by the absorbed X-ray photon, as the charge information incorporates the fluctuations of the gas amplification process, the energy resolution using this information is slightly worse compared to when using the pixel information. The behaviour of both curves can be well described by a $1/\sqrt{E}$ dependence (dotted lines). The few points deviating from the anticipated behaviour stem from spectra where the main peak could not be clearly isolated or identified. Published in [114].

mean and width for the three variables on energy is shown in Fig. 7.28 together with the distribution of each variable at 1.5 keV for illustration (the distributions for all eight energies can be found in appendix C). To select only clusters with the desired energy, in addition to the cuts from Table B.1 if necessary, the main peak has been selected from the charge spectra by narrowing the charge range to exclude e.g. the escape lines from the reference datasets. The applied cuts on the charge for each dataset are listed in Table C.1 in appendix C.

To check if the behaviour of the energy dependence of these three variables is as expected, a simple simulation was carried out. Starting from a single point at the top of the drift distance a number of electrons is distributed according to a two dimensional Gaussian distribution using the width from equation 7.7 taking into account the transverse diffusion constant simulated with `Magboltz`. Then the positions of the simulated electrons are matched to the Timepix ASIC's pixel grid taking into account the finite pixel pitch. The number of electrons at the starting point is varied from 10 to 300 in steps of 10. For each number of electrons the simulation is carried out 10 000 times and each artificial frame is passed through the same reconstruction chain as the real data. By applying the energy calibration from equation 7.11 an energy is assigned to the simulated datasets. The results of this fairly simple simulation are shown in Fig. 7.28(b), 7.28(d) and 7.28(f) as dotted lines illustrating that the energy dependence of mean and width of the distributions of the three event shape variables is well recreated considering that neither the length of the initial photoelectron track or the different drift distances are taken into account. Especially the latter indicates that indeed the three event shape variables are sufficiently independent of drift and diffusion properties.

For all three event shape variables the width of the distribution decreases with X-ray photon energy, this is easily understood, as with higher energy the number of primary electrons, and therefore the number of activated pixels, increases, thereby reducing the impact of single outliers in the distribution of pixels due to the statistical nature of the diffusion process.

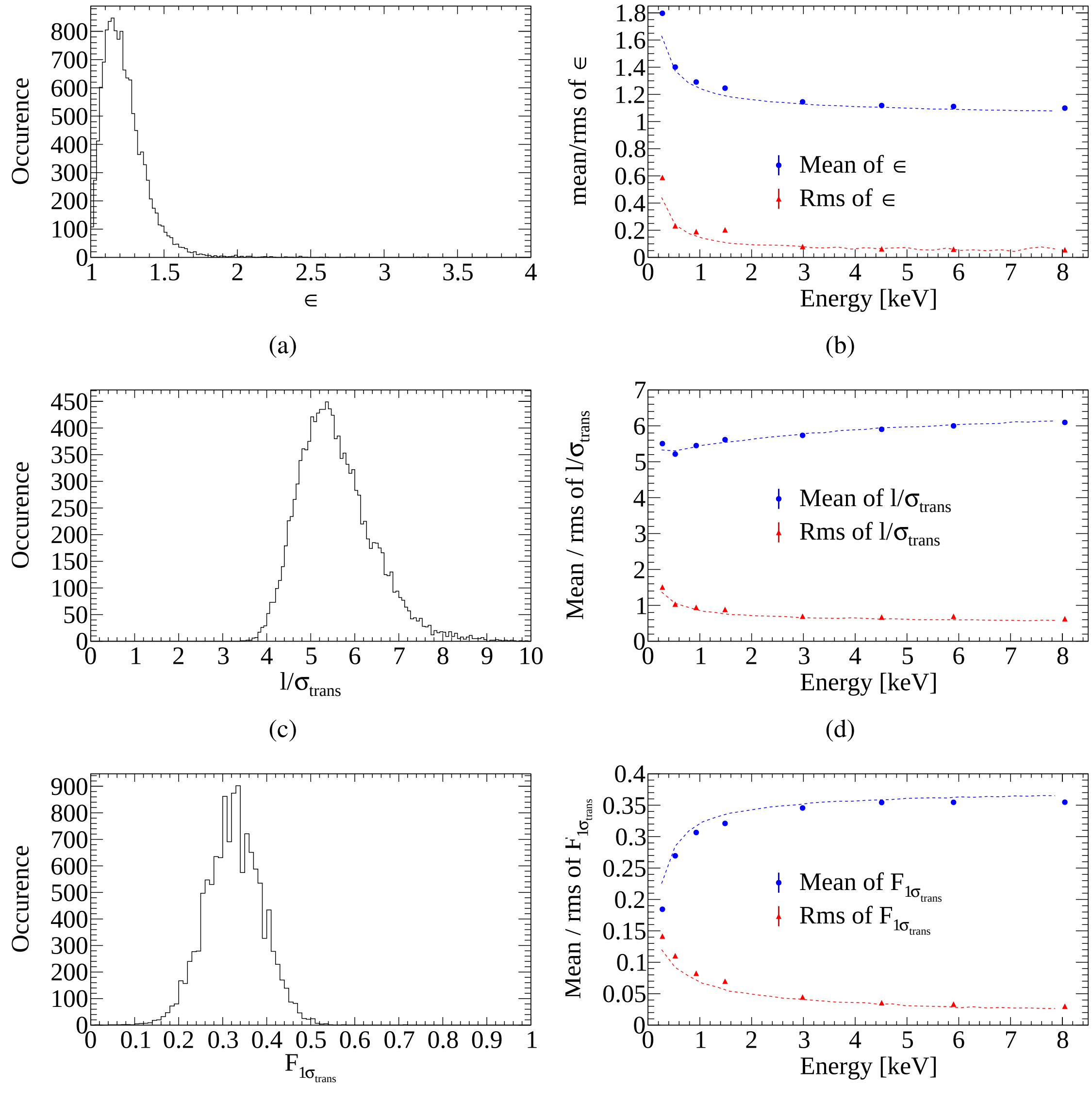

(a) (b)

(c) (d)

(e) (f)

Figure 7.28: Energy dependence of event shape variables eccentricity ϵ, (a) and (b), l/σ_{trans}, (c) and (d), and fraction $F_{1\sigma_{\text{trans}}}$, (e) and (f). On the left side, as example, the ϵ, l/σ_{trans} and $F_{1\sigma_{\text{trans}}}$ distributions are shown for an X-ray energy of 1.5 keV, on the right side the energy dependence of the distributions, characterized by their mean and width, are illustrated. The results of a simple simulation (described in the text) are plotted as dashed lines in (b), (d) and (f). Published in [114].

For the eccentricity ϵ the mean approaches a value slightly larger than one for rising X-ray energies. A value larger one is reached because, especially for high X-ray energies, the length of the initial photoelectron track causes a deviation from the circular shape. For low energies outliers in the distribution of pixels affect the choice of long and short axis resulting in larger values for ϵ. Length l divided by σ_{trans} approaches a value of about six starting at around five for the minimal energy shown, this indicates that, as assumed before, the cluster's pixels are contained within a radius of $3 \cdot \sigma_{\text{trans}}$. Due to the Gaussian nature of the pixels' distribution the probability for actually finding an active pixel in the outer tails of the distribution increases with the number of pixels per cluster, giving a lower mean l/σ_{trans} for low X-ray energies. The fraction $F_{1\sigma_{\text{trans}}}$ approaches a values around 35 % starting at about 20 % for low energy X-ray photons, for these outlying pixels may affect the calculation of the cluster's centre position which is pulled away from the actual centre resulting in a lower fraction $F_{1\sigma_{\text{trans}}}$.

Additionally, other event shape variables can be checked for their energy dependence and agreement with the simple simulation described before. Here, two of the central statistical momenta, the skewness S_{long} and the excess kurtosis K_{long} along the long axis are chosen. These properties are defined as

$$S_{\text{long}} = \frac{1}{n} \sum_{i=0}^{n} \frac{(x_i - \mu_x)^3}{\sigma_{\text{long}}^3} \tag{7.16}$$

$$K_{\text{long}} = \left(\frac{1}{n} \sum_{i=0}^{n} \frac{(x_i - \mu_x)^4}{\sigma_{\text{long}}^4} \right) - 3 \tag{7.17}$$

with n the number of pixels in a cluster, x_i the pixels' positions on the long axis, μ_x the mean position on the long axis and σ_{long} the width (second statistical moment) along the long axis. The excess kurtosis K_{long} is defined in a way so a Gaussian distribution gives a value of zero. The distributions of S_{long} and K_{long} for an X-ray photon energy of 1.5 keV are shown in Fig. 7.29 along with the energy dependence of their width and mean. Again, the results from the afore described simple simulation are shown as dotted lines in Fig. 7.29(b) and 7.29(d). The mean skewness is roughly zero independent of the X-ray energy indicating a fair symmetry of the cluster around its centre. For high X-ray energies the excess kurtosis approaches a value of about 0 as expected for the Gaussian distribution imprinted by the diffusion process. For low energies the clusters appear to be flatter compared to a Gaussian distribution, this is caused by single outlying pixels strongly impacting the choice of the long axis and thus resulting in a stretch of the distribution along this axis.

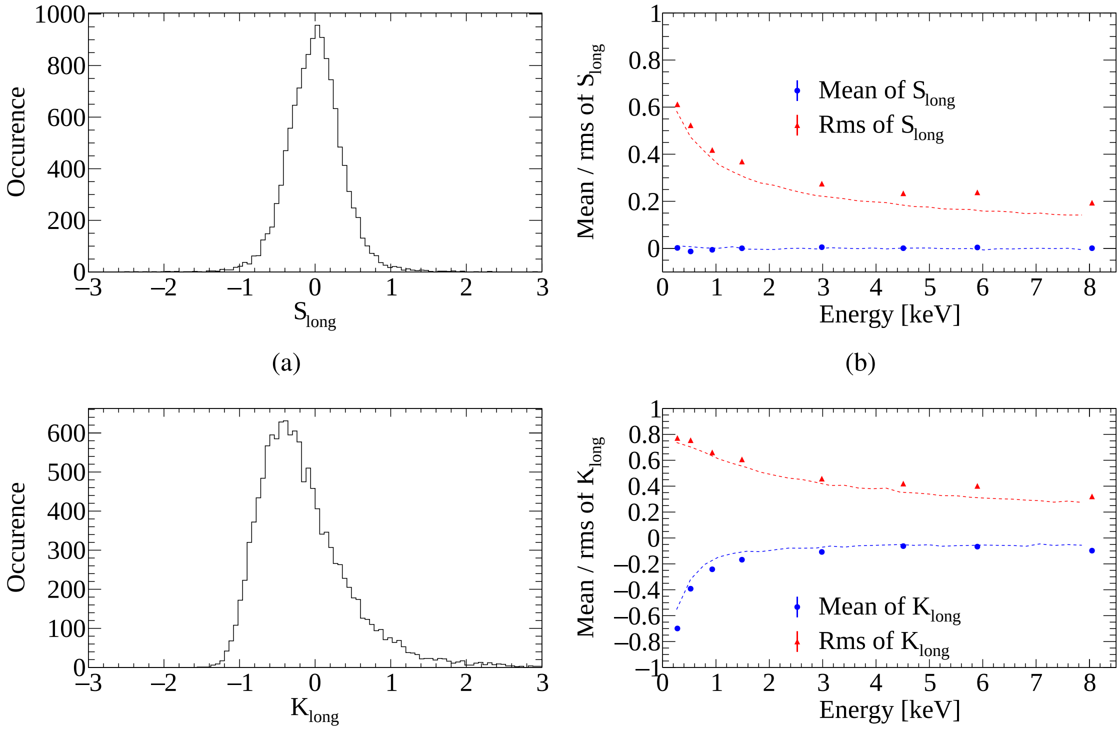

(a) (b)

(c) (d)

Figure 7.29: Energy dependence of skewness S_{long}, (a) and (b), and excess kurtosis K_{long} distributions, (c) and (d). On the left side, as example, the skewness and kurtosis distributions are shown for an X-ray energy of 1.5 keV, on the right side the energy dependence of the distributions, characterized by their mean and width, are illustrated. The results of a simple simulation (described in the text) are plotted as dashed lines in (b) and (d). Published in [114].

CHAPTER 8

Commissioning behind the MPE X-ray telescope of CAST

To prepare for the data taking, prior to searching solar chameleons with the CERN Axion Solar Telescope (CAST), the InGrid based X-ray detector was installed at the detector station VT4 to use the MPE X-ray telescope (XRT) which is installed there. In this chapter at first the detector station VT4 will be described introducing the sunrise platform of CAST as well as the MPE XRT and its vacuum system as all three define the environment in which the detector had to be installed.

Furthermore, details will be given on the infrastructure required to commission the InGrid based X-ray detector behind the MPE XRT on the sunrise platform. The required infrastructure splits in three main groups: the detector infrastructure, the interface vacuum system necessary to safely connect the detector to the MPE XRT and its vacuum system and the lead shielding for shielding the detector from environmental backgrounds.

At last, the commissioning procedure itself, carried out in October 2014, will be described focusing on the main steps. These include installation and start up of the interface vacuum system and the laser guided alignment of the detector mount to the focal spot and plane of the XRT prior to mounting the detector itself. Followed by the installation of the lead shielding after the detector's correct functioning had been verified. Additionally, a movable calibration source was installed later in April 2015 prior to the 2015 data taking campaign of CAST to complete the set-up and add the possibility of in situ calibration of the detector.

8.1 Detector station VT4

The four detector stations of CAST (see also chapter 4) are named VT1 through VT4 following the naming of the four gate valves limiting the two coldbores of CAST's magnet. While VT1 and VT2 are located on the sunset side of the experiment, VT3 and VT4 are on the sunrise side where a roughly 2 m long platform extends the structure supporting the magnet, the sunrise platform. The length of this platform allows for using an X-ray focusing device, like the MPE XRT, with a focal length in the order of a meter, due to space restraints this is not possible on the sunset side.

The MPE XRT is located on the sunrise platform and connected to detector station VT4 since the beginning of CAST in 2003 [54]. Until 2013 the pnCCD detector was mounted in a vacuum vessel behind the MPE XRT [54], after its dismantling, during a period where the MPE XRT was recalibrated at the PANTER X-ray test facility, a small silicon drift detector (SDD), built from commercially available off-the-shelf components was mounted at detector station VT4 and performed the first chameleon search conducted at CAST [42] in 2013. In 2014 the SDD was replaced by the InGrid based X-ray detector making use of the returned MPE XRT continuing the chameleon search at CAST with increased sensitivity during the data taking period 2014 and 2015.

8.1.1 The sunrise platform of CAST

The sunrise platform of CAST hosts the detectors, and their infrastructure. It was originally built and installed to hold the table on which the MPE XRT and its vacuum system are mounted. Also, the sunrise Micro-Mesh Gaseous Structure (MicroMegas) detector mounted behind VT3 is attached to the sunrise platform. In 2014 the sunrise MicroMegas detector was equipped with a custom XRT [59] specifically designed and manufactured for this detector, hence this XRT was made at the Lawrence Livermore National Laboratory (LLNL) in the USA, it is called the LLNL XRT. The sunrise MicroMegas detector and the LLNL XRT are part of an early pathfinder project for a possible CAST successor, the International Axion Observatory (IAXO) [24]. A computer-aided design (CAD) drawing of the sunrise platform with in addition to the MPE XRT, the LLNL XRT and the sunrise MicroMegas detector mounted, can be found in Fig. 8.1, illustrating the tight space constraints on the platform with two neighbouring XRTs and lines. The back end of the sunrise platform also presents a rather hard limit for all structures mounted on the platform, especially lead shielding and their containments or supports, which should not extend any further as else they might collide with the walls (or other structures) of the experimental hall while the magnet is moving during data taking.

8.1.2 The MPE X-ray telescope

The MPE XRT is a Wolter I type X-ray mirror optic with 1 600 mm focal length [54]. It is a spare module originally built for the A Broadband Imaging X-ray All-Sky Survey (ABRIXAS) satellite mission [54, 57, 58]. It consists of 27 nested shells with a maximum diameter of 163 mm (outermost shell) and a minimum diameter of 76 mm, a picture showing the nested mirror shells can be found in Fig. 8.2(a). The mirror shells are gold coated parabolic and hyperbolic nickel shells [57, 58] which are arranged con-focally, using X-ray reflection under grazing incident angle resulting in a focusing of the incoming X-rays, see Fig. 8.2(b) for illustration.

A spider-web like support structure with six arms holds the mirror shells and divides the XRT into six sectors as can be seen in Fig. 8.2(a), as the area of CAST's coldbore (diameter 43 mm) is much smaller compared to total diameter of the MPE XRT only one of the six sectors is used avoiding shadowing effects by the support structure [54]. For the chameleon search conducted with the InGrid based X-ray detector at CAST the MPE XRT is a key element as it allows to focus the X-ray photons stemming from converted chameleons onto the instrumented area of the GridPix ($14 \times 14\,\mathrm{mm}^2$), thus significantly increasing the signal to background ratio. The photon flux through the coldbore area ($14.5\,\mathrm{cm}^2$) to a spot of about $1\,\mathrm{cm}^2$ in the InGrid based X-ray detector, giving a chameleon image[1] of the Sun, for details see the calculations and simulations in chapter 11.

The transmission, or effective area, of the MPE XRT depends on the energy of the incoming X-ray photons and their off-axis angle [54, 56], highest throughput is, of course, achieved for X-ray beams parallel to the optical axis of the X-ray optic and for energies below 2 keV. The off-axis behavior is approximately linear but also depends on the X-ray photon energy [54, 56], e.g. for an energy of 1.5 keV the effective area, or transmission, at an off-axis angle of $10'$ is reduced to about 62 % [56] compared to

---

[1] As chameleons are produced in the Sun's tachocline region and due to their assumed emission characteristics the Sun is not a pointlike but an extended chameleon source, thus giving a rather large chameleon image of the Sun compared to e.g. an axion image of the Sun when using an X-ray optic as the MPE XRT.

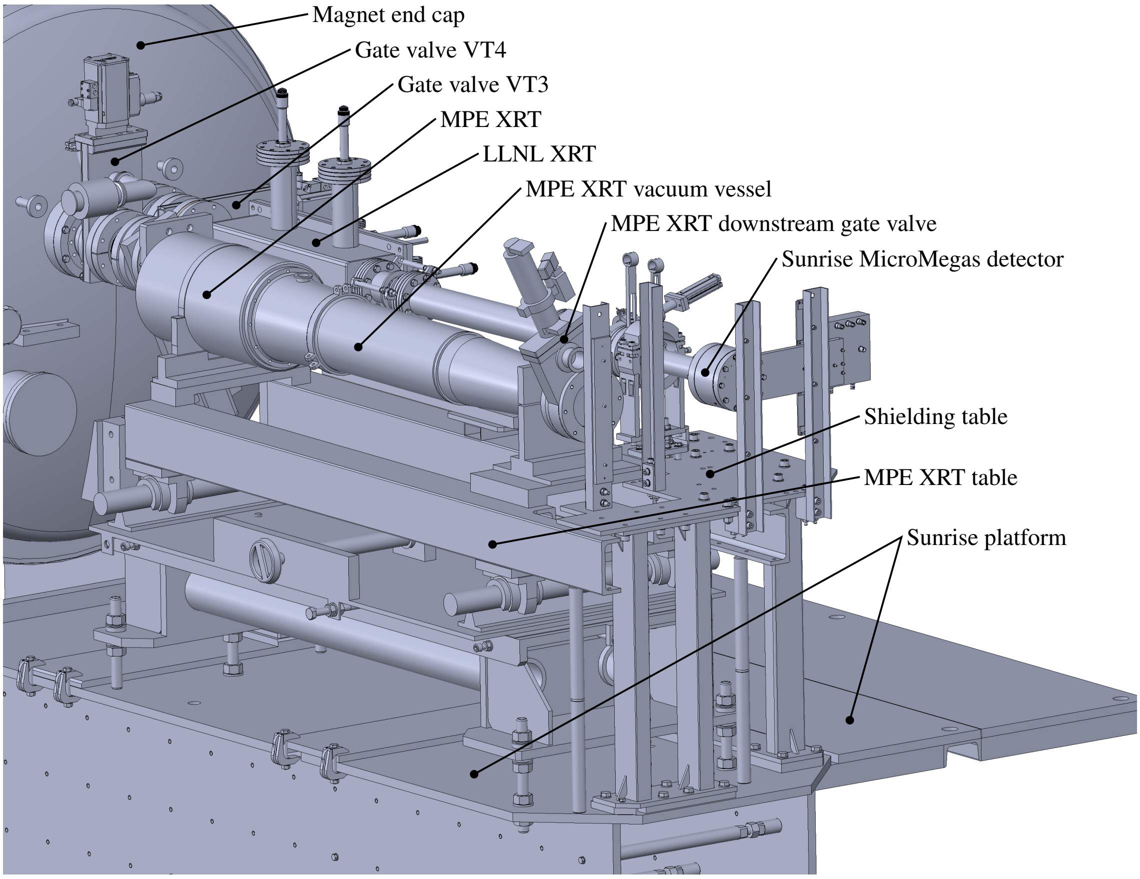

Figure 8.1: CAD drawing of the sunrise platform of CAST with the MPE XRT, the LLNL XRT and the sunrise MicroMegas detector mounted. Important parts are labelled. Due to the two neighbouring XRTs and lines space constraints for any system to be installed behind the downstream gate valve of the MPE XRT, like the InGrid based X-ray detector, are rather tight, especially concerning the (shared) lead shielding for the two detectors, which is not displayed here. The back end (bottom middle) represents a hard limit for anything to be installed on the platform as structures extending further may collide with the wall or other structures of the experimental hall when the magnet is moving.

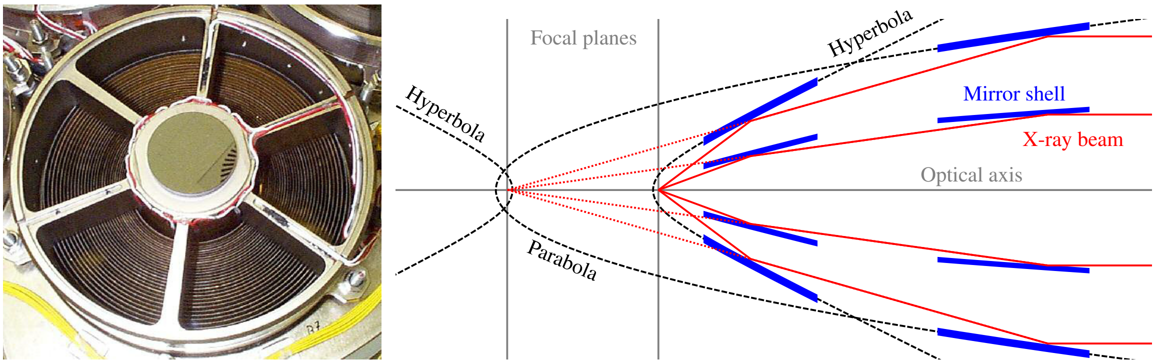

(a) (b)

Figure 8.2: Picture showing the mirror shells of an ABRIXAS X-ray optic (a) and sketch illustrating the working principle of a Wolter I type X-ray mirror optic (b). Parabolic shaped mirrors guide the incoming X-ray beams (parallel to the optical axis) towards a second mirror shell with hyperbolic shape focusing them into its focal point. The parabolic and hyperbolic mirror shells are arranged can-focally. The mirror shells are nested to achieve a focusing over the whole aperture of the optic (or at least a large fraction of it). Picture of the ABRIXAS X-ray optic has been taken from [54].

the on-axis value while for 8 keV X-ray photons it is reduced to roughly 12 % at $10'$ off-axis compared to the on-axis value. Details on the energy dependence of the effective area, taking into account the recalibration of the MPE XRT at the X-ray test facility PANTER in January 2014 [62], will be given in chapter 11 in the context of the calculation of the expected chameleon signal.

8.1.3 The vacuum system of the MPE X-ray telescope

The MPE XRT's mirror optic is housed in a large vacuum vessel (see also Fig. 8.1) enclosed by a downstream and an upstream gate valve. It is connected to one of the CAST coldbores via a short bellow between the gate valve VT4 and the upstream gate valve. Connected to the downstream gate valve was until 2013 a detector vessel housing the pnCCD detector which was replaced by the interface vacuum system, allowing to mount the InGrid based X-ray detector, in 2014.

The gate valve VT4 can only be opened if the vacuum pressure on both sides is better than 10^{-5} mbar. To pump the MPE XRT vacuum vessel, the detector vessel and the region between VT4 and the XRT's upstream gate valve a vacuum system controlled by a programmable logic controller (PLC) is used allowing (partial) remote operation. The schematic of this vacuum system is shown in Fig. 8.3, a picture of the system can be found in Fig. 8.4. Each of the three regions is pumped by a separate turbomolecular pump which share a common primary line which is pumped by a piston pump backed by an additional membrane pump. Several electropneumatic valves allow to separate the different regions of the system and seven pressure gauges are used for monitoring. Each region defined by the valves can be vented individually via password protected valves, some of them are equipped with an additional, manually operated needle valve, to control the venting speed. The two gate valves `V14` (upstream) and `V13` (downstream) separate the three regions of the system, they should only be opened if the pressure on both of their sides is better than 10^{-5} mbar to avoid contamination of the XRT vacuum which could reduce reflectivity and thus performance of the highly reflective mirror surfaces.

When the vacuum system has been successfully pumped down and is running a safety interlock can be engaged. If active this interlock will trigger, when any of the turbomolecular pumps in the system fail, any of the three pressures `PTV1`, `PTV2` and `PTV3` rises above 5×10^{-5} mbar or any of the primary line

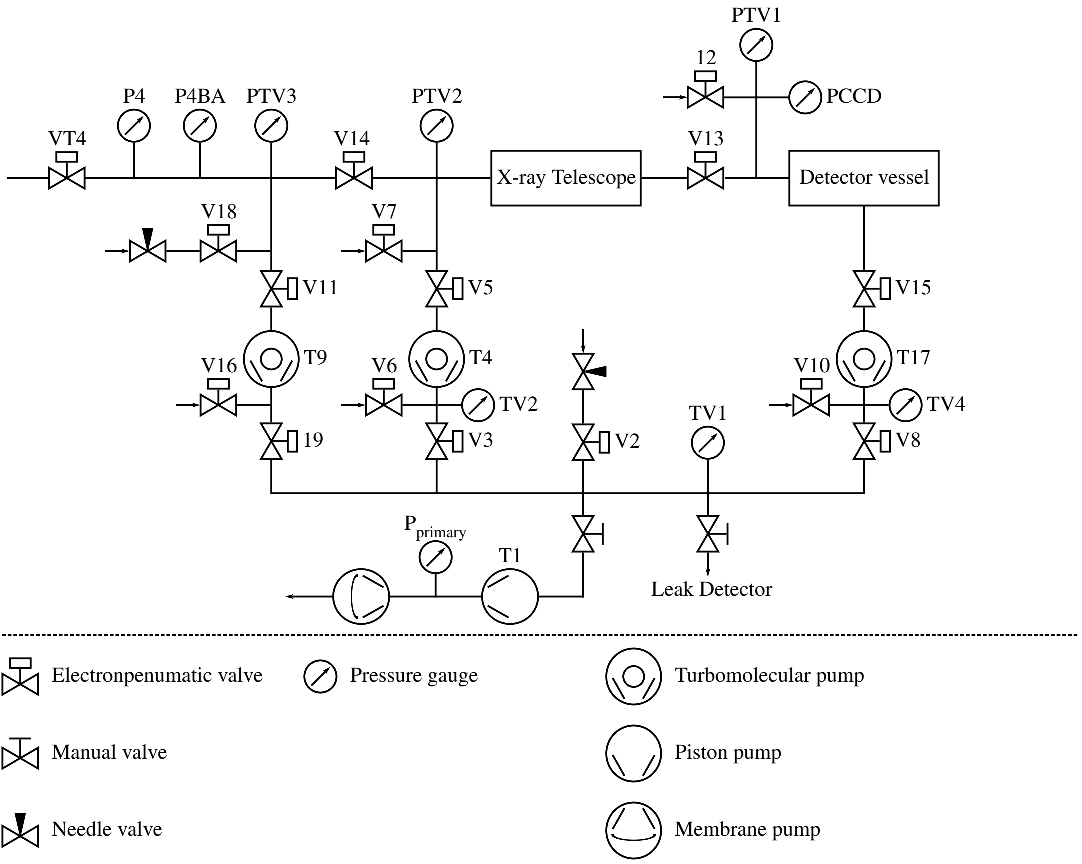

Figure 8.3: Schematic of the vacuum system of the MPE X-ray telescope. The system is divided into three regions which are separated by the valves `V14` and `V13`: the region between `VT4` and `V14`, the XRT and the detector vessel. `VT4` separates the XRT vacuum system from the general vacuum of CAST. Each region is pumped by its own turbomolecular pump and can be isolated and vented through a set of electropneumatic valves without affecting the rest of the system. Although each region features its own turbomolecular pump, they all share the same primary pump and line. A piston pump backed by an additional membrane pump provides the necessary primary vacuum.

pressures `TV1`, `TV2` and `TV4` rise above 5×10^{-2} mbar. When the safety interlock triggers all pumps are turned off and all valves, including especially the gate valves `V13` and `V14`, will be closed. The pressure of 10^{-2} mbar in the primary line is required as two of the turbomolecular pumps (`T4` and `T9`) are not equipped with a drag stage[2] and therefore require a lower backing pressure compared to modern types as `T17`. For this reason also, the backing of the main primary piston pump with a membrane pump is required to reach a primary pressure low enough. To avoid contamination of the system and especially the X-ray mirrors, only dry[3] pumps and gaskets are used throughout the system.

---

[2] Modern types of turbomolecular pumps are usually equipped with a so-called drag stage, helical channels on the walls surrounding the pump's rotor, which allow the turbomolecular pump to work with a backing pressure of a few mbar instead of a few 10^{-2} mbar.

[3] Dry in this context means that no oil or grease is used for (internal) sealing or in case of gaskets that those are not greased, which in general sets higher requirements to the sealing surfaces in terms of cleanliness and surface quality.

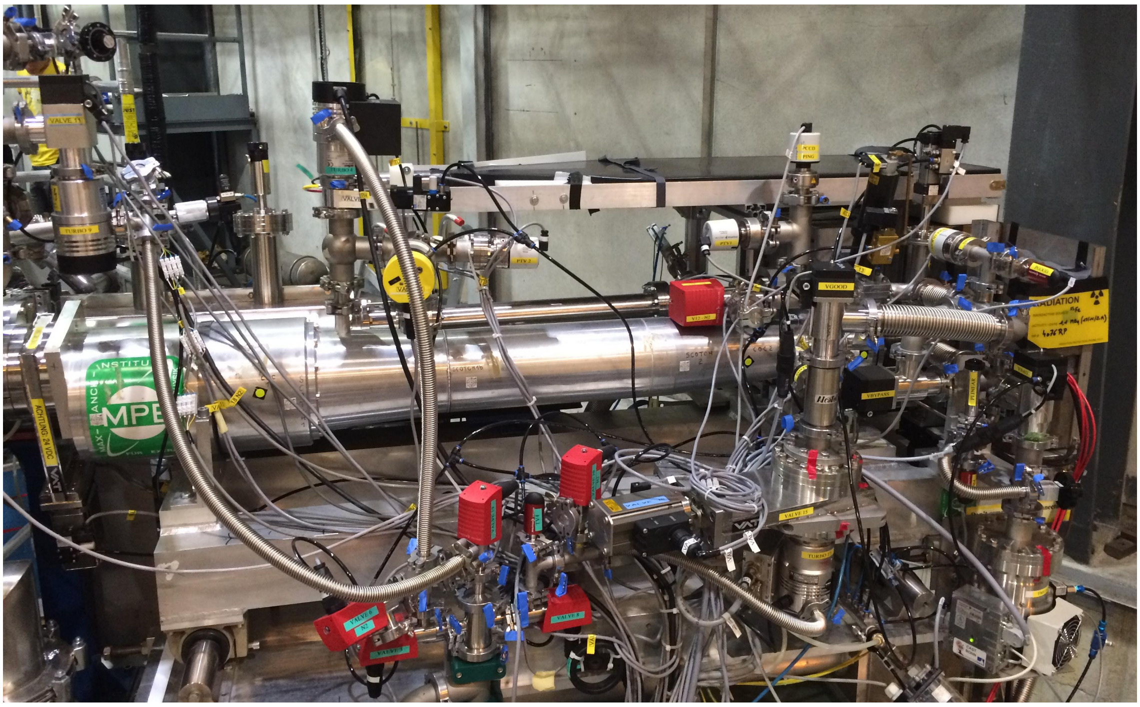

Figure 8.4: Picture showing the MPE XRT and its vacuum system on the sunrise platform. In the image center the vacuum vessel of the MPE XRT can be seen, the X-ray optic is housed in the part with the green sticker on it (middle right). In the upper part two of the turbomolecular pumps can be seen which are connected via the valves and manifolds (bottom) to the common primary line (not shown). In the right part of the image the former detector vessel has been replaced by the interface vacuum for the InGrid based X-ray detector.

8.2 Required infrastructure and interfacing systems

In order to mount the InGrid based X-ray detector behind the MPE XRT at CAST's detector station VT4 and to operate it, a set of infrastructure is required and had to be built and set up. In addition to an interface vacuum system, necessary to mechanically connect the InGrid based X-ray detector to the downstream gate valve of the MPE XRT vacuum vessel, the infrastructure for the detector itself is needed. The interface vacuum system not only connects the InGrid based X-ray detector to the MPE XRT but also allows for its alignment and pumps the region in front of the detector where a pressure of less than 10^{-5} mbar has to be reached in order to allow opening the gate valve towards the XRT. The infrastructure needed for the operation of the InGrid based X-ray detector, as already described in chapter 7, includes its readout system, power and gas supply. Parts of the infrastructure also require an interlock with the interface vacuum system to ensure a safe operation. Additionally, a lead shielding is required to suppress background induced by cosmic rays or environmental radiation. Due to space restraints the shielding was designed as a shared shielding for both detectors on the sunrise platform by the University of Zaragoza.

8.2.1 The interface vacuum system

The interface vacuum system which had to be designed and built for the operation of the InGrid based X-ray detector at CAST had to fulfil a set of requirements. On the mechanical side it has to position the detector in the focal plane which is in a distance of 301.2 mm from the flange surface of the downstream gate valve. To allow alignment of the detector, independent of the XRT, it had to incorporate an edge welded bellow and adjustable *xyz* linear stages with a precision of a few hundred micron. As the detector's cathode plate is at high voltage potential, an isolating adapter between detector and stainless steel vessel is necessary as well as a dedicated port for a movable radioactive source to allow for in situ calibration measurements. Everything had to be within the boundaries of the sunrise platform.

On the vacuum side the interface vacuum side must allow to reach a vacuum pressure of better than 10^{-5} mbar in the region between detector and downstream gate valve. To reach this pressure despite the gas permeation through the detector's thin X-ray entrance window, a differential pumping scheme was chosen to guarantee reaching the pressure required by the XRT. To ensure a safe operation, a set of safety interlocks had to be implemented to e.g. avoid accidental opening of a valve which could in the worst case result in damaging the MPE XRT, its vacuum system, the interface vacuum system itself or even the InGrid based X-ray detector. While the components (valves, gauges and a turbomolecular pump) formerly used to pump the detector vessel connected to the MPE XRT could be reused it was not possible to implement new components or extensions in the existing controls as the PLC's firmware is closed source and had to be treated as a black box. Therefore, the interface vacuum system had to have its own PLC based controls.

Schematics and functionality

The schematic of the complete system consisting of MPE XRT vacuum system and the interface vacuum system is shown in Fig. 8.5. The detector vessel (see Fig. 8.3) has been replaced by a vacuum vessel allowing to mount the InGrid based X-ray detector. This vessel is divided into a good and bad vacuum region by a thin differential window made from 0.9 µm Mylar®. Following the differential pumping scheme, both regions are connected via a normally open bypass valve $\mathtt{V}_{\mathtt{bypass}}$ and feature individual pumping lines including turbomolecular pumps (`T17` and `TMU261`). For the good vacuum region the pumping line of the former detector vessel is reused, only adding an additional valve ($\mathtt{V}_{\mathtt{good}}$) as well as pressure gauges to allow for controlling via the interface vacuum system. For the bad vacuum region a new pumping line is added: The turbomolecular pump `TMU261` connects to the common primary line via the valve $\mathtt{V}_{\mathtt{forevacuum}}$ and pumps the bad vacuum region through valve $\mathtt{V}_{\mathtt{bad}}$. A needle valve allows to bypass $\mathtt{V}_{\mathtt{bad}}$ when pumping or venting the system in a controlled way with a pressure gradient of about 1 mbar/s. This slow pumping/venting is used to protect both the differential window as well as the detector's X-ray entrance window. The bad vacuum region features also a linear pressure gauge which allows for monitoring the pressure (and pressure gradient) precisely during start-up or venting of the system to keep the pressure gradient stable at 1 mbar/s by manually adjusting the opening of the needle valve. All parts of the interface system which can be controlled or read out remotely are connected to a PLC which can be accessed from the slowcontrol computer inside CAST's control room.

On start-up all valves except for $\mathtt{V}_{\mathtt{bypass}}$ are closed, to start pumping the interface vacuum system, $V_{\text{forevacuum}}$ is opened, of course with the primary pumps of the MPE XRT vacuum system up and running. When the pressure $\mathtt{P}_{\mathtt{bad-forevacuum}}$ stabilizes below 1 mbar simultaneous pumping of the good and bad vacuum region is started through the needle valve, which is adjusted according to $\mathtt{P}_{\mathtt{linear}}$ to keep a pressure gradient of 1 mbar/s. When $\mathtt{P}_{\mathtt{linear}}$ reaches a few mbar the turbomolecular pump `TMU261` is started and spins up to full speed. After $\mathtt{P}_{\mathtt{bad}}$ goes below 5×10^{-2} mbar $\mathtt{V}_{\mathtt{bad}}$ is opened (and the needle valve closed) which increases the pumping speed significantly. To prepare for the individual pumping of good and bad vacuum regions $\mathtt{V}_{\mathtt{good}}$ is opened, connecting the good vacuum region to the pumping line incorporating `T17`[4]. As soon as both, $\mathtt{P}_{\mathtt{bad}}$ and $\mathtt{P}_{\mathtt{good}}$, measure pressures below 10^{-3} mbar, $\mathtt{V}_{\mathtt{bypass}}$ is

---

[4] Of course for this `T17` has to be up and running and `V15` has to be open, this is ensured by an interlock with $\mathtt{P}_{\mathtt{good-T17}}$.

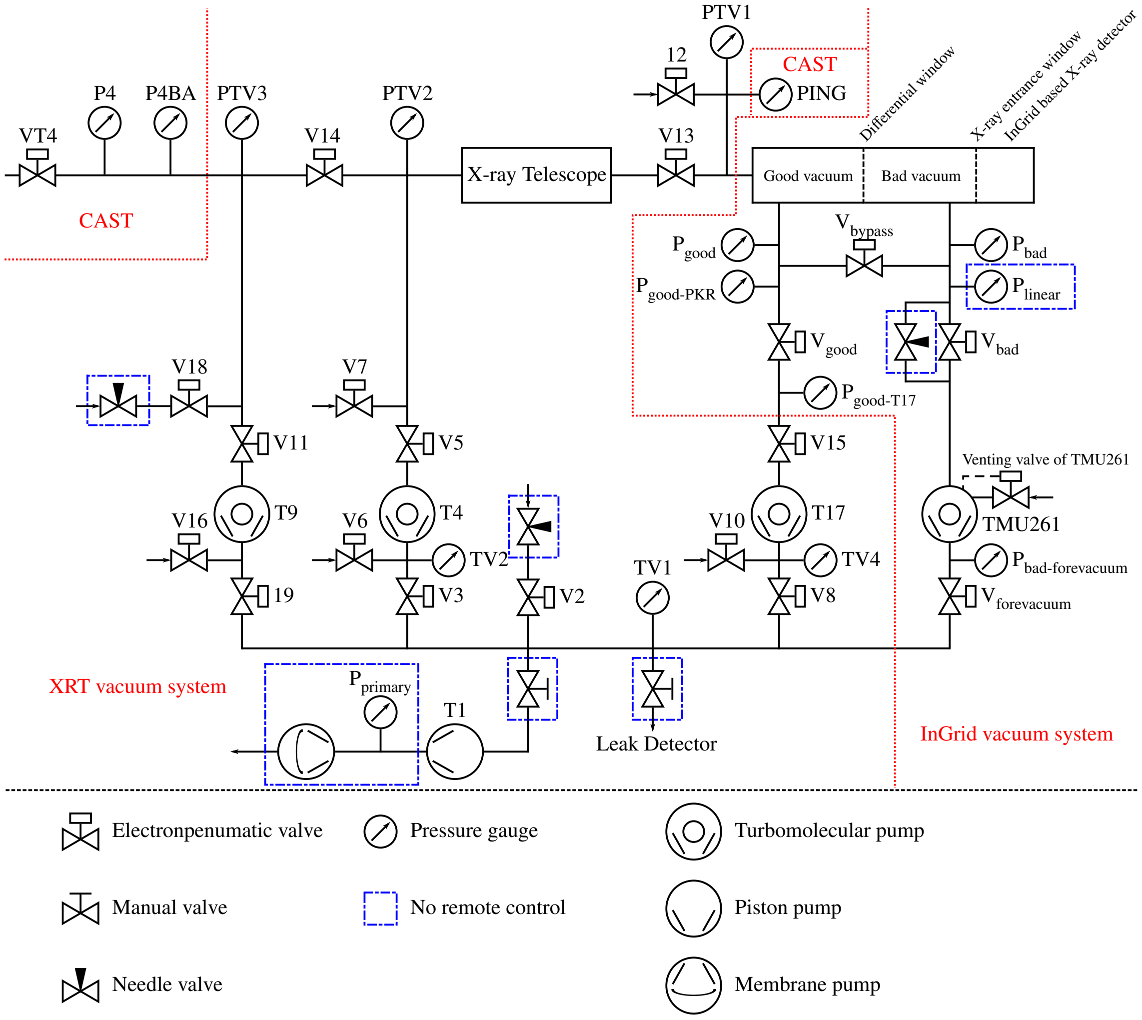

Figure 8.5: Schematic of the combined vacuum system of the X-ray telescope and the InGrid based X-ray detector. To allow for the use of a differential pumping scheme another turbomolecular pump and several valves and pressure gauges have been added to the original XRT vacuum system (see Fig. 8.3). Few parts of the system cannot be remotely controlled but have to be operated or read manually, these are marked with blue boxes. Although connected by pipes the newly added part of the system, the InGrid vacuum system, is not controlled by the XRT vacuum system but has its own PLC and control. Therefore special care has to be taken during operation of the combined system. Red lines and labels identify which part of the system is controlled by the XRT vacuum system, the InGrid vacuum system or the general CAST slowcontrol and interlock.

closed, separating the two vacuum regions. When `PTV1` (and `PTV2`) are below 10^{-5} mbar the downstream gate valve `V13` can be opened connecting the interface vacuum system to the MPE XRT.

Safety interlocks

To ensure a safe operation several safety interlocks have been implemented for the interface vacuum system which in addition to preventing accidental operation errors also secure the system in case of other failures and trigger a safe state to avoid damage to the systems, especially the InGrid based X-ray detector. The interlocks implemented for the interface vacuum system are:

- $\mathrm{V}_{\text{forevacuum}}$ can only be open if $\mathtt{P}_{\texttt{bad-forevacuum}}$ is below 1 mbar, this interlock can be temporarily bypassed for starting the pumping of the interface vacuum system
- `TMU261` can only be (turned) on if $\mathrm{V}_{\text{forevacuum}}$ is open, $\mathtt{P}_{\texttt{bad-forevacuum}}$ is below 1 mbar and either $\mathtt{V}_{\texttt{bad}}$ is closed or $\mathtt{P}_{\texttt{bad}}$ is below 5×10^{-2} mbar
- $\mathtt{V}_{\texttt{bad}}$ can only be open if `TMU261` is running at nominal speed, $\mathtt{P}_{\texttt{bad}}$ is below 5×10^{-2} mbar, $\mathrm{V}_{\text{forevacuum}}$ is open and $\mathtt{P}_{\texttt{bad-forevacuum}}$ is below 1 mbar; this interlock can be bypassed via a key switch
- $\mathtt{V}_{\texttt{good}}$ can only be open if $\mathtt{P}_{\texttt{bad}}$, $\mathtt{P}_{\texttt{good}}$ and $\mathtt{P}_{\texttt{good-T17}}$ are below 10^{-3} mbar, $\mathtt{V}_{\texttt{bad}}$ is open and `TMU261` is running at nominal speed; this interlock can be bypassed via a key switch
- $\mathtt{V}_{\texttt{bypass}}$ can only be closed if $\mathtt{V}_{\texttt{bad}}$ and $\mathtt{V}_{\texttt{good}}$ are open, $\mathtt{P}_{\texttt{bad}}$ and $\mathtt{P}_{\texttt{good}}$ are below 10^{-3} mbar and `TMU261` is running at nominal speed.

Mechanical implementation

CAD drawings of the mechanical implementation of the interface vacuum system can be seen in Fig. 8.6. A small xyz linear stage allows for alignment of the InGrid based X-ray detector with the MPE XRT. Flexible bellows (shown in blue) allow for a movement of the central vessel (to which the detector is mounted) without having to move other parts of the system. An adapter made of acrylic glass ensures electrical isolation of the stainless steel vessel from the detector, especially its cathode.

To allow for at least a few centimetres of lead shielding on the backside of the InGrid based X-ray detector the detector was moved towards the XRT so that the focal point is now 10 mm inside the detector.

8.2.2 The detector infrastructure

The infrastructure required for the operation of the InGrid based X-ray detector includes its readout system and power supply as well a high voltage power supply and a small gas system with pressure regulation. All this had to be installed close to the sunrise platform and is controlled from the control room of CAST via long network and Universal Serial Bus (USB) lines. Additionally, an ^{55}Fe source mounted to the tip of an electropneumatic linear feedthrough was mounted on the interface vacuum system allowing for in-situ calibrations of the detector.

Data acquisition system and detector power supply

The readout system based on the Xilinx® Virtex®-6 evaluation board (see chapter 7) was mounted on a frame which could be installed in a small 19" rack at the side of the sunrise platform in a distance

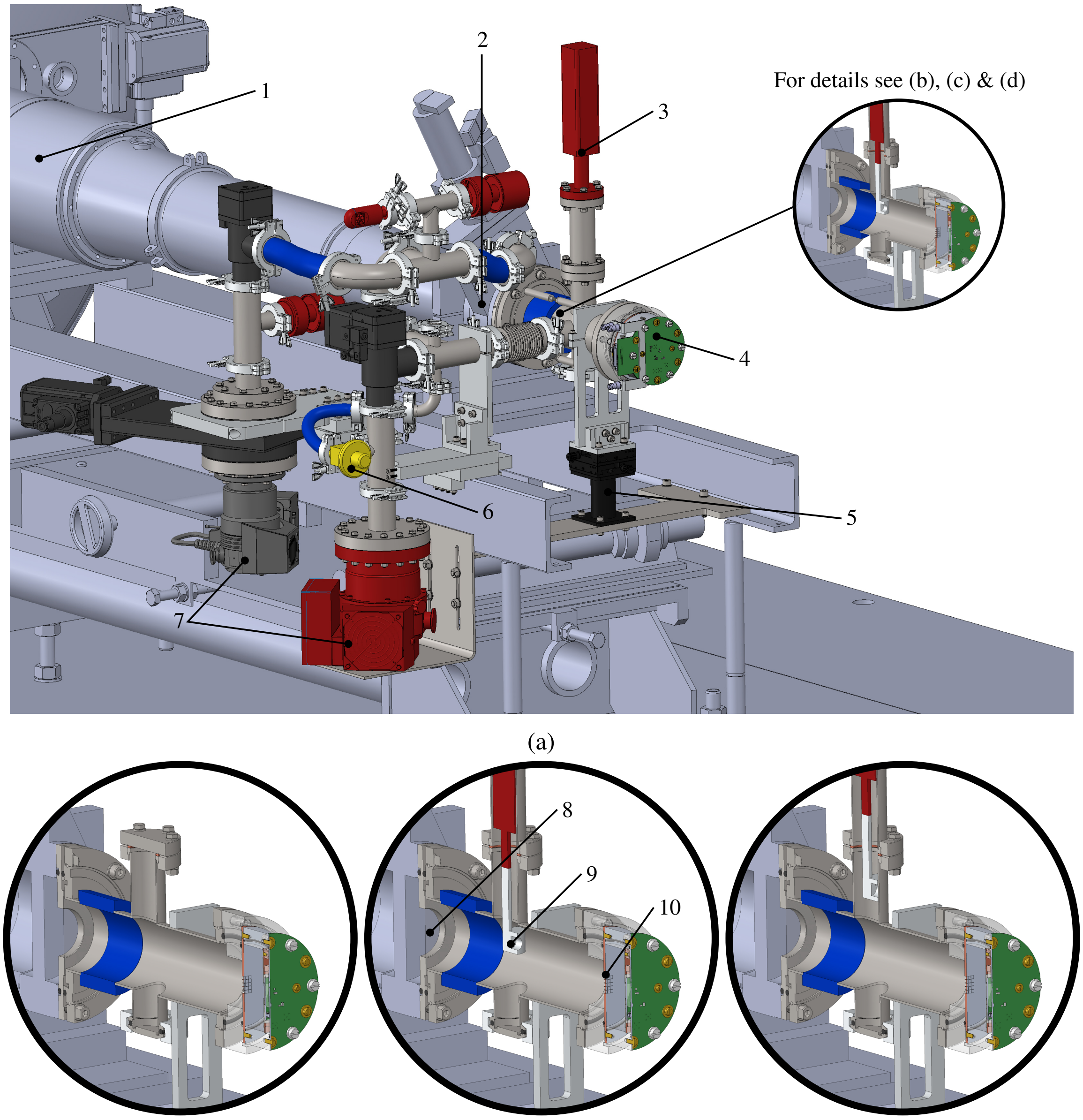

(a)

(b) (c) (d)

1	MPE X-ray telescope (XRT)
2	Downstream gate valve of MPE XRT
3	Electropneumatic linear feedthrough
4	InGrid based X-ray detector
5	*xyz* linear stage
6	Needle valve
7	Turbomolecular pumps
8	Differential window (0.9 µm Mylar®)
9	^{55}Fe source
10	X-ray entrance window

(e)

Figure 8.6: CAD drawing of the interface vacuum system for the InGrid based X-ray detector (a), main parts are labeled and explained in the legend which is shown in (e). Detailed cut views, (c) and (d), show the differential window, the position of the ^{55}Fe source used for calibrations and the detector's X-ray entrance window. While the radiocative source and its electropneumatic linear feedthrough were not available in 2014 the corresponding port was simply closed with a blind flange (b). When the radioactive source is not in use, it is pulled upwards where it is shielded by a stainless steel tube (d). The neighbouring sunrise MicroMegas beamline has been omitted for a better overview. Blue parts are flexible bellows.

close enough to the detector to not run into problems with the standard Very High Density Cable Interconnect (VHDCI) cable used. The power for the detector is provided by a stabilized laboratory power supply which could be installed on a counter weight below the actual sunrise platform. The readout board is connected via an ethernet cable to the readout computer, running Timepix Operation Software (TOS), in the CAST control room.

High voltage power supply

For the three high voltage channels required for the operation of the detector a small Versa Module Eurocard (VME) crate was installed in the small 19" rack at the side of the sunrise platform. This VME crate houses an Iseg VHS C040n high voltage module which is controlled from a slowcontrol computer in the control room via a USB connection. The high voltage module features a safety loop which was connected to the PLC controlling the interface vacuum system allowing to inhibit activation of the high voltage channels (or trigger immediate shut-down of all channels) by means of interlocks and from the slowcontrol computer.

Gas system with pressure regulation

A small gas system was set up for the operation of the InGrid based X-ray detector, its schematic can be found in Fig. 8.7. It resembles the schematic shown in Fig. 7.12 but in addition to the inlet pressure regulator and flow-meter with a needle valve more (electro)valves have been added. On the sunrise platform the InGrid based X-ray detector shares its input gas line with the sunrise MicroMegas detector mounted to detector station VT3, therefore the input line, providing the detector gas at a pressure of 1.45 bar(s) is split, valves allow to shut off the gas supply to one or both of the detectors.

The electrovalves $\mathtt{V}_{\mathtt{in}}$ and $\mathtt{V}_{\mathtt{out}}$ allow to isolate the InGrid based X-ray detector on its gas line, when $\mathtt{V}_{\mathtt{in}}$ is closed the input pressure may build up unto this valve, therefore an additional filling branch was added, bypassing $\mathtt{V}_{\mathtt{in}}$. The filling branch consists of another electrovalve $\mathtt{V}_{\mathtt{fill}}$ and a fine needle valve. To fill the detector $\mathtt{V}_{\mathtt{fill}}$ is opened and the flow limited by the needle valve allowing to gently increase the pressure inside the detector even if 1.45 bar(a) have been built up unto $\mathtt{V}_{\mathtt{in}}$ and $\mathtt{V}_{\mathtt{fill}}$. When the desired pressure inside the detector has been reached and the pressure regulation is active $\mathtt{V}_{\mathtt{in}}$ can be opened without the danger of a rapid inrush of gas causing a rapid pressure rise which the regulator cannot compensate for fast enough.

To prevent accidents and guarantee a safe operation, the electrovalves are also controlled by the PLC of the interface vacuum system allowing the implementation of safety interlocks and interlocking with the interface vacuum system. The safety interlocks are:

- $\mathtt{V}_{\mathtt{fill}}$ can be opened only if $\mathtt{V}_{\mathtt{out}}$ is open
- $\mathtt{V}_{\mathtt{in}}$ can be opened only if $\mathtt{V}_{\mathtt{out}}$ is open and $\mathtt{P}_{\mathtt{detector}}$ is within 20 mbar of its nominal value, typically 1 050 mbar.

As a drop of $\mathtt{P}_{\mathtt{detector}}$ might indicate a leak developing in the InGrid based X-ray detector's X-ray entrance window or even an imminent window burst, an interlock with the interface vacuum system was implemented. The same holds for a rise of $\mathtt{P}_{\mathtt{detector}}$, which, independent of its cause, could cause a window burst. Therefore, if active, the interlock between gas system and interface vacuum system will cause $\mathtt{V}_{\mathtt{in}}$, $\mathtt{V}_{\mathtt{out}}$ and $\mathtt{V}_{\mathtt{fill}}$ to close and a complete shut-down (safe state) of the interface vacuum system, if $\mathtt{P}_{\mathtt{detector}}$ deviates more than 20 mbar from its nominal value. Additionally, triggering of this interlock will also break the safety loop of the high voltage module, immediately shutting down all the high voltage channels in order to protect the GridPix in the detector.

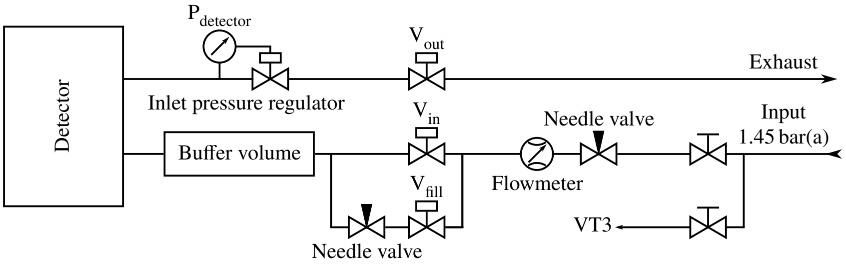

Figure 8.7: Schematic of the gas supply line for the InGrid based X-ray detector on the sunrise platform of CAST. The input line providing the gas at a pressure of about 1.45 bar(a) is shared with the sunrise MicroMegas detector connected to detector station VT3 on the same platform. In addition to the general set-up (see Fig. 7.12) electrovalves ($\texttt{V}_{\texttt{in}}$, $\texttt{V}_{\texttt{out}}$ and $\texttt{V}_{\texttt{fill}}$) and a separate filling branch have been added. The electrovalves allow to isolate the detector from the gas and the filling branch uses a fine needle valve for controlled flushing of the detector until the desired detector pressure is reached and the regulation by the inlet pressure regulator is active. This is especially important when the detector is isolated from the gas the input pressure can build up unto the valve $\texttt{V}_{\texttt{in}}$ which could cause a rapid pressure rise in the detector when opening $\texttt{V}_{\texttt{in}}$. The electrovalves are interlocked with each other and the detector pressure $\texttt{P}_{\texttt{detector}}$.

Movable radioactive calibration source

To allow for in situ calibrations of the InGrid based X-ray detector the movable calibration source of the pnCCD detector was reused. It is an electropneumatic linear feedthrough with an ^{55}Fe source mounted to its tip. It was mounted on the dedicated port on the interface vacuum system as can be seen from the CAD views in Fig. 8.6. When used, the source is held right in front of the detector while, when not used, the source is pulled upwards where it is shielded by a stainless steel tube. The electropneumatic feedthrough can be controlled remotely via the PLC of the interface vacuum system.

8.2.3 The shared lead shielding

As the mechanical and spatial constraints on the sunrise platform did not allow for separate lead shielding for both the InGrid based X-ray detector and the sunrise MicroMegas detector a shared shielding was designed and manufactured by the University of Zaragoza. The design of the shared shielding can be seen in the CAD views in Fig. 8.8. The lead shielding itself is built from lead bricks which are stacked in seven layers. The lead bricks rest on a common shielding platform, often called shielding table and are enclosed by steel plates stabilized with U-beams. This enclosure guarantees that the lead bricks do not move (or even fall off the platform) when the magnet is moving around or is tilted.

As can be seen from the cut views in Figs. 8.8(b) and 8.8(c), while on the left and right side of the InGrid based X-ray detector as well as below and above the detector it was possible to place 10 cm thick walls/layers, the front and backside of the detector are only shielded by 2.5 cm and 2 cm of lead respectively due to space restraints. In the left lead brick wall a small gap is left for the detector's cables and supplies (VHDCI cable, high voltage cables and gas tubes). The right lead brick wall is shared with the sunrise MicroMegas detector. The lead bricks used for the shielding of the InGrid based X-ray detector (not including the right lead brick wall) sum up to a weight of about 150 kg while the shielding of the sunrise MicroMegas detector sums up to about 500 kg, here a wall thickness of at least 10 cm to all sides could be ensured.

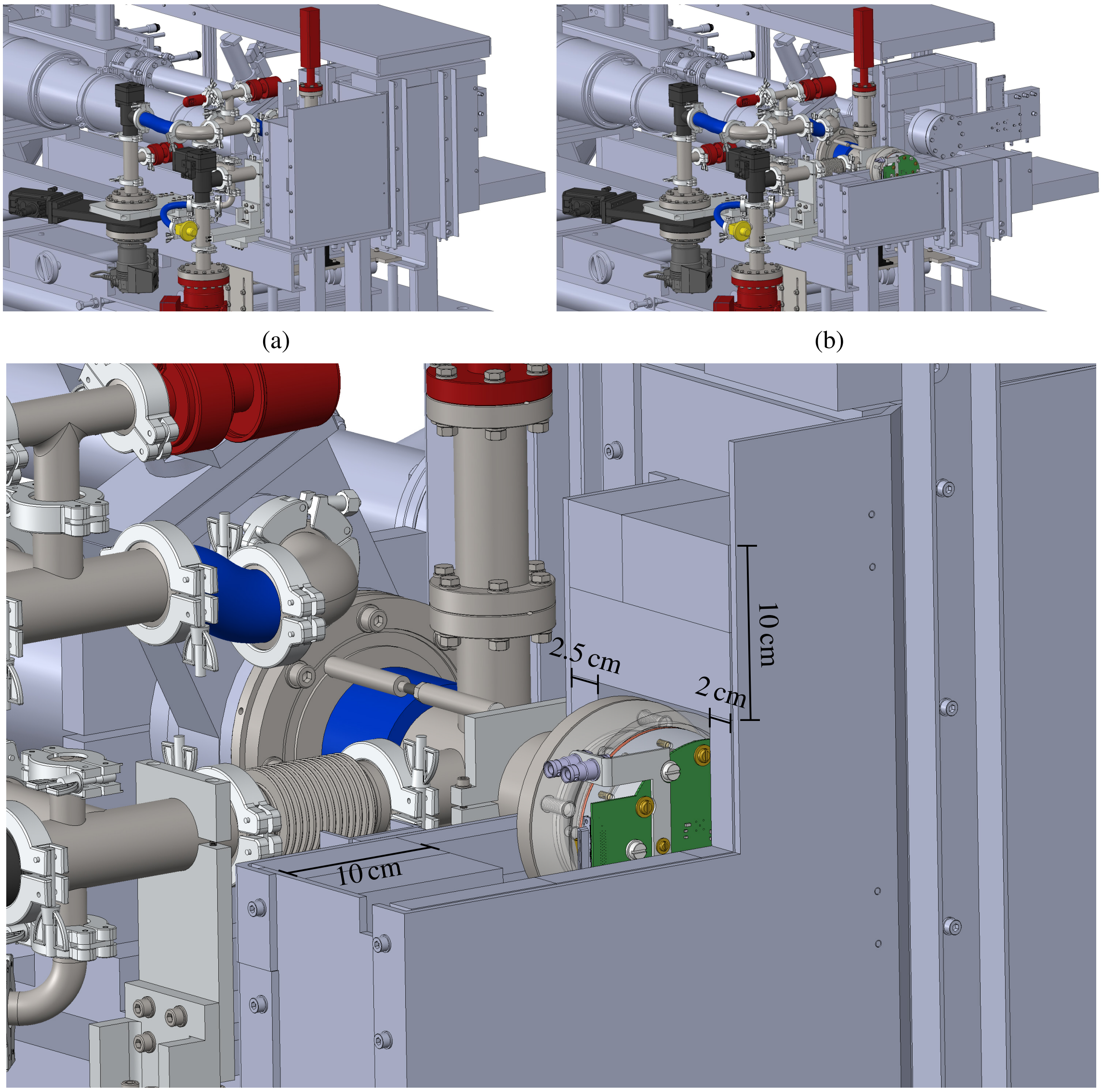

(a)

(b)

(c)

Figure 8.8: CAD drawings of the shared lead shielding. The lead shielding shared between the InGrid based X-ray detector and the sunrise MicroMegas detector is build from lead bricks and enclosed by a structure made from steel preventing any movement of the bricks when the magnet moves or is tilted. In (a) the complete and enclosed shielding is shown while in (b) a partial cut reveals the two detectors inside the shared shielding as well as the build up from lead bricks. In (c) a partial cut close-up only reveals the InGrid based X-ray detector and allows an insight into the structure of the lead shielding surrounding the detector, some measures of wall thickness are given for reference.

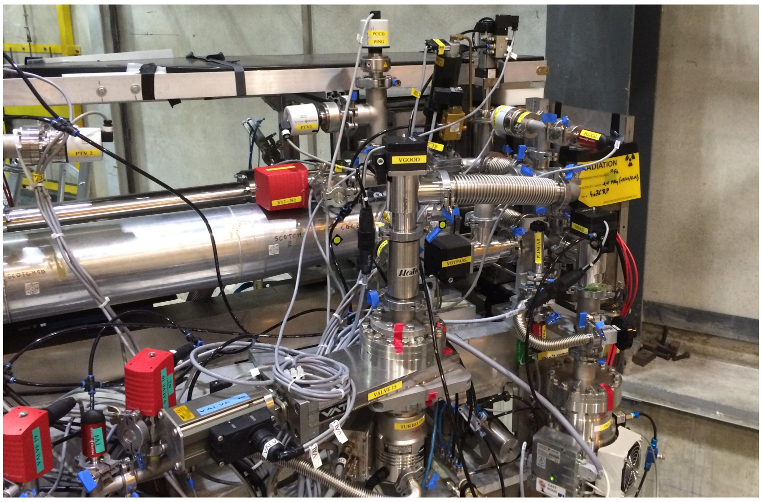

Figure 8.9: Picture showing the interface vacuum system mounted on the sunrise platform connecting the InGrid based X-ray detector to the MPE XRT and its vacuum system. In the lower right part of the image the two turbomolecular pumps used for the differential pumping scheme can be seen with the necessary electropneumatic valves above.

8.3 Installation & alignment of the detector in October 2014

In October 2014 the InGrid based X-ray detector was installed behind the MPE XRT on detector station VT4 on the sunrise platform of CAST to prepare for the data taking campaign 2014 and 2015 in order to search for solar chameleons. The installation started with mounting and commissioning of the interface vacuum system, followed by a laser alignment of the detector mount before, finally the detector was installed and started up. After ensuring proper functioning of the detector the shared lead shielding was mounted getting the whole set-up ready for data taking. The movable calibration source foreseen for in situ calibrations could however not be installed before 2015.

8.3.1 Commissioning of the interface vacuum system

The interface vacuum system was mounted at the downstream gate valve of the MPE XRT's vacuum system and connected to its common primary line and the turbomolecular pump of the former detector vessel was incorporated. After routing and connecting of all cables and start up of the PLC the system was tested with the detector being replaced by a blind flange. Fig. 8.9 shows a picture of the interface system installed on the sunrise platform. The detector mount was roughly adjusted to its anticipated position which later would be checked (and corrected) using the laser alignment.

To test the interface vacuum system, a normal pumping procedure was followed, just without a detector being mounted on the system, without any unforeseen issues the desired vacuum pressure of better than 10^{-5} mbar at the gauges `PTV1` and $\mathtt{P}_{\mathtt{good-PKR}}$ could be reached within less than two days. After several days of pumping a pressure of about 5×10^{-6} mbar was reached in the limit.

As final step in the commissioning of the interface vacuum system a standard vacuum leak test was performed. A leak tester is connected to the leak testing port of the combined vacuum system. The system is then pumped through the leak tester, the connection to the primary pumps of the system is closed via a valve. The leak tester is basically a turbomolecular pump with its own backing pump and a mass spectrometer in the backing line. The mass spectrometer is configured to give a signal if helium is

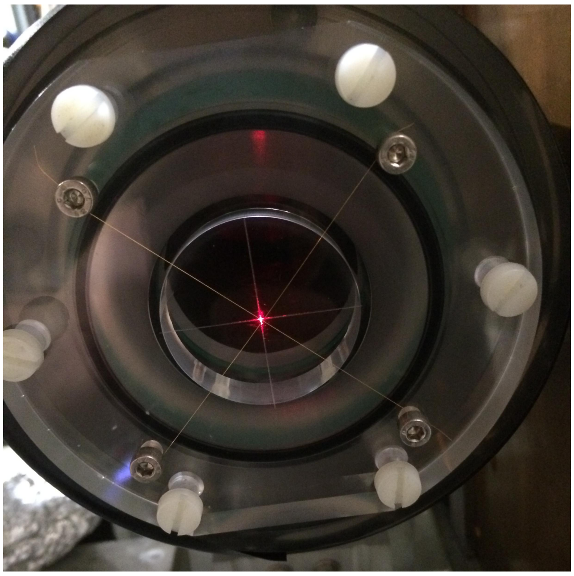

Figure 8.10: Laser spot on alignment target after successful alignment of the detector position with the MPE XRT. A laser beam aligned to the optical axis of the magnet's coldbore is sent in from the sunset side. The laser beam is focused by the MPE XRT to the focal point. For the alignment procedure the InGrid based X-ray detector is replaced by an alignment target made from acrylic glass featuring a cross-hair in the focal plane right in the centre (the cross wires were used for verification of the cross-hair position). After successful alignment of the detector mount the laser spot hits the centre of the cross-hair.

present in the gas stream. The actual leak test is performed by spraying small amounts of helium to joints, gaskets or other parts of the vacuum system. In case of a leak helium enters the system and is detected by the leak tester, the amount of helium detected (per time) gives a measure of the leak rate. Using this method a few minor leaks could be found which were caused by connections not being properly tightened, these could be fixed easily. At the end of the leak test, a leak rate in the range of a few 10^{-10} mbar l/s was reached with the whole system which is absolutely fine for the pressures which have to be reached and taking into account the many rubber seals in the system.

8.3.2 Laser alignment of the detector mount

For the laser alignment of the detector mount a laser beam aligned to the optical axis of the magnet's coldbore is sent in from the sunset side. The laser beam is focused by the X-ray mirror optic onto a point in the focal plane. To check if this laser spot coincides with the detector's centre a special alignment blind flange replaces the detector. The alignment flange is made from acrylic glass and has a polished surface at the nominal position of the focal plane (with respect to the detector mount). On this surface a cross-hair is engraved at the centre which can be additionally checked by the means of cross wires (see image in Fig. 8.10). For the laser alignment procedure the downstream gate valve of the MPE XRT needs to be opened, thus requiring the procedure to be done with the system under vacuum.

With the laser switched on the detector mount's position is adjusted via the xyz linear stages until the laser spot hits the cross-hair's centre. An image of the laser spot on the alignment flange after successful alignment of the detector mount can be found in Fig. 8.10. When the alignment procedure is finished the xyz linear stages are locked to keep the position when replacing the alignment flange with the InGrid based X-ray detector.

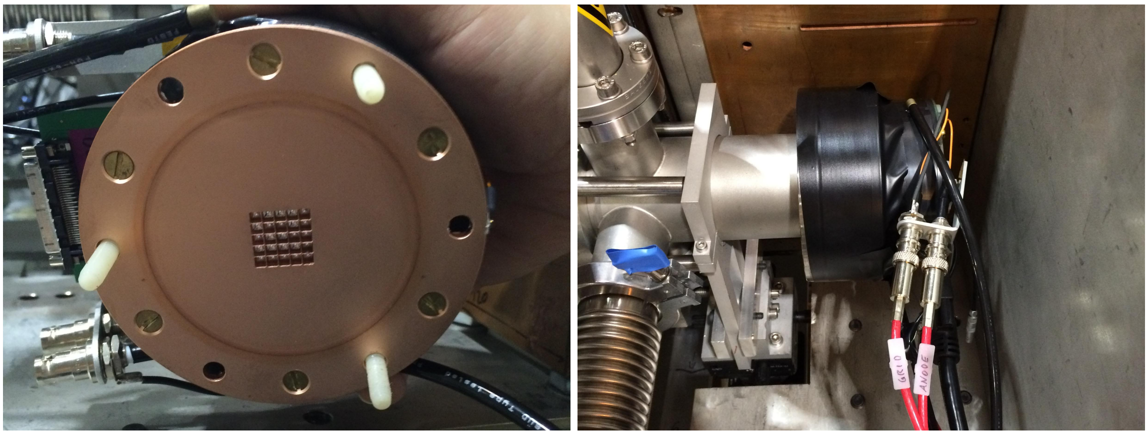

(a) (b)

Figure 8.11: InGrid based X-ray detector before (a) and after (b) mounting at the interface vacuum system connecting it to the MPE XRT and the detector station VT4 on the sunrise platform of CAST. In (a) the X-ray entrance window of the detector is visible as well as the imprint of an O-ring seal on the outer cathode surface. After mounting the InGrid based X-ray detector using plastic bolts the detector has been wrapped with black tape, as can be seen in (b), to shield from external light while testing without the lead shielding in place.

8.3.3 Mounting and start up of the detector

Prior to mounting the InGrid based X-ray detector the interface vacuum system is isolated, especially the downstream gate valve of the MPE XRT needs to be closed, and vented. Then the alignment flange is removed and the detector bolted on the detector mount using six plastic threaded bolts, see images in Fig. 8.11. When the detector is installed, it is connected to its infrastructure, especially its gas system. While the detector is being flushed with its gas mixture the interface vacuum system is being pumped again. To shield it from external light the detector is wrapped with black type, of course this is only necessary for testing while the lead shielding is not installed.

After several hours of flushing with gas at a flow of 2 l/h at a pressure of 1 050 mbar the detector can be turned on. For the installation in October 2014 the start up of the InGrid based X-ray detector went smoothly with everything within normal. After few hours of background data taking (the calibration source was not available at this point) the gas gain can be extracted from the recorded frames in order to adjust the grid high voltage. In this case the grid high voltage was adjusted to −295 V to achieve a gas gain of about 2 500. The anode and cathode voltage were consequently set to −345 V and −1 895 V respectively.

8.3.4 Installation of the lead shielding

After successful start up of the detector as a last step the lead shielding was installed. In October 2014, the sunrise MicroMegas detector and its lead shielding were already in place, so only the part shielding the InGrid based X-ray detector had to be added. Fig. 8.12 shows images of the lead shielding, one with the two top layers missing and one with the shielding completed. To avoid a change of load on the sunrise platform due to the additional weight of the lead shielding, lead plates were removed from the platform's counter weight to compensate for the added load.

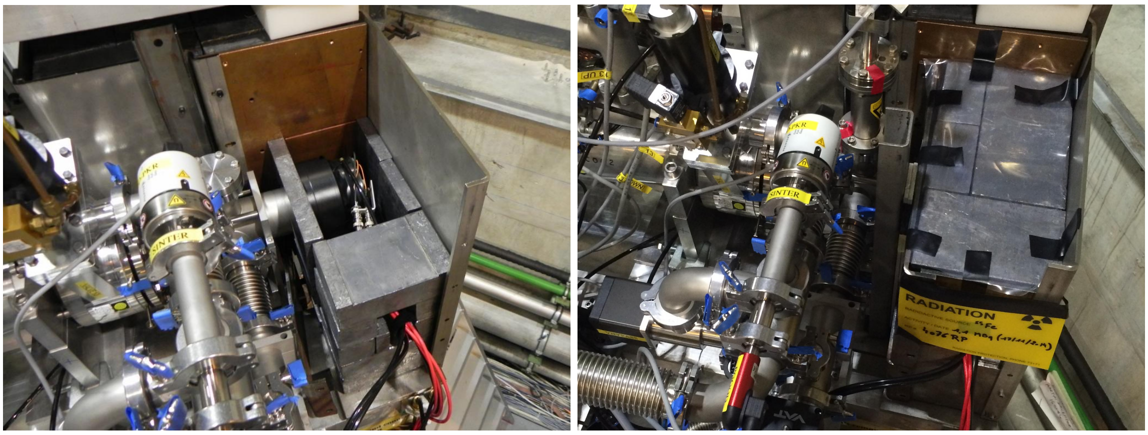

(a) (b)

Figure 8.12: Pictures of the lead shielding enclosing the InGrid based X-ray detector. In (a) the two top layers of lead bricks are missing, revealing the detector, while in (b) the shielding has been closed. On the left side, part of the interface vacuum system is visible in both images. While in (a) the port for the movable calibration source is closed with a blind flange, in (b) the electropneumatic linear feedthrough with the radioactive source mounted to its tip has been installed (top middle).

8.3.5 Delayed installation of the movable calibration source

Although the movable calibration source was foreseen to be installed along with the InGrid based X-ray detector in October 2014 it could not be mounted before April 2015. Due to a contamination with a silicon based vacuum grease of the electropneumatic linear feedthrough it had to be cleaned first using a bake out procedure of several weeks before the radioactive source could be reattached to its tip and the movable calibration source could be mounted. Else vapours of the silicon based vacuum grease might have mitigated onto the MPE XRT's mirror surfaces reducing their reflectivity and thus the performance of the X-ray mirror optic.

While the movable calibration source was absent the corresponding port in the system was closed with a blind flange (see CAD drawing in Fig. 8.6(b)). In April 2015 the interface system was vented, the blind flange removed and the movable calibration source installed.

CHAPTER 9

Detector operation in 2014 and 2015

The data used in the search for solar chameleons performed in the course of this thesis was taken during the 2014 and 2015 data taking campaigns of the CERN Axion Solar Telescope (CAST) which started in October 2014 right after the installation and commissioning of the InGrid based X-ray detector at CAST (see chapter 8) and ended in December 2015 with the detector and its systems being dismounted in January 2016. The data taking period splits in the 2014 and 2015 data taking campaigns due to a scheduled break from late November 2014 until June 2015 used mainly for maintenance of the whole experiment. In this chapter insight in the operation and supervision of the InGrid based X-ray detector during the data taking will be given along with operation statistics and figures underlining the detector's great performance without any detector related interruptions or problems over the whole data taking period of several months.

Also, measurements with a pyroelectric X-ray source, the X-ray finger, will be shown. Although these measurements cannot be used to check the absolute alignment of the detector, they can be used to compare the alignment at different times to detect possible changes, e.g. due to the frequent movement of the whole experimental set-up. X-ray finger measurements have been carried out prior to the start of the data taking campaign in October 2014 and at the end in December 2015 prior to dismantling of the detector.

9.1 Data taking campaigns 2014 and 2015

During the CAST data taking campaigns 2014 and 2015 the InGrid based X-ray detector, installed behind the MPE X-ray telescope (XRT) at detector station VT4, was operated continuously. To ensure reliable operation and a good data quality it was manually, but most times remotely, operated and supervised including quality and sanity checks of the raw data recorded. As the detector was recording frames (each about 0.98 s long) continuously a large background data sample was collected along with the sunrise and sunset data. The sunset data can be used to verify that the tracking of the Sun (magnet moving) does not affect the background by comparing the recorded spectrum during sunset with the background spectrum recorded with the magnet being stationary. During the sunset tracking of the Sun the conditions (e.g. magnet moving) are comparable to the sunrise tracking but the detector is pointing away from the Sun. Fig. 9.1 shows an image of CERN Axion Solar Telescope during a sunrise tracking of the Sun with the InGrid based X-ray detector taking data.

During the whole data taking period no detector related interruptions occurred underlining the great performance of the InGrid based X-ray detector. The only interruptions in data taking and lost sunrise tracking of the Sun were related to a leak in the MPE XRT's vacuum system, thunderstorms or operator errors, resulting in a large amount of background as well as sunset and sunrise data being recorded.

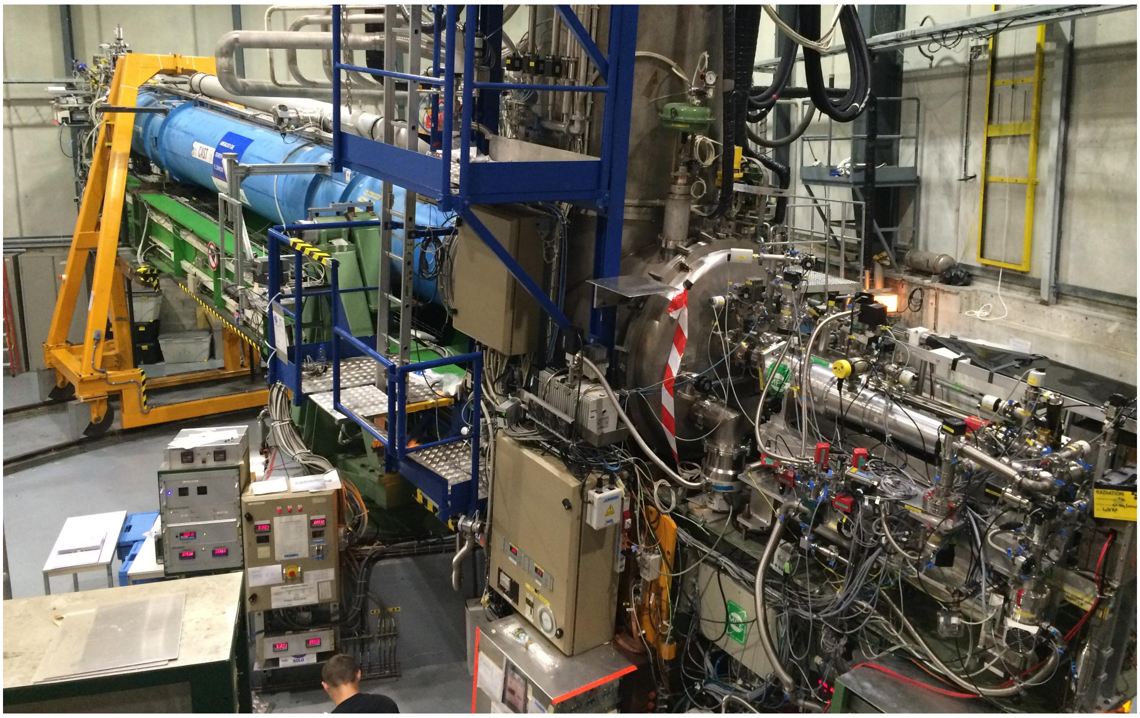

Figure 9.1: Image of CERN Axion Solar Telescope during a sunrise tracking of the Sun with the InGrid based X-ray detector (bottom right) taking data. The magnet is pointing towards the Sun which is behind the concrete wall in the background of the image which is transparent for chameleons (and axions) emitted from the sun.

From April 2015 on, after the movable calibration source had been mounted on the interface vacuum system, daily calibration runs using an ^{55}Fe source were performed which allowed to further verify the detector performance and to check if all parameters were within normal. The results obtained from these daily calibrations in 2015 further confirmed and underlined the great and stable performance of the InGrid based X-ray detector. This also underlines that the GridPix technology has reached the state of a mature detector technology as this was the first time a GridPix had been operated, quasi continuously, for such a prolonged time. Some of the details presented here, concerning the stable long-term operation of the InGrid based X-ray detector, have also been published in [111].

9.1.1 Detector operation and supervision

During data taking at CAST the InGrid based X-ray detector is recording continuously untriggered frames of about 0.98 s length (*shutter* signal low), one frame after the other. As each frame has a unique timestamp (standard Unix time) the splitting of the data in the three datasets background, sunset and sunrise is done later offline using the general slowcontrol data provided by CAST. During sunset or sunrise tracking of the Sun at least two shifters are present at the experiment and, among other tasks, regularly check the readout of the InGrid based X-ray detector via an online event display running on the readout computer, in case of observing anything unusual they would call the current operator of the detector who would log in remotely and take necessary actions.

Usually, the operator of the InGrid based X-ray detector logs in remotely once per day and starts a new run, the previous run is then checked using a slim raw data tool. The checks performed on the raw data include checking the occupancy obtained in the run for a uniform, expected illumination of the GridPix'

CAST data taking campaign 2014	
Data taking	16.10.2014 to 26.11.2014
Tracking of sun	16.10.2014 to 16.11.2014
Sunrise tracking	27 of 27 (100 %)
Sunset tracking	28 of 28 (100 %)
Total frames recorded	237 029 (background, sunrise & sunset)
Duty cycle	97.65 %
Integrated time	2 331 448.4 s (647.6 h)
Calibration runs	0 (no source installed)
Background time	2 032 108.2 s (564.5 h)
Sunrise time	147 766.9 s (41.0 h)
Sunset time	151 573.3 s (42.1 h)

Table 9.1: Statistics for the InGrid based X-ray detector during the CAST data taking campaign 2014.

surface (see also Fig. 7.19(b) for an example of the expected occupancy) and a look at the charge per pixel distribution which allows to check if the achieved gas gain is within normal range. Afterwards, the data is compressed and copied to a safe storage and to the systems on which later the offline data analysis is performed.

From April 2015 on, when the movable calibration source became available, before the new data taking run is started, the ^{55}Fe source is moved in and a one hour calibration run is recorded before the ^{55}Fe source is moved out again. The data obtained in these calibration runs allowed for further in situ checks on the raw data by checking the obtained spectrum for the expected peaks of the ^{55}Fe source in addition to the checks already performed on the data taking runs.

9.1.2 Operation statistics

In 2014 the InGrid based X-ray detector was operated for 42 days while in 2015 it took data for 217 days. Detailed statistics on the data recorded during the two data taking campaigns can be found in Tables 9.1 and 9.2. The official CAST data taking periods, during which tracking of the Sun was performed, lasted from 16.10.2014 until 16.11.2014 and from 18.06.2015 until 15.11.2015. At the end of the 2014 data taking period an additional dataset with the region in front of the detector not being evacuated but filled with dry nitrogen (at atmospheric pressure) was recorded for 9 days after the last tracking of the Sun before the detector was shut off for the winter break. During the 2015 data taking campaign 189 calibration runs have been recorded in situ.

During normal data taking throughout 2014 and 2015 a duty cycle of 97.65 % was achieved which fits the theoretical value which can be calculated from the frame length and the time needed for readout:

$$\frac{0.98\,\mathrm{s}}{0.98\,\mathrm{s} + 23\,\mathrm{ms}} \approx 97.7\,\%.$$

Excluding the calibrations runs, during the data taking campaign 2014 2 379 029 frames have been recorded (each about 0.98 s long) and during the data taking campaign 2015 17 022 741 frames have been gathered giving a total of 19 401 770 frames including background, sunrise and sunset data. Of these, already about 80 % are completely empty except for one (known) noisy pixel. All in all the data recorded by the InGrid based X-ray detector in 2014 and 2015 contains data from 171 sunrise trackings of the sun, taking into account the detector's duty cycle giving about 254 h of sunrise data and about 4 785 h

CAST data taking campaign 2015	
Data taking	21.04.2015 to 23.11.2015
Tracking of sun	18.06.2015 to 19.11.2015
Sunrise tracking	144 of 148 (97.3 %)
Sunset tracking	138 of 143 (96.5 %)
Total frames recorded	17 022 741 (background, sunrise & sunset)
Duty cycle	97.65 %
Integrated time	16 682 286.2 s (4 634.0 h)
Calibration runs	189
Background time	15 194 415.6 s (4 220.7 h)
Sunrise time	766 566.2 s (212.9 h)
Sunset time	721 304.4 s (200.4 h)

Table 9.2: Statistics for the InGrid based X-ray detector during the CAST data taking campaign 2015.

of background data plus about 242 h of sunset data recorded in 166 sunset tracking of the sun. Not all possible trackings of the Sun (sunrise and/or sunset) were performed by CAST during the data taking campaigns as some shifts were cancelled due to problems with the experiment itself or approaching thunderstorms which pose a thread to the magnet when it is powered. Also some sunrise trackings were lost due to a vacuum leak in the MPE XRT's vacuum system which caused the gate valve VT4 to be closed during the trackings. Except for a few incidents caused by human errors (e.g. accidental deploying of the calibration source during a tracking) no data was lost, especially no detector related problems or issues interrupted the data taking in 259 days of detector operation.

9.1.3 Daily detector calibration

During the data taking campaign 2015 189 in situ calibration runs were recorded with the InGrid based X-ray detector. The calibration runs were performed almost daily. For each calibration run the movable calibration source (^{55}Fe) is moved in front of the detector and frames are recorded for one hour before the calibration source is again retracted and a new data taking run is started. For the calibration runs the frame length is adjusted to about 1.2 ms which results in a low number of frames containing more than one X-ray photon while giving a reasonable fraction of empty frames at the given rate of the ^{55}Fe source used.

As stated before the raw data obtained from these calibration runs can be used for in situ checks of the detector performance and operation by looking at occupancy, the obtained spectrum and the charge per pixel histogram. Additionally, in an offline analysis using the reconstruction chain, which will be described in detail in chapter 10, and a loose selection to only get single photon frames for each calibration run the spectrum can be extracted using the charge information of the pixels. By fitting a dedicated function to these spectra taking into account the main peak as well as the escape peak and the corresponding K_β lines present, for each calibration run the energy resolution, as well as the position of the main photopeak and the calibration factor a_Q (see chapter 7 for details) can be extracted. In addition for each calibration run the mean gas gain can be extracted from the charge per pixel distribution, see Fig. 9.2. Fig. 9.3 shows the spectrum obtained from a calibration run with the appropriate function fitted. Taking into account the manganese K_α and K_β lines plus their corresponding escape lines one gets the complete function to describe the observed spectrum by adding four Gaussian distributions:

$$\begin{aligned} y(x) = N_{\mathrm{K}_\alpha} \cdot \exp\left(\frac{(x-\mu_{\mathrm{K}_\alpha})^2}{2\sigma_{\mathrm{K}_\alpha}^2}\right) + N_{\mathrm{K}_\beta} \cdot \exp\left(\frac{(x-\mu_{\mathrm{K}_\beta})^2}{2\sigma_{\mathrm{K}_\beta}^2}\right) \\ + N_{\mathrm{K}_\alpha}^{\mathrm{esc}} \cdot \exp\left(\frac{(x-\mu_{\mathrm{K}_\alpha}^{\mathrm{esc}})^2}{2(\sigma_{\mathrm{K}_\alpha}^{\mathrm{esc}})^2}\right) + N_{\mathrm{K}_\beta}^{\mathrm{esc}} \cdot \exp\left(\frac{(x-\mu_{\mathrm{K}_\beta}^{\mathrm{esc}})^2}{2(\sigma_{\mathrm{K}_\beta}^{\mathrm{esc}})^2}\right) \end{aligned} \tag{9.1}$$

with N, μ and σ being the parameters of the Gaussian distributions. Assuming the width of K_α and K_β lines being almost identical and using the known relation between their center positions and relative intensities [113] along with the linear energy calibration (see chapter 7) one can reduce the number of free parameters to six:

$$\begin{aligned} y(x) = N_{\mathrm{K}_\alpha} \cdot \left(\exp\left(\frac{(x-\mu_{\mathrm{K}_\alpha})^2}{2\sigma_{\mathrm{K}_\alpha}^2}\right) + k_N \cdot \exp\left(\frac{(x-k\cdot\mu_{\mathrm{K}_\alpha})^2}{2\sigma_{\mathrm{K}_\alpha}^2}\right)\right) \\ + N_{\mathrm{K}_\alpha}^{\mathrm{esc}} \cdot \left(\exp\left(\frac{(x-\mu_{\mathrm{K}_\alpha}^{\mathrm{esc}})^2}{2(\sigma_{\mathrm{K}_\alpha}^{\mathrm{esc}})^2}\right) + k_N \cdot \exp\left(\frac{(x-k_{\mathrm{esc}}\cdot\mu_{\mathrm{K}_\alpha}^{\mathrm{esc}})^2}{2(\sigma_{\mathrm{K}_\alpha}^{\mathrm{esc}})^2}\right)\right) \end{aligned} \tag{9.2}$$

with

$$\begin{aligned} k_N &= \frac{N_{\mathrm{K}_\beta}}{N_{\mathrm{K}_\alpha}} = \frac{17}{150} \\ k &= \frac{\mu_{\mathrm{K}_\beta}}{\mu_{\mathrm{K}_\alpha}} = \frac{6.49}{5.90} \\ k_{\mathrm{esc}} &= \frac{\mu_{\mathrm{K}_\beta}^{\mathrm{esc}}}{\mu_{\mathrm{K}_\alpha}^{\mathrm{esc}}} = \frac{3.53}{2.94}. \end{aligned}$$

The two peak positions (main photo peak and escape peak) obtained from each spectra allow to determine a_Q from a straight line fit with a y-intercept of zero. When plotting the calibration factors versus the mean gas gain[1] one can obtain the dependence of a_Q^{-1} on the gas gain which is approximately linear, see Fig. 9.4, by fitting a straight line of form

$$a_Q^{-1}(G_{\mathrm{mean}}) = b_1 \cdot G_{\mathrm{mean}} + b_0 \tag{9.3}$$

to the data points giving

$$b_0 = (2.4078 \pm 0.0029) \times 10^{-5}\,\mathrm{keV}/e \tag{9.4}$$

$$b_1 = (-5.645 \pm 0.011) \times 10^{-9}\,\mathrm{keV}/e. \tag{9.5}$$

---

[1] From the charge pixel histograms three different quantifiers for the gas gain can be extracted: G_{mean} (mean of the distribution), G_{MPV} (most probable value of the distribution) or $G_{\mathrm{Pólya}}$ (from fitting a Pólya distribution to the distribution). In this theses, usually the mean gas gain G_{mean} is used.

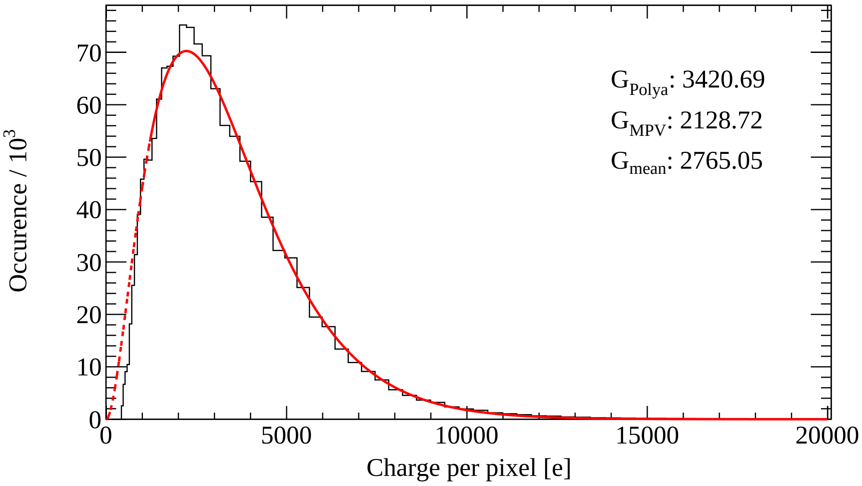

Figure 9.2: Charge per pixel histogram of a calibration run. An asymmetric binning matched to the used GridPix' ToT calibration [100] has been used to avoid binning artefacts. A Pólya distribution, described by equation 5.54, has been fitted to the data but only from 1 200 e onwards to avoid threshold effects (solid red line). The three different measures for the gas gain (G_{mean}, G_{MPV} and $G_{\mathrm{Pólya}}$) for this distribution are given in the plot.

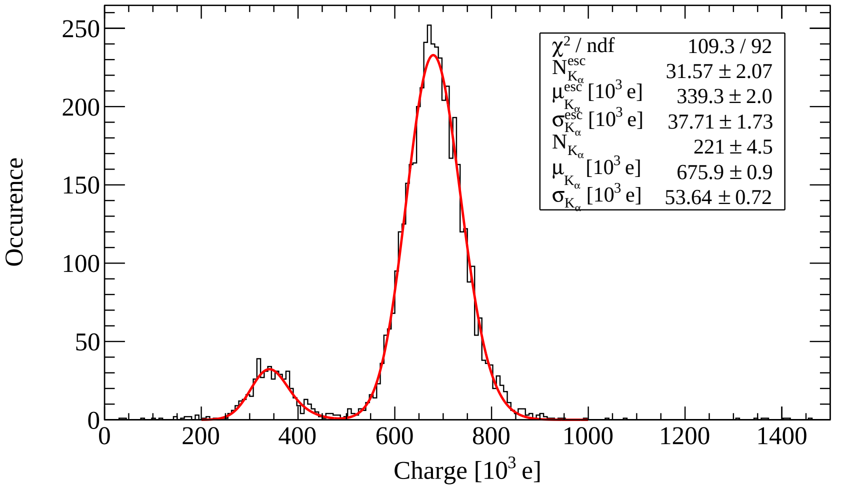

Figure 9.3: ^{55}Fe spectrum from a calibration run using the charge information as a measure of the X-ray photon energy. The fit function used (equation 9.2) takes into account the K_α and K_β lines for both main photopeak as well as escape peak but the number of free parameters is reduced by constraining the K_β parts relative to the K_α lines using the information from [113].

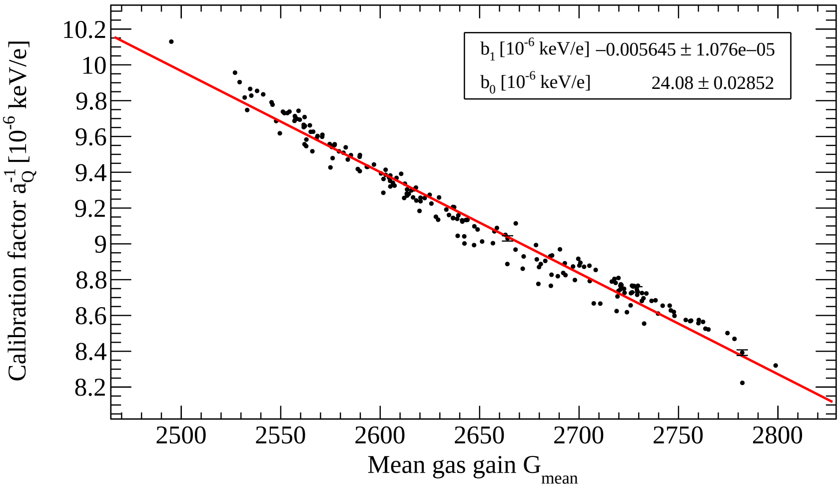

Figure 9.4: Dependence of calibration factor a_Q on the mean gas gain G_{mean}. A straight line (see equation 9.3) has been fitted to the data points to extract the information to later calculate the calibration factors for data taking runs from the measured gas gain.

This information later allows to calculate the calibration factors for each of the data taking runs using its mean gas gain which for each run can be obtained from the charge per pixel distribution.

9.1.4 Stable detector performance

As already mentioned, during the 259 days of operation at CAST the InGrid based X-ray detector did function almost perfectly and no detector related interruptions or problems did occur demonstrating the excellent performance of the detector. By using the information which can be extracted from the calibrations runs and taking a look at their development with time one can also show and underline the InGrid based X-ray detector's stable performance. In Fig. 9.5 the energy resolution at 5.75 keV using the charge information is shown as function of time demonstrating a stable detector performance at an energy resolution σ_E/E of 7.8 %. Also the development of the position of the main photopeak in the spectrum using the charge information can be evaluated, see Fig. 9.6. This peak position slightly fluctuates, this is caused by changes in the gas gain, see Fig. 9.7. The small fluctuations are caused by environmental changes. While the gas pressure inside the detector is stable due to the used inlet pressure regulator, the ambient temperature in the experimental hall, and therefore the temperature of the gas is not. This causes small variations in the gas gain which can be compensated for using the gas gain dependence of the calibration factors (see Fig. 9.4). Also, when comparing Figs. 9.6 and 9.7 it is clearly visible that the changes in the peak position are linked to the fluctuations of the mean gas gain.

9.2 X-ray finger measurements

Until end of 2015 a pyroelectric X-ray source, also called X-ray finger, was mounted on the sunset end of the CAST magnet attached to the tip of a linear feedthrough allowing to position the source, pointing towards the sunrise side, on the optical axis of the magnet's coldbore. As the pyroelectric source is point like it is not possible to use it for checking the alignment of the InGrid based X-ray detector with the

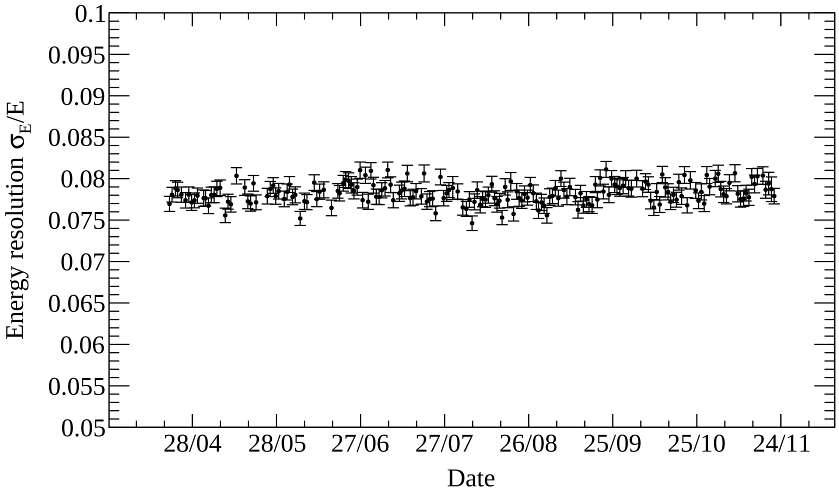

Figure 9.5: Development of energy resolution σ_E/E at 5.9 keV with time. Energy resolution is extracted from 189 calibration runs recorded throughout 2015 with the InGrid based X-ray detector using a movable ^{55}Fe source. Mean energy resolution is 7.8 %.

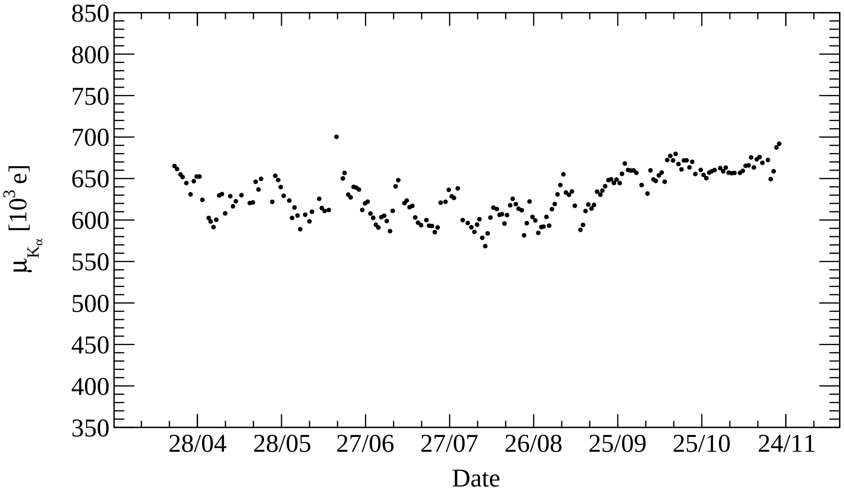

Figure 9.6: Development of manganese K_α peak position μ_{K_α} with time. Peak position is extracted from 189 calibration runs recorded throughout 2015 with the InGrid based X-ray detector using a movable ^{55}Fe source using the charge information as measure for the X-ray photon energy. Fluctuations can be linked to variations of the gas gain caused by changing environmental conditions such as temperature.

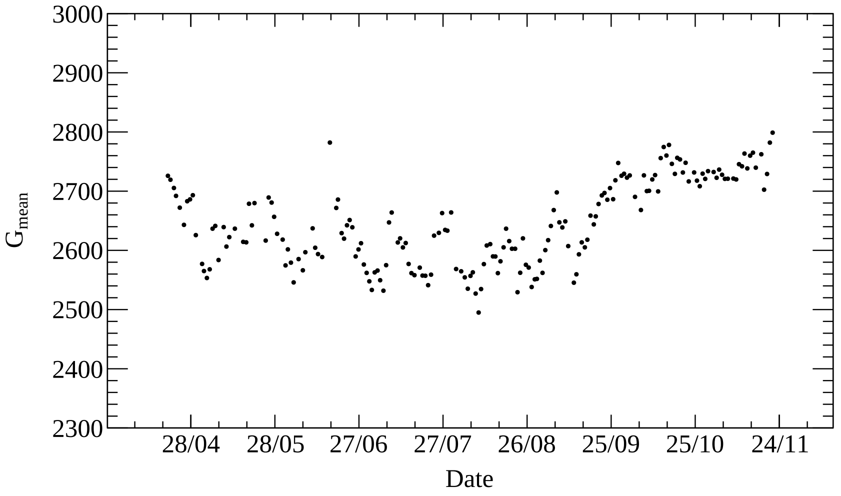

Figure 9.7: Development of mean gas gain G_{mean} with time. Gas gain is extracted from charge per pixel distributions of 189 calibration runs recorded throughout 2015 with the InGrid based X-ray detector using a movable ^{55}Fe source. Variations are caused by changing environmental conditions, such as temperature, in the CAST experimental hall.

MPE XRT but it can be used to verify the alignment and its stability at different times by comparing the image of the point like source, as seen through the X-ray optic, at different times. Although the rate emitted by the source itself is rather high, the small solid angle imaged through the XRT and the energy dependent transmission and off-axis behaviour of the X-ray optic cause the rate seen by the InGrid based X-ray detector to be quite low, in addition the rate is not constant but follows the cooling/heating cycle of the pyroelectric X-ray source. Therefore when recording data with the X-ray finger, the frame length has to be adjusted to approximate 150 ms to allow for recording of single X-ray photons at the maximum of the rate cycle. Due to the frames being recorded untriggered this causes a large number of empty frames accumulating during the minimum of the rate cycle (rate approximately zero) and even a significant number of non-X-ray events being collected in the dataset. To record an X-ray finger run with sufficient statistics about 12 h are needed.

During the data taking campaigns 2014 and 2015 on the whole six X-ray finger runs have been recorded: One prior to mounting the lead shielding, one at beginning and end of data taking in 2014 and three at the end of data taking in 2015 prior to dismantling the InGrid based X-ray detector. For two of the X-ray finger runs performed at the end of 2015 the magnet was not kept horizontally (as for the other X-ray finger runs) but either tilted upwards or downwards with its maximum tilting angle. Fig. 9.8 shows the images recorded in the six X-ray finger runs. For each run the centres of reconstructed X-ray photons are plotted, to suppress the non-X-ray events in addition to the reconstruction, briefly described in chapter 7, a background suppression has been applied, for details on both see chapter 10. The overall structure visible in all of the centre maps stems from the mirror shells of the MPE XRT's X-ray optic and the strongback of the InGrid based X-ray detector's X-ray entrance window. As a measure for a possible change in alignment one can compare the centre of gravity of the different X-ray finger images, which are given in the plots in Fig. 9.8. Depending on the statistics the error on the centre of gravity coordinates varies from 10 to 20 μm. All X-ray finger runs recorded in 2015 were done with 24 h per run while those recorded in 2014 were only 12 h long or less.

Slight changes in the centre of gravity position for the image of the point like X-ray source are observable but these are all within 250 μm which is acceptable as the overall alignment precision from the

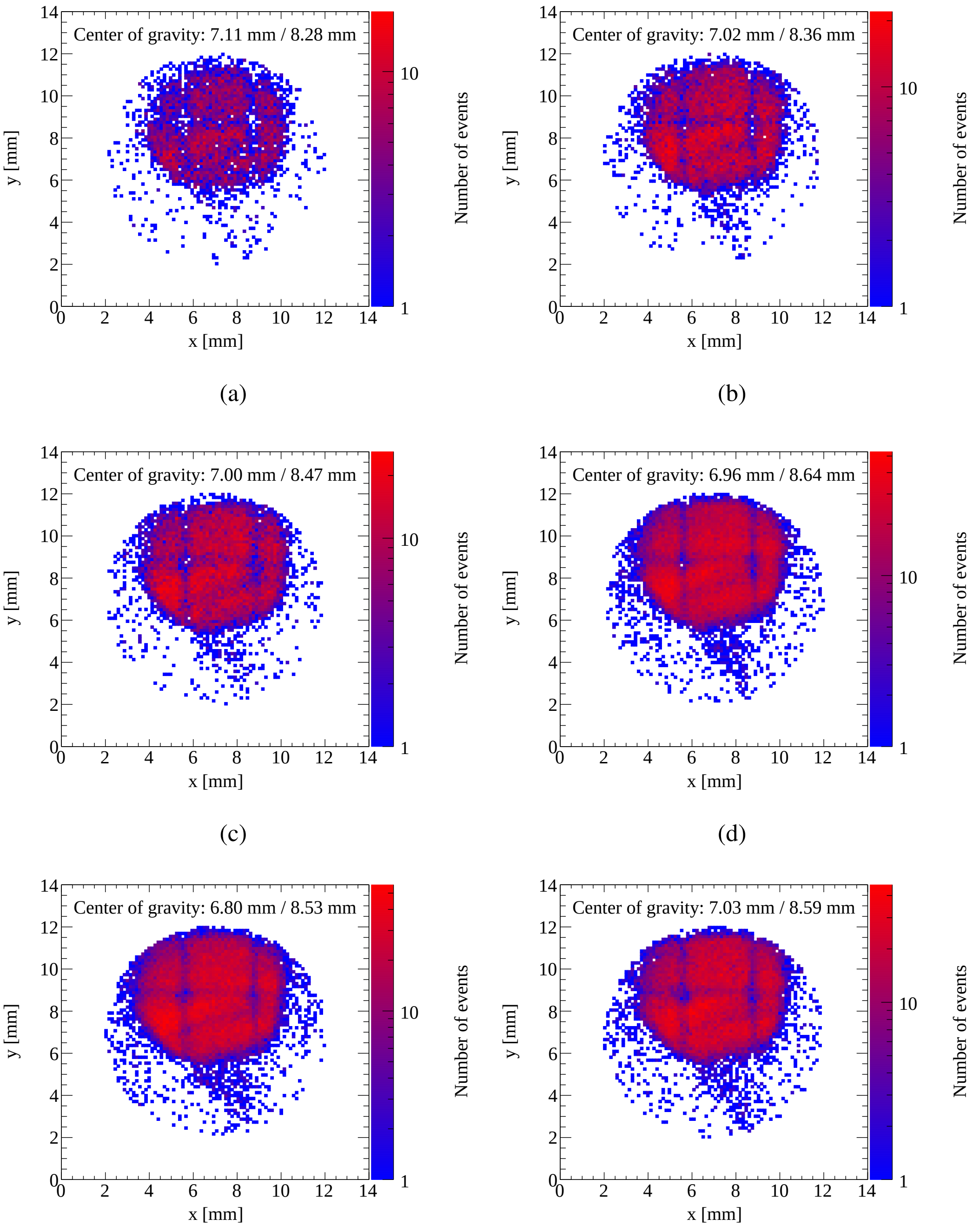

(a) (b) (c) (d) (e) (f)

Figure 9.8: X-ray finger measurements performed in 2014 and 2015. The point like pyroelectric X-ray source, X-ray finger, is mounted on the sunset end of the magnet and imaged through the MPE XRT. The structures visible are caused by the mirror shells of the X-ray optic and the strongback of the X-ray entrance window of the InGrid based X-ray detector. The centre of gravity position (given in the plots) can be used to monitor/detect changes of the alignment. The error on the centre of gravity coordinates varies from 10 to 20 µm. X-ray finger measurements were done prior to mounting the lead shielding in 2014 (a), at the beginning (b) and end (c) of the 2014 data taking as well as at the end of the 2015 data taking. At the letter the measurements were done in addition to the magnet being horizontal (d) also with the magnet being tilted upwards (e) and downwards (f).

laser alignment procedure is estimated to about 0.5 mm. The difference between the first measurements in 2014 with (Fig. 9.8(b)) and without (Fig. 9.8(a)) the lead shielding is about 0.1 mm which is more or less expected as, though the shielding weight is compensated for by removing parts of a counter weight, but still causes a change in the distribution of weight on the sunrise platform. The changes observed between begin (Fig. 9.8(b)) and end (Fig. 9.8(c)) of data taking 2014 and the end of data taking 2015 (Fig. 9.8(d)) are mostly along the y-axis which is the direction in which the magnet moves vertically and therefore are expected. The frequent tilting (upwards and downwards) of the CAST magnet with more than 500 kg quasi mounted to the very end of the sunrise platform might easily cause a small deformation of the sunrise platform. Same holds for the difference observed between the magnet being horizontal (Fig. 9.8(d)), tilted upwards (Fig. 9.8(e)) and tilted downwards (Fig. 9.8(f)), especially at is known that the tilting leads to a very tiny warping of the whole structure on which the magnet is mounted. Of course the observed changes in alignment will be taken into account for the estimation of systematic uncertainties for the limit calculation in chapter 11.

CHAPTER 10

Data reconstruction and background reduction

The data recorded with the InGrid based X-ray detector has to be processed through a reconstruction chain to identify and reconstruct (possible) clusters stemming from converted X-ray photons. This is done within the MarlinTPC framework [119] making use of many elements of the chain, especially those for (pre)processing the Timepix application specific integrated circuit (ASIC)'s data, being already implemented and available. In this chapter the reconstruction and analysis chain will be described and introduced, starting with the preprocessing of the data followed by identification of possible clusters and reconstruction of X-ray photons. An energy calibration based on the characterization of the InGrid based X-ray detector performed in the CAST Detector Lab (CDL) (see chapter 7) and daily calibration runs carried out during the data taking campaigns in 2014 and 2015 (see chapter 9) is applied before event shape variables are calculated followed by a data post-processing which, among other things, includes a cross referencing with logged slowcontrol data of the CERN Axion Solar Telescope (CAST) and a separation into different datasets: background, sunset & sunrise.

As for a low rate experiment, as CAST, a low background rate in the detector is one of the key figures to achieve a high sensitivity for exotic and weakly interacting particles, like axions or chameleons, the data recorded needs to be cleaned from any event which does not stem from an X-ray photon but e.g. from a cosmic ray passing the detector. Every method applied has to guarantee that the majority of real X-ray photons still passes the selection to keep a high software efficiency and not remove a possible signal. For the InGrid based X-ray detector a likelihood method, based on event shape variables and reference datasets recorded during the detector's characterization in the CDL, has been implemented making use of the InGrid based X-ray detector's high spatial resolution and single electron efficiency allowing for detecting (almost) every primary electron created in the conversion of the initial X-ray photon.

This likelihood method, adjusted to a software efficiency of 80 %, is applied to the data taken at CAST. The distribution of remaining background events over the instrumented area lead to a definition of two areas, an inner, so called *gold*, region and an outer, so called *silver*, region with different background levels. Along with the background spectra observed in these two regions, and the known features therein, possible causes for the different background levels will be briefly discussed. As the conditions under which the different datasets are recorded are slightly different (e.g. during sunrise and sunset periods the magnet is moving while during background phases it is stationary) a comparison between background spectra of background and sunset datasets will be done to establish that the background dataset can indeed be used to predict the background events contained in the sunrise dataset along with a possible but unknown signal.

10.1 Reconstruction of data recorded with the InGrid based X-ray detector

Each frame has a number of activated pixels with their corresponding x- and y-coordinates as well as the Time-over-Threshold (ToT) value which gives a measure for the charge collected on a pixel. These frames have to be passed through a reconstruction chain in order to end up with a dataset consisting of clusters (possibly) originating from X-ray photons which then can be used for the search of solar axions or chameleons. Of course, after selecting only real X-ray events with high efficiency to reach a low background rate.

The reconstruction chain consists of several steps and is realized in the MarlinTPC framework [119] as already some of the chain links needed, mostly concerning (generic) processing of the data recorded with a Timepix ASIC, were implemented. The reconstruction chain can be divided into smaller chunks: data preprocessing, the actual reconstruction including cluster identification, energy calibration, computation of event shape variables and a post-processing step which exports all identified clusters as a single `ROOT` file and allows separation into the different datasets corresponding to background, sunset and sunrise data taking.

10.1.1 Data preprocessing

In the data preprocessing at first all completely empty frames are removed before the remaining frames are imported into MarlinTPC's data format, the unique timestamp of each frame is kept with each frame inside the framework. In a next step, the one known, noisy pixel is removed from the imported data using a mask before the ToT value of each pixel is converted into a charge measured in electrons by applying the ToT calibration of the GridPix (see chapter 7, especially equation 7.3).

10.1.2 Cluster finding and X-ray reconstruction

To identify possible clusters originating from an X-ray photon conversion in a recorded frame and collect all pixels belonging to this cluster, a modified clustering algorithm is used [10, 99, 114]. This algorithm allows for a gap between pixels identified as part of a cluster. Starting in a rowwise scheme from the left bottom corner of the chip the first pixel found is used as seed for a possible cluster, any further pixel found not more than 50 pixels away in x- or y-direction is added to the cluster. This results in possible neighbours for each pixel being searched in a 101×101 pixels array centred around any pixel already assigned to the cluster. If no more pixels can be added to the cluster in a frame a new search is started with the pixels not yet assigned to a cluster. For every cluster found, the total charge (sum over charges measured on the pixels of the cluster), number of pixels in the cluster and x- and y-position of its centre of gravity in the chip's reference frame are stored. Clusters with less than three pixels are discarded.

The maximum allowed distance of 50 pixels used for the cluster search was chosen based on the results of the detector characterization in the CDL and ensures that also for low energy X-ray photons (low number of pixels, and maximum spread through maximal drift distance) all pixels are collected. Comparing the resulting search array around each pixel of 101×101 pixels with the pixel matrix of the GridPix used (256×256 pixels) it is clear that this setting does not allow for correct reconstruction of multiple X-ray photons in a single frame but merely can reject a few randomly activated pixels uncorrelated to the cluster. As for a low rate experiment such as CAST the expected X-ray photon rate is very low the inability to separate two or more X-ray photons recorded in a single frame is not considered an issue. For calibration runs (like performed during data taking using the movable calibration source) the frame length has to be adjusted to collect mostly frames with a single X-ray photon. By using a

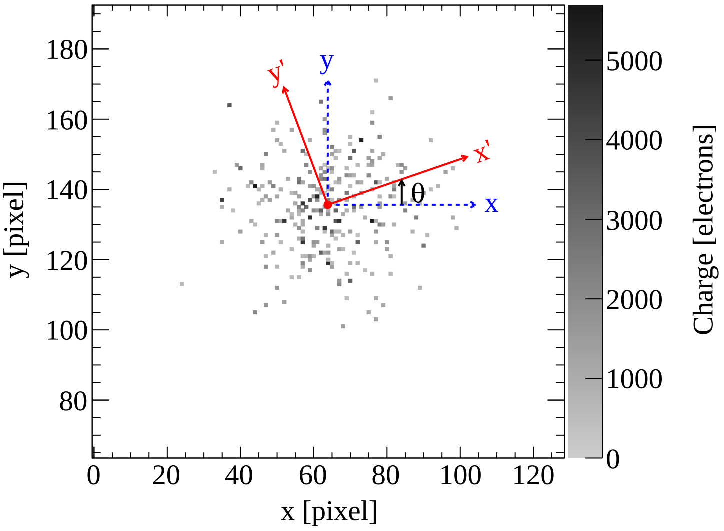

Figure 10.1: Sketch illustrating the relation between rotation angle θ and long and short axis, x' and y'. By rotating the coordinate system of the GridPix' reference frame with axes x and y by the angle θ around the cluster's centre of gravity, the long and short axis are derived.

gas mixture with lower diffusion coefficient one could reduce the search radius allowing for correct reconstruction of multiple clusters in a single frame.

When the clusters have been identified and all pixels have been assigned to a cluster, as a last step of the reconstruction the long and short axis of the cluster have to be identified which later can be used as reference axes for the computation of event shape variables. It is assumed that long and short axis are perpendicular to each other so they can be derived from the chip's reference frame by a rotation of the coordinate system by an angle θ. This angle is found by minimizing the width (root mean square) along the short axis as function of the rotation angle θ. When calculated, θ is stored with the identified cluster. Fig. 10.1 illustrates the connection of θ and long and short axis.

10.1.3 Energy calibration

For each run a charge per pixel histogram (using the binning adopted to the GridPix' ToT calibration) is created and the mean gas gain G_{mean} is extracted automatically. Using the relation between the energy calibration factor a_Q and G_{mean} (see equation 9.3) and the parameters b_0 and b_1 derived from the calibration runs the energy calibration factor a_Q is computed for each run. This information is then used to calculate the energy E for each reconstructed cluster using its total charge Q:

$$E = a_Q^{-1} \cdot Q. \tag{10.1}$$

The energy E is afterwards stored with each cluster. Here, the total charge Q and not the number of activated pixels is used as measure for the X-ray photon's energy as it gives the correct energy independent of the position of the X-ray photon conversion. For X-ray photons converting at a height above the GridPix where diffusion is insufficient to fully separate the primary electrons so that more than one may enter a single grid hole, the energy determined from the number of activated pixels is too low.

10.1.4 Calculation of event shape variables

For each cluster a set of event shape variables is calculated from the positions of all of its pixels. All event shape variables are computed in the reference frame of long and short axis. In the following the long axis will be denoted as x' while y' denotes the short axis. The event shape variables which are computed, include central statistical momenta such as the variance V and the corresponding widths σ along long and short axis respectively:

$$V_{x'} = \frac{1}{N}\sum_{i=1}^{N}\left(x_i' - \mu_{x'}\right)^2 = \sigma_{x'}^2 \equiv \sigma_{\text{long}}^2 \tag{10.2}$$

$$V_{y'} = \frac{1}{N}\sum_{i=1}^{N}\left(y_i' - \mu_{y'}\right)^2 = \sigma_{y'}^2 \equiv \sigma_{\text{trans}}^2 \tag{10.3}$$

where $\mu_{x'}$ and $\mu_{y'}$ denote the cluster's centre of gravity coordinates within the rotated coordinate system and N is the number of pixels in a cluster. Often, the long axis is referred to as longitudinal axis while the short axis is referred to as transverse axis due to their connection with the direction of the photoelectron released in the X-ray photon conversion. Additional central momenta available as event shape variables are the skewness S

$$S_{x'} = \frac{1}{N}\sum_{i=1}^{N}\frac{\left(x_i' - \mu_{x'}\right)^3}{\sigma_{x'}^3} \equiv S_{\text{long}} \tag{10.4}$$

$$S_{y'} = \frac{1}{N}\sum_{i=1}^{N}\frac{\left(y_i' - \mu_{y'}\right)^3}{\sigma_{y'}^3} \equiv S_{\text{trans}} \tag{10.5}$$

and the excess kurtosis K

$$K_{x'} = \frac{1}{N}\sum_{i=1}^{N}\frac{\left(x_i' - \mu_{x'}\right)^4}{\sigma_{x'}^4} - 3 \equiv K_{\text{long}} \tag{10.6}$$

$$K_{y'} = \frac{1}{N}\sum_{i=1}^{N}\frac{\left(y_i' - \mu_{y'}\right)^4}{\sigma_{y'}^4} - 3 \equiv K_{\text{trans}}. \tag{10.7}$$

Other event shape variables are the eccentricity ϵ which gives a measure for the cluster's circularity and is defined as

$$\epsilon = \frac{\sigma_{\text{trans}}}{\sigma_{\text{long}}} \tag{10.8}$$

or the fraction $F_{1\sigma_{\text{trans}}}$ of pixels contained within a radius of one σ_{trans}. Additionally, also the length l and width w of a cluster are computed as its extent when projected on the long or short axis respectively. As other information before, the computed event shape variables are stored along with the clusters and can later be used for a background suppression algorithm.

10.1.5 Data post-processing

At the end of the reconstruction chain, each reconstructed cluster along with all the additional information (e.g. time stamp, energy E or event shape variables) is exported from MarlinTPC to a `ROOT` file in form of a `ROOT` tree for further analysis. In the first post-processing step the exported cluster data is joined with the slowcontrol data of CAST. This is done by adding all necessary slowcontrol information to each cluster based on its time stamp. Based on this slowcontrol information the data is divided into three datasets: background, sunset and sunrise. The latter two containing all clusters recorded during the periods when the magnet was tracking the Sun during sunset or sunrise respectively. The remaining clusters are assigned to the background dataset accumulating all periods during which the Sun was not tracked and the magnet was stationary.

10.2 Background reduction using a likelihood method

All of the datasets (background, sunset and sunrise) contain in addition to very few real X-ray photon events a large number of non-X-ray photon events which may originate e.g. from cosmic rays traversing the detector and leaving a trace. In order to gain a high sensitivity for the solar chameleon search a low background rate is crucial. Therefore the non-X-ray photon events have to be suppressed in the datasets. As the typical shape of X-ray photon events (circular/elliptical) is known from e.g. the detector characterization performed in the CDL, event shape information can be used. Here, a likelihood algorithm has been implemented exploiting the reference datasets gathered in the CDL for different X-ray photon energies. As usual for a background suppression it has to be adjusted to let, at best, all real X-ray photon events pass while all non-X-ray photon events are rejected. In reality a trade-off has to be chosen between background suppression on the one hand and software efficiency on the other hand, this is done by selecting a working point.

10.2.1 Likelihood based background reduction

Three event shape variables have been identified which each provide a good separation power individually and can be linked to the known shape of X-ray photon events and the underlying diffusion process. These three variables are the eccentricity ϵ, the length l divided by σ_{trans} and the fraction $F_{1\sigma_{\text{trans}}}$ of pixels contained within a radius of one σ_{trans}, they have already been introduced in the context of the detector characterization in chapter 7. They have been chosen and constructed in a way that they do not depend on the drift properties. Therefore they do not depend on environmental factors such as temperature. This allows for comparison of the characterization datasets and the datasets recorded at CAST without the need of compensating for different conditions. By assigning an energy range to each of the reference datasets (see table 7.1) as done in table 10.1 one can compare the distributions from the CDL measurement campaign (see appendix C) with the distributions during data taking at CAST (see appendix D) showing a good separation power of each of the three variables alone. For convenience the energy ranges, corresponding to the reference datasets A through H have been named a through h.

By combining the three event shape variables in a single likelihood value the separation power is enhanced. Basically, the likelihood value gives a measure for how much a cluster looks like it has originated from an X-ray photon. The likelihood $\mathcal{L}$ for a cluster with measured event shape variables ϵ', $l'/\sigma'_{\text{trans}}$ and $F'_{1\sigma_{\text{trans}}}$ is computed as

$$\mathcal{L}\left(\epsilon', l'/\sigma'_{\text{trans}}, F'_{1\sigma_{\text{trans}}}\right) = P_{\epsilon}\left(\epsilon = \epsilon'\right) \cdot P_{l/\sigma_{\text{trans}}}\left(l/\sigma_{\text{trans}} = l'/\sigma'_{\text{trans}}\right) \cdot P_{F_{1\sigma_{\text{trans}}}}\left(F_{1\sigma_{\text{trans}}} = F'_{1\sigma_{\text{trans}}}\right) \quad (10.9)$$

range	E_{low}/keV	E_{high}/keV	setup	E_{line}/keV
h		0.4	H	0.277
g	0.4	0.7	G	0.525
f	0.7	1.2	F	0.930
e	1.2	2.1	E	1.487
d	2.1	3.2	D	2.984
c	3.2	4.9	C	4.511
b	4.9	6.9	B	5.899
a	6.9		A	8.048

Table 10.1: Energy ranges and corresponding reference datasets for background suppression. Each energy range is defined as $E_{\text{low}} < E \leq E_{\text{high}}$ and E_{line} gives the energy of the main line in the assigned reference dataset. The edges are always approximately centred between two of the reference lines.

or when using the negative logarithm of the likelihood

$$\begin{aligned} -\log\mathcal{L}\left(\epsilon', l'/\sigma'_{\text{trans}}, F'_{1\sigma_{\text{trans}}}\right) = &-\log P_{\epsilon}\left(\epsilon = \epsilon'\right) \\ &-\log P_{l/\sigma_{\text{trans}}}\left(l/\sigma_{\text{trans}} = l'/\sigma'_{\text{trans}}\right) \\ &-\log P_{F_{1\sigma_{\text{trans}}}}\left(F_{1\sigma_{\text{trans}}} = F'_{1\sigma_{\text{trans}}}\right) \end{aligned} \tag{10.10}$$

with $P_x(x = x')$ being the probability for a cluster to feature the value x' for the event shape variable x. The probabilities can be approximated from the reference distributions with the normalized bin height. The negative logarithm of the likelihood $-\log\mathcal{L}$ has the advantage that the multiplication operations are replaced by simple subtraction and that it features larger values which are strictly positive.

Using the reference distributions (see appendix C) for each cluster $-\log\mathcal{L}$ is calculated and stored with the cluster by adding this information to the `ROOT` trees in the `ROOT` file. Of course, based on the cluster's energy E the corresponding reference dataset (and event shape variable distributions) are selected. The $-\log\mathcal{L}$ distributions for the different energy ranges and also the reference datasets themselves can be found in appendix E, for the energy range from 1.2 to 2.1 keV (range e) and reference dataset E (aluminium K_α line at 1.487 keV) the respective distributions are also shown in Fig. 10.2 demonstrating a good separation between non-X-ray photon events and clusters originating from X-ray photons.

10.2.2 Definition of the working point

To define the working point of the likelihood based background suppression method, a cut value has to be chosen for each energy range. By applying the background suppression method to the reference datasets themselves, for each energy range the software efficiency can be estimated which is the fraction of real X-ray photons passing the likelihood cut. The choice of the cut value is always a trade off between software efficiency and background suppression. Assuming that the background dataset (mostly) contains only non-X-ray photon events, the latter can be approximated as the fraction of events from the background dataset being rejected by the cut. This allows for plotting the background suppression as function of the software efficiency, in Fig. 10.3 this is done for energy range e, the plots for all energy ranges can be found in Fig. F.1 in appendix F. From these plots one can conclude that a software efficiency of about 80 % defines a good working point as a large part of the background is suppressed while a further sacrifice in terms of software efficiency would not significantly increase the background

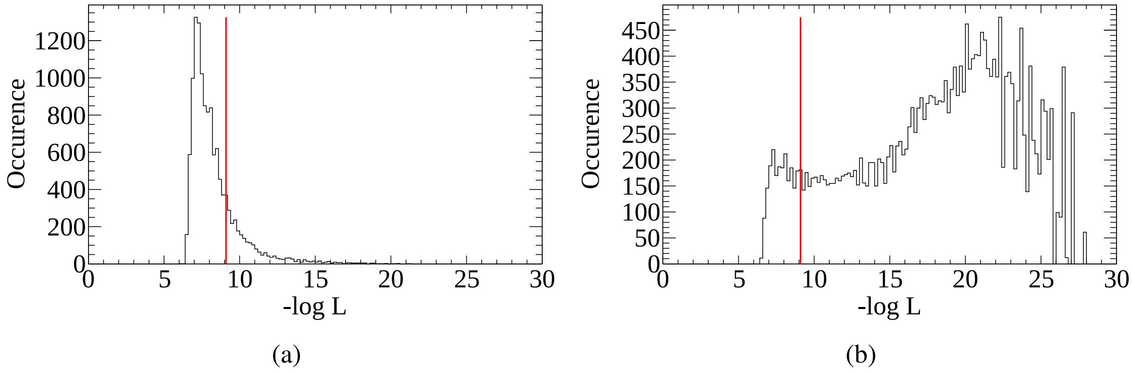

(a)

(b)

Figure 10.2: Likelihood ($-\log\mathcal{L}$) distribution for reference dataset E (a) and energy range e of background dataset (b). The red lines indicate the cut on the likelihood value used to achieve a software efficiency of 80 %.

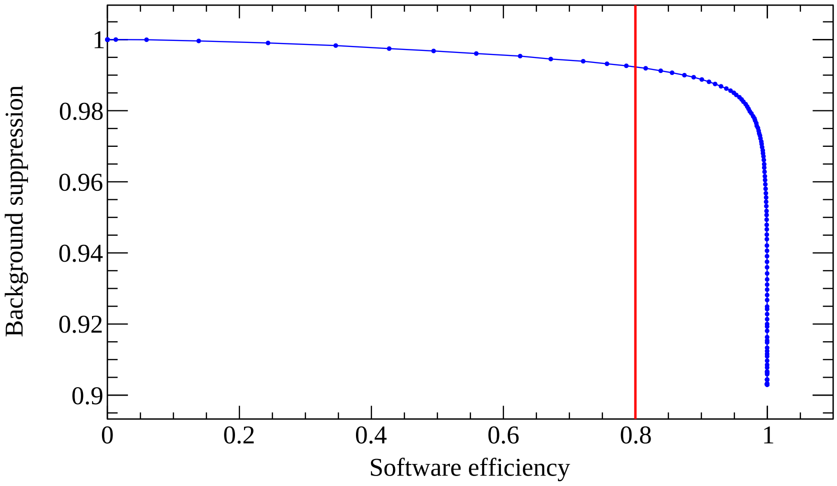

Figure 10.3: Background suppression as function of software efficiency for energy range e. The chosen working point at a software efficiency of 80 % is indicated as red line.

suppression. Applying the 80 % software efficiency condition one gets the likelihood cut values listed in table 10.2 for the eight energy ranges.

As the distributions of the three event shape variables are broadened with decreasing X-ray photon energy (see chapter 7) also the likelihood distributions derived from them become broader for lower X-ray photon energies which is resembled in the cut value required to maintain a software efficiency of 80 % rising with decreasing X-ray photon energy. This, of course, causes the likelihood based background suppression method's power (in terms of background suppression) to decrease for low X-ray photon energies.

10.3 Background rates achieved in 2014 and 2015

Applying the likelihood based background rejection method to the datasets recorded during the data taking campaigns in 2014 and 2015, especially the background dataset, gives the background rate or

energy range	$-\log \mathcal{L}$ cut value
a	7.4
b	7.6
c	7.7
d	8.1
e	9.1
f	9.7
g	10.7
h	11.7

Table 10.2: Likelihood cut values defining the working point with 80 % software efficiency for all energy ranges. Energy ranges are listed in table 10.1.

spectrum of the InGrid based X-ray detector. For the background suppression the working point as defined before in table 10.2 is used. As the event shape variables used for the likelihood, are by design and conception independent of drift properties an additional loose cleaning cut on σ_{trans} is necessary to reject those events which look like clusters originating from X-ray photons but are incompatible with a maximum drift distance of 3 cm. Rejecting events with $\sigma_{\text{trans}} > 1.5$ mm ensures the successful removal of those kind of events without touching the region of possible clusters from X-ray photons.

After applying the background suppression it is wise to first look at the distribution of remaining events over the instrumented area of the InGrid based X-ray detector to identify possible hot spots or regions with different background rates and spectra. For the then defined regions one can examine the background spectra for their rate in different energy regimes and for visible features and discuss their origins.

In a last step it has to be established that indeed the background spectra derived from the background dataset can be used to predict the background contribution in the sunrise dataset which adds to a possible signal from solar chameleons. The easiest way to do this it to check whether the background spectra of the sunset dataset are compatible with the background prediction. During the sunset periods the external and environmental conditions are comparable to those during the sunrise periods while no signal can appear as the detector is pointing away from the Sun.

10.3.1 Distribution of background events

The distribution of events over the GridPix which remain after the background suppression is shown in Fig. 10.4 split in two energy ranges: below and above 2 keV. In general only events with their centre of gravity less than 4.5 mm away from the GridPix' centre should be used as for these it is guaranteed that the event is fully contained on the instrumented area even for maximum drift distance. From the 2 329 101 reconstructed clusters with more than three pixels (found in about 20.7 million frames), 1 074 422 are within the circle of 4.5 mm radius around the GridPix' centre. Of these only 12 719 pass the background suppression. From the distribution of background events is clearly visible that the background rate in the central region of the detector is much lower compared to its outer parts. The most likely reason for a large number of background events accumulating at the edges of the GridPix, and especially at the corners are partial tracks of charged particles traversing the detector mimic X-ray like events. For example a charged particle passing right over the corner of the instrumented area creates a track of primary electrons of which only a part is visible in the detector. Due to truncation at the GridPix' edges this part of a track looks rather roundish and may mimic a cluster originating from an X-ray photon. The only way to discriminate those kind of events would be to instrument the area around the GridPix so that a larger part

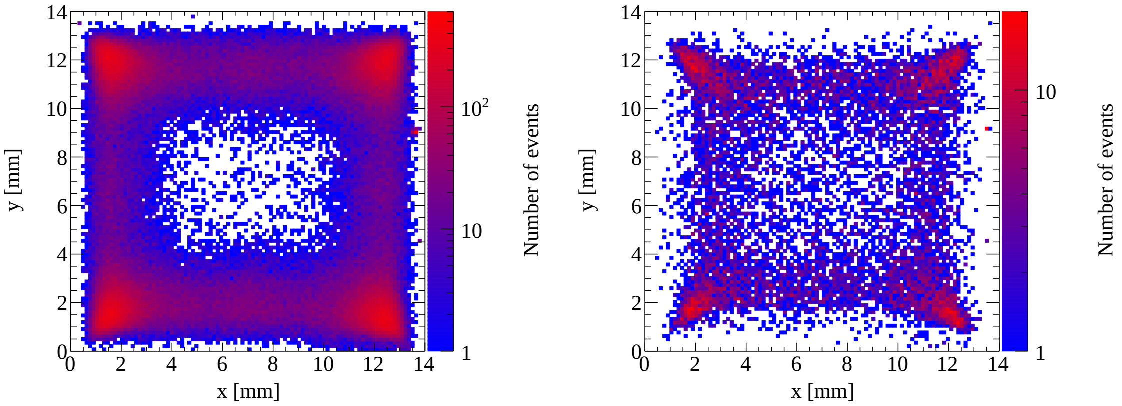

(a) (b)

Figure 10.4: Distribution of background events passing the likelihood based background suppression. (a) shows all events with energies below 2 keV while (b) shows the events above 2 keV. An accumulation of events in the corners and at the edges of the GridPix is visible for both energy ranges. The lowest background rate is achieved in the centre of the detector.

cut	*gold* region	*silver* region
none	524 067	550 355
σ_{trans}	478 109	527 657
$log\mathcal{L}$	1 536	11 183

Table 10.3: Number of events remaining after different stages of the background suppression in gold and silver region. The cuts are applied cumulative.

of the track is visible and reveals its true nature, this path is followed in the upgrade of the detector as described in chapter 12.

As the accumulation of events at the edges and corners is more prominent for energies below 2 keV an additional, possible explanation is that X-ray photons are emitted from detector materials, e.g. the field shaping anode, through fluorescence emission caused by cosmic rays depositing energy in the material. As X-ray photons below 2 keV have a very short range in the detector gas (a few millimetre at most) these could contribute to the events at the edges.

As, with the present background suppression method, the background events at the edges cannot be discriminated further, the instrumented area of the InGrid based X-ray detector is divided into two regions, the *gold* and the *silver* region. The *gold* region is defined as the inner $5 \times 5\,\text{mm}^2$ area around the GridPix' centre and thus shows a lower background rate compared to the *silver* region which is a circle of 9 mm diameter around the GridPix' centre with the *gold* region excluded. The number of clusters in the gold and *silver* region before and after the background suppression are listed in table 10.3, only about 3 ‰ of the clusters in the *gold* region remain.

10.3.2 Background spectrum of different chip regions

Fig. 10.5 shows the background spectra observed in the *gold* and *silver* region respectively before and after application of the likelihood based background suppression method in the range of 0.2 to 10 keV. The background rates are given in the unit $/\text{keV/cm}^2/\text{s}$ which is commonly for detectors used at CAST.

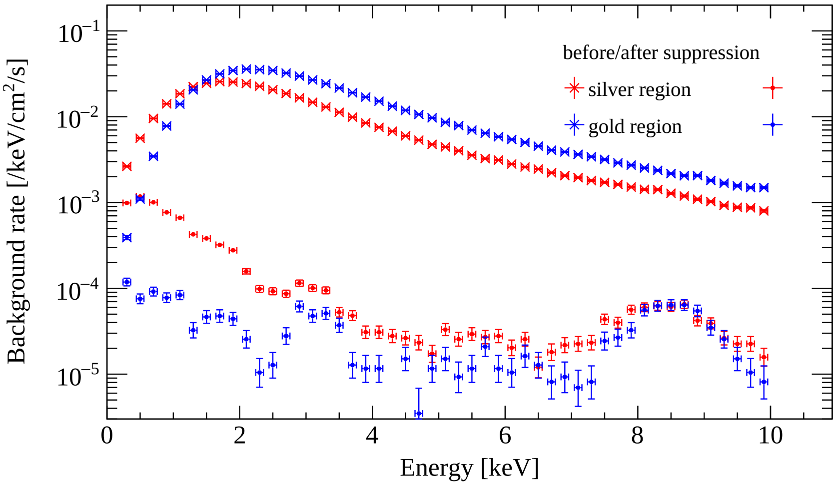

Figure 10.5: Background rates in gold and silver region before and after background suppression.

The raw background rate (before background suppression) is slightly larger in the *gold* region, the reason for this is, that most of the raw background events are tracks parallel to the GridPix' surface and taking into account the different ways to lay a track over the instrumented area results in the events centre of gravity being in the central region of the GridPix.

It is also visible that the power of the background suppression method decreases for lower X-ray energies due to the widening of the reference distributions used to compute the likelihood for each reconstructed cluster. Looking at the individual background spectra of *silver* (Fig. 10.6) and *gold* region (Fig. 10.7) one can see that in the energy range relevant for the solar chameleon search (0.2 to 2 keV) the background rate in the *gold* region is about one order of magnitude lower compared to the *silver* region. Both spectra show visible features (in the *silver* region they are slightly less pronounced): a peak at about 3 keV corresponding to the X-ray fluorescence line of argon (detector gas) and a broad peak slightly above 8 keV. The peak around 8 keV is caused by two effects, on the one hand X-ray fluorescence photons of the copper cathode contribute and on the other hand also charged particle tracks, which traverse the detector perpendicular to the GridPix' surface. Taking into account the drift distance of 30 mm and assuming minimum ionizing particles (MIPs), these tracks, which look rather roundish and X-ray photon like due to diffusion, feature a number of primary electrons along the track which correspond to about 8 to 9 keV. The energy assigned depends on the path length in the detector and therefore on the inclination of the MIP. In both spectra also visible is a small peak at about 5 to 5.5 keV which stems from the escape line corresponding to the copper K_α line at 8 keV.

In the energy range relevant for the solar chameleon search, 0.2 to 2 keV, a background rate below 10^{-4} /keV/cm^2/s is reached in the inner *gold* region (respectively below 10^{-3} /keV/cm^2/s in the *silver* region) while for higher energies a background rate down to a few 10^{-5} /keV/cm^2/s is reached between 4 to 7 keV. Comparing this to the Micro-Mesh Gaseous Structure (MicroMegas) detectors used at CAST which achieve nowadays background rates down to a few 10^{-6} to 10^{-7} /keV/cm^2/s in the range of 2 to 7 keV [35, 59] the InGrid based X-ray detector is, at the moment, not competitive, but in contrast to the MicroMegas detectors, the InGrid based X-ray detector reaches sensitivity below 1 keV and outperforms the silicon drift detector (SDD), used for CAST's first solar chameleon search, by at least one order of magnitude in terms of background rate [42].

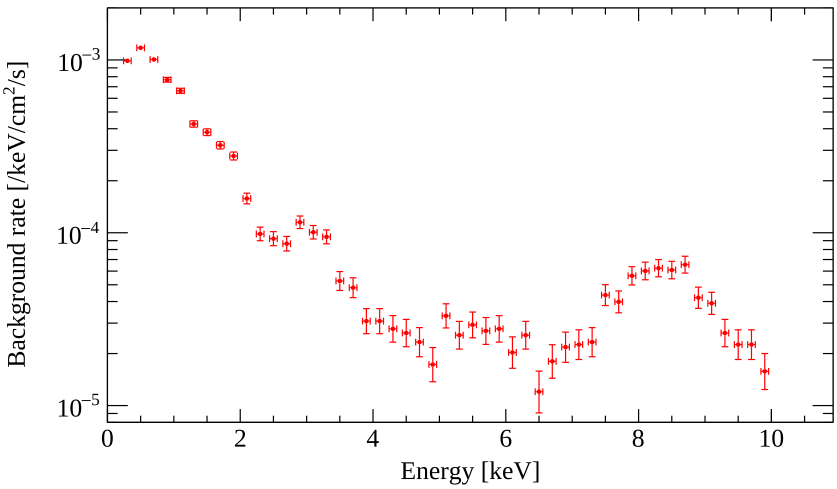

Figure 10.6: Background rate in silver region after application of a likelihood based background suppression method.

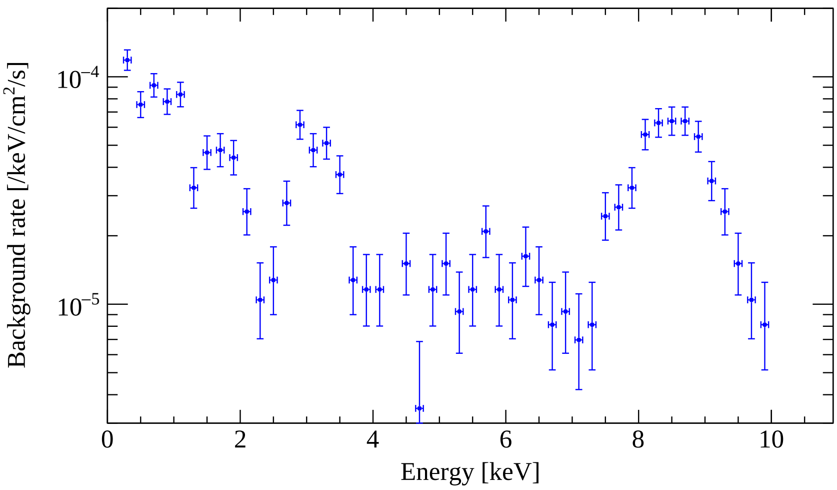

Figure 10.7: Background rate in gold region after application of a likelihood based background suppression method.

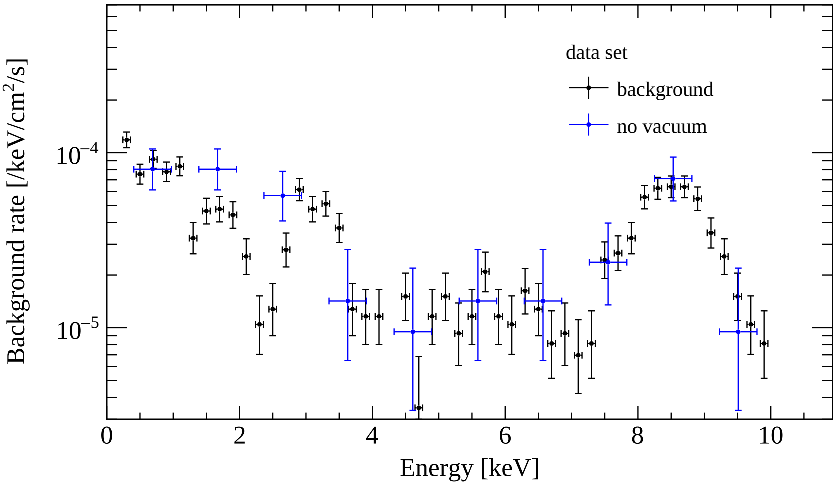

Figure 10.8: Comparison of background rates in gold region between background and no-vacuum dataset after application of a likelihood based background suppression method.

To enable a future reduction of the background rates either by an improved detector design, a better background suppression method or other measures it is crucial to understand where the background events are originating from. For instance, it would be possible that something inside the coldbore, the X-ray telescope (XRT) or the interface vacuum system emits X-ray photons which can enter the detector, e.g. certain types of vacuum pressure gauges may emit low energy X-ray photons due to their working principle. To exclude any significant emitter of X-ray photons inside the vacuum upstream of the detector, end of 2014 for a period of roughly one week, the detector was operated with all upstream gate valves shut and the vacuum region in front of the detector filled with dry nitrogen at atmospheric pressure. A few centimetres of nitrogen at atmospheric pressure are basically opaque for X-ray photons below 2 keV. In case of an X-ray emitter inside the vacuum, the background spectra of this no-vacuum period should deviate from the overall background rate obtained from the background dataset. Comparisons of the spectra for *gold* and *silver* region are shown in Figs. 10.8 and 10.9 respectively. The spectra obtained from the background dataset and the no-vacuum period are in good agreement taking into account the statistical uncertainties. Thus, significant sources of, especially low energy, X-ray photons inside the vacuum can be excluded.

10.3.3 Comparison of background and sunset spectra

Figs. 10.10 and 10.11 show comparisons of the background spectra observed during sunset and background periods for the *gold* and *silver* region respectively. Due to accumulated measurement time of the sunset dataset being much smaller than of the background dataset, for the former the bin width has been increased to achieve reasonable sized statistical errors and avoiding empty bins allowing a decent comparison. One can see that, taking into account the statistical uncertainties, the sunset and background spectra are indeed compatible. Due to the higher overall background rate and therefore higher statistic, this is especially good visible in Fig. 10.11 for the *silver* region where the sunset spectrum very well reproduces the shape of the background spectrum. Based on this comparison, one can justify the assumption, that the background spectra provide a fairly good prediction of the background contribution contained in the sunrise dataset.

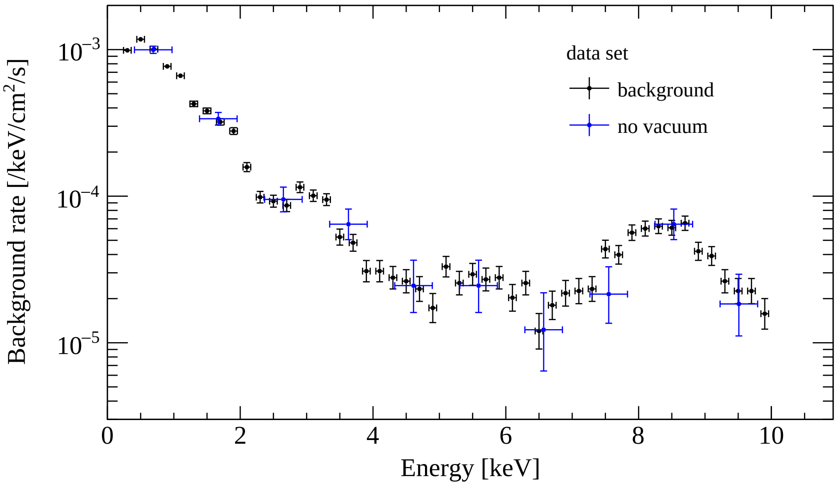

Figure 10.9: Comparison of background rates in silver region between background and no-vacuum dataset after application of a likelihood based background suppression method.

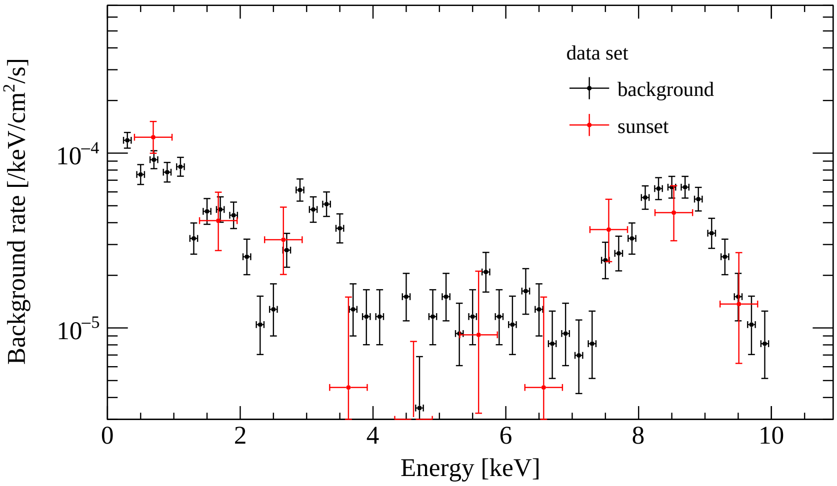

Figure 10.10: Comparison of background rates in gold region between background and sunset dataset after application of a likelihood based background suppression method.

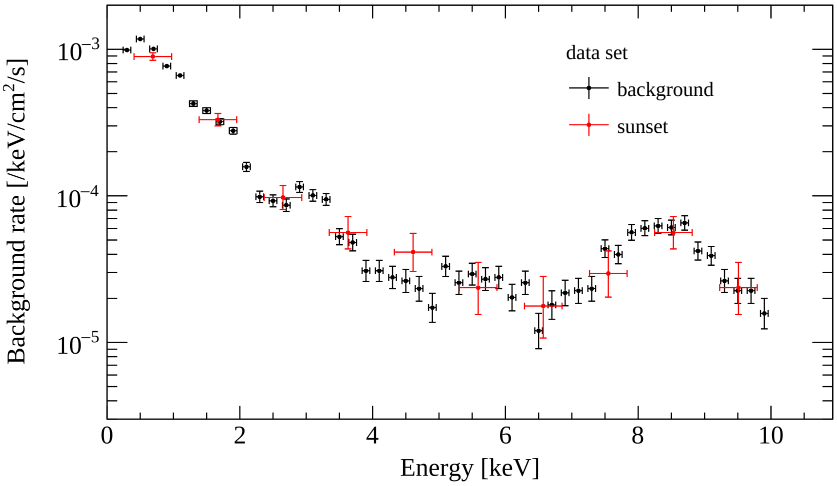

Figure 10.11: Comparison of background rates in silver region between background and sunset dataset after application of a likelihood based background suppression method.

CHAPTER 11

Calculating an upper bound for the chameleon photon coupling

In this chapter an upper bound for the chameleon photon coupling will be computed using a likelihood ratio method. The basic principle of this method will be briefly explained using a simple example, then the tool `TLimit` will be introduced which is the implementation of `mclimit` in `ROOT`. It incorporates the likelihood ratio method and allows to compute confidence levels for given input data from which a limit or upper/lower bound can be derived.

To calculate an upper bound for the chameleon photon coupling from the data taken at the CERN Axion Solar Telescope (CAST) in 2014 and 2015 with the InGrid based X-ray detector `TLimit` is used. It will be explained how the different inputs, required by `TLimit` for the computation of a confidence level, are extracted or generated. While the expected background as well as the data (background plus a possible signal) are extracted from the background and sunrise dataset respectively, the expected signal for a given chameleon photon coupling is generated based on the theoretical prediction and taking into account the imaging of the MPE X-ray telescope (XRT) and the geometry of CAST's coldbore as well as detector properties such as transmission of the different windows, detection efficiency and energy resolution. In addition systematic uncertainties on the generated signal are taken into account by `TLimit`, the estimation of these and their sources will be explained. Prior to unblinding the data (sunrise dataset) the expected upper limit on the chameleon photon coupling is computed and checked for sanity and sensitivity achieved. After unblinding the data, at first it is compared with the background prediction derived from the background dataset. As the measured data is absolutely compatible with the predicted background the signal hypothesis is rejected and an observed upper bound on the chameleon photon coupling is computed.

11.1 Likelihood ratio and confidence level

To discriminate between two hypotheses, a test statistic is required. In general the likelihood ratio is a good, or even optimal, choice for the latter in terms of separation (or decision) power [120, 121]. In the context of the search for solar chameleons described here, the two hypotheses are that the observed data d can be explained either with the expected background b or the expected background plus an additional signal s, hence $b + s$. In this case the likelihood ratio X is the ratio of the likelihoods $\mathcal{L}$ for both hypotheses:

$$X(d) = \frac{\mathcal{L}_{b+s}(d)}{\mathcal{L}_b(d)}. \tag{11.1}$$

Assuming that each individual measurement d_i (e.g. bins of a histogram like an observed energy spectrum) can be treated as an individual counting experiment [120] one can write X as

$$X(d) = \prod_{i=1}^{n} X_i = \prod_{i=1}^{n} \frac{\mathcal{L}_{b+s,i}(d_i)}{\mathcal{L}_{b,i}(d_i)} \tag{11.2}$$

with n the dimension of d. Furthermore, when the observed (and expected) counts d_i are small it is possible to approximate a likelihood by a Poisson distribution [120], giving

$$X_i = \frac{e^{-(b_i+s_i)}(b_i + s_i)^{d_i}}{d_i!} \cdot \frac{d_i!}{e^{-b_i} b_i^{d_i}} \tag{11.3}$$

with b_i and s_i being the expected values for background and signal contribution in bin i. To make a decision between hypotheses b and $b + s$ based on the observed value of the likelihood ratio $X_{\text{obs}} \equiv X(d)$ typically confidence levels (CLs) are used. The confidence level CL_b is defined as the probability to observe a smaller likelihood value compared to the observed one given that the background hypothesis is true:

$$\text{CL}_b = P_b(X \leq X_{\text{obs}}) \tag{11.4}$$

where P_b is usually calculated using Monte Carlo techniques. $1 - \text{CL}_b$ gives the probability for falsely accepting the background plus signal hypothesis although the background hypothesis is true. Analogue to CL_b a similar expression is defined for the $b + s$ hypothesis:

$$\text{CL}_{b+s} = P_{b+s}(X \leq X_{\text{obs}}) \tag{11.5}$$

where again P_{b+s} usually is computed by means of Monte Carlo techniques. CL_{b+s} gives the probability to falsely reject the background plus signal hypothesis although it is true. Often instead of CL_{b+s} the quantity

$$\text{CL}_s = \frac{\text{CL}_{b+s}}{\text{CL}_b} \tag{11.6}$$

is used as it is more stable against underfluctuations in the observed data [120] ($d_i < b_i$). To exclude a signal (or background plus signal) hypothesis usually the quantity CL_s is used, for given data, a signal can be excluded at a CL of $1 - \text{CL}_s$. Often $\log X$ is used instead of X as it eases the computation.

In the following the application of the likelihood ratio method will be illustrated in a simple, single bin example. For a single bin the CLs can easily be computed analytically.

The software `mclimit` [120] implements the likelihood ratio method and Monte Carlo based computation of the different CLs. It is also implemented in `ROOT` as `TLimit`. For the computation of the upper bound on the chameleon photon coupling in the course of this thesis `Tlimit` is used, its interface, required inputs and possible outputs will be briefly introduced here.

11.1.1 A simple example

To illustrate the exclusion of a signal hypothesis a simple, single bin example can be used. Assuming a counting experiment with an expected mean number of background counts $b = 4.5$ and a signal hypothesis predicting $s = 5.5$ counts in addition to the expected background, one can compute the likelihood ratio distributions for both the background and the background plus signal hypothesis. The distributions are shown in Fig. 11.1. The observed $\log X_{\text{obs}}$ for an observed number of counts $d = 5$ is

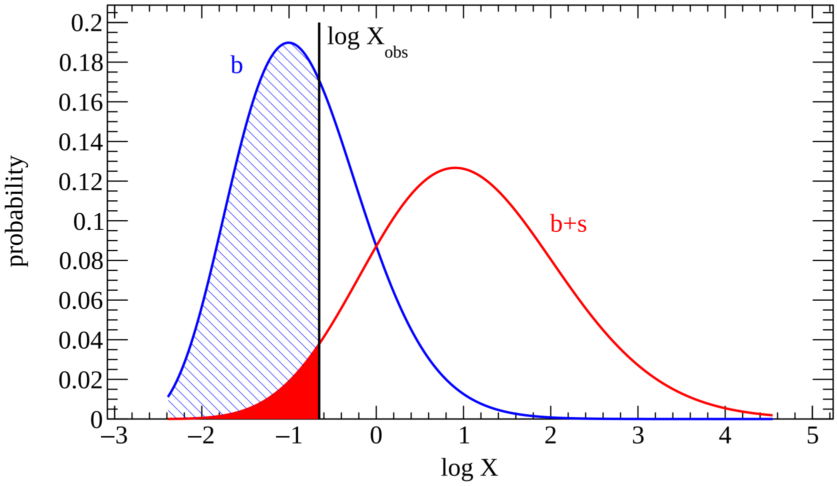

Figure 11.1: Likelihood ratio curves for background (b) and signal ($b + s$) hypothesis for a simple, single bin example. The expected mean number of background counts is 4.5 while the expected mean number of additional signal counts is 5.5. The observed likelihood ratio value X_{obs} for an observed number of counts of 5 is indicated as black line. The shaded regions indicate the meaning of CL_b (hashed blue) and CL_{b+s} (solid red) as cumulative probabilities. For the given example the signal hypothesis may be rejected at a CL of 93 % using CL_{b+s}.

shown in the plot and the area under the curves corresponding to CL_b and CL_{b+s} are highlighted. For the simple example shown one finds $\text{CL}_b \approx 0.7$ and $\text{CL}_{b+s} \approx 0.07$, thus allowing to exclude the hypothetical signal at a CL of 93 % (or 90 % when using CL_s instead of CL_{b+s}).

11.1.2 TLimit – The ROOT implementation of mclimit

`TLimit` is the `ROOT` implementation of the `mclimit` [120] code. The latter implements the likelihood ratio method for small number of counts in many independent search channels such as e.g. bins in an observed energy spectrum. The likelihood ratio distributions and the corresponding CLs are computed using Monte Carlo techniques. `mclimit` as well as `TLimit` allow for taking into account statistical as well as systematic uncertainties of the background and signal prediction.

`TLimit` supports multiple search channels. For each channel a set of three histograms (of identical binning and range) is required: the background prediction, the expected signal and the observed data. The bin errors of signal and background histograms are used as statistical uncertainty on the individual bins of signal and background prediction. Additionally, for both the expected signal and the background prediction a set of systematic uncertainties can be given which is taken into account in the Monte Carlo based computation of the likelihood ratio distributions as well as the CLs. The systematic uncertainties can differ between different channels fed into `TLimit`.

For each channel as set of histograms is given: expected signal, expected background and observed data. The different CLs are then calculated on the basis of a Monte Carlo simulation, taking into account statistical as well as systematic uncertainties. CL_b, CL_{b+s} and CL_s are derived from the input data. Also, the expected value for CL_s under assumption of the background hypothesis, $\left\langle \text{CL}_s \right\rangle_b$, can be computed. For this, not the observed data is used, but artificial data is produced through a Monte Carlo simulation according to the predicted background. This allows for calculating a prediction (including an uncertainty) for any lower/upper bound prior to unblinding the data.

11.2 Deriving an upper bound for the chameleon photon coupling

To derive an upper bound for the chameleon photon coupling one can use `TLimit`. Given the histograms containing the expected background and signal as well as the observed data `TLimit` for all channels allows for computing the corresponding observed CL_s value as well as the expected $\left\langle \mathrm{CL}_s \right\rangle_b$ value and its uncertainty. By rescaling the expected signal(s) according to their β_γ^4 dependence it is possible to compute the observed CL_s value as well as the expected $\left\langle \mathrm{CL}_s \right\rangle_b$ value for different values of β_γ. To find the 95 % CL limit, β_γ is reduced stepwise until

$$\mathrm{CL}_s < 5\,\%$$

is reached, which corresponds to a probability of more than 95 % to measure data looking more signal like compared to the data observed given the signal hypothesis is true. The same can be done with respect to $\left\langle \mathrm{CL}_s \right\rangle_b$ to get the expected upper bound on β_γ, and its uncertainty. The expected limit can be computed prior to unblinding the observed data, allowing for checking the limit calculation and procedure.

To derive an upper bound for the chameleon photon coupling from the measurements performed with the InGrid based X-ray detector two channels are used which are the *gold* and *silver* region of the chip which are treated separately due to the large difference in background rates. The expected background is estimated from the measured background datasets giving reasonably low statistical uncertainty due to the long measurement time available for the background estimation. For the expected background histograms the statistical bin errors are used to describe the uncertainty of the background prediction. The expected signal is computed using the theoretical prediction from [42] and [43]. To get the signal, which could be observed in the InGrid based X-ray detector, its efficiency and energy resolution (see chapter 7) as well as the software efficiency of the likelihood based background suppression method (see chapter 10) are taken into account. Also, the imaging of the MPE XRT including its off-axis behaviour and transmission are incorporated along with the geometry of the CAST magnet and its influence on the signal and chameleon image. For the expected signal a set of systematic uncertainties is identified and estimated. `TLimit` allows to include these, to model the uncertainty of the signal prediction.

With the expected background and signal histograms for both the *gold* and the *silver* region the expected 95 % CL limit on β_γ can be computed prior to unblinding the observed data. In case the signal hypothesis can be rejected, the observed limit is derived from the observed data. As `TLimit` uses Monte Carlo techniques to compute the different CL_s and $\left\langle \mathrm{CL}_s \right\rangle_b$ each step at a given β_γ takes a certain amount of time. Therefore, a fine scan of the range $10^{10} < \beta_\gamma < 10^{11}$ would take a lot of time. To fasten up the limit finding, at first a coarse scan of β_γ from 10^{11} down to 10^{10} is performed with a step width of 10^9. After the coarse expected or observed 95 % CL upper bound is identified, a finer scan around the coarse values is done using a step width of 10^8 to compute the final expected or observed 95 % CL upper bound on the chameleon photon coupling β_γ.

11.2.1 Computing the expected signal

The expected signal is computed using the theoretically predicted spectrum [42] and taking into account the effects and influence of the X-ray optics (transmission, off-axis behaviour and imaging), the characteristics of the InGrid based X-ray detector (efficiency and energy resolution) as well as the software efficiency of the used likelihood based background suppression method. In a last step the observable spectrum is translated into number of observable counts in dependence of X-ray energy by scaling it to the measurement time of the sunrise dataset and filling the signal histogram with the resulting data.

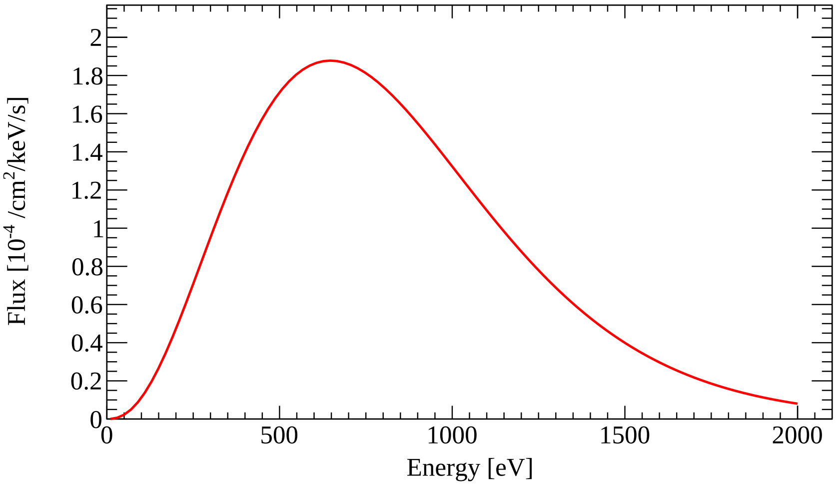

Figure 11.2: Photon flux from solar chameleons reconverting in a 9.26 m long 9 T magnet (CAST magnet). Flux is computed with $\beta_\gamma = \beta_\gamma^{\mathrm{sun}}$ and for the tachocline being at 0.7 $R_\odot$ with a width of 0.01 $R_\odot$ and a tachocline magnetic field of 10 T for a chameleon model with index $n = 1$ and non-resonant chameleon production. Flux is taken from [42].

The solar chameleon spectrum

The expected solar chameleon spectrum can be computed numerically and depends on the chameleon photon coupling β_γ, the index n describing the chameleon model, the position and width of the solar tachocline as well as the magnetic field within the tachocline, for details about the prediction of the solar chameleon emission see chapter 3 as well as references [42, 43, 122]. Taking into account the reconversion of solar chameleons to X-ray photons in the CAST magnet (magnetic field of 9 T over a length of 9.26 m [42]) and assuming a chameleon model with $n = 1$ one gets the expected photon flux from solar chameleons as shown in Fig. 11.2, which was computed in [42] for a tachocline located at 0.7 $R_\odot$ featuring a constant magnetic field of 10 T over a tachocline width of 0.01 $R_\odot$ and $\beta_\gamma = \beta_\gamma^{\mathrm{sun}}$, the upper bound on the chameleon photon coupling derived from a solar luminosity bound (for the given model and assumptions on the tachocline $\beta_\gamma^{\mathrm{sun}} \approx 6.457 \times 10^{10}$ [42]). For this flux non-resonant production of chameleons in the Sun was assumed, restricting the chameleon matter coupling to $1 < \beta_m < 10^6$. The magnitude of the photon flux from solar chameleons scales with β_γ^4 allowing an easy computation of the flux for different values of β_γ through simple rescaling of the spectrum shown in Fig. 11.2.

The chameleon image of the Sun as seen through the MPE XRT and CAST

The photon flux numerically predicted in [42, 43] (see also Fig. 11.2) does not take into account the geometry of the CAST magnet except for its length, it merely gives the flux from reconverted solar chameleons for a 9.26 m long 9 T magnet of infinite transverse dimension. The vacuum pipe inside CAST's magnet, also called coldbore, has an inner diameter of 43 mm. Only those photons passing through the sunrise end of the coldbore can enter the MPE XRT and be focused onto the InGrid based X-ray detector. As the angular size of the tachocline is larger than the opening aperture of CAST's coldbore, not all possible trajectories of recovered X-ray photons entering the XRT pass through the full length of the coldbore, but a reduced length l, as depicted in the sketch shown in Fig. 11.3. Only

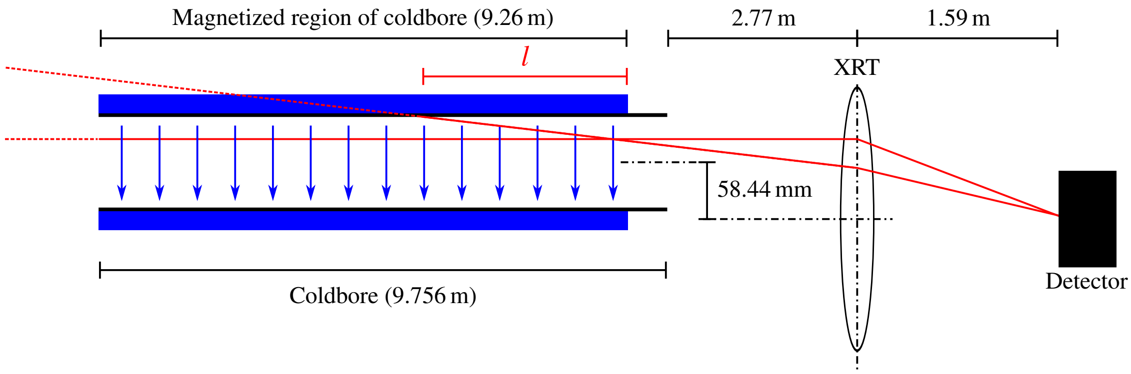

Figure 11.3: Sketch illustrating chameleon trajectories (red) inside the CAST coldbore. Chameleons can only convert into X-ray photons within the magnetized region of the coldbore (blue). Only those X-ray photons can reach the XRT which pass through the end of the coldbore. For chameleons not passing directly through the coldbore's entrance (left side) the length available for conversion is not the full length of the magnetized coldbore but a reduced length l. Not to scale.

chameleons converting inside the coldbore can reach the XRT. The chameleon to photon conversion probability (see equation 3.20 in chapter 3) depends on l^2, therefore this has to be taken into account for the expected signal observable with the detector.

The X-ray photons reaching the MPE XRT are focused towards the detector (see chapter 8 for a brief description of the MPE XRT working principle). The efficiency (or transmission) of the MPE XRT depends on the X-ray photon energy as well as the off-axis angle under which the X-ray photon enters the XRT [54, 56–58]. The energy dependence of the MPE XRT's on-axis efficiency (or transmission) was re-evaluated at the X-ray test facility PANTER in January 2014 [62] and shown in Fig. 11.4, for the energy range relevant for the solar chameleon search (up to 2 keV) it's approximately constant. The off-axis behaviour is a decrease with the off-axis angle which can be approximated as linear [54] and can be characterized by the relative efficiency (or transmission) at an off-axis angle of $10'$. For energies below 2 keV it decreases to 62.2 % of the on-axis value [56]. For higher energies the loss of efficiency is much higher, e.g. at an energy of 8 keV at an off-axis angle of $10'$ the transmission drops to about 12 % of the on-axis value [54, 56].

To get the expected chameleon image of the Sun as it would be observable with the InGrid based X-ray detector a simple ray tracing Monte Carlo is performed, similar to the one used in the analysis of the silicon drift detector (SDD) data [42]. A number of random points (typically 10 000) on the coldbore's sunrise end, uniformly distributed over the area, is generated. For each of these points, typically, 1 000 random points within the Sun's tachocline are created giving a set of possible (chameleon) trajectories for each point on the coldbore's end. For each trajectory the path length l within the coldbore is calculated and the trajectory weighted with $l^2/(9.26\,\mathrm{m})^2$ according to the l^2 dependence of the chameleon photon conversion probability. To model the focusing through the MPE XRT the XRT is approximated by a lens with the correct focal length f of 1.6 m [54] and the correct position relative to the coldbore. Using ray transfer matrices the trajectory behind the XRT is computed and the corresponding position on the detector's X-ray entrance window is derived. To take into account the XRT's off-axis behaviour each trajectory is additionally weighted with the relative transmission of the XRT depending on its angle to the optical axis of the XRT. Taking into account the weights of the trajectories and the energy dependence of the XRT's transmission one can predict the chameleon image of the Sun as it would be observed. To

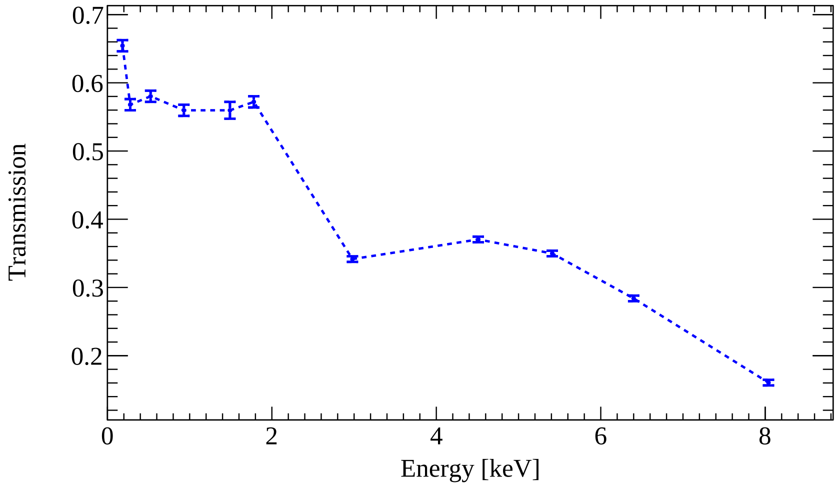

Figure 11.4: On-axis transmission of the MPE XRT as function of X-ray energy. The data points stem from the recalibration at the X-ray test facility PANTER in January 2014 [62]. The dashed line shows a linear interpolation between the measured points.

incorporate the energy dependence of the MPE XRT the expected photon flux (see Fig. 11.2) is folded with the XRT's transmission curve (see Fig. 11.4), transmission at a given energy is interpolated linearly between neighbouring data points from the calibration at the X-ray test facility PANTER [62]. Using the coldbore area of 14.5 cm^2 and integrating over energy one ends with the chameleon image of the Sun which is shown in Fig. 11.5 as observable with the detector (the differential window of the interfacing vacuum system is not considered here). The ring-like image is caused by the emission from the tachocline instead of the Sun's core. The rectangular *gold* and circular *silver* regions are indicated in the chameleon image of the Sun. The solar chameleon image is slightly off centre, this caused by the optical axis of the XRT being parallel but not coaxial to the optical axis of the coldbore.

A significant part of the image is outside the *gold* and *silver* regions but cannot be used for the chameleon search here as first of all the background level in the outer regions of the detector is even larger than in the *silver* region, spoiling any sensitivity in these detector regions and second, events recorded in those regions may not be fully contained within the sensitive area making a meaningful energy measurement and background suppression difficult and error-prone. The X-ray photon fluxes originating from solar chameleons reconverting inside the CAST magnet reaching the detector's X-ray entrance window above *gold* and *silver* region are shown in Fig. 11.6.

Detector efficiencies and energy resolution

To incorporate the detector efficiencies including the transmission curves of the differential and the X-ray entrance window as well as absorption in the gas volume, the previously computed X-ray photon fluxes reaching the X-ray entrance window above *gold* and *silver* region (see Fig. 11.6) are folded with the detector's efficiency curve (including the differential window), see Fig. 7.23. As the absorption for energies below 2 keV is close to 100 % at 1 050 mbar(a) the resulting spectra are mostly influenced by the window transmissions. The resulting fluxes for *gold* and *silver* region are shown in Fig. 11.7.

The energy resolution is energy dependent and was measured during the characterization campaign carried out in the CAST Detector Lab (CDL) at CERN (see chapter 7 for details). Fig. 7.27 shows the

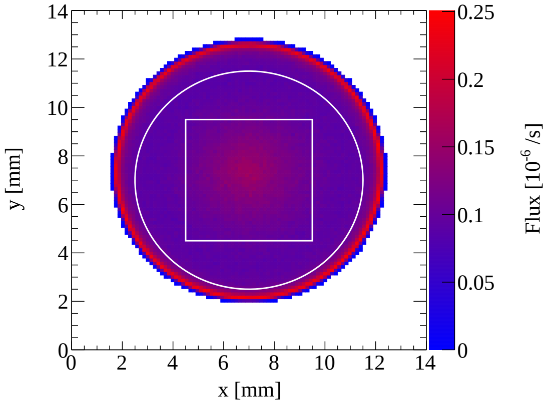

Figure 11.5: Chameleon image of the Sun as seen through CAST and the MPE XRT with the InGrid based X-ray detector. The instrumented area of the detector is depicted and on the z-axis the integrated flux from reconverted solar chameleons to X-ray photons is shown colour coded. The bright outer ring is caused by the emission within the shell like solar tachocline. The *gold* region is depicted as white square while the *silver* region is defined by the area between the white circle and the white square of the *gold* region. The image has been produced by a simplified ray tracing and incorporates the geometry of the CAST magnet as well as the effect of the X-ray optics including its off-axis behaviour.

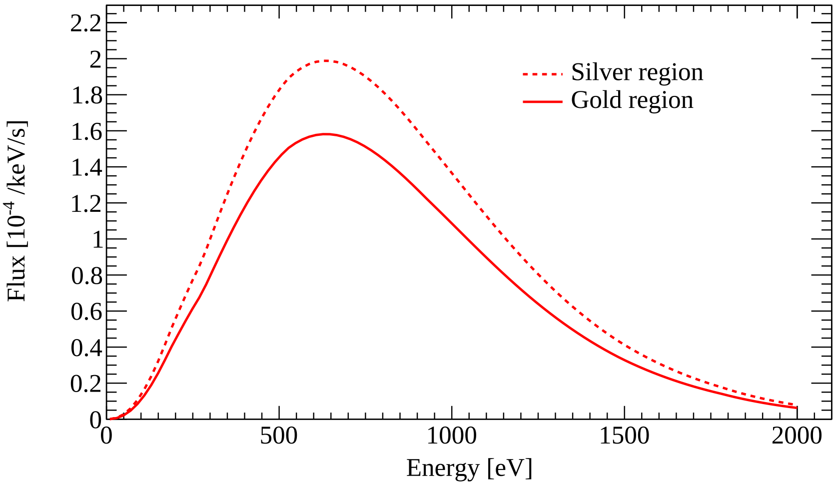

Figure 11.6: X-ray spectrum from reconverted solar chameleons as observable behind the MPE XRT, the differential window is not taken into account here. The flux is shown separately for *gold* (solid line) and *silver* region (dashed line) as function of photon (chameleon) energy. The influence of the CAST magnet's geometry as well as the focusing and transmission of the MPE XRT were included in a simplified ray tracing described in text, including the XRT's off-axis behaviour.

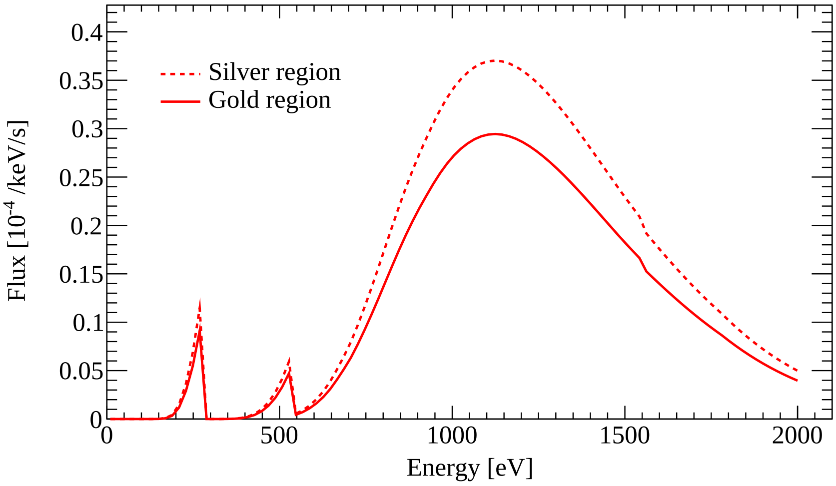

Figure 11.7: X-ray spectrum from reconverted solar chameleons as observable with the InGrid based X-ray detector. In addition to the effects of the CAST magnet's geometry and the behaviour of the MPE XRT, the efficiency curve of the InGrid based X-ray detector was taken into account including both windows (differential and X-ray entrance window) as well as the detector's absorption efficiency. The resulting flux is shown separately for *gold* (solid line) and *silver* region (dashed line) as function of photon (chameleon) energy.

energy resolution as a function of energy. The energy resolution for a given energy can be interpolated linearly between neighbouring data points, of course omitting the outlying data point from set-up G where the main peak could not be separated from close by lines most likely originating from target contaminants. By smearing the flux spectra from Fig. 11.7 according to the energy dependent energy resolution one gets the X-ray photon fluxes as they actually should be recorded by the detector.

Software efficiency

As all data recorded is passed through the likelihood based background suppression method (see chapter 10) after reconstruction, the resulting software efficiency has to be taken into account. The working point of the background suppression method was adjusted to achieve an efficiency of 80 % for all energy ranges, the spectra simply have to be scaled by a factor 0.8.

Creation of the signal histograms

In the last step the expected signal is computed from the calculated fluxes for *gold* and *silver* region by taking into account the total measurement time of the sunrise dataset and filling the signal histograms for *gold* and *silver* region. The signal histograms range from 0.2 to 2 keV divided into nine bins. The number of nine bins is chosen to avoid empty bins in the measured data histograms. The energy threshold of 0.2 keV accommodates for the fact that chameleons with very low energy are not able to pass through the lead shielding of CAST's sunset detectors as their effective mass in lead would be higher than their energy. The maximum effective mass of chameleons in lead is 135 eV ($n = 1$ and $\beta_m = 10^6$) [42]. The histograms with the expected signal for $\beta_\gamma = \beta_\gamma^{\mathrm{sun}}$ are shown in Figs. 11.8 and 11.9 for *gold* and *silver* region respectively. Although the expected signal is larger in the *silver* region, due to the lower background rate the *gold* region contributes most to the sensitivity.

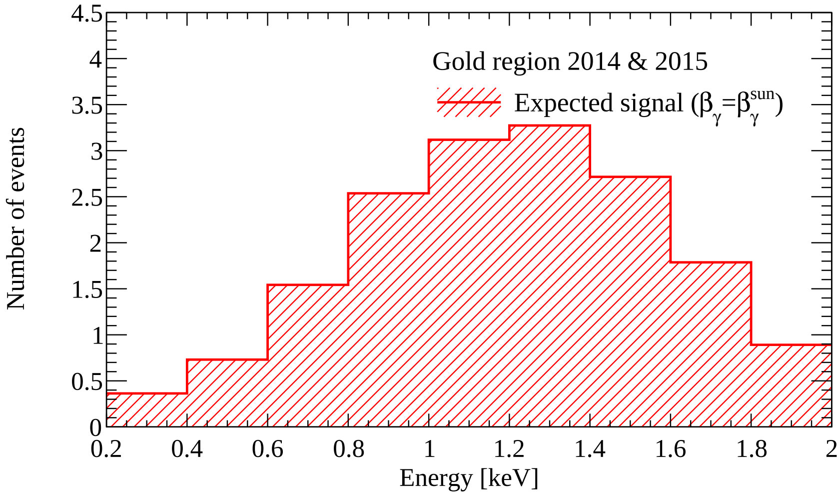

Figure 11.8: Expected solar chameleon signal in the gold region. Solar chameleon spectrum with $\beta_\gamma = \beta_\gamma^{\text{sun}}$ is assumed for the tachocline located at $0.7\,R_\odot$ with a width of $0.01\,R_\odot$ and a tachocline magnetic field of 10 T for a chameleon model with index $n = 1$ and non-resonant chameleon production.

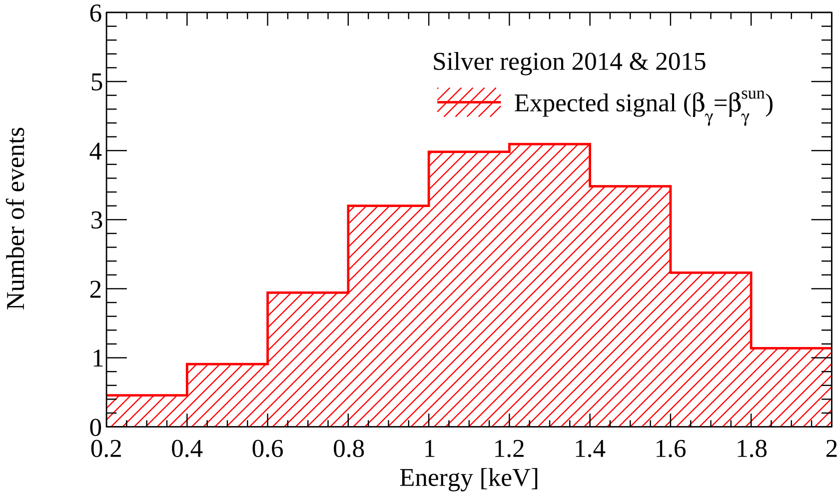

Figure 11.9: Expected solar chameleon signal in the silver region. Solar chameleon spectrum with $\beta_\gamma = \beta_\gamma^{\text{sun}}$ is assumed for the tachocline located at $0.7\,R_\odot$ with a width of $0.01\,R_\odot$ and a tachocline magnetic field of 10 T for a chameleon model with index $n = 1$ and non-resonant chameleon production.

11.2.2 Extracting the measured data

The data histograms (*gold* and *silver* region) for `TLimit` are created by applying the likelihood based background suppression method (adjusted to the working point with 80 % software efficiency) to the sunrise dataset. The remaining events, split into *gold* and *silver* region are filled into histograms using the same range and binning as the signal histograms, 0.2 to 2 keV divided into nine bins. Until the data histograms are unblinded to check for a possible excess compared to the expected background or the computation of an observed upper bound of the chameleon photon coupling β_γ, dummy data is used as `TLimit` requires non-empty data histograms to allow calculation of expected CL_s values.

11.2.3 Extracting the expected background

To create the background histograms containing the expected background events for *gold* and *silver* region respectively, the measured background is extracted from the background dataset using the likelihood based background suppression method using the working point defined to achieve 80 % software efficiency for the full energy range. These are split into *gold* and *silver* region. To get the expected number of background events contained in the data histograms the resulting background histograms are scaled to the total measurement time of the sunrise dataset. The statistical bin errors are, of course, scaled accordingly and set explicitly as binwise statistical uncertainty on the expected background. The two resulting background histograms (*gold* and *silver* region) use the same range and binning as the signal histograms, 0.2 to 2 keV divided into nine bins.

11.2.4 Estimation of systematic uncertainties

Systematic uncertainties are assumed to only affect the expected signal, the uncertainty of the different bins of the background histograms are considered completely statistical and are taken care of by `TLimit`. However, for the computation of the expected signal a set of systematic uncertainties has been identified corresponding to nine independent sources for a systematic deviation. The nine resulting systematic uncertainties are linked to the following effects:

- **Pointing accuracy**; CAST is tracking the Sun with a precision of less than 10 % of the solar radius [35], corresponding to a pointing accuracy of $1.6'$

- **Detector alignment**; the precision of the detector alignment with the MPE XRT is estimated to be 0.5 mm considering the spot size used in the laser alignment procedure as well as the results of the X-ray finger measurements

- **XRT off-axis behaviour**; the (approximately) linear off-axis behaviour of the MPE XRT is characterized by the relative transmission at $10'$ off-axis, the value is given with 62.2 % [56] and an uncertainty of ±2.2 % is considered based on the uncertainty stated for the latest calibration measurement of the MPE XRT at an energy of 1.5 keV [62]

- **XRT on-axis transmission**; the data points from the latest characterization of the MPE XRT [62] are used to interpolate the on-axis transmission at a given energy, measurement uncertainties are stated for each data point

- **differential window transmission**; the uncertainty on the thickness of the differential window is assumed to follow the tolerances of ±10 % as stated by suppliers

	systematic uncertainty	
chip region	gold	silver
pointing accuracy	3.0 %	9.0 %
detector alignment	1.0 %	5.0 %
XRT off-axis behavior	1.5 %	3.0 %
XRT on-axis transmission	1.8 %	
differential window transmission	1.7 %	
detector window transmission	3.9 %	
detector window optical transparency	2.0 %	
detector gas absorption	0.1 %	
software efficiency	3.7 %	
total	7.2 %	12.4 %

Table 11.1: List of estimated systematic uncertainties for the scenario with the tachocline region starting at $0.7\,R_\odot$ and with a width of $0.01\,R_\odot$. The uncertainties resulting from imaging effects differ for *gold* and *silver* region and are therefore stated separately if necessary.

- **detector window transmission**; the uncertainty on the thickness of the detector window is assumed to follow the tolerances of ±10 % as stated by suppliers

- **detector window optical transparency**; the rib width of the detector window's strongback was measured to vary between 250 µm and 350 µm affecting the optical transparency of the strongback structure

- **detector gas absorption**; although the detector gas pressure is kept constant at 1 050 mbar by an inlet pressure regulator, the gas temperature varies approximately between 285 and 305 K due to temperature changes inside the experimental hall, this slightly affects the absorption curve

- **software efficiency**; the software efficiency achieved in the data recorded at CAST may vary from the software efficiency achieved in datasets from the detector characterization which are used to define the working point at a nominal software efficiency of 80 %.

To estimate the value for most of the systematic uncertainties the corresponding input parameters are varied within their respective accuracy, precision, tolerance or uncertainty and the effect on the integrated signal is studied and quantified. If necessary the resulting variation is translated into a standard deviation. For the systematic uncertainty assumed on the software efficiency, the software efficiency is measured at the energies 2.93 and 5.75 keV using the datasets from the daily calibration runs. From the total of 189 calibration runs the standard deviation for the measured software efficiency is computed and assumed to be a proper estimate for the systematic uncertainty. As the energy range for the chameleon search is below the energies used to quantify the spread in software efficiency this is assumed to be even a conservative estimator as with decreasing energy the event shape variable distributions used in the background suppression method widen resulting in a larger acceptance and smaller impact of slight variations and shifts in the distributions. The resulting systematic uncertainties for the benchmark chameleon model can be found in table 11.1, for other models (with different tachocline parameters) can be found in appendix G.

11.2.5 Calculating the expected limit on the chameleon photon coupling

Prior to unblinding the sunrise data and computing the observed upper limit on the chameleon photon coupling β_γ, one can compute the expected upper limit by using only the expected background and signal histograms for *gold* and *silver* regions of course taking into account the statistical uncertainty on the expected background as well as the estimated systematic uncertainties on the expected signal. To find the expected 95 % CL upper limit the output $\left\langle \mathrm{CL}_s \right\rangle_b$ is used which is the expected CL_s value assuming the *background* only hypothesis.

Assuming the, kind of, benchmark solar chameleon model also treated in CAST's first chameleon search [42] with index $n = 1$, the tachocline located at $0.7\,R_\odot$ with a width of $0.01\,R_\odot$ and a tachocline magnetic field of 10 T one gets an expected upper limit on the chameleon photon coupling of

$$\beta_\gamma < \left(5.53^{+0.52}_{-0.43}\right) \times 10^{10} \tag{11.7}$$

at 95 % CL for $1 < \beta_m < 10^6$. This fits to the rough assumptions made on base of the improvement in key figures compared to the SDD used for CAST's first solar chameleon search. Compared to the observed upper limit achieved in the latter search ($\beta_\gamma < 9.26 \times 10^{10}$ at 95 % CL for $1 < \beta_m < 10^6$ [42]) the expected improvement is about a factor of 1.6 which translates to an improvement in terms of signal s over square-root of background b of a factor 7.6 according to

$$\beta_\gamma^4 \propto \frac{\sqrt{b}}{s}. \tag{11.8}$$

The expected upper bound on the chameleon photon coupling β_γ derived here is below the upper limit derived from a luminosity bound of the sun. At maximum 10 % of the solar luminosity are allowed to be emitted in form of chameleons [42], giving an upper limit of

$$\beta_\gamma^{\mathrm{sun}} = 10^{10.81} \approx 6.46 \times 10^{10}. \tag{11.9}$$

Thus, with the solar chameleon search conducted at CAST a sensitivity beyond the solar luminosity bound is expected, Fig. 11.10 shows the expected improvement of CAST's upper bound on the chameleon photon coupling β_γ in relation to the solar luminosity bound.

11.2.6 Unblinding of data

With the analysis tools, the estimated systematic uncertainties as well as the expected upper bound on chameleon photon coupling β_γ fixed, the sunrise data can be unblinded. To check for a possible excess of X-ray photons below 2 keV during the sunrise periods during which the CAST magnet was tracking the sun, the observed data (of course after background suppression) is compared to the expected background extrapolated from the measured background rate and spectrum (see chapter 10). An observed excess might hint to the detection of a solar chameleon signal. The spectrum below 2 keV observed in the sunrise dataset is shown in Fig. 11.11 and 11.12 for the *gold* and *silver* region respectively in comparison to the expected background in the respective region.

In both plots it is obvious that, within the statistical uncertainties, the observed data during sunrise tracking of the Sun is perfectly compatible[1] with the expected background, thus indicating the absence of a possible chameleon signal. Due to the absence of any, observable, excess the observed data can be

---

[1] As expected from statistical fluctuations about half of the data points are below and the other half above the prediction with about two thirds of the points less than one standard deviation deviating from the predicted values.

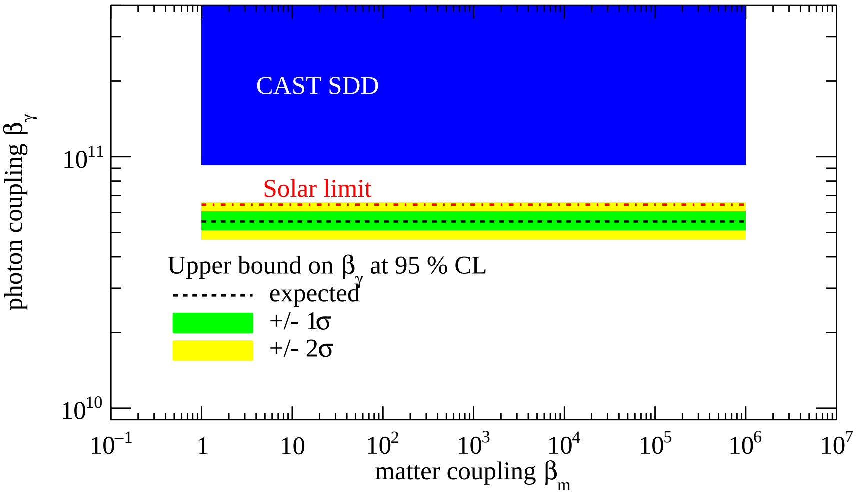

Figure 11.10: Exclusion plot showing the expected upper bound on the chameleon photon coupling β_γ obtained from the measurements in 2014 and 2015. The previous upper bound achieved by CAST using an SDD [42] is depicted in blue. The expected upper bound from the InGrid based X-ray detector is shown as dashed black line with the $\pm 1\sigma$ and $\pm 2\sigma$ shown in green and yellow respectively. The upper limit given by the solar luminosity bound is shown as dashed and dotted line in red.

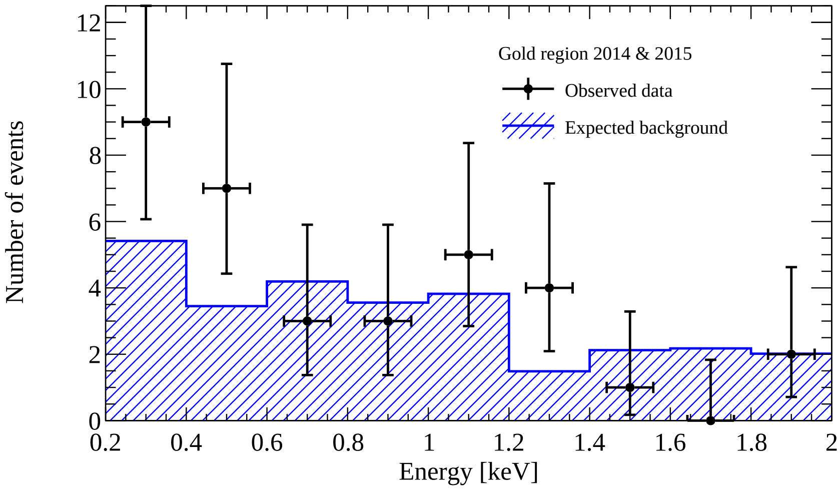

Figure 11.11: Observed data points and background prediction in *gold* region. Data points from sunrise dataset are almost perfectly compatible with the predicted background considering fluctuations within statistical uncertainties.

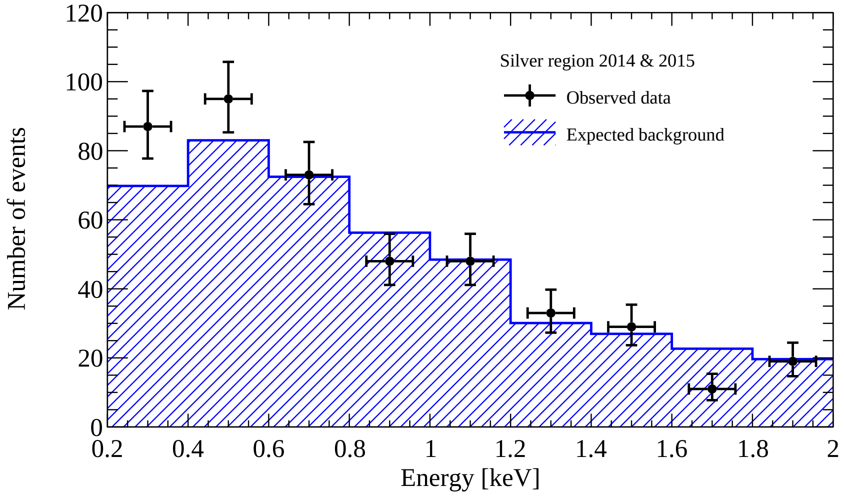

Figure 11.12: Observed data points and background prediction in *silver* region. Data points from sunrise dataset are well compatible with the predicted background considering fluctuations within statistical uncertainties.

used to compute an upper bound on the chameleon photon coupling β_γ which should, due to the good agreement of data and background prediction, be close to the expected upper bound of $\beta_\gamma < 5.53 \times 10^{10}$ for $1 < \beta_m < 10^6$.

11.2.7 Computing the observed upper bound on the chameleon photon coupling

As the data, in the *gold* as well as in the *silver* region, shows no significant excess and is definitely compatible with the expected background, one can compute the observed limit applying the `TLimit` based tool to the background, data and signal histograms taking into account the statistical uncertainty on the background prediction as well as the systematic uncertainties on the expected signal. Thus one gets the observed upper bound on the chameleon photon coupling with

$$\beta_\gamma < 5.74 \times 10^{10} \tag{11.10}$$

at 95 % CL for $1 < \beta_m < 10^6$. This value is indeed close to the expected upper bound computed before and extends the previous upper bound derived from CAST's first search for solar chameleons beyond the solar luminosity bound. The excluded region in the β_m-β_γ plane is depicted in Fig. 11.13 showing separately the old upper bound achieved by CAST, the expected and observed upper bounds from the search using the InGrid based X-ray detector at CAST as well as their relation to the solar luminosity bound.

11.2.8 Discussion of the observed upper bound on the chameleon photon coupling

The observed upper bound on the chameleon photon coupling derived from the data in 2014 and 2015 depends on the assumptions made on the tachocline magnetic field as well as size and position. For different values of these parameters one can recompute the observed upper bound, for some of the parameters also the solar luminosity bound $\beta_\gamma^{\text{sun}}$ changes. Here, the same variations as in [42] are

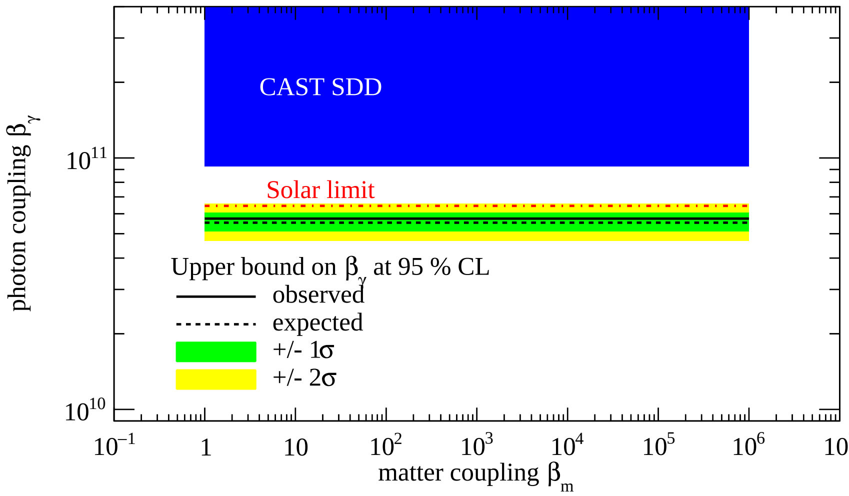

Figure 11.13: Exclusion plot showing the observed upper bound on the chameleon photon coupling β_γ obtained from the measurements in 2014 and 2015. The previous upper bound achieved by CAST using an SDD [42] is depicted in blue. The observed upper bound from the InGrid based X-ray detector is shown as solid black line, the expected value as dashed black line with the $\pm 1\sigma$ and $\pm 2\sigma$ shown in green and yellow respectively. The upper limit given by the solar luminosity bound is shown as dashed and dotted line in red.

Tachocline		β_γ at 95 % CL		
position [$R_\odot$]	width [$R_\odot$]	expected	observed	$\beta_\gamma^{\text{sun}}$
0.7	0.01	$\left(5.53^{+0.52}_{-0.43}\right) \times 10^{10}$	5.74×10^{10}	6.46×10^{10}
0.66	0.01	$\left(4.94^{+0.45}_{-0.39}\right) \times 10^{10}$	4.98×10^{10}	5.89×10^{10}
0.66	0.04	$\left(3.54^{+0.31}_{-0.28}\right) \times 10^{10}$	3.58×10^{10}	2.95×10^{10}
0.7	0.1 linear	$\left(4.19^{+0.38}_{-0.33}\right) \times 10^{10}$	4.36×10^{10}	4.47×10^{10}

Table 11.2: Upper bound on β_γ derived from the measurements with the InGrid based X-ray detector at CAST for different solar models, all using the 10 % solar luminosity bound. The values for the solar luminosity bound were taken from [42].

discussed to allow for comparing with the previous results achieved by CAST. The tachocline magnetic field is believed to be in the range of 4 T up to 25 T [44, 45, 123], the influence of the assumed tachocline magnetic field on the observed limit is illustrated in Fig. 11.14. The observed limit may shift up or down by a factor of $\sqrt{2.5}$, for tachocline magnetic fields up to about 11 T the observed limit is always lower than the solar luminosity bound.

Additionally, one can change the values of the tachocline position and width, table 11.2 shows the observed upper bounds on the chameleon photon coupling β_γ for a tachocline shifted deeper into the Sun and starting at $0.66\,R_\odot$ and with a width increased from $0.01\,R_\odot$ to $0.04\,R_\odot$. Also, the case of the tachocline starting at $0.7\,R_\odot$ with a magnetic field of 10 T which decays linearly to zero over a distance of $0.1\,R_\odot$ was considered and is included in table 11.2. Taking these results into account one can generalize the observed upper bound on the chameleon photon coupling to be $\beta_\gamma < 6.0 \times 10^{10}$ independent of the assumptions made on the tachocline, thus improving the result of [42] by roughly a factor of 1.6.

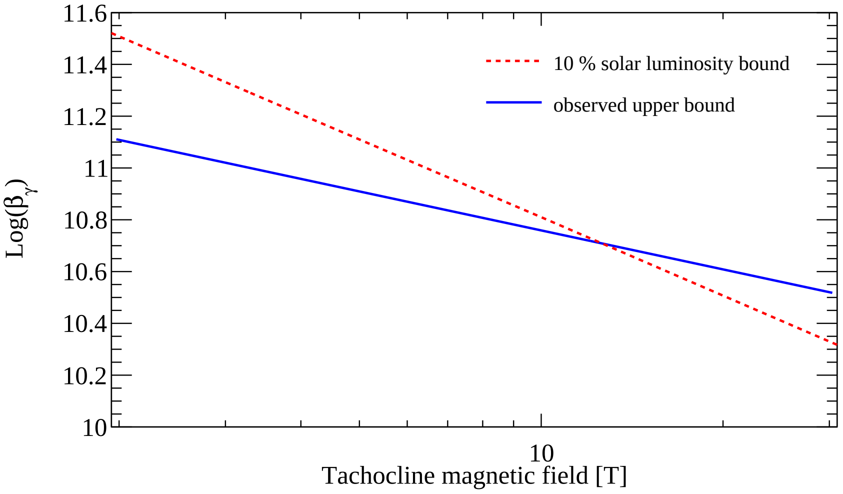

Figure 11.14: Upper bound on β_γ for different tachocline magnetic fields in blue. As comparison the 10 % solar luminosity bound is drawn as dashed red line. The values for the solar luminosity bound were taken from [42].

	β_γ at 95 % CL	
Index n	expected	observed
1	$\left(5.53^{+0.52}_{-0.43}\right) \times 10^{10}$	5.74×10^{10}
2	$\left(5.51^{+0.51}_{-0.43}\right) \times 10^{10}$	5.69×10^{10}
4	$\left(5.49^{+0.49}_{-0.44}\right) \times 10^{10}$	5.67×10^{10}
6	$\left(5.50^{+0.50}_{-0.44}\right) \times 10^{10}$	5.67×10^{10}

Table 11.3: Upper bound on β_γ derived from the measurements with the InGrid based X-ray detector at CAST for different values of the index n which defines the chameleon model.

As for the observed bound on the chameleon photon coupling computed here only non-resonant production of solar chameleons was considered, the search is more or less insensitive to the index n describing the chameleon model used. In table 11.3 the observed limit has been computed for different values for the index n, showing the insensitivity to this chameleon model parameter.

To put the upper bound on the chameleon photon coupling β_γ observed in the course of this thesis in relation to results from other experiments one can look at the parameter space defined by the chameleon photon coupling β_γ and the chameleon matter coupling β_m, due the insensitivity to the index n with the chameleon searches conducted at CAST, including this one, only $n = 1$ is considered. Taking into account the observed upper bound on β_γ derived from the measurements performed in the course of this thesis, the region excluded by CAST is shown in Fig. 11.15 along with experimental bounds from other experiments. Some of these are completely insensitive to the chameleon photon coupling, thus resulting in vertical lines in Fig. 11.15. Torsion pendulum experiments testing for new scalar forces give a lower bound on β_m [47], shown in green, while neutron interferometry experiments provide an upper bound on the chameleon matter coupling [48], shown in lilac. Results obtained with the atom interferometry technique [49, 50], shown as red line, narrow the β_m range not yet excluded down to a small stripe around $\beta_m \sim 10^2$. Precision tests of the Standard Model (SM) [70] provide a large upper bound on

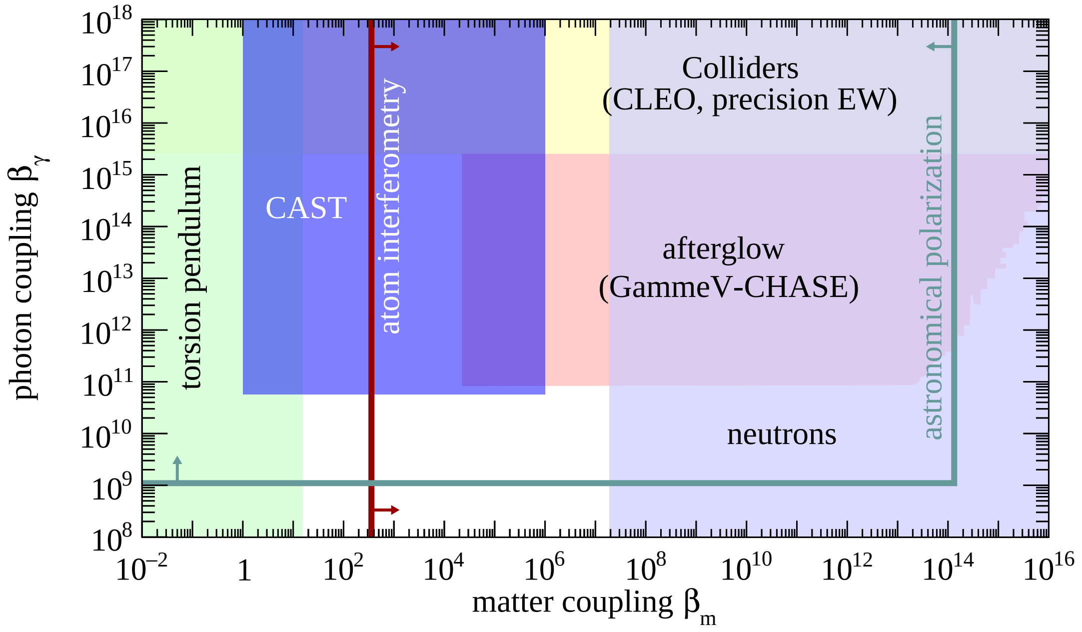

Figure 11.15: Exclusion region for chameleons in the β_γ-β_m plane, achieved by CAST in 2014 and 2015 using the data taken with the InGrid based X-ray detector (purple). Also shown are the bounds set by torsion pendulum tests (green) [47], neutron interferometry measurements (lilac) [48], CHASE (pale orange) [51] and collider experiments (yellow) [70]. The forecasts of the atom-interferometry technique [49, 50] and the astronomical polarization [71] are represented with lines.

β_γ, shown in yellow, while being insensitive to β_m. An analysis of the polarization of light coming from astronomical objects gives an upper bound on β_γ of $\beta_\gamma < 1.1 \times 10^9$ [71]. The upper bound on β_γ observed here, is shown in purple, extending the previous results of CAST's solar chameleon search [42]. As only non-resonant production of solar chameleons is considered, it is only valid for $1 < \beta_m < 10^6$. The CHASE experiment is sensitive to the chameleon photon coupling β_γ for larger values of β_m, up to $\beta_m \sim 10^{14}$ [51], the region excluded by CHASE is shown in pale orange in Fig. 11.15. Only a small part of the parameter space has not been excluded yet, in the narrow β_m range ($15.3 < \beta_m < 3.571 \times 10^2$) limited by the results of torsion pendulum [47] and atom interferometry experiments [49, 50], the not excluded range for β_γ is now limited by the CAST result derived in this thesis to $\beta_\gamma < 5.74 \times 10^{10}$. Thus, the work performed in the course of this thesis has contributed to further reduce the not excluded parameter space.

CHAPTER 12

The upgraded InGrid based X-ray detector for 2017 & 2018

Based on the experiences and results from the operation at the CERN Axion Solar Telescope (CAST) in 2014 and 2015 an upgraded version of the InGrid based X-ray detector has been designed and built which will be briefly introduced in this chapter. In order to increase the detector's sensitivity, especially concerning the search for solar chameleons, features have been implemented following both paths, the enhancement of a possible signal as observable in the detector, and the further reduction of the background level. For the former, new ultrathin silicon nitride windows have been developed in cooperation with the Canadian company Norcada. The key features aiming for a further decrease of the detector's background level include a readout scheme incorporating the analogue signal induced on the grid, veto scintillators and an enlargement of the instrumented area by surrounding the central GridPix with six additional GridPixes.

The implementation of the upgrade's key features required many changes of the detector itself but also adopting its readout system and software. Especially, the use of now seven GridPixes required the implementation of an active cooling scheme due to the increased heat load caused by the additional chips. Also, as the outer GridPixes are close to the detector's inner walls, a field-shaping device was necessary to keep a homogeneous drift field above all of the GridPixes to avoid the influence of field distortions.

End of October 2017 the upgraded InGrid based X-ray detector has been installed at CAST for the data taking campaign 2017 and 2018. It has not been installed behind the MPE X-ray telescope (XRT) as in 2014 and 2015 but at detector station VT3 on the same platform. There, the Lawrence Livermore National Laboratory (LLNL) XRT previously used by the sunrise Micro-Mesh Gaseous Structure (MicroMegas) detector is mounted. It is part of a International Axion Observatory (IAXO) pathfinder project [24, 59].

12.1 Design and key features of the upgraded InGrid based X-ray detector

The design of the upgraded detector follows the baseline design described in chapter 7 but introduces several changes and new key features. An exploded computer-aided design (CAD) view of the detector can be found in Fig. 12.1. The cathode has been equipped with a, newly developed, ultrathin X-ray entrance window made from 300 nm silicon nitride to increase the detectable solar chameleon signal. The instrumented area has been increased by adding six additional GridPixes around a central GridPix on a new carrier board also featuring a temperature sensor. The field-shaping anode has been adopted to the seven GridPixes and a field-cage has been added to the detector body to reduce distortions of the electric drift field close to the GridPixes' edges.

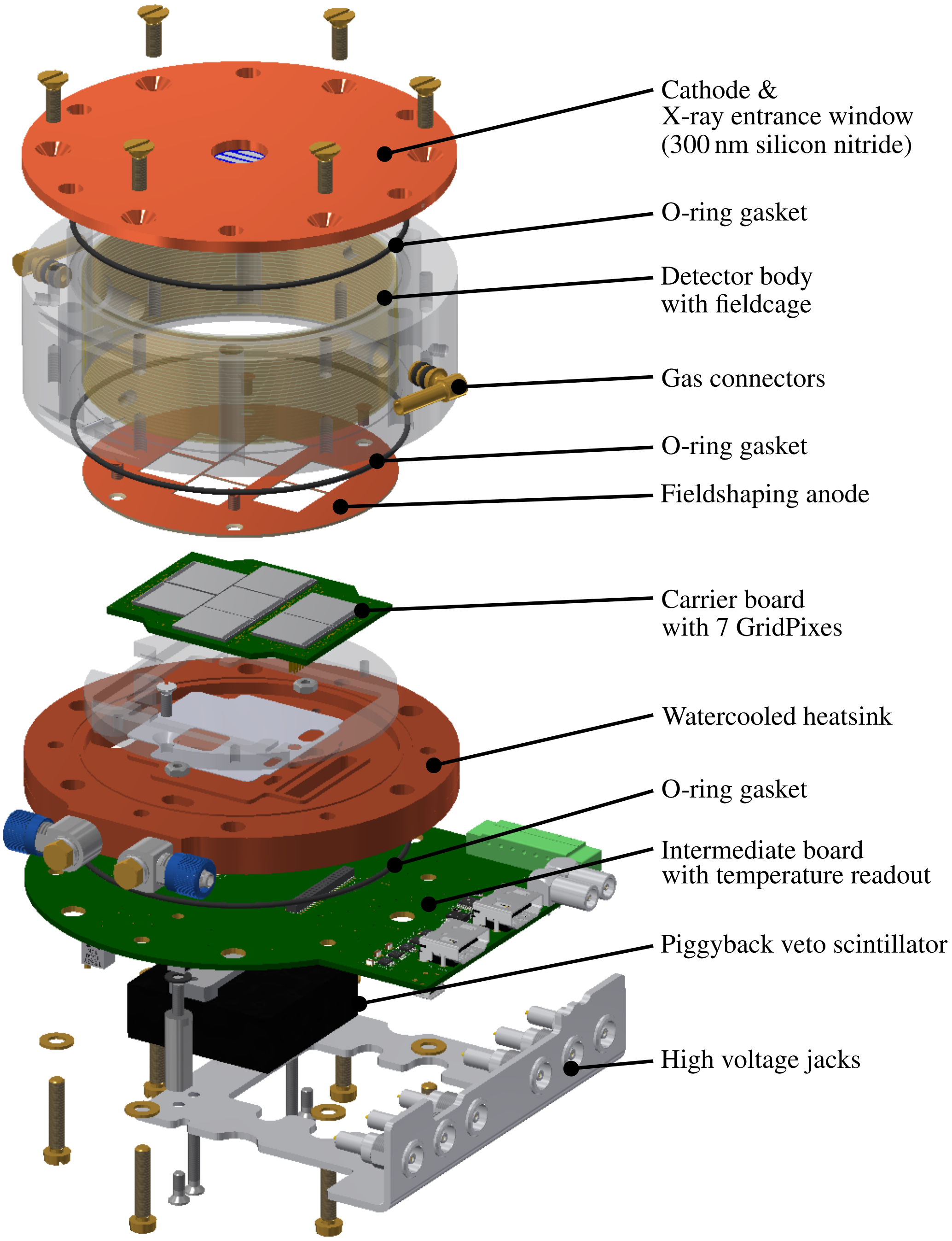

Figure 12.1: Exploded CAD drawing of the upgraded InGrid based X-ray detector with main parts labelled. A CAD drawing of the assembled detector with all its supply lines and tubes can be found in Fig. 12.2.

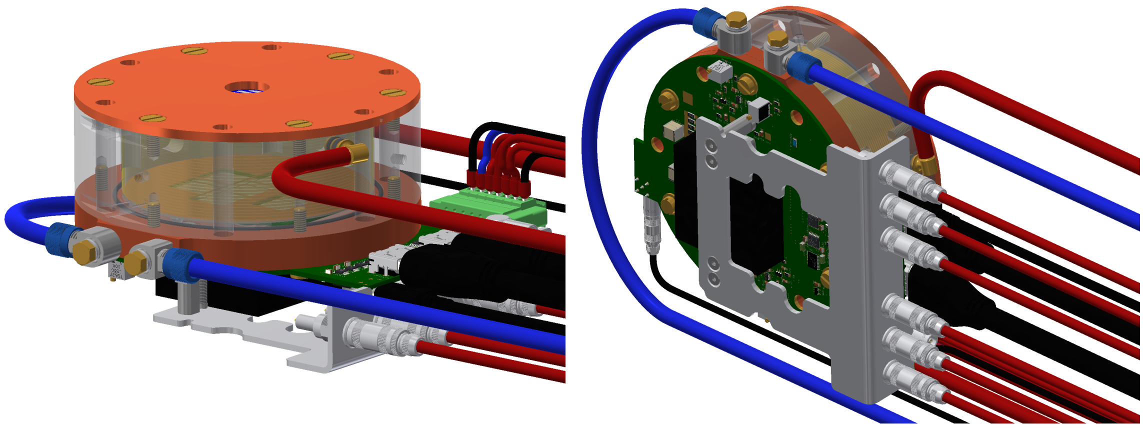
(a) (b)

Figure 12.2: CAD drawings of the upgraded InGrid based X-ray detector. (a) shows the detector from the side allowing view through its acrylic glass body and the partially transparent field cage onto the seven GridPixes inside. In (b) the detector's backside is shown in detail revealing the small piggyback veto scintillator mounted behind the central GridPix (middle, depicted as black box). All supply lines and cables needed for operation of the upgraded InGrid based X-ray detector are illustrated: six high voltage lines, two HDMI cables, a USB line, five supply voltages and tubes for gas supply (red) and water cooling (blue).

A custom water-cooled heat-sink was developed and built to take on the increased heat load produced by the seven GridPixes, the water flow and cooling is realized using commercially available components intended for use in water-cooled desktop computer set-ups. Switching to a more modern version of the readout system based on the Xilinx® Virtex®-6 evaluation board required a new intermediate board which now also features a temperature readout for the sensors implemented on carrier and intermediate board. The temperature is read out via a separate Universal Serial Bus (USB) connection. The updated readout system uses two High Definition Multimedia Interface (HDMI) cables instead of the Very High Density Cable Interconnect (VHDCI) cable which has been used before allowing longer distances between detector and readout system. A CAD drawing of the assembled detector can be found in Fig. 12.2 where also all detector supply lines have been visualized. Compared to the detector used in 2014 and 2015 the number of necessary supply lines (including gas, water cooling, readout, low and high voltages) has more than doubled. Fig. 12.3 shows pictures of the assembled readout module and the complete detector during tests in the laboratory. In Fig. 12.3(a) especially the water-cooled heat-sink with the carrier board holding seven GridPixes hidden under the field-shaping anode is shown, the heat-sink has been manufactured from oxygen-free high thermal conductivity (OFHC) copper utilizing brazing techniques.

The analogue signal induced on the grid of the central GridPix is decoupled and recorded with a flash analogue-to-digital converter (FADC). With the analogue signal as time reference also veto scintillators could be implemented in the readout scheme, one is mounted as piggyback scintillator on the backside of the detector (see Fig. 12.2(b)) and read out with silicon photomultipliers (SiPMs) while a second large scintillator spans the detector, its lead shielding and parts of the beamline the detector is mounted on.

12.1.1 Ultrathin silicon nitride windows

For the upgraded detector new ultrathin X-ray entrance windows have been developed in cooperation with the Canadian company Norcada. After a couple of iterations and tests a working design has been established using 300 nm silicon nitride as window material, pictures of such a window (under test) can

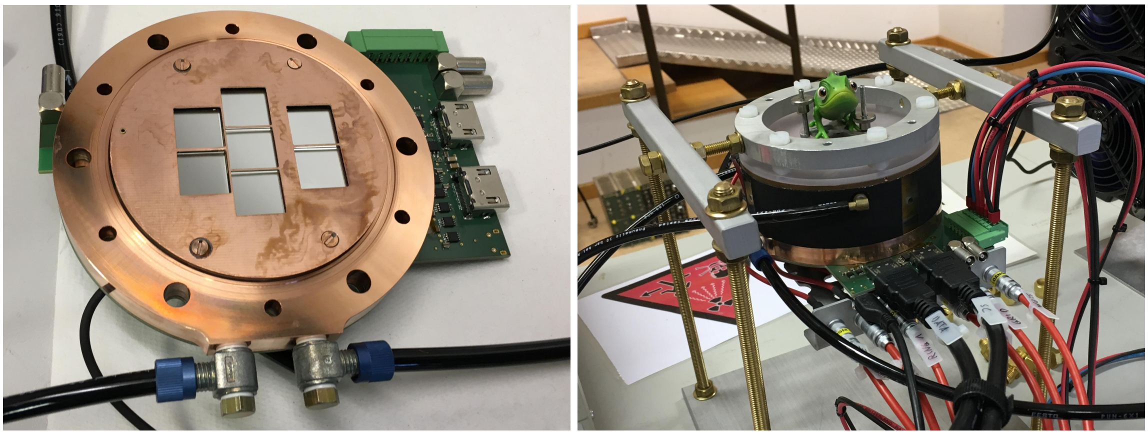

(a) (b)

Figure 12.3: Pictures of the upgraded InGrid based X-ray detector's readout module (a) and the fully assembled detector (b) during tests in the laboratory.

be found in Fig. 12.4. The resulting design has an open aperture of 14 mm diameter and features four straight ribs made from 200 µm silicon (same as the window's frame) to reinforce the structure, the ribs are 500 µm wide giving an optical transparency of 76.8 %. These type of ultrathin windows has proven to successfully withstand a pressure difference of 1 500 mbar making it reasonably safe for operation at 1 050 mbar, the typical operation gas pressure of the upgraded detector. Vacuum tests, including a standard helium leak test, showed that the leak rate of such a 300 nm silicon nitride window is better than a few 10^{-8} mbar l/s, rendering the differential window and pumping scheme unnecessary. Taking into account the transmission curve of silicon nitride (see appendix A), the optical transparency of the working windows and the shape of the solar chameleon spectrum (see chapter 11), the use of the ultrathin silicon nitride X-ray entrance window results in a gain of a factor of about two in terms of integrated signal rate compared to the setup used in 2014 and 2015.

12.1.2 Readout of the analogue signal induced on the grid

The analogue signal induced on the grid of the central GridPix (the one covered by the X-ray entrance window) is decoupled from the high voltage line supplying the grid using a 10 nF capacitor. The signal is amplified using an `Ortec 142 B` preamplifier together with an `Ortec 474` shaping amplifier and then digitized by an FADC, a `CAEN Mod. V1429 A` [124, 125]. The trigger generated by the FADC has been implemented in the readout scheme and interacts with the digital readout of the GridPixes. The FADC trigger is transmitted to the readout board which can inhibit the FADC triggers by sending a veto signal to it [125]. Readout, control and configuration of the FADC is done by the same software handling the communication and readout of the GridPixes, Timepix Operation Software (TOS). The interplay via trigger and veto is illustrated in Fig. 12.5. As any communication with the GridPix(es), e.g. during configuration or readout, influences signals on the grid causing the FADC to trigger, the veto signal inhibiting the FADC triggers is only released when the *shutter* signal is low (GridPix(es) are in measurement mode). As the chipwide switching of the *shutter* signal also would cause an FADC trigger, the veto is only released a few microseconds after the *shutter* signal switched to low. When no FADC trigger occurs during a frame (of typically a few seconds) the veto signal is activated again, the frame closed and read out. If an FADC trigger is registered during a frame, the veto signal is set to avoid a second trigger in the same frame, a defined time (typically some tens of microseconds) after the trigger,

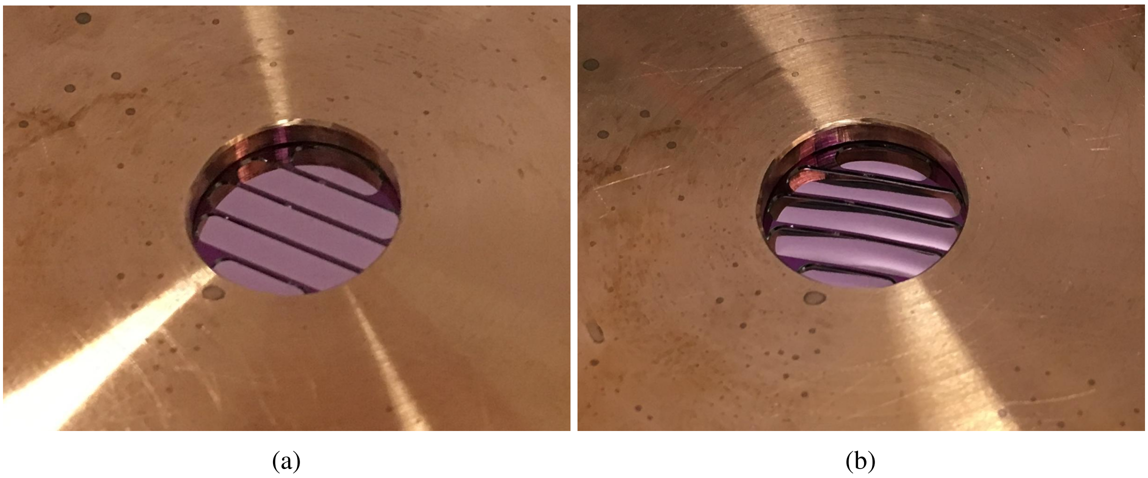
(a) (b)

Figure 12.4: Pictures showing an ultrathin X-ray entrance window made from 300 nm silicon nitride. The window has an open aperture of 14 mm and features four 0.5 mm wide supporting ribs made of 200 µm silicon. The window is glued onto a copper cathode from the backside. In (a) the window is shown unstressed (no pressure difference) while in (b) it is successfully withstanding a pressure difference of 1 200 mbar resulting in the silicon nitride being significantly but elastically deformed.

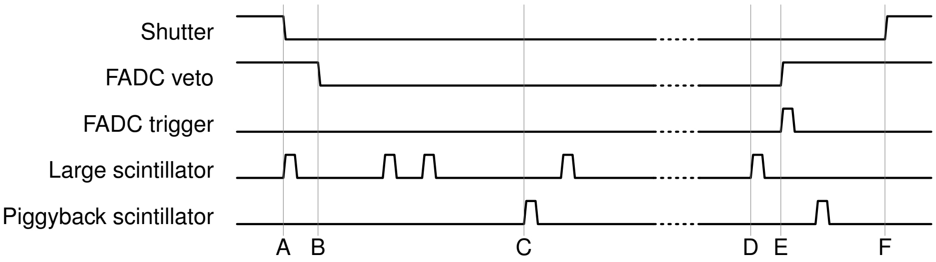

Figure 12.5: Timing scheme illustrating the interplay of FADC, veto scintillators and GridPix readout in the upgraded InGrid based X-ray detector. In the illustrated example six points in time are marked as A through F. When recording a frame with the upgraded InGrid based X-ray detector at first the *shutter* goes low (A) marking the start of the measurement. A few microseconds later the FADC veto signal is turned off (B) allowing the FADC to trigger. When the FADC triggers (E) the veto signal is switched back on to avoid a second trigger in the same frame. A defined time after the trigger (typically a few microseconds) the *shutter* signal is set back to high (F) closing the frame which is then read out before the next is started. For each scintillator a counter is implemented which is reset and started with any scintillator signal until the FADC trigger occurs, resulting in the time between the last scintillator signal previous to the FADC trigger (C & E) being measured and recorded for the large as well as the small piggyback scintillator.

the frame is closed (*shutter* signal going high) and read out together with the waveform recorded by the FADC. The position of the FADC trigger within a frame is measured and recorded as well. Analysis of the recorded waveform should give access to measures describing the event shape in drift direction and thus to additional variables useful for the background suppression.

12.1.3 Implementation of two veto scintillators

The implementation of the analogue signal induced on the GridPix' grid also allowed the use of veto scintillators as with the FADC trigger a reference position in time for the event recorded on the GridPix(es)

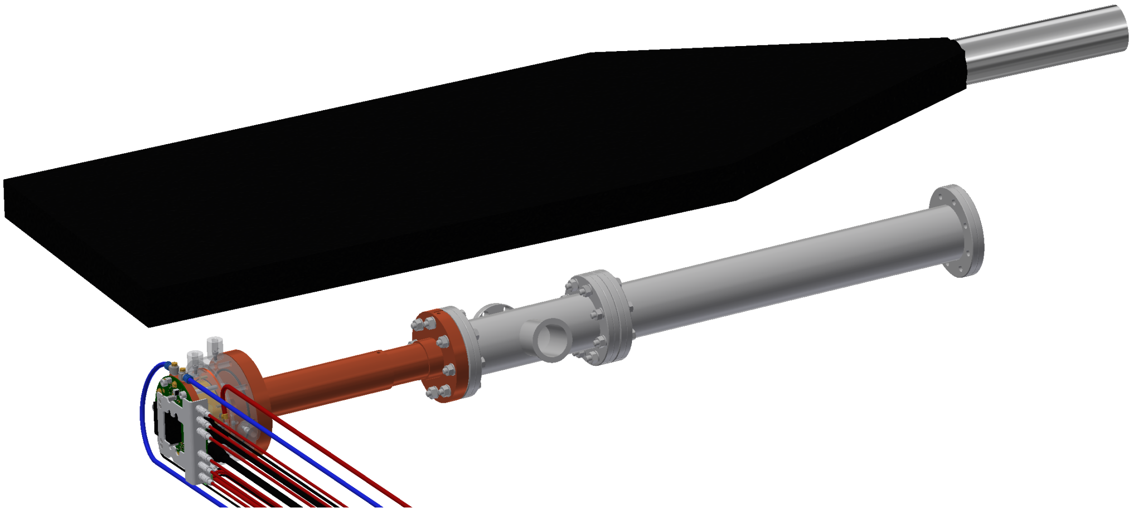

Figure 12.6: CAD drawing depicting the application of the large veto scintillator (top) relative to the upgraded InGrid based X-ray detector (lower left). The large veto scintillator not only covers the region above the detector and its lead shielding (not shown) but spans part of the beamline connecting the detector to the LLNL XRT (also not shown).

is available with high enough precision. Two veto scintillators have been implemented in the readout scheme: a small piggyback scintillator on its backside and a large one spanning parts of the beamline, the detector and its lead shielding. They are intended for vetoing two different kinds of background events. The small piggyback scintillator (see Fig. 12.2(b)) has been added to tag frames containing charged particles (mostly cosmic rays) traversing the detector perpendicular to the instrumented area, as shortly explained in chapter 10 these kind of events mimic X-ray photon events as their roundish shape makes them almost impossible to distinguish from X-ray photons using the GridPix(es) alone.

The large scintillator is intended to tag those frames containing real X-ray photons which were created through X-ray fluorescence caused by cosmic rays depositing energy in the detector materials, the lead shielding or even parts of the beamline connecting the detector to the XRT. Especially a tagging of the latter is important as X-ray photons created in the beampipe may be emitted with the X-ray entrance window in line of sight, thus entering the detector easily. The position of the large veto scintillator relative to the detector and its beampipe is depicted in the CAD image shown in Fig. 12.6, it is spanning the detector, its lead shielding (not shown in the image) and large parts of its beamline.

However, not every signal from either of the two veto scintillators is linked to an event recorded with the GridPixes. Therefore a measure for the correlation of a veto signal with the recorded event is required to use the veto scintillators for background suppression. The correlation is done in the time domain by recording the time between the last veto signal before an FADC trigger. For both veto scintillators a counter is implemented in the readout system which is reset and started with each veto signal until an FADC trigger occurs, then the counters are frozen and read out along with the frame recorded by the GridPixes. If a veto signal occurred within a few microseconds prior to an FADC trigger the event can be tagged with either the large and/or the piggyback veto, this is done offline. In a last step of the (offline) background suppression those background events having a veto tag may be removed. The large veto scintillator has already been used with the sunrise MicroMegas detector [59] before with a similar tagging scheme.

12.1.4 Enlargement of the instrumented area

As mentioned in chapter 10 a large amount of the events remaining after the background suppression close to the GridPix' corners and edges are most likely caused by small parts of charged particles' tracks mimicking X-ray photons. The straight forward approach to discriminate those kind of events is to instrument the area around the central GridPix in order to see a larger part of the event thus revealing its true, e.g. track like, nature. For the upgraded detector this is done by placing six additional GridPixes around the central one to veto track fragments mimicking X-ray photons. The arrangement of the six additional 'veto' GridPixes can be seen in the exploded CAD view in Fig. 12.1 and the image of the readout module in Fig. 12.3(a). The seven GridPixes are mounted on a newly designed carrier board and are read out via a daisy chain. Only the central GridPix can detect a possible solar chameleon signal as only it is covered by the aperture of the X-ray entrance window.

As each of the GridPixes produces a heat load of about 1 W during operation, seven GridPixes close together required the implementation of an active cooling scheme. Therefore, a water-cooled heat-sink has been manufactured to dissipate the heat generated by the seven GridPixes. The heat-sink is made from OFHC copper by brazing two machined parts together forming the cooling channel directly below the carrier board holding the GridPixes. The cooling circuit is made from commercially available components usually used for water-cooled desktop computers. A temperature monitoring with two sensors, one on the backside of the carrier board and one on the intermediate board, has been implemented which is also used for a software interlock with the high voltage supply of the detector. In case the GridPixes become too hot, frequent sparks and discharges occur on and between the GridPixes, especially at edges. As these render the GridPixes basically inoperable and may even cause permanent damage to the grid, the software interlock shuts down the grid high voltage in case the carrier board temperature exceeds a safe threshold. The underlying processes of these temperature effects and quantitative measurements on their thresholds will be studied in detail soon in the course of a master thesis.

12.2 Installation behind the LLNL X-ray telescope in 2017

In 2017 the upgraded InGrid based X-ray detector has been installed at detector station VT3 of CAST for the upcoming data taking campaigns 2017 and 2018. By switching from detector station VT4 to station VT3 the infrastructure of the sunrise MicroMegas detector of 2014 and 2015 [59] can be used. This includes especially the LLNL XRT, which was built as part of a IAXO pathfinder project [24, 59], and the lead shielding previously used by the sunrise MicroMegas detector which features a full coverage with at least 10 cm lead in each direction. The upgraded detector was installed on the former sunrise MicroMegas beamline and aligned to the LLNL XRT using a laser beam shone in from the sunset side of the CAST magnet and an alignment target featuring a cross hair at the detector's centre position (same method as used for alignment to the MPE XRT in 2014, see also chapter 8). The resulting laser spot 'right on target' after successful alignment is shown in Fig. 12.7(a) while the completed beamline with the detector mounted and operable is shown in the image in Fig. 12.7(b). The detector inside the (partially assembled) lead shielding is shown in Fig. 12.8. Since late October 2017 the detector is taking data at CAST in the course of the 2017 run, the detector will take data until March 2018, presumably.

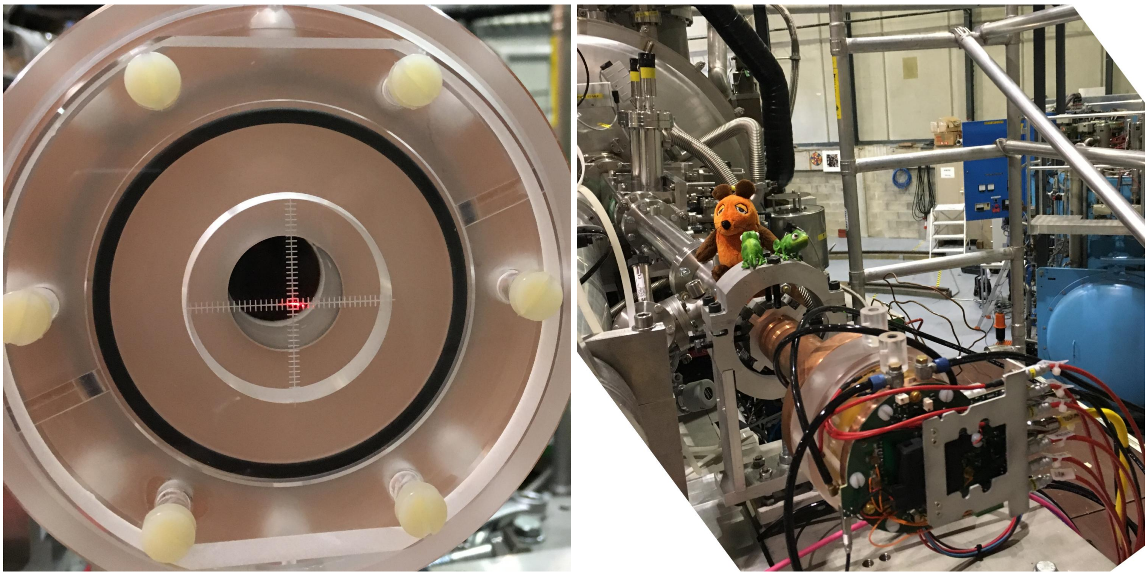

(a) (b)

Figure 12.7: Images of the laser spot after successful alignment of the LLNL XRT line (a) and of the InGrid based X-ray detector mounted to the beamline (b). Reference holes on the detector can be used to verify its position and alignment without a laser guided through the XRT from the sunset side. The mouse, a famous German TV star, is sitting on the beamline and inspecting the detector.

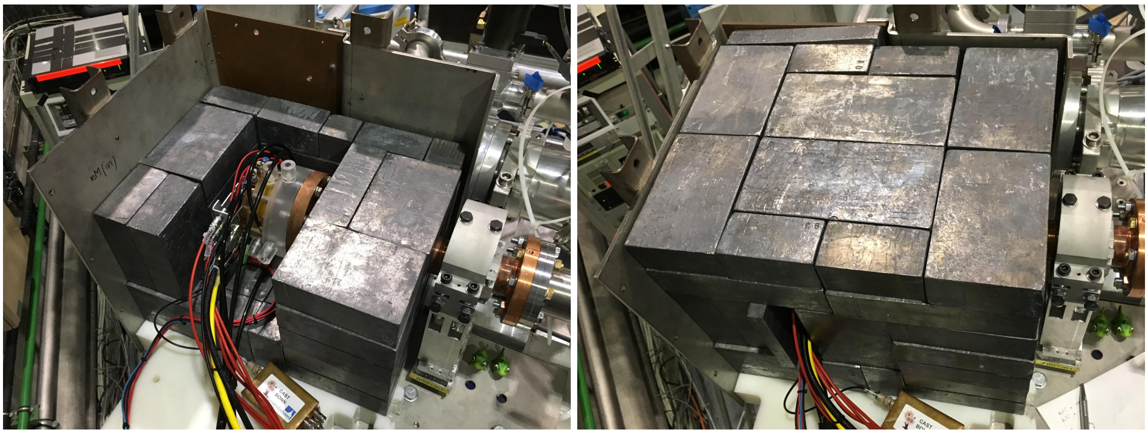

(a) (b)

Figure 12.8: Images of the upgraded InGrid based X-ray detector inside its lead shielding at CAST's detector station VT3 behind the LLNL XRT. The lead shielding was previously used for the sunrise MicroMegas detector at the same detector station and has been slightly modified. It features a wall thickness of at least 10 cm to all sides. In (a) the shielding is only partially assembled, allowing a view on the detector inside while (b) shows the closed shielding.

CHAPTER 13

Conclusion and Outlook

An InGrid based X-ray detector was successfully developed and built to continue the search for solar chameleons at the CERN Axion Solar Telescope (CAST), which was started in 2013 with a silicon drift detector (SDD). The continuation of this search lead to an improved upper bound on the chameleon photon coupling exceeding the solar luminosity bound for the first time with CAST.

The X-ray detector built, is based on a GridPix, a pixelized readout with an integrated gas amplification stage called Integrated Grid (InGrid). It was developed with a focus on allowing for detection of X-ray photons below 2 keV and thus, especially requiring an X-ray entrance window with high transmission. The detector was fully characterized at the variable X-ray generator of the CAST Detector Lab (CDL) at CERN. It could be proven that the detector is able to detect single X-ray photons with energies ranging down to a few hundred eV. The data collected in the CDL at eight different X-ray energies between 8 keV and 277 eV also served as reference datasets for a likelihood based background suppression method using eventshape variables for differentiating between X-rays and other types of events. With this method, and a lead shielding, background rates of 10^{-4} /keV/cm^2/s and below could be achieved at an X-ray efficiency of 80 % in the central region of the detector for the energy range up to 2 keV, which is relevant for solar chameleon searches. For higher X-ray energies background rates down to a few 10^{-5} /keV/cm^2/s were reached.

In 2014 the InGrid based X-ray detector was mounted at CAST behind the MPE X-ray telescope (XRT) for the upcoming data taking periods 2014 and 2015. For this, a small vacuum system was designed and built, interfacing the detector and the XRT. From October 2014 on, the detector was operated almost continuously until its dismantling begin of 2016. Until then, no detector related interruptions occurred and a stable performance was achieved with an energy resolution σ_E/E of 7.8 % at an X-ray energy of 5.9 keV at a gas gain of approximately 2 600 to 2 700. This was the first time a GridPix based detector was operated at a running physics experiment such as CAST quasi continuously for more than a year.

As no excess was found in the data taken during sunrise solar trackings of CAST, over the expected background derived from the long-term background measurements performed at CAST, an upper bound on the chameleon photon coupling could be derived using `TLimit` and taking into account statistical as well as estimated systematic uncertainties. The new upper bound on the chameleon photon coupling computes to $\beta_\gamma < 5.74 \times 10^{10}$ at 95 % confidence level (CL) for $1 < \beta_m < 10^6$ as only non-resonant production of chameleons in the Sun is considered. This limit improves CAST's previous result, obtained with the SDD, by a factor of roughly 1.6 and, for the first time at CAST, exceeds the solar luminosity bound.

Taking into account the experiences gained from the operation of the InGrid based X-ray detector at CAST in 2014 and 2015 and also the knowledge about the observed background, especially its distribution and presumed sources, an upgraded detector was built and commissioned in 2017. This detector also incorporates background suppression methods previously introduced by the MicroMegas detectors used for CAST's solar axion searches, including the recording of the analogue signal induced on the GridPix' grid and the use of veto scintillators, which provide further observables for the off-line background suppression. In addition, different background suppression methods will be tested including the application of convolutional neural networks. To further increase the detector's sensitivity ultrathin X-ray entrance windows made from 300 nm silicon nitride have successfully been developed in cooperation with the Canadian company Norcada. The upgraded detector was installed at CAST late in 2017 behind the LLNL XRT and is supposed to take data until March 2018.

The upgraded detector is supposed to achieve sensitivity to lower chameleon photon couplings, taking into account the anticipated improvement regarding background rates and the increased transmission of the ultrathin X-ray entrance window. Also, the upgraded detector presents a new step towards demonstrating that an InGrid based X-ray detector is a viable option for future axion helioscope experiments such as e.g. the International Axion Observatory (IAXO).

Bibliography

[1] G. Hinshaw et al., *Five-Year Wilkinson Microwave Anisotropy Probe Observations: Data Processing, Sky Maps, and Basic Results*, Astrophys. J., Suppl. Ser. **180** (2009) 225 (cit. on p. 1).

[2] Ade, P. A. R. et al., *Planck 2013 results. I. Overview of products and scientific results*, Astron. Astrophys. **571** (2014) A1 (cit. on p. 1).

[3] S. Weinberg, *The U(1) problem*, Phys. Rev. D **11** (1975) 3583 (cit. on p. 3).

[4] G. 't Hooft, *Symmetry Breaking through Bell-Jackiw Anomalies*, Phys. Rev. Lett. **37** (1976) 8 (cit. on p. 3).

[5] G. 't Hooft, *Computation of the quantum effects due to a four-dimensional pseudoparticle*, Phys. Rev. D **14** (1976) 3432 (cit. on p. 3).

[6] C. Baker et al., *Improved Experimental Limit on the Electric Dipole Moment of the Neutron*, Phys. Rev. Lett. **97** (2006) 131801 (cit. on p. 4).

[7] R. Peccei and H. Quinn, *CP Conservation in the Presence of Pseudoparticles*, Phys. Rev. Lett. **38** (1977) 1440 (cit. on p. 4).

[8] F. Wilczek, *Problem of Strong P and T Invariance in the Presence of Instantons*, Phys. Rev. Lett. **40** (1978) 279 (cit. on pp. 4, 6).

[9] S. Weinberg, *A New Light Boson?*, Phys. Rev. Lett. **40** (1978) 223 (cit. on pp. 4, 6).

[10] C. Krieger, *Construction and First Measurements of a GridPix based X-ray Detector*, BONN-IB-2012-05, Master thesis: Universität Bonn, 2012 (cit. on pp. 5, 6, 57, 62, 63, 66, 70, 126).

[11] R. Peccei and H. Quinn, *Constraints imposed by CP conservation in the presence of pseudoparticles*, Phys. Rev. D **16** (1977) 1791 (cit. on p. 6).

[12] I. Antoniadis and T. Truong, *Lower Bound for Branching Ratio of $K^+ \rightarrow \pi^+$ Axion and Nonexistence of Peccei-Quinn Axion*, Phys. Lett. B **109** (1982) 67 (cit. on p. 6).

[13] J. Kim, *Weak-Interaction Singlet and Strong CP Invariance*, Phys. Rev. Lett. **43** (1979) 103 (cit. on p. 7).

[14] M. Shifman, A. Vainshtein and V. Zakharov, *Can Confinement Ensure Natural CP Invariance of Strong Interactions?*, Nucl. Phys. B **166** (1980) 493 (cit. on p. 7).

[15] M. Dine, W. Fischler and M. Srednicki, *A simple solution to the strong CP problem with a harmless axion*, Phys. Lett. B **104** (1981) 199 (cit. on p. 7).

[16] X. Chen and M. Kamionkowski, *Particle decays during the cosmic dark ages*, Phys. Rev. D **70** (2004) 043502 (cit. on p. 7).

[17] K. van Bibber et al., *Design for a practical laboratory detector for solar axions*, Phys. Rev. D **39** (8 1989) 2089 (cit. on pp. 7, 9, 23).

[18] P. Sikivie, *Experimental Tests of the "Invisible" Axion*, Phys. Rev. Lett. **51** (16 1983) 1415 (cit. on p. 7).

[19] C. Hagmann et al., *Results from a High-Sensitivity Search for Cosmic Axions*, Phys. Rev. Lett. **80** (1998) 2043 (cit. on p. 8).

[20] S. Asztalos et al., *SQUID-Based Microwave Cavity Search for Dark-Matter Axions*, Phys. Rev. Lett. **104** (2010) 041301 (cit. on p. 8).

[21] J. Hoskins et al., *Search for nonvirialized axionic dark matter*, Phys. Rev. D **84** (2011) 121302(R) (cit. on p. 8).

[22] B. Brubaker et al., *First Results from a Microwave Cavity Axion Search at 24 μeV*, Phys. Rev. Lett. **118** (2017) 061302 (cit. on p. 8).

[23] A. Caldwell et al., *Dielectric Haloscopes: A New Way to Detect Axion Dark Matter*, Phys. Rev. Lett. **118** (2017) 091801 (cit. on p. 8).

[24] E. Armengaud et al., *Conceptual design of the International Axion Observatory (IAXO)*, J. Instrum. **9** (2014) T05002 (cit. on pp. 8, 10, 22, 24, 26, 96, 157, 163).

[25] S. Andriamonje et al., *An improved limit on the axion-photon coupling from the CAST experiment*, J. Cosmol. Astropart. Phys. **2007** (2007) 010 (cit. on pp. 9, 10, 22, 25).

[26] J. Bahcall and M. Pinsonneault, *What Do We (Not) Know Theoretically about Solar Neutrino Fluxes?*, Phys. Rev. Lett. **92** (12 2004) 121301 (cit. on p. 9).

[27] D. Lazarus et al., *Search for Solar Axions*, Phys. Rev. Lett. **69** (16 1992) 2333 (cit. on pp. 10, 21).

[28] S. Moriyama et al., *Direct search for solar axions by using strong magnetic field and X-ray detectors*, Phys. Lett. B **434** (1998) 147 (cit. on pp. 10, 21, 27).

[29] Y. Inoue et al., *Search for sub-electronvolt solar axions using coherent conversion of axions into photons in magnetic field and gas helium*, Phys. Lett. B **536** (2002) 18 (cit. on pp. 10, 21, 27).

[30] K. Zioutas et al., *First Results from the CERN Axion Solar Telescope*, Phys. Rev. Lett. **94** (2005) 121301 (cit. on pp. 10, 22, 25).

[31] E. Arik et al., *Probing eV-scale axions with CAST*, J. Cosmol. Astropart. Phys. **2009** (2009) 008 (cit. on pp. 10, 23, 26).

[32] M. Arik et al., *Search for Sub-eV Mass Solar Axions by the CERN Axion Solar Telescope with ^{3}He Buffer Gas*, Phys. Rev. Lett. **107** (2011) 261302 (cit. on pp. 10, 23, 26).

[33] M. Arik et al., *Search for Sub-eV Mass Solar Axions by the CERN Axion Solar Telescope with ^{3}He Buffer Gas: Closing the Hot Dark Matter Gap*, Phys. Rev. Lett. **112** (2014) 091302 (cit. on pp. 10, 23, 26).

[34] M. Arik et al., *New solar axion search using the CERN Axion Solar Telescope with ^{4}He filling*, Phys. Rev. D **92** (2015) 021101(R) (cit. on pp. 10, 23, 26).

[35] V. Anastassopoulos et al., *New CAST Limit on the Axion-Photon Interaction*, Nat. Phys. **13** (2017) 584 (cit. on pp. 10, 21, 22, 24–27, 134, 149).

[36] R. Bernabei et al., *Search for solar axions by Primakoff effect in NaI crystals*, Phys. Lett. B **515** (2001) 6 (cit. on pp. 10, 27).

[37] F. D. Valle et al., *The PVLAS experiment: measuring vacuum magnetic birefringence and dichroism with a birefringent Fabry-Perot cavity*, Eur. Phys. J. C **76** (2016) 24 (cit. on pp. 10, 27).

[38] K. Ehret et al., *New ALPS results on hidden-sector lightweights*, Phys. Lett. B **689** (2010) 149 (cit. on p. 11).

[39] R. Ballou et al., *New exclusion limits on scalar and pseudoscalar axionlike particles from light shining through a wall*, Phys. Rev. D **92** (2015) 092002 (cit. on pp. 11, 27).

[40] R. Bähre et al., *Any light particle search II — Technical Design Report*, J. Instrum. **8** (2013) T09001 (cit. on p. 11).

[41] C. Burrage and J. Sakstein, *Tests of Chameleon Gravity*, version 1, 2017, arXiv: `1709.09071v1 [astro-ph.CO]` (cit. on pp. 13–15).

[42] V. Anastassopoulos et al., *Search for chameleons with CAST*, Phys. Lett. B **749** (2015) 172 (cit. on pp. 16–19, 21, 25, 28, 96, 134, 142–144, 147, 151–156).

[43] P. Brax, A. Lindner and K. Zioutas, *Detection prospects for solar and terrestrial chameleons*, Phys. Rev. D **85** (2012) 043014 (cit. on pp. 16–18, 23, 142, 143).

[44] M. Weber, Y. Fan and M. Miesch, *Comparing Simulations of Rising Flux Tubes Through the Solar Convection Zone with Observations of Solar Active Regions: Constraining the Dynamo Field Strength*, Sol. Phys. **287** (2013) 239 (cit. on pp. 16, 154).

[45] P. Caligari, F. Moreno-Insertis and M. Schüssler, *Emerging flux tubes in the solar convection zone: I. Asymmetry, tilt, and emergence latitude*, Astrophys. J. **441** (1995) 886 (cit. on pp. 16, 154).

[46] E. A. D.J. Kapner T.S. Cook et al., *Tests of the Gravitational Inverse-Square Law below the Dark-Energy Length Scale*, Phys. Rev. Lett. **98** (2007) 021101 (cit. on p. 18).

[47] A. Upadhye, *Dark energy fifth forces in torsion pendulum experiments*, Phys. Rev. D **86** (2012) 102003 (cit. on pp. 19, 28, 155, 156).

[48] H. Lemmel et al., *Neutron interferometry constrains dark energy chameleon fields*, Phys. Lett. B **743** (2015) 310 (cit. on pp. 19, 28, 155, 156).

[49] P. Hamilton et al., *Atom-interferometry constraints on dark energy*, Science **349** (6250 2015) 849 (cit. on pp. 19, 28, 155, 156).

[50] M. Jaffe et al., *Testing sub-gravitational forces on atoms from a miniature in-vacuum source mass*, Nat. Phys. **13** (2017) 938 (cit. on pp. 19, 28, 155, 156).

[51] J. Steffen et al., *Laboratory Constraints on Chameleon Dark Energy and Power-Law Fields*, Phys. Rev. Lett. **105** (2010) 261803 (cit. on pp. 20, 28, 156).

[52] C. Aalseth et al., *A solar axion search using a decommissioned LHC test magnet*, Proposal to the SPSC, 1999 (cit. on p. 21).

[53] K. Zioutas et al., *A decommissioned LHC model magnet as an axion telescope*, Nucl. Instr. Meth. Phys. Res. A **425** (1999) 480 (cit. on p. 21).

[54] M. Kuster et al., *The x-ray telescope of CAST*, New J. Phys. **9** (2007) 169 (cit. on pp. 22, 25, 95, 96, 98, 144).

[55] P. Friedrich, "ABRIXAS: an imaging x-ray survey in the 0.5- to 10-keV range", *X-Ray Optics, Instruments, and Missions*, vol. 3444, 1998 342 (cit. on p. 22).

[56] P. Friedrich et al., "X-ray tests and calibrations of the ABRIXAS mirror systems", *X-Ray Optics, Instruments, and Missions*, vol. 3444, 1998 369 (cit. on pp. 22, 96, 144, 149).

[57] W. Egle et al., "Mirror System for the German X-ray Satellite ABRIXAS: II. Design and Mirrors Development", *X-Ray Optics, Instruments, and Missions*, vol. 3444, 1998 359 (cit. on pp. 22, 96, 144).

[58] J. Altmann et al., "Mirror System for the German X-ray Satellite ABRIXAS: I. Flight Mirrors Fabrication, Integration and Testing", *X-Ray Optics, Instruments, and Missions*, vol. 3444, 1998 350 (cit. on pp. 22, 96, 144).

[59] F. Aznar et al., *A Micromegas-based low-background x-ray detector coupled to a slumped-glass telescope for axion research*, J. Cosmol. Astropart. Phys. **12** (2015) 008 (cit. on pp. 22, 24, 26, 46, 96, 134, 157, 162, 163).

[60] S. Aune et al., *Low background x-ray detection with Micromegas for axion research*, J. Instrum. **9** (2014) P01001 (cit. on pp. 24, 46, 57).

[61] K. Barth et al., *CAST constraints on the axion-electron coupling*, J. Cosmol. Astropart. Phys. **2013** (2013) 010 (cit. on pp. 25, 26).

[62] B. menz, *Test report CAST*, tech. rep., X-ray Test Facility PANTER, 2014 (cit. on pp. 25, 98, 144, 145, 149).

[63] D. Autiero et al., *The CAST time projection chamber*, New J. Phys. **9** (2007) 171 (cit. on p. 25).

[64] G. Luzón et al., *Background studies and shielding effects for the TPC detector of the CAST experiment*, New J. Phys. **9** (2007) 208 (cit. on p. 25).

[65] S. Baum et al., *Detecting solar chameleons through radiation pressure*, Phys. Lett. B **739** (2014) 167 (cit. on pp. 25, 26).

[66] A. Payez et al., *Revisiting the SN1987A gamma-ray limit on ultralight axion-like particles*, J. Cosmol. Astropart. Phys. **2015** (2015) 006 (cit. on p. 27).

[67] N. Vinyoles et al., *New axion and hidden photon constraints from a solar data global fit*, J. Cosmol. Astropart. Phys. **2015** (2015) 015 (cit. on p. 27).

[68] A. Ayala et al., *Revisiting the Bound on Axion-Photon Coupling from Globular Clusters*, Phys. Rev. Lett. **113** (2014) 191302 (cit. on p. 27).

[69] M. Archidiacono et al., *Axion hot dark matter bounds after Planck*, J. Cosmol. Astropart. Phys. **2013** (2013) 020 (cit. on p. 27).

[70] P. Brax et al., *Collider constraints on interactions of dark energy with the Standard Model*, J. High Energy Phys. **09** (2009) 128 (cit. on pp. 28, 155, 156).

[71] C. Burrage, A. Davis and D. Shaw,
Detecting chameleons: The astronomical polarization produced by chameleonlike scalar fields,
Phys. Rev. D **79** (2009) 044028 (cit. on pp. 28, 156).

[72] C. Patrignani et al., *Review of Particle Physics*, Chin. Phys. C **40** (2016) 100001
(cit. on pp. 31, 34–36, 70, 88).

[73] C. Grupen, *Particle Detectors*, Cambridge University Press, 1996, ISBN: 0-521-55216-8
(cit. on pp. 30, 32–34, 36).

[74] W. Blum, W. Riegler and L. Rolandi, *Particle Detection with Drift Chambers*, 2nd ed.,
Springer-Verlag Berlin Heidelberg, 2008, ISBN: 978-3-642-09538-2 (cit. on pp. 36, 38–41).

[75] S. Biagi, *Monte Carlo simulation of electron drift and diffusion in counting gases under the influence of electric and magnetic fields*, Nucl. Instr. Meth. Phys. Res. A **421** (1999) 234
(cit. on pp. 38, 84).

[76] E. Wagner, F. Davis and G. Hurst,
Time-of-Flight Investigations of Electron Transport in Some Atomic and Molecular Gases,
J. Chem. Phys. **47** (1967) 3138 (cit. on p. 39).

[77] M. Chefdeville, *Development of Micromegas-like gaseous detectors using a pixel readout chip as collecting anode*, PhD thesis: Universiteit van Amsterdam, Université Paris Sud XI, 2009
(cit. on pp. 40, 41, 49, 51).

[78] Y. Giomataris et al., *MICROMEGAS: a high-granularity position-sensitive gaseous detector for high particle-flux environments*, Nucl. Instr. Meth. Phys. Res. A **376** (1996) 29
(cit. on pp. 43, 45).

[79] Y. Giomataris, *Development and prospects of the new gaseous detector "Micromegas"*,
Nucl. Instr. Meth. Phys. Res. A **419** (1998) 239 (cit. on p. 43).

[80] G. Charpak et al., *First beam test results with Micromegas, a high-rate, high-resolution detector*,
Nucl. Instr. Meth. Phys. Res. A **412** (1998) 47 (cit. on p. 43).

[81] I. Giomataris et al., *Micromegas in a bulk*, Nucl. Instr. Meth. Phys. Res. A **560** (2006) 405
(cit. on pp. 43, 45).

[82] G. Charpak et al.,
The Use of Multiwire Proportional Counters to Select and Localize Charged Particles,
Nucl. Instr. Meth. **62** (3 1968) 262 (cit. on p. 43).

[83] F. Sauli, *GEM: A new concept for electron amplification in gas detectors*,
Nucl. Instr. Meth. Phys. Res. A **386** (1997) 531 (cit. on p. 44).

[84] F. Sauli, *The gas electron multiplier (GEM): Operating principles and applications*,
Nucl. Instr. Meth. Phys. Res. A **805** (2016) 2 (cit. on pp. 44, 50).

[85] S. Andriamonje et al., “Development and performance of Microbulk Micromegas detectors”,
Proceedings, 1st International Conference on Micro Pattern Gaseous Detectors: Kolympari, Chania, Crete, Greece, 12-15 Jun 2009, vol. 5, 2010 P02001 (cit. on pp. 46, 48).

[86] F. Iguaz et al., “New developments in Micromegas Microbulk detectors”,
Proceedings, 2nd International Conference on Technology and Instrumentation in Particle Physics 2011: Chicago, Illinois, United States, 9-14 Jun 2011, vol. 37, 2012 448 (cit. on p. 46).

[87] S. Cebrián et al., *Radiopurity of micromegas readout planes*, Astropart. Phys. **34** (2011) 354
(cit. on p. 48).

[88] X. Llopart et al., *Timepix, a 65k programmable pixel readout chip for arrival time, energy and/or photon counting measurements*, Nucl. Instr. Meth. Phys. Res. A **581** (2007) 485 (cit. on pp. 48, 60, 61).

[89] X. Llopart et al., *Medipix2: a 64-k Pixel Readout Chip With 55-µm Square Elements Working in Single Photon Counting Mode*, IEEE Trans. Nucl. Sci. **49** (2002) (cit. on pp. 48, 60, 62).

[90] M. Campbell et al., *Detection of single electrons by means of a Micromegas-covered MediPix2 pixel CMOS readout circuit*, Nucl. Instr. Meth. Phys. Res. A **540** (2005) 295 (cit. on pp. 48, 60).

[91] M. Chefdeville et al., *An electron-multiplying 'Micromegas' grid made in silicon wafer post-processing technology*, Nucl. Instr. Meth. Phys. Res. A **556** (2006) 490 (cit. on p. 49).

[92] H. van der Graaf, *GridPix: An integrated readout system for gaseous detectors with a pixel chip as anode*, Nucl. Instr. Meth. Phys. Res. A **580** (2007) 1023 (cit. on p. 49).

[93] W. Koppert et al., *GridPix detectors: Production and beam test results*, Nucl. Instr. Meth. Phys. Res. A **732** (2013) 245 (cit. on pp. 49, 51, 53).

[94] M. Lupberger et al., *Toward the Pixel-TPC: Construction and Operation of a Large Area GridPix Detector*, IEEE Trans. Nucl. Sci. **64** (2017) (cit. on pp. 49, 53, 60, 66).

[95] Y. Bilevych et al., *Spark protection layers for CMOS pixel anode chips in MPGDs*, Nucl. Instr. Meth. Phys. Res. A **629** (2011) 66 (cit. on p. 50).

[96] Y. Bilevych et al., *TwinGrid: A wafer post-processed multistage Micro Patterned Gaseous Detector*, Nucl. Instr. Meth. Phys. Res. A **610** (2009) 644 (cit. on p. 50).

[97] M. Lupberger et al., "InGrid: Pixelated Micromegas detectors for a Pixel-TPC", *Proceedings, 3rd International Conference on Technology and Instrumentation in Particle Physics 2014: Amsterdam, the Netherlands, 2-6 Jun 2014*, 2014, URL: `https://pos.sissa.it/archive/conferences/213/060/TIPP2014_225.pdf` (cit. on p. 51).

[98] L. Scharenberg, *Charakterisierung verschiedener Produktionsserien von InGrids*, Bachelor thesis: Universität Bonn, 2016 (cit. on p. 53).

[99] C. Krieger, J. Kaminski and K. Desch, *InGrid based X-ray detector for low background searches*, Nucl. Instr. Meth. Phys. Res. A **729** (2013) 905 (cit. on pp. 57, 75, 85, 126).

[100] J. Ottnad, *Studies on field distortions and quenching gas properties of an InGrid based X-ray detector*, Master thesis: Universität Bonn, 2014 (cit. on pp. 57, 63, 70, 77, 81, 118).

[101] E. Gullikson, *X-Ray Interactions With Matter*, 2010, URL: `http://henke.lbl.gov/optical_constants/` (visited on 20/11/2017) (cit. on pp. 58, 67, 83, 176).

[102] B. Henke, E. Gullikson and J. Davis, *X-Ray Interactions: Photoabsorption, Scattering, Transmission, and Reflection at E = 50-30,000 eV, Z = 1-92*, At. Data Nucl. Data Tables **54** (1993) 181, ISSN: 0092-640X (cit. on pp. 58, 67, 83, 176).

[103] A. Bamberger et al., *Readout of GEM detectors using the Medipix2 CMOS pixel chip*, Nucl. Instr. Meth. Phys. Res. A **573** (2007) 361 (cit. on p. 60).

[104] C. Brezina et al., *Operation of a GEM-TPC With Pixel Readout*, IEEE Trans. Nucl. Sci. **59** (2012) (cit. on p. 60).

[105] T. Poikela et al., "Timepix3: a 65k channel hybrid pixel readout chip with simultaneous ToA/ToT and sparse readout", *Proceedings, 15th International Workshop on Radiation Imaging Detectors: Paris, France, 23-27 Jun 2013*, vol. 9, 2014 C05013 (cit. on p. 63).

[106] D. S. S. Bello et al., *An interface board for the control and data acquisition of the Medipix2 chip*, Nucl. Instr. Meth. Phys. Res. A **509** (2003) 164 (cit. on p. 66).

[107] T. Holy et al., *Data acquisition and processing software package for Medipix2*, Nucl. Instr. Meth. Phys. Res. A **563** (2006) 254 (cit. on p. 66).

[108] D. Turecek et al., "Pixelman: a multi-platform data acquisition and processing software package for Medipix2, Timepix and Medipix3 detectors", *Proceedings, 12th International Workshop on Radiation Imaging Detectors: Robinson College, Cambridge, U.K., 11-15 Jul 2010*, vol. 6, 2011 C01046 (cit. on p. 66).

[109] M. Lupberger, K. Desch and J. Kaminski, *Implementation of the Timepix ASIC in the Scalable Readout System*, Nucl. Instr. Meth. Phys. Res. A **830** (2016) 75 (cit. on p. 66).

[110] S. Martoiu, H. Muller and J. Toledo, "Front-end electronics for the Scalable Readout System of RD51", *2011 IEEE Nuclear Science Symposium Conference Record*, 2011 2036 (cit. on p. 66).

[111] C. Krieger et al., *A GridPix-based X-ray detector for the CAST experiment*, Nucl. Instr. Meth. Phys. Res. A **867** (2017) 101 (cit. on pp. 66, 83, 114).

[112] R. Bellazzini and F. Muleri, *X-ray polarimetry: A new window on the high energy sky*, Nucl. Instr. Meth. Phys. Res. A **623** (2010) 766 (cit. on p. 70).

[113] A. Thompson et al., *X-ray Data Booklet*, online available at http://xdb.lbl.gov/ (accessed on Juli 31st, 2017), 2009 (cit. on pp. 70, 80, 84, 85, 117, 118, 181).

[114] C. Krieger et al., *Energy Dependent Features of X-ray Signals in a GridPix Detector*, version 1, submitted to Nucl. Instr. Meth. Phys. Res. A, 2017, arXiv: `1709.07631v1 [physics.ins-det]` (cit. on pp. 79, 86, 87, 89–91, 93, 126, 177–179).

[115] T. Vafeiadis, *Contribution to the search for solar axions in the CAST experiment*, CERN-THESIS-2012-349, PhD thesis: Aristotle University of Thessaloniki / CERN, 2012 (cit. on p. 79).

[116] P. V. GmbH, *The Vacuum Technology Book Volume II: Band 2 – Know-how Book*, Pfeiffer Vacuum GmbH, 2013 (cit. on p. 81).

[117] G. Villa et al., *The Optical/UV Filters for the EPIC Experiment*, IEEE Trans. Nucl. Sci. **45** (3 1998) 921 (cit. on p. 84).

[118] K.-H. Stephan et al., "Performance of an Optical Filter for the XMM Focal Plane CCD-Camera EPIC", *EUV, X-Ray, and Gamma-Ray Instrumentation for Astronomy VII*, vol. 2808, 1996 421 (cit. on p. 84).

[119] J. Abernathy et al., "MarlinTPC: A common software framework for TPC development", *2008 IEEE Nuclear Science Symposium Conference Record*, 2008 1704 (cit. on pp. 82, 125, 126).

[120] T. Junk, *Confidence level computation for combining searches with small statistics*, Nucl. Instr. Meth. Phys. Res. A **434** (1999) 435 (cit. on pp. 139–141).

[121] G. Cowan, *Statistical Data Analysis*, Oxford University Press, 1998, ISBN: 0-198-50155-2 (cit. on p. 139).

[122] P. Brax and K. Zioutas, *Solar chameleons*, Phys. Rev. D **82** (2010) 043007 (cit. on p. 143).

[123] H. Antia, S. Chitre and M. Thompson, *On variation of the latitudinal structure of the solar convection zone*, Astron. Astrophys. **399** (2003) 329 (cit. on p. 154).

[124] A. Deisting, *Readout and Analysis of the Induced Ion Signal of an InGrid Detector*, Master thesis: Universität Bonn, 2014 (cit. on p. 160).

[125] S. Schmidt, *Search for particles beyond the SM using an InGrid detector at CAST*, Master thesis: Universität Bonn, 2016 (cit. on p. 160).

[126] S. Huebner et al., *High Performance X-ray Transmission Windows Based on Graphenic Carbon*, IEEE Trans. Nucl. Sci. **62** (2 2015) 588 (cit. on pp. 175, 176).

APPENDIX A

X-ray transmission of different window materials

The InGrid based X-ray detector described and used throughout this thesis (see chapter 7) is equipped with an X-ray entrance window made from a 2 µm Mylar® film (thickness of the aluminisation is typically 40 nm) glued on a copper strongback. Of course their exist alternative window materials, some of them are presented with their X-ray transmission in Fig. A.1. Thinner Mylar films are in principle possible but are on the hand not commercially available in an aluminzed from and on the other hand with decreasing film thickness the number of pin holes increases which spoils the required gas or vacuum tightness of the window. Beryllium is a common window material in vacuum technology but is problematic and difficult to handle due to its toxicity, especially when considering a possible window burst. Also, to be a vacuum tight and withstand a pressure difference of 1 000 mbar a beryllium window requires a minimum thickness of approximately 10 µm which results in a performance, especially below 2 keV, slightly worse compared to the 2 µm Mylar window.

Promising alternative materials are graphenic carbon [126] and silicon nitride as can be seen from Fig. A.1(b) but both require extensive research and development. For the upgraded InGrid based X-ray detector, see chapter 12, a 300 nm silicon nitride window has been developed in cooperation with the Canadian company Norcada. Especially for the silicon nitride windows a strongback structure is required for the windows to withstand pressure differences of more than 1 000 mbar, those are typically integrated in the form of silicon ribs of a few hundred micron thickness and reduce the overall optical transparency of the resulting window. Taking into account the required strongback structures it may happen that a 200 nm silicon nitride window achieves an X-ray transmission only slightly higher (or even lower) than a 300 nm silicon nitride window as more and/or thicker ribs may be required for a working strongback structure.

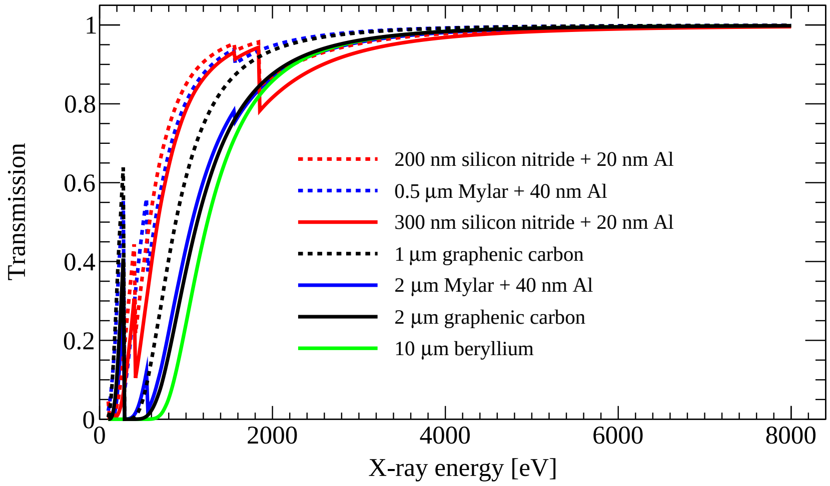

(a)

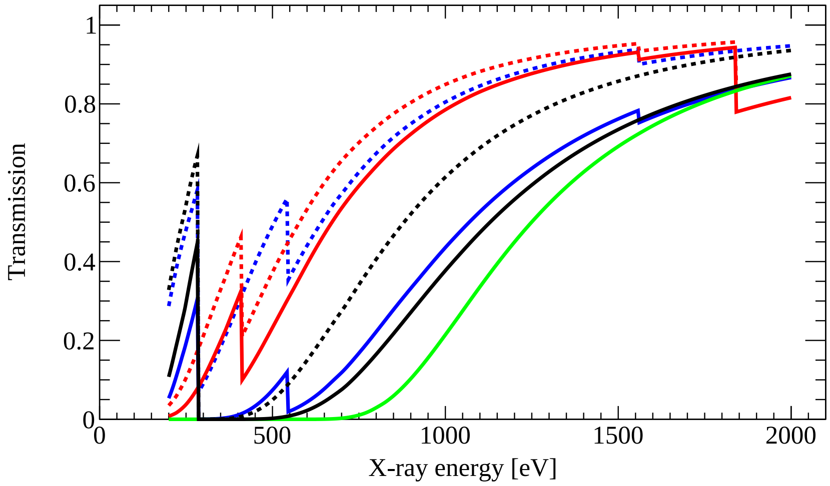

(b)

Figure A.1: X-ray transmission of different window materials: aluminized Mylar® with 0.5 µm and 2 µm thickness, silicon nitride in 200 nm and 300 nm thickness, graphenic carbon [126] with 1 µm and 2 µm thickness and beryllium with 10 µm thickness. (a) shows the X-ray transmission in the range up to 8 keV while (b) zooms into the region below 2 keV, both plots use the same legend which is shown in (a). Optical transparency of strongback structure maybe required is not taken into account. The transmission data has been generated with a web based tool [101] based on the semi-empicrical approach described in [102].

APPENDIX B

X-ray spectra recorded in the CAST Detector Lab in April 2014

During the measurement campaign carried out with the InGrid based X-ray detector in the CAST Detector Lab (CDL) at CERN using a variable X-ray generator datasets at eight different set-ups have been recorded in order to obtain datasets for eight different X-ray energies ranging from 8 keV down to 277 eV. The results obtained from these measurements are described in chapter 7 and have also been published as [114]. The eight different set-ups used are listed in Table 7.1 in chapter 7. To clean the datasets loose cuts have been applied to the reconstructed clusters, these cuts are listed in Table B.1.

The resulting, (almost) clean X-ray spectra are shown in Figs. B.1 and B.2 in both the pixel as well as the charge representation. For the sake of completeness also the four spectra already introduced in Fig. 7.24 are included. To each spectrum a dedictaed function is fitted taking into account all known and/or visible peaks which in addition to the main peak of interest can stem from close-by K_β lines, escape lines or contaminations of the target material, the functions used for each set-up are listed in Tables B.2 (pixel spectra) and B.3 (charge spectra). To reduce the number of free parameters in the fit functions some parameters were constrained by making use fort example the known relative distance or relative intensity of different lines, the main peak of interest and, for energies above 3.2059 keV, their corresponding escape line have always been left unconstrained to avoid biasing the results of the fit. The lines appearing in each spectrum and the parameters constrained are listed in Table B.4.

set-up	applied cuts
A	$\epsilon < 1.3$, $0.1\,\mathrm{mm} < \sigma_{\mathrm{trans}} \leq 1.0\,\mathrm{mm}$
B	$\epsilon < 1.3$, $0.1\,\mathrm{mm} < \sigma_{\mathrm{trans}} \leq 1.0\,\mathrm{mm}$
C	$\epsilon < 1.3$, $0.1\,\mathrm{mm} < \sigma_{\mathrm{trans}} \leq 1.0\,\mathrm{mm}$
D	$\epsilon < 1.4$, $0.1\,\mathrm{mm} < \sigma_{\mathrm{trans}} \leq 1.0\,\mathrm{mm}$, $l \leq 6\,\mathrm{mm}$
E	$\epsilon < 2.0$, $0.1\,\mathrm{mm} < \sigma_{\mathrm{trans}} \leq 1.1\,\mathrm{mm}$
F	$\epsilon < 2.0$, $0.1\,\mathrm{mm} < \sigma_{\mathrm{trans}} \leq 1.1\,\mathrm{mm}$
G	$\epsilon < 2.0$, $0.1\,\mathrm{mm} < \sigma_{\mathrm{trans}} \leq 1.1\,\mathrm{mm}$
H	$0.1\,\mathrm{mm} < \sigma_{\mathrm{trans}} \leq 1.1\,\mathrm{mm}$, $l \leq 6\,\mathrm{mm}$

Table B.1: Cuts on eccentricity ϵ, transverse rms σ_{trans} and length l, applied to the data recorded with the different X-ray generator set-ups. Cut values are chosen rather loose in order to only reject events incompatible with the single photon hypothesis. Additionally, for all set-ups a minimum number of 3 active pixels is required to reject empty events. Also, all accepted events are required to have their center of gravity within a 4.5 mm radius around the GridPix' center to avoid clusters only partially contained within the active area.

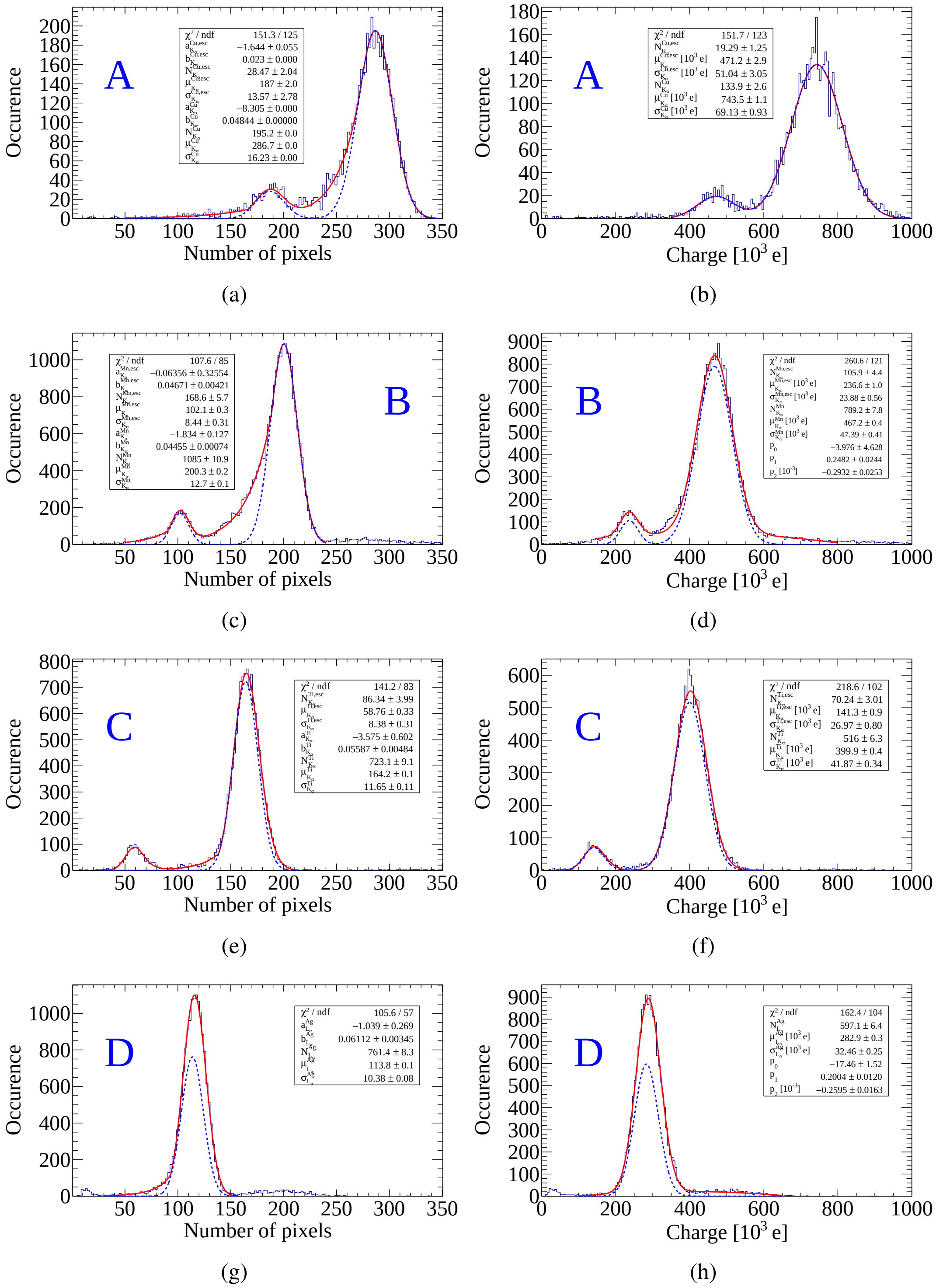

(a) (b)

(c) (d)

(e) (f)

(g) (h)

Figure B.1: X-ray spectra of settings A to D (see Table 7.1) using both the pixel representation (left) and the charge representation (right). Main peaks shown are the copper K_α line at 8 keV: (a) and (b); the manganese K_α line at 5.9 keV: (c) and (d); the titanium K_α line at 4.5 keV: (e) and (f); and the silver L_α line at 3 keV: (g) and (h). The functions fitted to the spectra are shown in solid red while the Gaussian distributions describing the main peaks are plotted in addition as blue dashed line. Spectra published in [114].

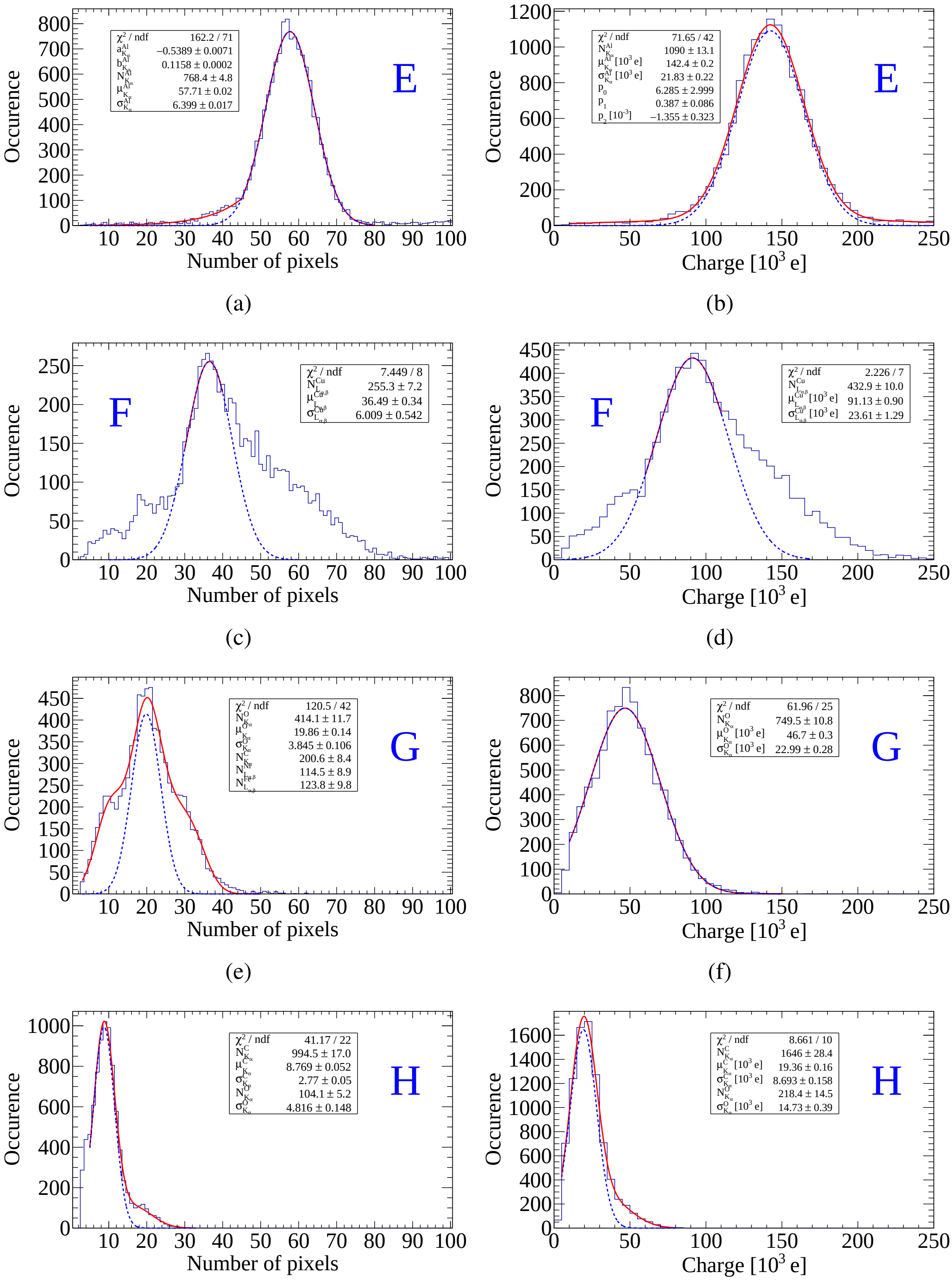

(a) (b)

(c) (d)

(e) (f)

(g) (h)

Figure B.2: X-ray spectra of settings E to H (see Table 7.1) using both the pixel representation (left) and the charge representation (right). Main peaks shown are the aluminum K_α line at 1.5 keV: (a) and (b); the copper L_α line at 0.9 keV: (c) and (d); the oxygen K_α line at 0.5 keV: (e) and (f); and the carbon K_α line at 277 eV: (g) and (h). The functions fitted to the spectra are shown in solid red while the Gaussian distributions describing the main peaks are plotted in addition as blue dashed line. Spectra published in [114].

set-up	fit function
A	$EG^{\mathrm{Cu,esc}}_{\mathrm{K}_\alpha}(a,b,N,\mu,\sigma) + EG^{\mathrm{Cu}}_{\mathrm{K}_\alpha}(a,b,N,\mu,\sigma)$
B	$EG^{\mathrm{Mn,esc}}_{\mathrm{K}_\alpha}(a,b,N,\mu,\sigma) + EG^{\mathrm{Mn}}_{\mathrm{K}_\alpha}(a,b,N,\mu,\sigma)$
C	$G^{\mathrm{Ti,esc}}_{\mathrm{K}_\alpha}(N,\mu,\sigma) + G^{\mathrm{Ti,esc}}_{\mathrm{K}_\beta}(N,\mu,\sigma)$ $+EG^{\mathrm{Ti}}_{\mathrm{K}_\alpha}(a,b,N,\mu,\sigma) + G^{\mathrm{Ti}}_{\mathrm{K}_\beta}(N,\mu,\sigma)$
D	$EG^{\mathrm{Ag}}_{\mathrm{L}_\alpha}(a,b,N,\mu,\sigma) + G^{\mathrm{Ag}}_{\mathrm{L}_\beta}(N,\mu,\sigma)$
E	$EG^{\mathrm{Al}}_{\mathrm{K}_\alpha}(a,b,N,\mu,\sigma)$
F	$G^{\mathrm{Cu}}_{\mathrm{L}_{\alpha,\beta}}(N,\mu,\sigma)$
G	$G^{\mathrm{O}}_{\mathrm{K}_\alpha}(N,\mu,\sigma) + G^{\mathrm{C}}_{\mathrm{K}_\alpha}(N,\mu,\sigma)$ $+G^{\mathrm{Fe}}_{\mathrm{L}_{\alpha,\beta}}(N,\mu,\sigma) + G^{\mathrm{Ni}}_{\mathrm{L}_{\alpha,\beta}}(N,\mu,\sigma)$
H	$G^{\mathrm{C}}_{\mathrm{K}_\alpha}(N,\mu,\sigma) + G^{\mathrm{O}}_{\mathrm{K}_\alpha}(N,\mu,\sigma)$

Table B.2: Fit functions used for the pixel spectra in Figs. B.1, B.2 and 7.24. A Gaussian with amplitude N, mean μ and width σ is abbreviated with $G(N,\mu,\sigma)$ while the Gaussian joined with an exponential decay to the left (see Equation 7.10) is noted as $EG(a,b,N,\mu,\sigma)$. The upper and lower indexes of the parameters are noted at the function itself as all parameters of a function share the same index, e.g. $G(N_\alpha,\mu_\alpha,\sigma_\alpha)$ will be noted as $G_\alpha(N,\mu,\sigma)$. Not all parameters were left free for the fits, Table B.4 lists the parameters fixed for each setting.

set-up	fit function
A	$G^{\mathrm{Cu,esc}}_{\mathrm{K}_\alpha}(N,\mu,\sigma) + G^{\mathrm{Cu}}_{\mathrm{K}_\alpha}(N,\mu,\sigma)$
B	$G^{\mathrm{Mn,esc}}_{\mathrm{K}_\alpha}(N,\mu,\sigma) + G^{\mathrm{Mn}}_{\mathrm{K}_\alpha}(N,\mu,\sigma) + p_0 + p_1 \cdot x + p_2 \cdot x^2$
C	$G^{\mathrm{Ti,esc}}_{\mathrm{K}_\alpha}(N,\mu,\sigma) + G^{\mathrm{Ti,esc}}_{\mathrm{K}_\beta}(N,\mu,\sigma)$ $+G^{\mathrm{Ti}}_{\mathrm{K}_\alpha}(N,\mu,\sigma) + G^{\mathrm{Ti}}_{\mathrm{K}_\beta}(N,\mu,\sigma)$
D	$G^{\mathrm{Ag}}_{\mathrm{L}_\alpha}(N,\mu,\sigma) + G^{\mathrm{Ag}}_{\mathrm{L}_\beta}(N,\mu,\sigma) + p_0 + p_1 \cdot x + p_2 \cdot x^2$
E	$G^{\mathrm{Al}}_{\mathrm{K}_\alpha}(N,\mu,\sigma) + p_0 + p_1 \cdot x + p_2 \cdot x^2$
F	$G^{\mathrm{Cu}}_{\mathrm{L}_{\alpha,\beta}}(N,\mu,\sigma)$
G	$G^{\mathrm{O}}_{\mathrm{K}_\alpha}(N,\mu,\sigma)$
H	$G^{\mathrm{C}}_{\mathrm{K}_\alpha}(N,\mu,\sigma) + G^{\mathrm{O}}_{\mathrm{K}_\alpha}(N,\mu,\sigma)$

Table B.3: Fit functions used for the charge spectra in Figs. B.1, B.2 and 7.24. A Gaussian with amplitude N, mean μ and width σ is abbreviated with $G(N,\mu,\sigma)$. The upper and lower indexes of the parameters are noted at the function itself as all parameters of a function share the same index, e.g. $G(N_\alpha,\mu_\alpha,\sigma_\alpha)$ will be noted as $G_\alpha(N,\mu,\sigma)$. Not all parameters were left free for the fits, Table B.4 lists the parameters fixed for each setting.

fluorescence line	additional peaks	fixed parameters
Cu K_α (8.048 keV)	Cu K_α escape (5.057 keV)	none
Mn K_α (5.899 keV)	Mn K_α escape (2.925 keV)	none
Ti K_α (4.511 keV)	Ti K_β (4.932 keV)	$\mu^{\mathrm{Ti}}_{\mathrm{K}_\beta}, \sigma^{\mathrm{Ti}}_{\mathrm{K}_\beta}, N^{\mathrm{Ti}}_{\mathrm{K}_\beta}/N^{\mathrm{Ti}}_{\mathrm{K}_\alpha}$
	Ti K_α escape (1.537 keV)	
	Ti K_β escape(1.959 keV)	$\mu^{\text{Ti-esc}}_{\mathrm{K}_\beta}, \sigma^{\text{Ti-esc}}_{\mathrm{K}_\beta}$
Ag L_α (2.984 keV)	Ag L_β (3.151 keV)	$\mu^{\mathrm{Ag}}_{\mathrm{L}_\beta},\sigma^{\mathrm{Ag}}_{\mathrm{L}_\beta},N^{\mathrm{Ag}}_{\mathrm{L}_\beta}/N^{\mathrm{Ag}}_{\mathrm{L}_\alpha}$
Al K_α (1.487 keV)	none	none
Cu L_α (0.930 keV)	see note in caption	see note in caption
O K_α (0.525 keV)	C K_α (0.277 keV)	$\mu^{\mathrm{C}}_{\mathrm{K}_\alpha},\sigma^{\mathrm{C}}_{\mathrm{K}_\alpha}$
	Fe $\mathrm{L}_{\alpha,\beta}$ (0.71 keV)	$\mu^{\mathrm{Fe}}_{\mathrm{K}_{\alpha,\beta}},\sigma^{\mathrm{Fe}}_{\mathrm{K}_{\alpha,\beta}}$
	Ni $\mathrm{L}_{\alpha,\beta}$ (0.86 keV)	$\mu^{\mathrm{Ni}}_{\mathrm{K}_{\alpha,\beta}},\sigma^{\mathrm{Ni}}_{\mathrm{K}_{\alpha,\beta}}$
C K_α (0.277 keV)	O K_α (0.525 keV)	$\mu^{\mathrm{O}}_{\mathrm{K}_\alpha},\sigma^{\mathrm{O}}_{\mathrm{K}_\alpha}$

Table B.4: X-ray lines visible in the different spectra. For some of the spectra additional lines have to be taken into account in the fitted functions which stem from argon escape lines, close-by β lines and/or additional elements present in the target material (possible contaminations). To simplify the fits as many parameters as possible have been fixed for the additional lines: The mean μ of the fitted Gaussian is usually fixed relative to the position of the main peak while the width σ is assumed to be the same as for the close-by main peak. For β lines also the relative intensity is used to fully fix the additional peak through the main peak. In case of the copper L_α line there are definitely contributions by other X-ray lines visible in the spectrum but no neighboring peaks could be clearly identified, therefore in this case the fit range was narrowed to the main peak. In case of the oxygen K_α line many contaminants show up, possibly present in the form of stainless steel screws used to mount the target. Additional peaks were identified using the tabulated X-ray fluorescence energies in [113] from which also the information used to fix some of the fit parameters were taken.

APPENDIX C

Reference datasets

From the datasets obtained from a measurement campaign at the variable X-ray generator of the CAST Detector Lab (CDL) (see chapter 7) eight reference datasets have been created to be used for the likelihood based background suppression method described in chapter 10. The three event shape variables obtained from reconstructed clusters (excentricity ϵ, length l divided by σ_{trans} and fraction $F_{1\sigma_{\text{trans}}}$ of pixels within radius of σ_{trans} around the cluster's center) are computed for the reference datasets. The resulting distributions for these variables are shown for eight energies in Fig. C.1 (excentricity ϵ), C.2 (l/σ_{trans}) and C.3 (fraction $F_{1\sigma_{\text{trans}}}$). The reference datasets correspond to the eight datasets obtained with the X-ray generator settings listed in Table 7.1, the datasets have been cleaned applying the cuts listed in Table C.1, where the cut on the charge Q is used to select the main peak and to remove e.g. the escape lines from the dataset.

set-up	charge cut	eventshape cuts
A	$5.9 \times 10^5\,e < Q < 10.0 \times 10^5\,e$	$l \leq 7\,\text{mm}$, $0.1\,\text{mm} < \sigma_{\text{trans}} \leq 1.1\,\text{mm}$
B	$3.5 \times 10^5\,e < Q < 6.0 \times 10^5\,e$	$l \leq 7\,\text{mm}$, $0.1\,\text{mm} < \sigma_{\text{trans}} \leq 1.1\,\text{mm}$
C	$2.9 \times 10^5\,e < Q < 5.5 \times 10^5\,e$	$l \leq 7\,\text{mm}$, $0.1\,\text{mm} < \sigma_{\text{trans}} \leq 1.1\,\text{mm}$
D	$2.0 \times 10^5\,e < Q < 4.0 \times 10^5\,e$	$l \leq 7\,\text{mm}$, $0.1\,\text{mm} < \sigma_{\text{trans}} \leq 1.1\,\text{mm}$
E	$0.9 \times 10^5\,e < Q < 2.1 \times 10^5\,e$	$l \leq 7\,\text{mm}$, $0.1\,\text{mm} < \sigma_{\text{trans}} \leq 1.1\,\text{mm}$
F	$0.7 \times 10^5\,e < Q < 1.3 \times 10^5\,e$	$l \leq 7\,\text{mm}$, $0.1\,\text{mm} < \sigma_{\text{trans}} \leq 1.1\,\text{mm}$
G	$0.3 \times 10^5\,e < Q < 0.8 \times 10^5\,e$	$l \leq 6\,\text{mm}$, $0.1\,\text{mm} < \sigma_{\text{trans}} \leq 1.1\,\text{mm}$
H	$Q < 0.5 \times 10^5\,e$	$l \leq 6\,\text{mm}$

Table C.1: Cuts used for creation of reference datasets. These cuts were applied to the datasets recorded at the variable X-ray generator of the CDL using the settings listed in Table 7.1. Main purpose of the cuts on the charge Q is to select the main peak only and to remove e.g. escape lines.

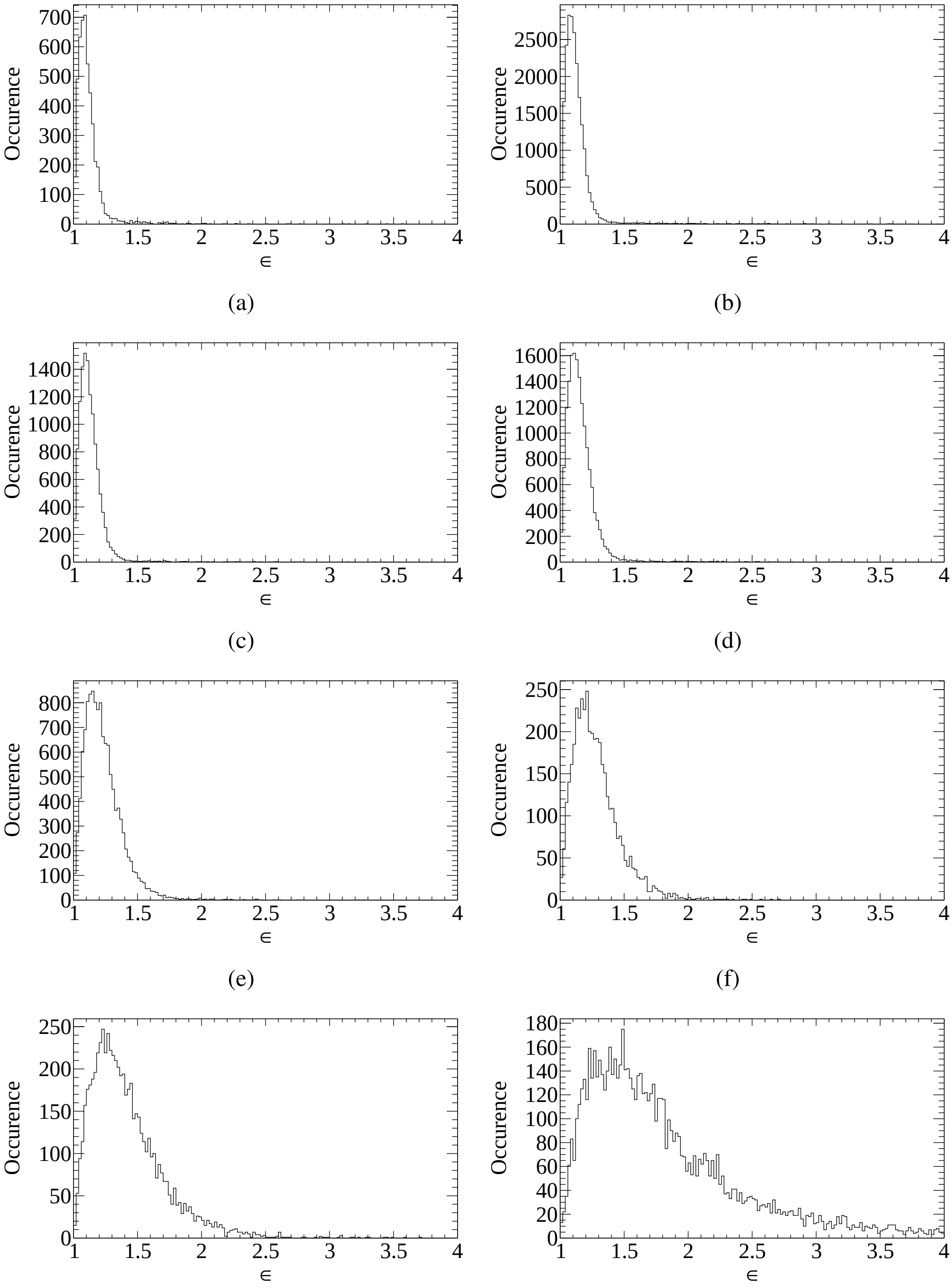

(a)

(b)

(c)

(d)

(e)

(f)

(g)

(h)

Figure C.1: Distributions of event shape variable excentricity ϵ for all eight reference datasets recorded at the variable X-ray generator of the CDL using the settings listed in Table 7.1. To clean the datasets the cuts listed in Tables B.1 and C.1 were applied. The references correspond to the X-ray generator set-ups characterizing the datasets, e.g. (a) corresponds to set-up A, (b) to set-up B and so forth.

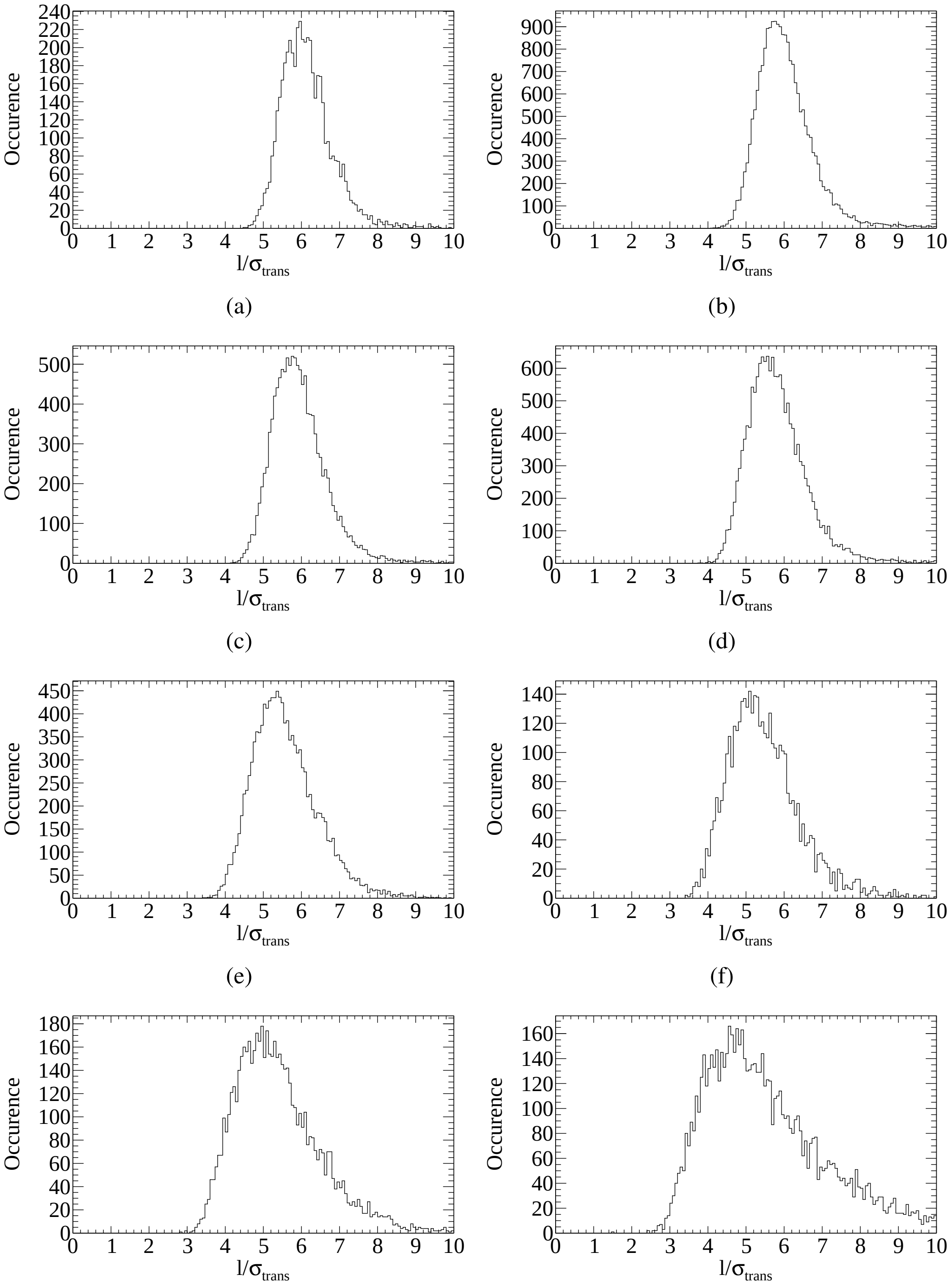

(a) (b) (c) (d) (e) (f) (g) (h)

Figure C.2: Distributions of event shape variable l/σ_{trans} for all eight reference datasets recorded at the variable X-ray generator of the CDL using the settings listed in Table 7.1. To clean the datasets the cuts listed in Tables B.1 and C.1 were applied. The references correspond to the X-ray generator set-ups characterizing the datasets, e.g. (a) corresponds to set-up A, (b) to set-up B and so forth.

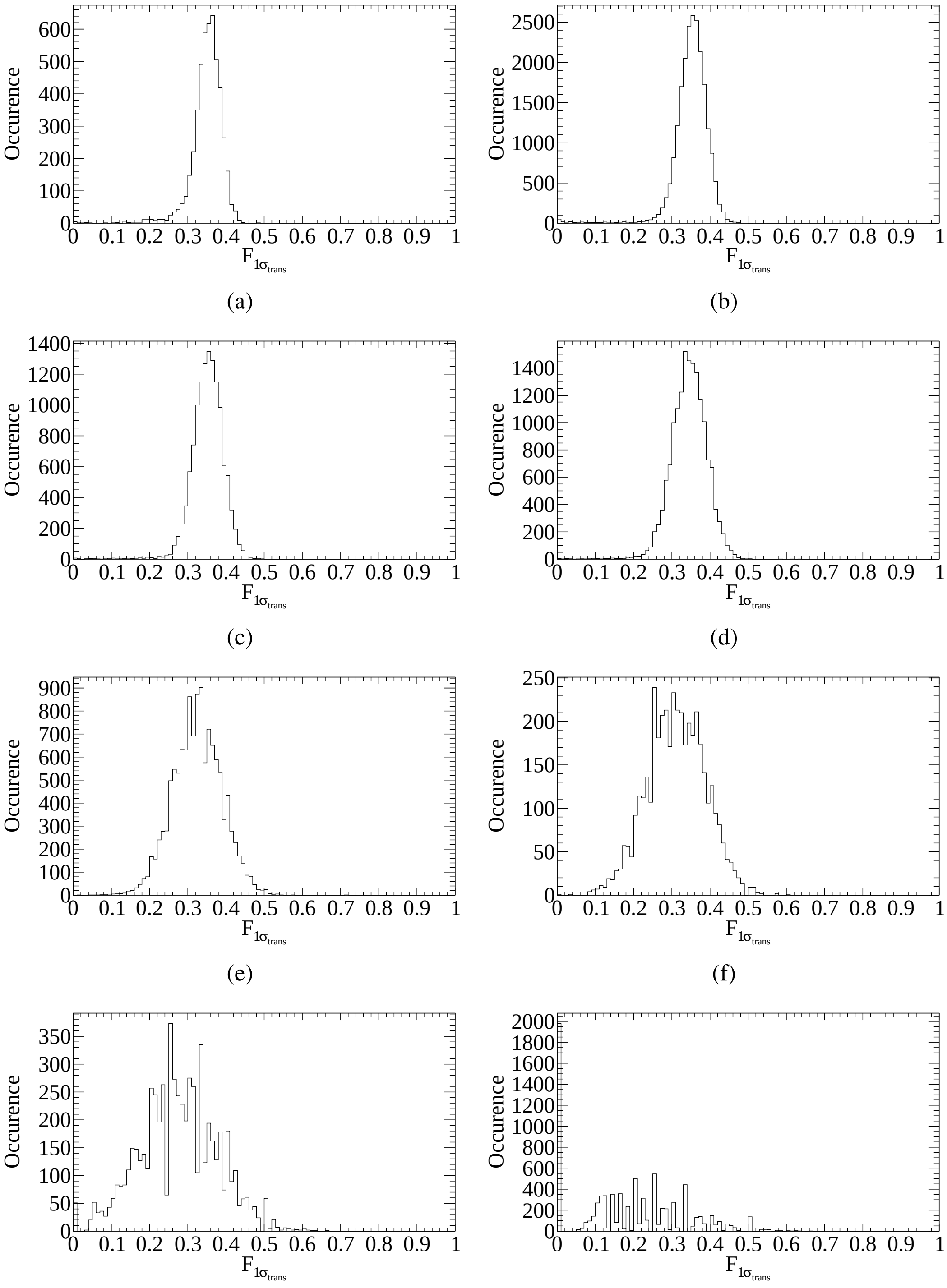

(a) (b)

(c) (d)

(e) (f)

(g) (h)

Figure C.3: Distributions of event shape variable fraction $F_{1\sigma_{\text{trans}}}$ for all eight reference datasets recorded at the variable X-ray generator of the CDL using the settings listed in Table 7.1. To clean the datasets the cuts listed in Tables B.1 and C.1 were applied. The references correspond to the X-ray generator set-ups characterizing the datasets, e.g. (a) corresponds to set-up A, (b) to set-up B and so forth.

APPENDIX D

Distribution of event shape variables for mostly non X-ray photon events

The background dataset (see chapter 9) recorded during the data taking campaign 2014 and 2015 of CERN Axion Solar Telescope (CAST) mostly contains non X-ray photon events. Event shape variables can be used to separate those from the few clusters originating from X-ray photons. To allow comparison with the reference distributions (see appendix C) the data has been split in eight energy ranges, defined in table 10.1 and named a through h and corresponding through the reference datasets A through H listed in table 7.1. Three event shape variables were identified and constructed for use in a likelihood based background suppression method (see chapter 10): excentricity ϵ, length l divided by σ_{trans} and fraction $F_{1\sigma_{\text{trans}}}$ of pixels within radius of σ_{trans} around the cluster's center. The distributions of those variables are shown for the different energy ranges in Figs. D.1, D.2 and D.3 respectively.

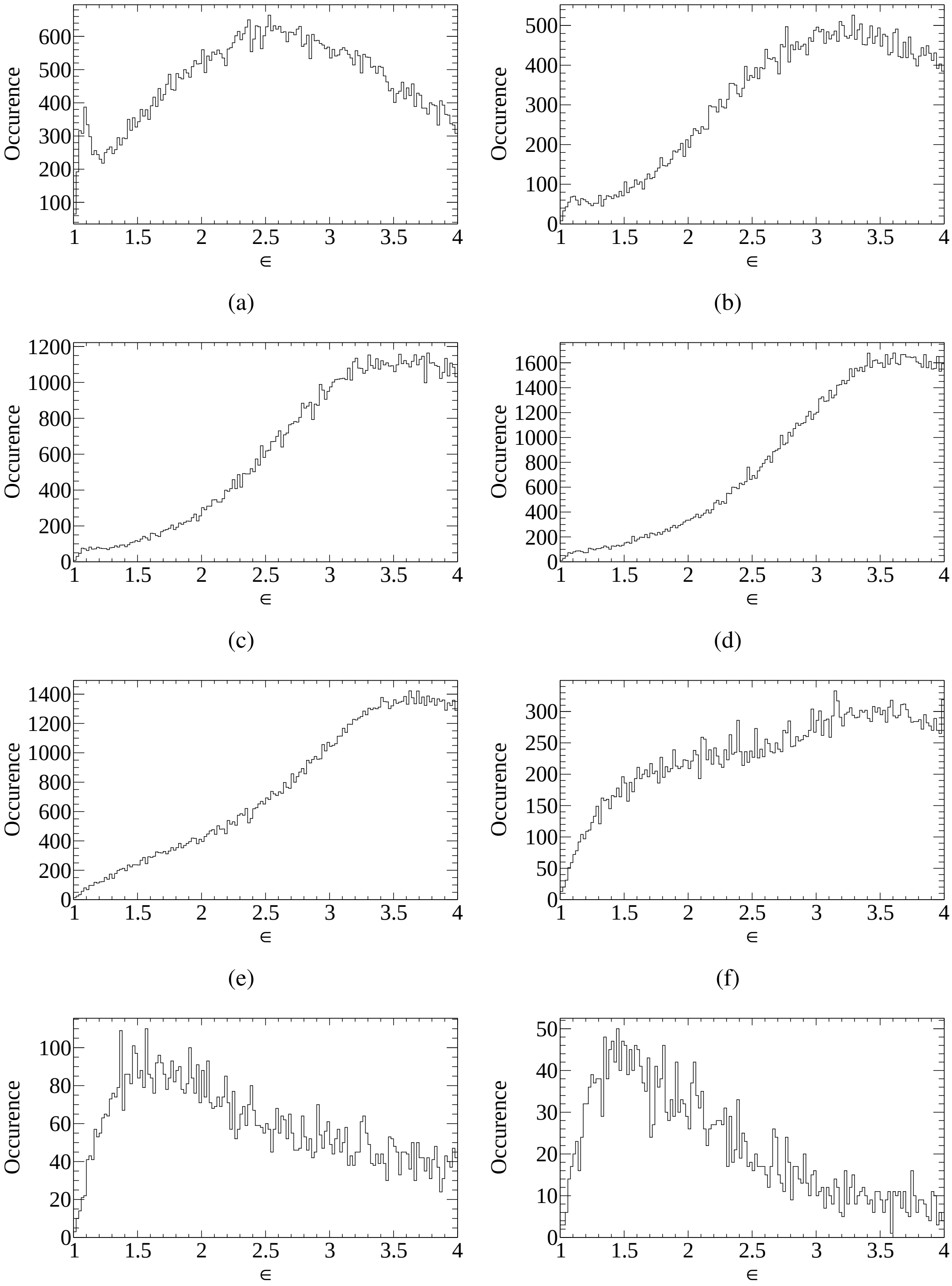

(a) (b)

(c) (d)

(e) (f)

(g) (h)

Figure D.1: Distributions of event shape variable excentricity ϵ for all eight energy ranges defined for the background dataset recorded at CAST during data taking in 2014 and 2015. The energy ranges are listed in table 10.1 and correspond to the eight reference datasets. The references correspond to the energy range, e.g. (a) corresponds to range a, (b) to range b and so forth.

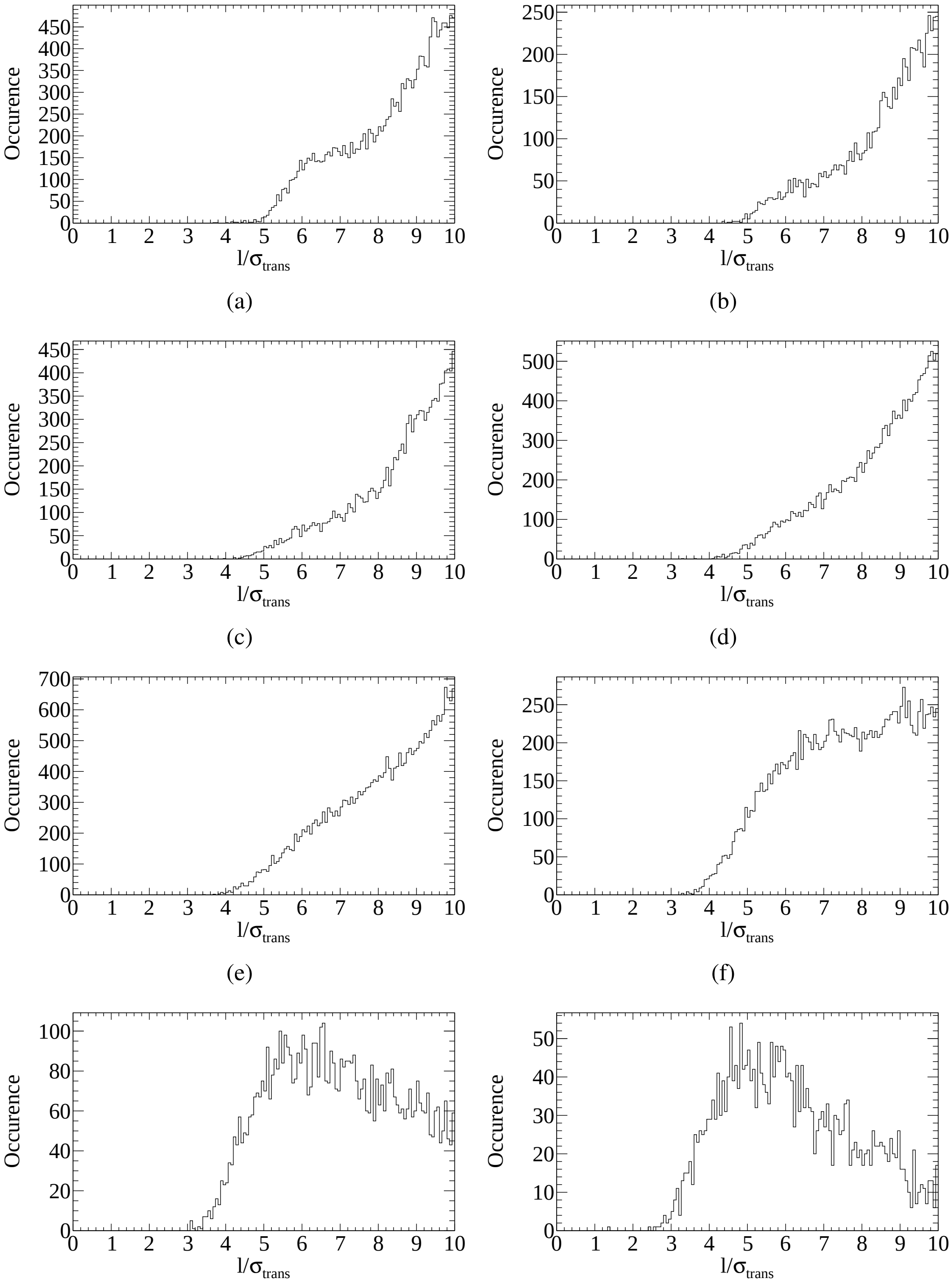

(a) (b)

(c) (d)

(e) (f)

(g) (h)

Figure D.2: Distributions of event shape variable l/σ_{trans} for all eight energy ranges defined for the background dataset recorded at CAST during data taking in 2014 and 2015. The energy ranges are listed in table 10.1 and correspond to the eight reference datasets. The references correspond to the energy range, e.g. (a) corresponds to range a, (b) to range b and so forth.

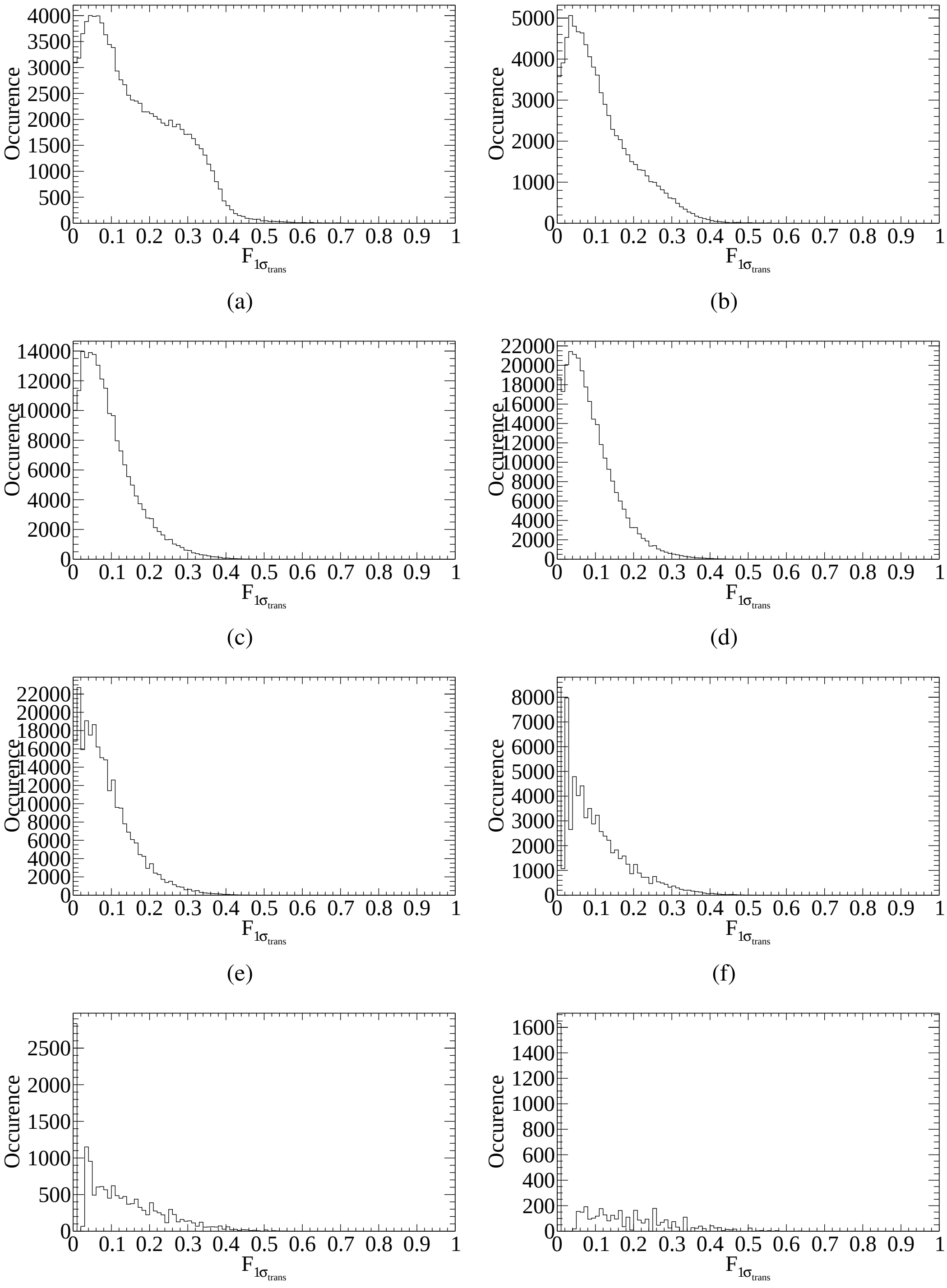

(a) (b) (c) (d) (e) (f) (g) (h)

Figure D.3: Distributions of event shape variable fraction $F_{1\sigma_{\mathrm{trans}}}$ for all eight energy ranges defined for the background dataset recorded at CAST during data taking in 2014 and 2015. The energy ranges are listed in table 10.1 and correspond to the eight reference datasets. The references correspond to the energy range, e.g. (a) corresponds to range a, (b) to range b and so forth.

APPENDIX E

Likelihood distributions for reference and background datasets

The background suppression method introduced in chapter 10 used a likelihood value based on reference distributions of three chosen event shape variables. The resulting likelihood distributions for the eight different energy ranges are shown in Figs. E.1 and E.2. In the left column the likelihood distributions for the reference datasets themselves are shown while the right column always shows the distribution for the corresponding energy range of the background dataset. Especially the likelihood distributions for the reference datasets are the basis for selecting a working point by adjusting the cut on the likelihood value. The cut values defining the working point are indicated in the plots as red line and are listed in table 10.2.

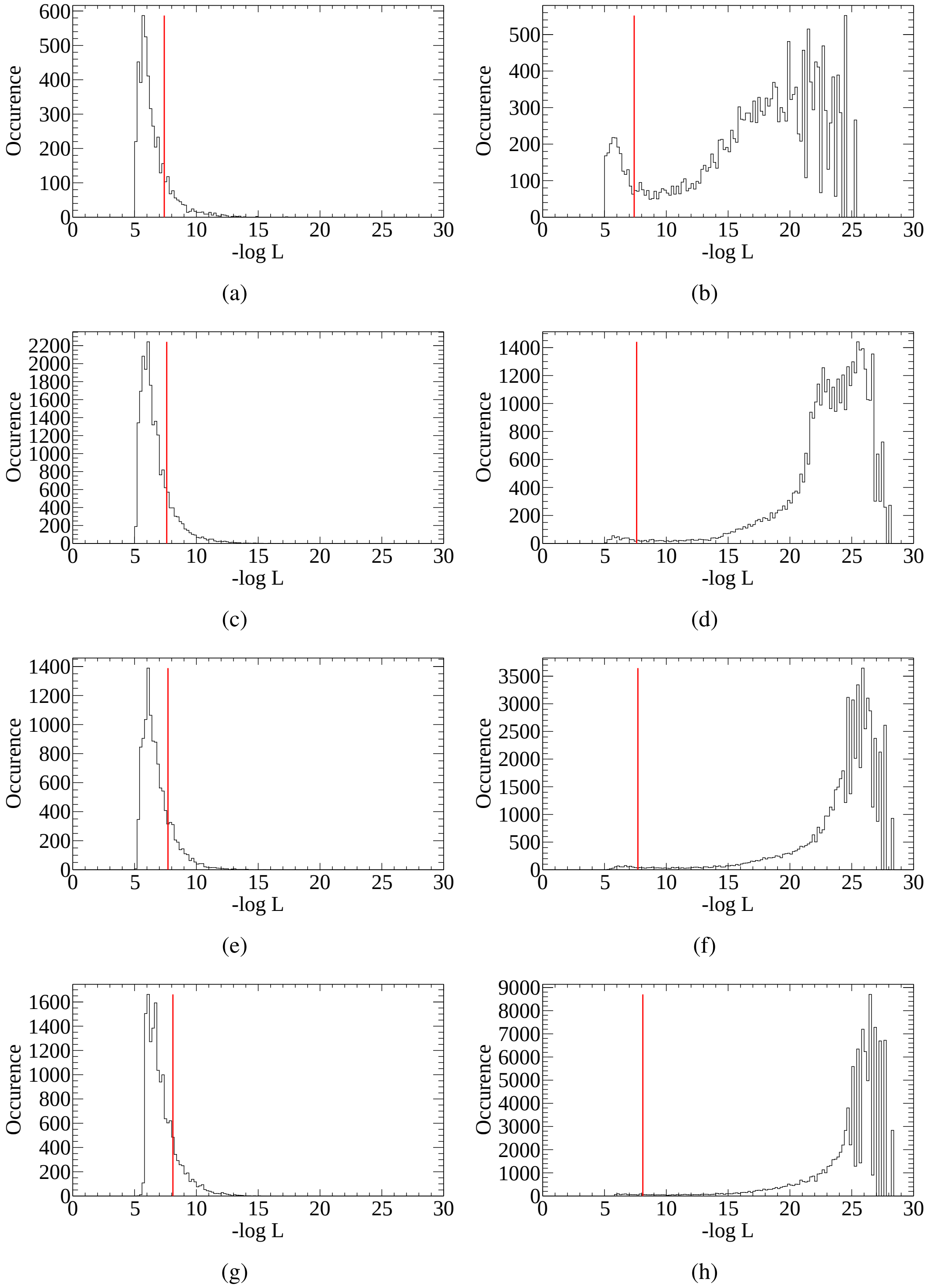

Figure E.1: Likelihood ($-\log\mathcal{L}$) distributions of reference and background datasets. Left column shows distributions for reference datasets while right column shows distributions for according energy range of background dataset. Reference datasets A through D ((a), (c), (e) and (g)) are shown along with the corresponding energy ranges a through d ((b), (d), (f) and (h)). The likelihood cuts of the chosen working point are illustrated as red lines.

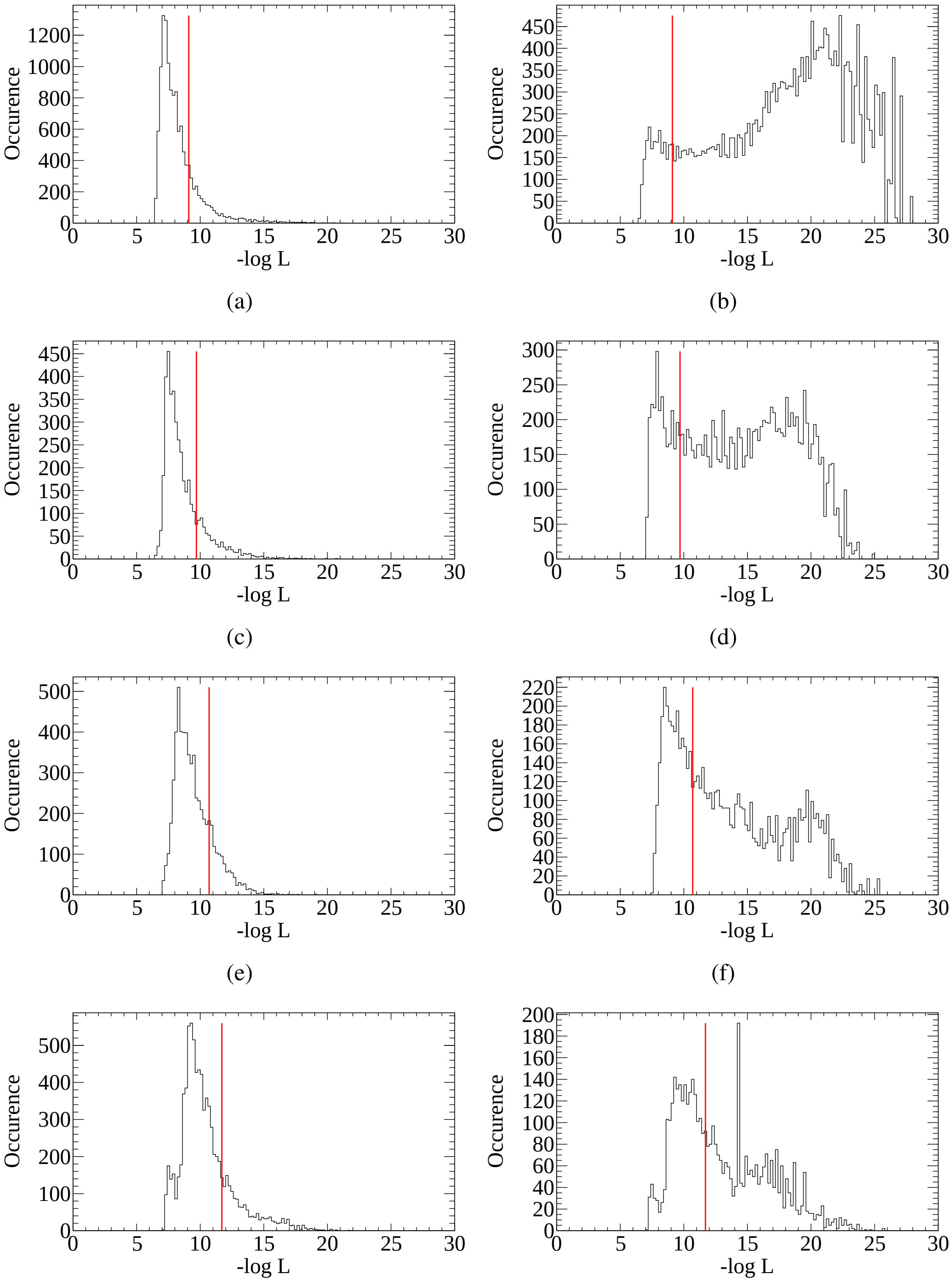

(a) (b)

(c) (d)

(e) (f)

(g) (h)

Figure E.2: Likelihood ($-\log \mathcal{L}$) distributions of reference and background datasets. Left column shows distributions for reference datasets while right column shows distributions for according energy range of background dataset. Reference datasets E through H ((a), (c), (e) and (g)) are shown along with the corresponding energy ranges e through h ((b), (d), (f) and (h)). The likelihood cuts of the chosen working point are illustrated as red lines.

APPENDIX F

Working point of the likelihood based background suppression

To define the working point of the likelihood based background suppression method, for each energy range a cut on $-\log \mathcal{L}$ has to be chosen. The cut values chosen for energy ranges a through h are listed in table 10.2. The choice of the cut values always is a trade-off between high software efficiency (fraction of real X-ray photons passing the cut) and high background suppression (fraction of non X-ray photon events rejected by the cut). In Fig. F.1 the background suppression is shown as function of the software efficiency for the eight energy ranges. The working point chosen is at a software efficiency of 80 % and marked in the plots. The software efficiency is estimated by applying the reference dataset itself to the background suppression method while the background suppression is approximated by assuming that the background dataset consists only of non X-ray photon events which is mostly true.

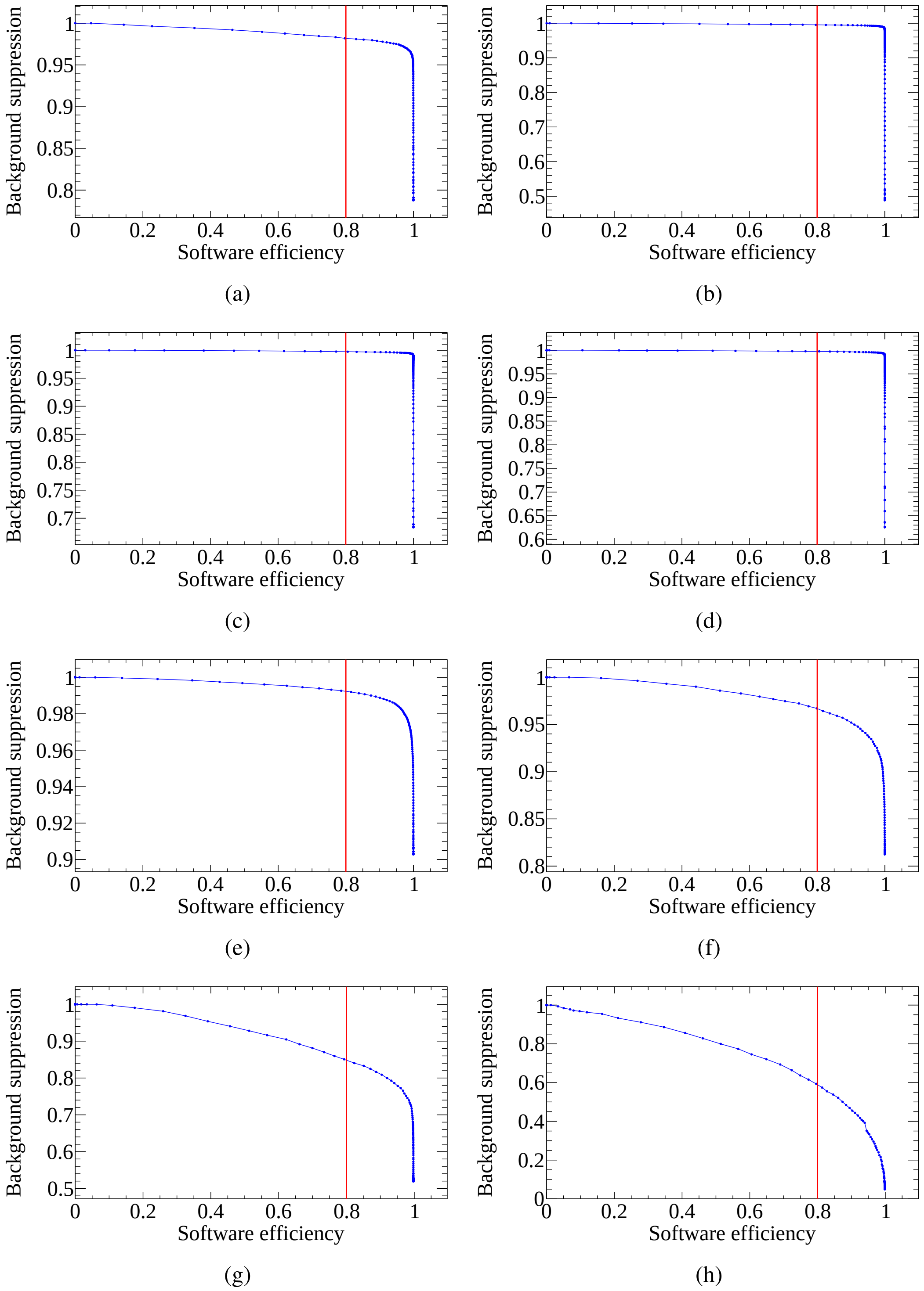

(a) (b) (c) (d) (e) (f) (g) (h)

Figure F.1: Background suppression as function of software efficiency for the eight different energy ranges listed in table 10.1. Software efficiency is estimated by applying the reference datasets themselves to the background suppression method while the background suppression is approximated by assuming that the background dataset consists only of non X-ray photon events. The chosen working point at a software efficiency of 80 % for all energy ranges is marked as red line.

APPENDIX G

Systematic uncertainties

In tables G.1, G.2 and G.3 the estimated systematic uncertainties for the calculation of an upper bound on the chameleon photon coupling β_γ are given for different assumptions on the tachocline position, width and magnetic field.

	systematic uncertainty	
chip region	gold	silver
pointing accuracy	4.0 %	6.0 %
detector alignment	0.7 %	2.5 %
XRT off-axis behavior	1.2 %	2.7 %
XRT on-axis transmission	1.8 %	
differential window transmission	1.6 %	
detector window transmission	3.4 %	
detector window optical transparency	2.0 %	
detector gas absorption	0.1 %	
software efficiency	3.7 %	
total	7.3 %	9.2 %

Table G.1: List of estimated systematic uncertainties for the scenario with the tachocline region starting at $0.66\,R_\odot$ and with a width of $0.01\,R_\odot$. The uncertainties resulting from imaging effects differ for *gold* and *silver* region and are therefore stated separately if necessary.

	systematic uncertainty	
chip region	gold	silver
pointing accuracy	3.2 %	7.5 %
detector alignment	0.8 %	3.0 %
XRT off-axis behavior	1.5 %	3.0 %
XRT on-axis transmission	1.9 %	
differential window transmission	1.6 %	
detector window transmission	3.5 %	
detector window optical transparency	2.0 %	
detector gas absorption	0.1 %	
software efficiency	3.7 %	
total	7.0 %	10.5 %

Table G.2: List of estimated systematic uncertainties for the scenario with the tachocline region starting at $0.66\,R_\odot$ and with a width of $0.04\,R_\odot$. The uncertainties resulting from imaging effects differ for *gold* and *silver* region and are therefore stated separately if necessary.

	systematic uncertainty	
chip region	gold	silver
pointing accuracy	2.8 %	10.0 %
detector alignment	1.5 %	4.0 %
XRT off-axis behavior	1.2 %	2.5 %
XRT on-axis transmission	1.8 %	
differential window transmission	1.9 %	
detector window transmission	4.3 %	
detector window optical transparency	2.0 %	
detector gas absorption	0.1 %	
software efficiency	3.7 %	
total	7.4 %	12.9 %

Table G.3: List of estimated systematic uncertainties for the scenario with the tachocline region starting at $0.7\,R_\odot$ and with a width of $0.1\,R_\odot$ where the tachocline magnetic field decreases linear from 10 T to zero with increasing radial coordinate. The uncertainties resulting from imaging effects differ for *gold* and *silver* region and are therefore stated separately if necessary.

List of Figures

List of Tables

List of Acronyms

ABRIXAS	A Broadband Imaging X-ray All-Sky Survey	96
ADC	analogue-to-digital converter	68
ALP	axion like particle	13
ALPS	Any Light Particle Search	11
ADMX	Axion Dark Matter eXperiment	8
ASIC	application specific integrated circuit	125
BODELAIRE	Boron Detector With Light and Ionization Reconstruction	49
CAD	computer-aided design	157
CAST	CERN Axion Solar Telescope	187
CDL	CAST Detector Lab	183
CHASE	Chameleon Afterglow Search	20
CL	confidence level	165
CMOS	complementary metal-oxide-semiconductor	60
CSA	charge sensitive amplifier	60
CVD	chemical vapour deposition	51
DAC	digital-to-analogue converter	61
ENC	equivalent noise charge	60
FADC	flash analogue-to-digital converter	159
FIB	focussed ion beam	53
FPGA	field programmable gate array	66
FWHM	full width half maximum	24
GEM	Gas Electron Multiplier	44
GR	General Relativity	13
HDMI	High Definition Multimedia Interface	159
IAXO	International Axion Observatory	166
IC	integrated circuit	68
ILC	International Linear Collider	49
ILD	International Large Detector	49
InGrid	Integrated Grid	165
IZM	Institut für Zuverlässigkeit und Mikrointegration	63

KWISP	Kinetic WISP detection	25
LHC	Large Hadron Collider	43
LLNL	Lawrence Livermore National Laboratory	157
LSW	light-shining-through-wall	10
LVDS	low voltage differential signaling	68
MADMAX	Magnetized Disc and Mirror Axion Experiment	8
MicroMegas	Micro-Mesh Gaseous Structure	157
MIP	minimum ionizing particle	134
MPE	Max-Planck-Institut für extraterrestrische Physik	22
MPGD	Micropattern Gaseous Detector	60
MPV	most probable value	88
MUROS	Medipix Universal Read-Out System	66
MWPC	Multiwire Proportional Chamber	43
OFHC	oxygen-free high thermal conductivity	159
OSQAR	Optical Search for QED Vacuum Bifringence, Axions and Photon Regeneration	11
PCB	printed circuit board	57
PLC	programmable logic controller	98
PE	polyethylene	25
PP	polypropylene	24
PTFE	polytetrafluorethylene	24
PVLAS	Polarizzazione del Vuoto con LASer	10
QCD	Quantum Chromodynamics	3
SDD	silicon drift detector	165
SEM	scanning electron microscope	49
SIP	sputter ion pump	
SiPM	silicon photomultiplier	159
SM	Standard Model	155
SRS	Scalable Readout System	66
SRSN	silicon rich silicon nitride	63
ToA	Time-of-Arrival	62
ToT	Time-over-Threshold	126
TOS	Timepix Operation Software	160
TPC	Time Projection Chamber	66
USB	Universal Serial Bus	159
UV	ultraviolet	41
via	vertical interconnect access	59

VHDCI	Very High Density Cable Interconnect	159
VME	Versa Module Eurocard	105
WMAP	Wilkinson Microwave Anisotropy Probe	1
XRT	X-ray telescope	165

Acknowledgements

First of all, I would like to thank Prof. Dr. Klaus Desch for giving me the opportunity to work on this challenging and exciting project, and to be part of his research group. He also gave me the opportunity to live and work abroad at the research facility CERN for several months, which became an unforgettable experience. I want to warmly thank all of my colleagues at Bonn for the great working atmosphere, the support and encouragement throughout the work of this thesis, but of course also for the awesome time we had together not only during the many Jamborees and DPG spring conferences. Especially I want to thank my (former) office mates, Christoph Brezina, Tobias Schiffer and Sebastian Schmidt for the great team spirit and mutual support. Oliver Ricken, with whom I spend a lot of my free time at CERN and who contributed largely to the time at CERN being highly productive as well as enjoyable, I would like to thank as well, we will never forget the devil’s Tarte Flambee from hell. To Jochen Kaminski, Tobias Schiffer and Sebastian Schmidt goes a special ’Thank you’ for proofreading (parts) of this thesis.

I thank the members of the CAST collaboration for all the help, support and advise during commissioning and operation of the InGrid based X-ray detector at the experiment, especially CAST’s former technical coordinator Martyn Davenport, CAST’s vacuum guru Jean-Michel Laurent and Madalin Rosu, but also all fellow shifters who helped keeping the experiment running and with whom I spend many early mornings at CAST waiting for the Sun to rise.

Also, I want to think my friends from the rowing club ARC Rhenus for the many great days and evenings we spent together on land, the Rhine or other rivers, channels and lakes. These always were and are a tremendous source of joy and recreation, especially the tablerounds. To all of you, a sounding ’Αριστον μεν υδωρ’.

Another off-work activity, which definitely helped me in keeping the balance between life and work, was the small tabletop round of fellow physicists. In the Legends of Andor we saved the kingdom from the evil dragon and started our journey north, facing dark storms and malicious creatures while enjoying one or another fine scotch single malt. And while the journey north is almost at its end, still the next adventures await.

At the end, I want to thank my mother, Gerlind Krieger, for her tremendous and unconditional support throughout the many years and especially during the last months while I was writing my thesis. Without her, I would not be where and who I am today.